Hybrid heterostructures and materials based on transition metal dichalcogenides

Universitat de València

Instituto de Ciencia Molecular (ICMol)

***

Memoria presentada por Marc Morant Giner para aspirar al grado de Doctor en Nanociencia y Nanotecnología

***

Dirigida por el Prof. Eugenio Coronado Miralles

y

la Dra. Alicia Forment Aliaga

***

Julio 2020

Informe favorable

D. EUGENIO CORONADO MIRALLES, catedrático del Departamento de Química Inorgánica de la Universitat de València y DÑA. ALICIA FORMENT ALIAGA, doctora por la Universitat de València y actualmente investigadora en el Instituto de Ciencia Molecular de la Universitat de València,

CERTIFICAN:

Que la memoria presentada por D. Marc Morant Giner con título *"Hybrid heterostructures and materials based on transition metal dichalcogenides"* corresponde a su Tesis Doctoral y ha sido realizada bajo su dirección en el Instituto de Ciencia Molecular, autorizando mediante este escrito la presentación de la misma para optar al grado de Doctor.

En Paterna, a 2 de junio de 2020.

Prof. Eugenio Coronado Miralles Dra. Alicia Forment Aliaga

All truth passes through three stages. First, it is ridiculed. Second, it is violently opposed. Third, it is accepted as being self-evident.

A. Schopenhauer

A mis padres, a mi hermana y a cuantos confiaron en mí.

Agradecimientos

Aunque solo reluzca mi nombre en la portada, esta tesis es el resultado de coordinar muchas mentes y manos. Y, como *es de bien nacidos ser agradecidos*, paso sin más dilación a dar las gracias a todas aquellas personas que han contribuido de manera directa o indirecta al desarrollo del presente manuscrito.

Por tanto, en primer lugar, me gustaría dedicarles unas palabras de agradecimiento a mis directores, Eugenio Coronado y Alicia Forment. Al lado de Eugenio, he comprobado que se puede explicar magnetismo con los dedos índices y que el humor no está reñido con la nanociencia y el buen hacer. También he sido testigo de su innegable talento, generosidad, grandilocuencia y poder de convicción. En ocasiones, sus palabras me han confundido; en otras tantas, me han hecho entender que la única lucha que se pierde es la que se abandona. ¡Muchas gracias por haberme brindado la oportunidad de crecer como profesional y persona en uno de los mejores grupos de investigación! Por otro lado, me gustaría dejar constancia del rigor científico, la paciencia, la humildad y la abnegación de Alicia, recalcando especialmente su carácter conciliador y empático a la hora de resolver cualquier problema. ¡Muchas gracias por haberme acompañado durante todo el camino! ¡No hay obstáculo que se nos resista!

A continuación, debo confesar que, a lo largo de la aventura del doctorado, he contado con el apoyo y la confianza de investigadores magníficos. A Sergio Tatay le debo buena parte del éxito por haberme ayudado a poner a punto el enrevesado método de la exfoliación química. Además, cuando me asaltaban las dudas o tenía que hacer frente a las dificultades de dicha metodología, siempre encontraba abierta la puerta de su despacho, entre volutas de cigarrillo electrónico. La estancia de Antonio Alberola en el instituto fue fugaz, pero aun así, consiguió dejar una impronta azulada (debido al azul de Prusia, claro) en mi trayectoria. Más tarde, Marta Viciano marcó el comienzo de una nueva era (la de las moléculas fotocrómicas) y nuestras mentes se inundaron de luz. Con Rodrigue Lescouëzec, sembramos otro campo de investigación, justo en las postrimerías del doctorado. ¡Ya queda poco para recolectar el fruto!

Llegados a este punto, me siento en la obligación de darles las gracias a todos los colaboradores que han hecho posible la publicación de mis dos artículos.

A pesar de que mi estancia en el grupo de Andreas Hirsch no dio lugar a publicación alguna, me permitió descubrir otros escenarios y *modus operandi*. Y, gracias a Gonzalo Abellán, Edurne Nuin y Stefan Wild, tuve una cálida acogida en una Bavaria terriblemente castigada por el frío. Alemania tampoco me defraudó. Al fin y al cabo, no es tan fiero el león como lo pintan.

En el laboratorio, he tenido la suerte de trabajar estrechamente con otros doctorandos de mi instituto, como Roger Sanchis, Ramón Torres, Alejandro Núñez, Isaac Brotons, José Miguel Carbonell, Iván Gómez y Natalia Vassilyeva. Asimismo he mantenido colaboraciones a distancia con Luke T. Norman y Jana Glatz, a quienes no he tenido el gusto de conocer en persona. Espero que algún día se crucen nuestros caminos. Entre todos, hemos puesto en alza el valor del MoS_2.

A mis compañeros de oficina también les debo muchísimo. Ha sido un placer haber compartido despacho con Marian Cervera, Miguel Gavara, Garin Escorcia, Javi Castells, Alejandra Soriano, Yan Duan, Vero Jornet, Ramón Torres, Roger Sanchis, Isaac Brotons, Katia Caamaño, Helena Prima, Marta Galbiati, Josef Svetlik, Safaa Elidrissi y Christian Dolle.

También es de justicia reconocer los méritos de Ruth Manzanares, Estela Vives, Paco Escrig, Manuel Pérez, Paco Cuenca, Raquel Ballesteros, Manuel Quesada, Eva Amparo Jaime, Santiago Collado, Fina Civera, Mayte López, José Vicente Usagre, Ángel López, Chema Martínez, Gloria Agustí, Cristian Zoia, Pascual Fernández, Álex Gómez, Carlos Gómez, Sam Benmansour, Magdalena Fitta, Efrén Navarro, Carlos Martí, Marta Galbiati, Artem Gushchin, Miguel Clemente, Mónica Giménez, Guillermo Mínguez, Josep Canet, Elena Pinilla, Prakash Mondal, Eleni Mazarakioti, Manuel Souto, Eduardo Andrés, Samuel Mañas, Luis Escalera, Víctor Rubio, Néstor Calvo, José Alberto Carrasco, Euge Miguel, Víctor García, Javi López, Aman Ullah, Luis León, Marta Alcázar, Carlos Prado, Marta Vegas, Fani Tiburcio, Cristina Negro, Paula Escamilla, Loli Jordán, María Monrabal y Eva Tormos. Y los de todos los colegas del ICMol que me han allanado el camino.

En el terreno personal, el ICMol ha sido una excelente cantera de amigos. Al poco de haber empezado el máster en Nanociencia y Nanotecnología Molecular, trabé amistad con los expatriados del grupo: Michele Mattera (de Italia), Tato López (de Colombia) y Alex Abhervé (de Francia). Posteriormente, se nos unió Ramón Torres, otro trasnochador de campeonato. Aún recuerdo nuestras idas y venidas por el barrio del Carmen mientras se nos escurría la noche entre los dedos, la Ruta del Mojito, la *bomba china*, la penumbra de Mogambo, el Carnaval de Canals (en el que Eva Tormos demostró ser una anfitriona soberbia), el reparto de *souvenirs* en casa de Álex (a mí me tocó en herencia una nevera portátil y unas luces de discoteca)…

Me siento muy orgulloso de mi pequeña familia científica y amistades porque sinceramente creo que han hecho mucho más por mí de lo que yo he podido hacer por ellos, violando así el principio universal de la reciprocidad. Por tanto, les agradezco a todos ellos su incondicional apoyo. A Yan Duan, mi mentora en la sombra, por sus impagables consejos y su comedimiento a la hora de echarme la bronca. A Paco Escrig, por su plena disponibilidad, su simpatía y su espíritu conciliador. A José Jaime Baldoví, por sus teorías fantásticas, su dialéctica y su conocimiento absoluto sobre cualquier tema de interés. A Vero Jornet, mi alma gemela, por su comprensión, su humildad y su entrega absoluta. Al "comandante" Garín Escorcia, por su inestimable ayuda, su imperturbable paciencia y su infinita serenidad. A Isabel Pont, por su sonrisa y su curiosidad. A José Miguel Carbonell, por su franqueza, su perspicacia y sus ideas de bombero. A Euge Miguel, por su confianza y su buena predisposición. A María Molina, por su alegría, su amabilidad y su sed de aventuras. A Marcel Disl, por sus ganas de fiesta y sus aires de juventud. A Josef Světlík, por su fiel compañía y su buen gusto musical. A Àlvar Camarena, por su campechanía y su sabiduría. A Safaa Elidrissi, por su optimismo, su generosidad y su lealtad. A Silvia Giménez, por su cordialidad, su empatía y su sentido del humor. A Chandan Dey, por su bondad, su sencillez y sus dotes de cocinero. A Ziqui Hu, por su cercanía y su entusiasmo. A Dorye Esteras, por su discurso positivo, su energía vital y su afición al baile. A Natalia Vassilyeva, por su halo de misterio, su talento artístico y sus ideas innovadoras. A la comunidad turca (Muharrem Çiftçi, Zahida Sultanova y Gokhan Gureser). Çok teşekkürler! A Lorena Bareño, por su dulzura, su risa contagiosa y sus locuras. A la comunidad rumana

(Alina Chezan y Mihaela Mocanu). Mulţumesc pentru tot! A Marie Bob, por su carácter desenfadado y sus ritmos africanos. A Vicent Monzó, por su espontaneidad y su instinto aventurero. A Ez Elddine Derkawski, por su atenta mirada y su magnanimidad. A mis compañeros y amigos de la carrera (Antonio López, Paco Guillamón, Marina Polo, Alba Sereno, Pasqual Serra y Neus Torres), por haberme "sufrido" durante tantos años. Y a la comunidad West Coast Swing de Valencia, por haberme recibido con los brazos abiertos.

Por último, también me gustaría dedicarle este triunfo a mi familia. Desde que empezó la aventura, mis padres y mi hermana han tenido que soportar mis continuos cambios de humor, especialmente durante el confinamiento provocado por la Covid-19. Si he llegado lejos es porque los que me precedieron me revelaron el secreto de la paciencia. ¡Muchas gracias por haberme enseñado a desplegar las velas ante la tormenta y a porfiar en la empresa! Moltes gràcies per la vostra confiança!

List of abbreviations

0D	zero-dimensional
1D	one-dimensional
1H-MoS_2	MoS_2 polytype with one S-Mo-S layer per unit cell and hexagonal symmetry
1T-MoS_2	MoS_2 polytype with one S-Mo-S layer per unit cell and tetragonal symmetry
2D	two-dimensional
2D/2D	that implies an interface made of two different 2D materials
2H-MoS_2	MoS_2 polytype with two S-Mo-S layers per unit cell and hexagonal symmetry
3D	three-dimensional
3R-MoS_2	MoS_2 polytype with three S-Mo-S layers per unit cell and rhombohedral symmetry
a	lattice parameter associated to *x*-axis
A	area
ac	alternating current
ACI	alternating current impedance
AFM	atomic force microscopy
At%	atomic percentage
ATR	attenuated total reflectance
b	lattice parameter associated to y-axis
bpy	2,2'-bipyridine
BET	Brunauer-Emmett-Teller
c	lattice parameter associated to z-axis
C	capacitance
ce-MoS_2	chemically exfoliated MoS_2
CV	cyclic voltammetry
CVD	chemical vapour deposition
dc	direct current
DFT	density functional theory
DMSO	dimethyl sulfoxide
DVD	digital versatile disc
EDS	energy-dispersive X-ray spectroscopy
EIS	electrochemical impedance spectroscopy
EPR	electron paramagnetic resonance
ETCST	electron transfer coupled to a spin transition
FFT	fast Fourier transform
FTIR	Fourier transform infrared

FWHM	full width at half maximum
HER	hydrogen evolution reaction
HOMO	highest occupied molecular orbital
HRTEM	high-resolution transmission electron microscopy
HS	high spin
I	intensity
I	nuclear spin
I-V	intensity-voltage
ICP-OES	inductively coupled plasma optical emission spectrometry
IS	isomer shift
LCC	liquid cascade centrifugation
LIB	lithium-ion battery
LS	low spin
LPE	liquid-phase exfoliation
LUMO	lowest unoccupied molecular orbital
m	mass
M	metal (if referred to TMDCs, a transition metal)
M_W	molecular weight
me-MoS_2	mechanically exfoliated MoS_2
MeOH	methanol
n	number of equivalent nuclei
***n*-BuLi**	*n*-butyllithium
NMR	nuclear magnetic resonance
NP	nanoparticle
NSDFT	non-linear solid density functional theory
OER	oxygen evolution reaction
PB	Prussian blue
PBA	Prussian blue analogue
PEC	photoelectrochemical
PL	photoluminescence
PSD	pore size distribution
PVD	physical vapour deposition
PXRD	powder X-ray diffraction
Q	1) capacity or 2) parameter due to constant phase element
QS	quadrupole splitting
R	resistance
R_p	profile residual
R_{wp}	weighted profile residual
rGO	reduced graphene oxide
SA	surface area

SAED	selected-area electron diffraction
SAM	self-assembled monolayer
SCO	spin crossover
SEM	scanning electron microscopy
SIB	sodium-ion battery
SQUID	superconducting quantum interference device
STEM	scanning transmission electron microscopy
t	time
$\mathbf{T_C}$	Curie temperature
$\mathbf{T_{relax}}$	relaxation temperature
TEM	transmission electron microscopy
TGA	thermogravimetric analysis
TIP	temperature-independent paramagnetism
TMDC	transition metal dichalcogenide
tu	thiourea
UV/Vis	ultraviolet/visible
v	scan rate
V	voltage
vdW	van der Waals
W	Warburg element
X	chalcogenide
XPS	X-ray photoelectron spectroscopy
ZFC-FC	zero field cooled-field cooled
ZP	zeta potential
Γ	full width at half height for Mössbauer peaks
χ_m	molar magnetic susceptibility

Specific nomenclature of reagents, products or samples

Chapter II

sample 1	$(K_{0.47}Fe_4^{III}[Fe^{II}(CN)_6]_{3.14})@(MoSO_{1.7})_{0.44}\cdot 26H_2O$
sample 2	PB grown on top of ce-MoS_2 flakes deposited over a SiO_2 (285 nm)/Si substrate as a result of treating the deposited material with a $K_3Fe(CN)_6$:$FeCl_3$ aqueous solution
sample 3	PB grown on top of ce-MoS_2 flakes deposited over a SiO_2 (285 nm)/Si substrate as a result of treating the deposited material with a $K_3Fe(CN)_6$:$FeCl_3$ aqueous solution 2.5 times more diluted than the one used for preparing **sample 2**
sample 4	PB grown on top of ce-MoS_2 flakes supported onto prepatterned interdigitated Au electrodes
sample 5	PB grown on top of me-MoS_2 flakes deposited over a SiO_2 (285 nm)/Si substrate as a result of treating the deposited material with *i*) *n*-BuLi and *ii*) $K_3Fe(CN)_6$:$FeCl_3$ aqueous solution
sample 6	me-MoS_2 flakes deposited over a SiO_2 (285 nm)/Si substrate and treated with a $K_3Fe(CN)_6$:$FeCl_3$ aqueous solution
sample 7	$(KFe^{III}{}_4[Fe^{II}(CN)_6]_{3.27})@(MoS_2)_{0.61}\cdot 23H_2O$

Chapter III

FeCo@MoS_2	$Cs\subset\{[Fe^{II}(Tp)CN)_3]_4[Co^{III}(Tp)]_3[Co^{II}(Tp)]\}\cdot[MoS_2]_2$
FeCo PBA	Prussian blue analogue based on Fe and Co
dia-FeCo cube	$Cs\subset\{[Fe^{II}(Tp)CN)_3]_4[Co^{III}(Tp)]_4\}ClO_4$
para-FeCo cube	$Cs\subset\{[Fe^{II}(Tp)CN)_3]_4[Co^{III}(Tp)]_3[Co^{II}(Tp)]\}$

Chapter IV

CDD-H	closed-structure 1,2-bis(2-methyl-5-phenylthien-3-yl)cyclopentene
CDD-H+MoS_2	mixture of 7.4 mg of ce-MoS_2 flakes and 2.2 mg of CDD-H grinded in a mortar
CDD-MoS_2	product resultant from mixing ce-MoS_2 flakes with CDD-$N_2^+Cl^-$
CDD-NH_2	closed-structure 1,2-bis[2-methyl-5-(4-aminophenyl)-thien-3-yl]cyclopentene
CDD-$N_2^+Cl^-$	diazonium salt resultant from the diazotization of CDD-NH_2 in HCl medium
DD-H	ODD-H and CDD-H
DD-H+MoS_2	ODD-H+MoS_2 and CDD-H+MoS_2
DD-MoS_2	ODD-MoS_2 and CDD-MoS_2
DD-NH_2	ODD-NH_2 and CDD-NH_2
ODD-H	open-structure 1,2-bis(2-methyl-5-phenylthien-3-yl)cyclopentene
ODD-H+MoS_2	mixture of 7.2 mg of ce-MoS_2 flakes and 2.3 mg of ODD-H grinded in a mortar
ODD-MoS_2	product resultant from mixing ce-MoS_2 flakes with ODD-$N_2^+Cl^-$
ODD-NH_2	open-structure 1,2-bis[2-methyl-5-(4-aminophenyl)-thien-3-yl]cyclopentene
ODD-$N_2^+Cl^-$	diazonium salt resultant from the diazotization of ODD-NH_2 in HCl medium

Chapter V

cluster@MoS_2	ce-MoS_2 flakes electrostatically functionalized with W_3S_4 clusters
Mo_3S_4 (cluster)	$[Mo_3S_4(tu)_8(H_2O)]Cl_4 \cdot 4H_2O$ cluster
W_3S_4 (cluster)	$[W_3S_4(tu)_{8-x}(L)_{1+x}]Cl_4 \cdot 2H_2O$ cluster (x = integer between 0 and 8), where tu stands for thiourea and L for other type of ligand, like H_2O or MeOH.
WS_2/MoS_2 heterostructure	heterostructures that contain with WS_2/MoS_2 interface like that resulting from calcining cluster@MoS_2 or from mechanically stacking layers

Motivation and organization

The outbreak of nanomaterials is a clear sensor of the scientific advance. The design of nano-sized materials at will permits to tailor the fascinating novel properties resulting from a drastic reduction in dimensionality. In this vein, we have done our particular contribution to the field of the so-called 2D materials

The main goal that has motivated the development of this Thesis is the functionalization and combination of ultrathin MoS_2 flakes obtained by chemical exfoliation with different molecular-based systems. Over the last five years, we have pursued the idea of preparing new MoS_2-based materials in order to exploit the synergistic effects occurring in nanocomposites or tune some MoS_2 properties by means of external stimuli.

This Thesis is divided into the following blocks:

Chapter I begins with a brief introduction to nanomaterials. After that, two-dimensional (2D) materials are succinctly described. Subsequently, the family of layered transition metal dichalcogenides (TMDCs) is presented. Next, the focus turns to MoS_2, the most studied layered TMDC. In this latter section, we can find detailed information about the most common polytypes, dry and wet exfoliation methods, and composites based on MoS_2 layers. Finally, the molecular functionalization of MoS_2 is described.

Chapter II is focussed on the preparation of a new MoS_2-based composite by combining chemically exfoliated MoS_2 (ce-MoS_2) flakes and Prussian blue (PB) precursors. The synthetic strategy takes profit from negative-charged MoS_2 flakes as both reducing agent and 2D platform for the PB nucleation. We show that MoS_2 layers are fully oxidized after functionalization. Interestingly, the resultant composite exhibits an excellent performance as cathode material for sodium- and potassium-ion batteries (SIBs and KIBs, respectively). Finally, we give some insights about how to reduce the oxidation extent into our final composite.

Chapter III is addressed to the preparation of a novel composite by combining ce-MoS_2 flakes and a preformed diamagnetic FeCo cube.

We provide evidence to support the idea that the diamagnetic system is transformed into a paramagnetic compound, as a result of the electron transfer from negative-charged MoS_2 flakes to the starting FeCo cube.

Chapter IV talks about the covalent functionalization of ce-MoS_2 flakes *via* the well-known diazonium strategy, starting from a photochromic dithienylethene derivative (in its open- and closed-structure forms) bearing two reactive sites. The results obtained from several characterization techniques confirm the formation of new C–S bonds between both interacting components. Interestingly, it appears that the inherent photoluminescence (PL) of the organic molecule is quenched after functionalization, indicating a possible charge transfer between the 2D material and the attached dithienylethene derivative.

Chapter V tackles the formation of WS_2/MoS_2 heterostructures through the thermal treatment of MoS_2 layers electrostatically functionalized with W_3S_4-core clusters. This chemical strategy combines the advantages of a solution approach (simplicity, scalability, and low cost) with the formation of good quality interfaces (usually, reached by more complex physical methods). The PL of both counterparts is significantly quenched, which would confirm an efficient interlayer coupling.

Chapter VI summarizes the main conclusions of this Thesis.

At the end of the manuscript, we have included an appendix that explains in much more detail certain specific aspects about UV/Vis, Mössbauer and electrochemistry results. We hope that this information helps the readers to follow better the results presented here.

List of publications

1. Marc Morant-Giner, Roger Sanchis-Gual, Jorge Romero, Antonio Alberola, Leticia García-Cruz, Said Agouram, Marta Galbiati, Natalia. M. Padial, João C. Waerenborgh, Carlos Martí-Gastaldo, Sergio Tatay, Alicia Forment-Aliaga, and Eugenio Coronado, Prussian Blue@MoS_2 Layer Composites as Highly Efficient Cathodes for Sodium- and Potassium-Ion Batteries. *Adv. Funct. Mater.* **28**, 1706125 (2018).

2. Marc Morant-Giner, Isaac Brotons-Alcázar, Nikita Y. Shmelev, Artem L. Gushchin, Luke T. Norman, Andrei N. Khlobystov, Antonio Alberola, Sergio Tatay, Josep Canet Ferrer, Alicia Forment-Aliaga, and Eugenio Coronado, WS_2/MoS_2 Heterostructures via Thermal Treatment of MoS_2 Layers Electrostatically Functionalized with W_3S_4 Molecular Clusters. *Chem. Eur. J.* **26**, 6670–6678 (2020).

3. Ramón Torres-Cavanillas, Marc Morant-Giner, Garin Escorcia-Ariza, Julien Dugay, Josep Canet-Ferrer, Sergio Tatay, Salvador Cardona-Serra, Mónica Giménez-Marqués, Marta Galbiati, Alicia Forment-Aliaga, and Eugenio Coronado, Smart molecular/MoS_2 Heterostructures Featuring Light and Thermally-Induced Strain Driven by Spin Switching (submitted).

4. Marc Morant-Giner, Jana Glatz, Rodrigue Lescouëzec, Alicia Forment-Aliaga, and Eugenio Coronado, A Novel Prussian Blue@MoS_2 Layer Composite with Photomagnetism (in preparation).

5. Marc Morant-Giner, José M. Carbonell-Vilar, Marta Viciano-Chumillas, Alicia Forment-Aliaga, and Eugenio Coronado, Covalent Functionalization of MoS_2 with Dithyelethene Molecules (in preparation).

Table of contents

List of figures

List of tables

Ⅰ. General introduction

I.1. Nanomaterials

The emergence of nano-sized materials (or just nanomaterials), understood as engineered materials wherein at least one of the three spatial dimensions is less than or equivalent to 100 nm, has revolutionized practically every field of science and technology. The properties of nano-structured materials differ from those observed in their bulk counterparts as a result of strong quantum confinement of the electrons and surface effects.[1] Thus, the possibility of synthesizing materials with an accurate control over the final dimensionality not only permits the tunability of their physical and chemical properties but also the fabrication of miniaturized devices and machines.

Depending on the number of dimensions exceeding the nanometric scale (1 nm = 10^{-9} m), nanomaterials can be classified as zero-, one-, or two-dimensional (0D, 1D, and 2D, respectively).[2] Thus, 0D nanoparticles, 1D nanowires, and 2D nanolayers are archetypal examples of nanomaterials (see **Figure I-1**).

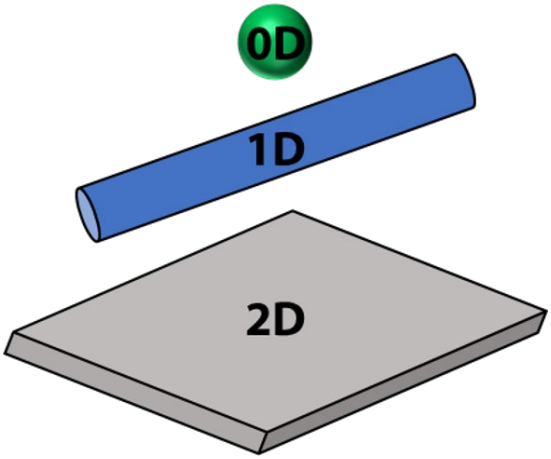

Figure I-1. Schematic representation of 0D, 1D, and 2D nanomaterials.

I.2. 2D materials

Once explained the classification of nanomaterials according to the dimensionality criterion, it is important to emphasize that the present Thesis is set within the context of 2D nanomaterials (2D materials, in short). For further understanding, the introduction goes from general to specific issues, covering sections devoted to 2D materials, then moving into layered transition metal dichalcogenides (TMDCs) family, and finally focusing on the target material of this Thesis: molybdenum disulphide (MoS_2).

2D materials[3,4] not only refer to single layers (named as monolayers as well), with a thickness of one to very few atoms, but also to those crystalline layered materials thin enough (*i.e.*, with reduced periodicity in the z-axis) to exhibit quantum confinement of the electrons in the 2D plane. By extension, the third meaning of this expression stands for those bulk layered compounds susceptible to be transformed into mono- or few-layers. In these highly anisotropic materials, electrons are free to move in the 2D plane, yet their motion in the out-of-plane direction is restricted by quantum mechanics (**Figure I-2**).

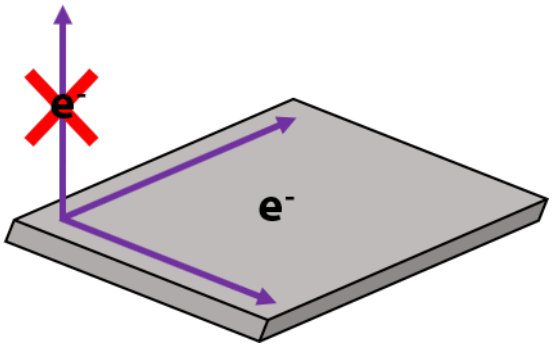

Figure I-2. Schematic representation of the electronic motion in a 2D material.

Another remarking feature of 2D materials is that they afford high surface-area-to-volume ratios since most of their constituent atoms are located on the surface. This peculiarity renders these materials attractive for catalysis,[5] sensing,[6] or energy storage[7,8] and conversion applications,[8] among others. Moreover, as a large fraction of atoms is exposed to the chemical environment, their reactivity is enhanced. In this context, surface functionalization represents an excellent strategy

to effectively modify or even tune their properties, in addition to impart them new functionalities.[9,10]

The one-atom-thick graphene tops the list of 2D materials as the first one to be discovered. In 2004, A. K. Geim, K. S. Novoselov and co-workers produced it by cleaving graphite with sticky tape (*i.e.*, by means of the well-known Scotch tape method) at the University of Manchester.[11] Apart from proving the dubious existence/stability of 2D materials, the isolation of graphene, a single layer of graphite, motivated the search for other non-carbonaceous examples (see **Figure I-3** and **Table I-1**).[3,4,12–14] Remarkedly, in 2010, A. K. Geim and K. S. Novoselov were honoured with Nobel Prize in Physics for the ground-breaking experiments regarding the 2D material graphene.

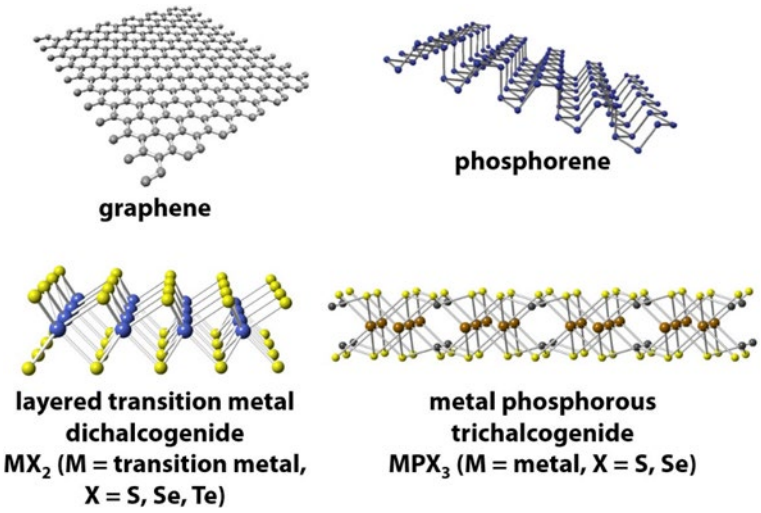

Figure I-3. Schematic representation of different 2D materials.

As shown in **Table I-1**, the 2D materials ranges from graphene and its analogues (for instance, silicene, germanene, or stanene), involving just one element, to compounds with more complex formulas, such as layered silicate minerals. In their bulk form (stacked 2D layers), the most common interlayer interactions are the vdW (*e.g.*, TMDCs) and electrostatic (*e.g.*, LDHs) ones, which are more easily breakable than intralayer covalent bonds.

Table I-1. Classification of 2D materials.

Group	General formula	Examples	Ref.
Graphene	C	C	15
Elemental graphene analogues	silicene (Si)	Si	16
	germanene (Ge)	Ge	16
	stanene (Sn)	Sn	16
	phosphorene (P)	P	16
	arsenene (As)	As	17
	antimonene (Sb)	Sb	17
	bismuthene (Bi)	Bi	17
Hexagonal boron nitride (h-BN)	h-BN	h-BN	18,19
Graphitic carbon nitride	g-C_3N_4	g-C_3N_4	18,20
Layered TMDCs	see TMDCs in this Chapter	MoS_2, WS_2	21-24
Phosphides	M_xP_y (M = metal)	MoP_2	25
III-VI layered semiconductors	MX (M = Ga, In; X = S, Se, Te)	GaS, InSe	26,27
MXenes	$M_{n+1}AX_n$ (n =1, 2, 3) (M = transition metal; A = element from group IIIA or IVA; X = C and/or N)	Ti_2AlC, Ti_3AlC_2, Ti4AlC3	28
Metal phosphorous trichalcogenides	MPX_3 (M = metal; X = S, Se)	$MnPS_3$ $FePS_3$ $NiPSe_3$	29
Layered metal hydroxides (LMHs)	layered single hydroxides (LSHs): $M^{II}(OH)_2$	$Ni(OH)_2$	30,31
	layered double hydroxides (LDHS): $[M_{1-x}{}^{II}M_x{}^{III}(OH)_2]^{x+}$	$Co(OH)_2$ $Zn(OH)_2$	
	(M^{II} = Ni^{II}, Co^{II}, etc.; M^{III} = Fe^{III}, Co^{III}, etc.)	Co^{II}/Al^{III}	
Metal oxides	MO_3 (M = Mo, Ta, etc.)	MoO_3	30,32
Transition metal oxyhalides	MOX (M = Fe, Cr, V, Ti; X = halogen)	FeOCl CrOF	33,34
Metal halides	MX_n (M = Fe, Cr, V, Ti; X = halogen)	$CrCl_3$	35
Perovskites	AMX_3 (A, M = cations; X = O, Cl, Br, etc.)	$CaTiO_3$	36,37
Layered silicate minerals	$[M_x(Al_{4-x}Mg_x)Si_8O_{20}(OH)_4]$ (M = monovalent cation; x = degree of isomorphous substitution) $X_2Y_{4-6}Z_8O_{20}(OH,F)_4$ (X = K, Na, Ca, Ba, Rb, Cs; Y = Al, Mg, Fe, Mn, Cr, Ti, Li, etc.; Z = Si, Al)	aluminium phyllosilicates	38
Metal-organic frameworks (MOFs)	no general formula	NiPc MOF MUV-1-Cl	39,40
Covalent-organic frameworks (COFs)	no general formula	HHTP-DPB COF-5	40

2D materials can be prepared by top-down (*i.e.*, by etching out crystal planes from the 3D structure) and bottom-up (*i.e.*, by constructing them

from atomic or molecular precursors that are suitable to react and grow in all the spatial directions except along the *c*-axis), as shown in **Figure I-4**. Whilst the top-down approach is based on the exfoliation technique, the bottom-up approach includes strategies as varied as wet chemical synthesis, chemical vapor deposition (CVD), physical vapor deposition (PVD), molecular beam epitaxy and atomic layer epitaxy.[41] Generally, top-down approaches are scalable and performable under ambient conditions. In contrast, bottom-up methods demand harsh reaction conditions (*i.e.*, high temperature and vacuum) and complex post-treatments.

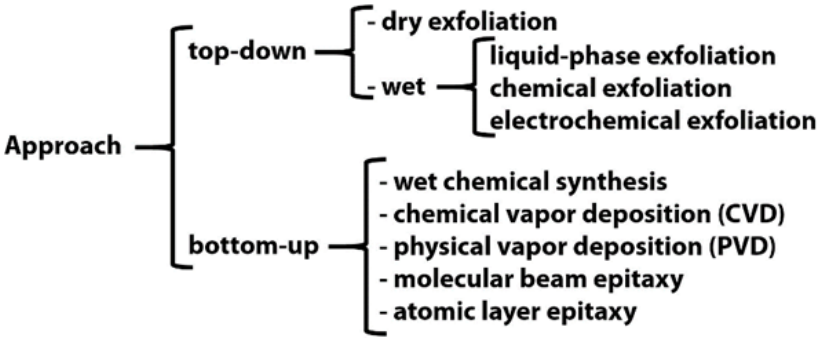

Figure I-4. General classification of the main methods for obtaining 2D materials.

I.3. Layered TMDCs

After graphene, the most studied family of 2D materials is that of layered TMDCS.[22,42] These compounds consist of vertically stacked X-M-X slabs with a general chemical formula of MX_2, where M stands for a transition metal (usually appertaining to groups IV-VII) and X refers to a chalcogen (S, Se, or Te). Within each X-M-X layer (typically 6–7 Å thick), one M atom lattice is sandwiched by two X atom lattices.[22] Individual X-M-X slabs are accessible by exfoliation as the interlayer van der Waals (vdW) interactions are much weaker than the intralayer covalent bonding (see **Figure I-5**).[43] This family of compounds displays a broad spectrum of electronic properties that may drastically vary depending on the composition (identity of M and X), structure (polytype) and dimensionality (number of X-M-X slabs). Such versatility covers electronic properties as varied as metallic, semi-metallic, semiconducting, superconducting, Mott transition, or

charge density wave behaviours.[21,22] The electronic structure of TMDCs relies on the filling of the *d* orbitals corresponding to M.[44]

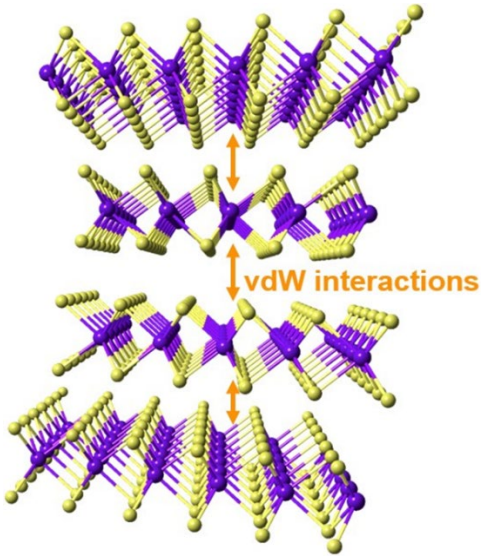

Figure I-5. Schematic representation of a layered TMDC (MX_2). Orange double-headed arrows indicate interlayer vdW interactions. Purple and yellow balls represent transition metal (M) and chalcogen (X) atoms, respectively.

I.4. MoS_2

MoS_2, traditionally used as dry lubricant[45] and catalyst for CO hydrogenation and hydrodesulfurization processes,[46] is one of the most studied TMDCs. Bulk MoS_2 can be described as a weak stacking of S-Mo-S layers, in which each Mo atom is coordinated to six S atoms in a trigonal prismatic or octahedral fashion.

I.4.1. MoS_2 polytypes

Whilst the octahedral coordination is only found in the 1T polytype, the trigonal prismatic coordination of Mo atoms occurs in 2H (also known as 1H in the case of a single layer) and 3R polytypes (see **Figure I-6**). Each polytype is identified according to an alphanumeric code, where the digit alludes to the number of S-Mo-S layers per unit cell and the letter indicates the structural symmetry (T = tetragonal, H = hexagonal, R = rhombohedral). The stacking order of S-Mo-S layers within a single crystallographic unit cell is expressed by a

combination of capital and lowercase letters (AbC, AbA, AbA-BaB, and AbA-CaC-BcB for 1T, 1H, 2H, and 3R, respectively), as illustrated in **Figure I-6**. These heterogeneities in stacking order may lead to interesting new phenomena due to the breaking of symmetry.[44] Apart from sharing crystallographic parameters, 2H and 3R properties are almost identical.[47] Therefore, only the main differences between 1H/2H and 1T properties are explained in the following lines.

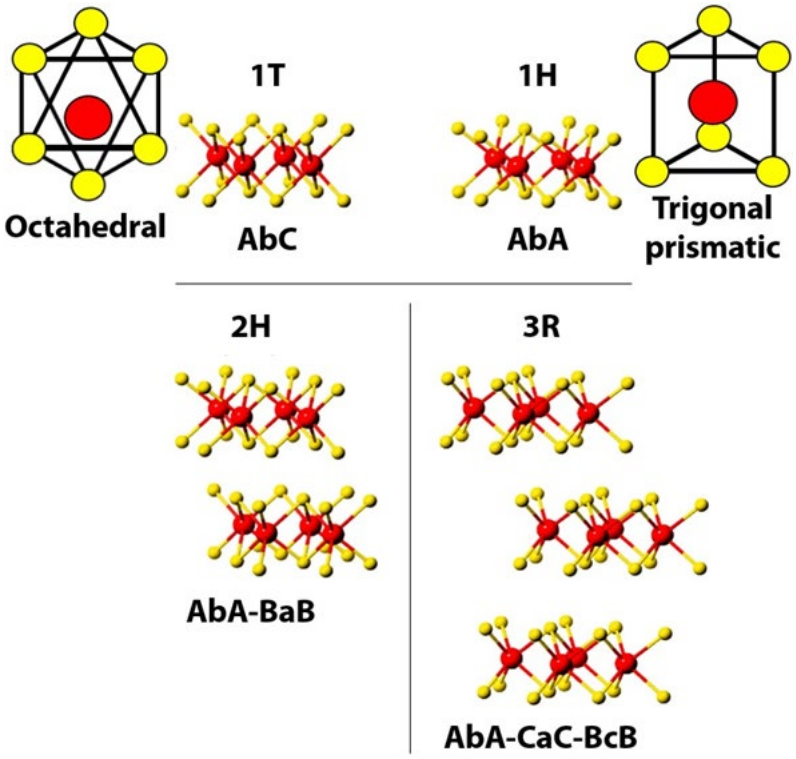

Figure I-6. Schematic representation of Mo coordination and the stacking sequence of S-Mo-S-layers in 1T-, 1H-, 2H-, and 3R-MoS_2 polytypes. Mo and S atoms are represented by red and yellow balls, respectively. Adapted from ref 48.

I.4.1.1.1H/2H polytypes

Bulk 2H-MoS_2 is chemically inert and thermodynamically stable,[44] existing in nature as mineral (molybdenite). 1H/2H-MoS_2 flakes can be synthesized by top-down (dry or wet mechanical exfoliation), as detailed in **MoS_2 exfoliation** section, and bottom-up (commonly, hydrothermal/solvothermal synthesis[49,50] or CVD[51]) approaches.

As established by the ligand field theory, the diamagnetic and semiconducting behaviour of 2H-MoS_2 results from the fully filled d_{z^2} and empty d_{xy} and $d_{x^2-y^2}$ orbitals (see **Figure I-7**).[52–54] Interestingly, this *n*-type semiconductor undergoes a transition from an indirect bandgap of 1.29 eV in (2H) bulk to a direct one of 1.90 eV in its (1H) monolayer form.[55] Thus, on account of its direct bandgap, 1H-MoS_2 exhibits photoluminescence (PL).[55] As the bandgap of this polytype can be engineered as a function of the number of layers, it is extensively used in the fabrication of electronic devices, like field-effect transistors (FETs).[56]

I.4.1.2.1T polytype

1T-MoS_2 does not exist in nature and its preparation involves different strategies: alkali metal ion intercalation followed by exfoliation,[57–60] electron-beam irradiation,[61] plasmonic hot injection,[62] Ar-plasma treatment,[63] strain engineering,[64] and hydrothermal[65,66] or solvothermal[67,68] synthesis starting from Mo and S molecular precursors.

1T-MoS_2 is metastable and may undergo structural distortions to give other non-stable polytypes showing tetragonal symmetry but with Mo-Mo clustering (dimerization or trimerization of Mo atoms).[69] As stated by the ligand field theory, the paramagnetic and metallic behaviour of 1T-MoS_2 results from the partially filled t_{2g} (d_{xy}, d_{xz}, d_{yz}) and empty e_g ($d_{x^2-y^2}$, d_{z^2}) orbitals (see **Figure I-7**).[22] In fact, 1T-MoS_2 is $\approx 10^7$ times more conductive than 2H-MoS_2.[70,71] The metallic behaviour, along with the presence of abundant active sites both at the edges and on the basal plane, endows 1T-MoS_2 with excellent properties for electrochemical catalysis.[72] Furthermore, 1T-MoS_2 possesses enlarged interlayer distance,[72] hydrophilicity[73] and optical transparency.[74]

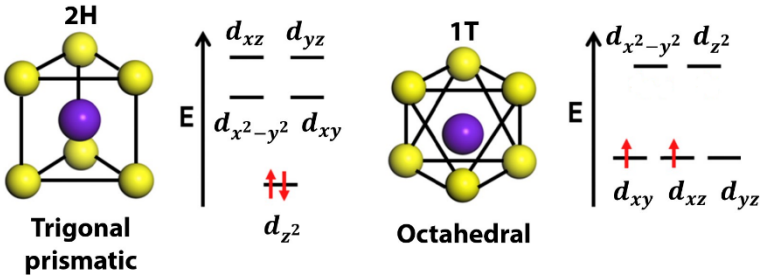

Figure I-7. Schematic representation of Mo coordination and energy level diagrams for 2H- and 1T-MoS_2. Mo and S atoms are represented by purple and yellow balls, respectively. Adapted from ref 75.

I.4.1.3.1H/2H↔1T interconversion

1H/2H and 1T polytypes are interconvertible through an intralayer atomic plane glide (*i.e.*, involving a transversal displacement of one of the S planes).[61] On one hand, the 1H/2H→1T transition can be carried out by following any of the top-down methods cited in the section corresponding to 1T polytype. On the other hand, the 1T→1H/2H transition can be triggered by thermal annealing,[76] laser irradiation[59] or microwave exposure.[77] Even simple aging is enough to induce this structural transformation.[78] In **Figure I-8**, the main interconversion strategies are enumerated. From here on, the expression 2H encompasses 1H and 2H structures for simplicity, as commonly done in this field.

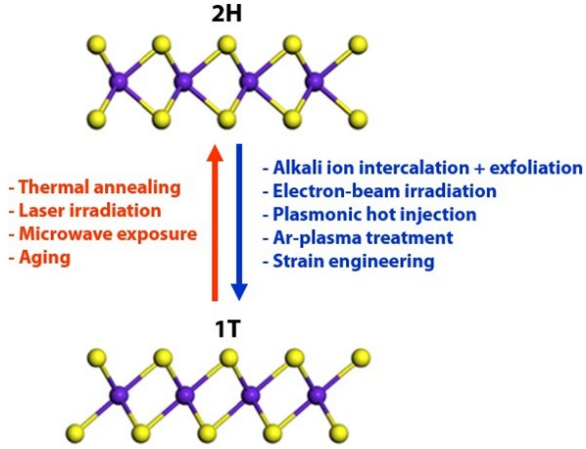

Figure I-8. Schematic representation of 2H↔1T interconversion. Structures extracted from ref 75.

I.4.2. MoS_2 exfoliation

To obtain 2D MoS_2 flakes, one of the most extensively used strategies is the exfoliation, which benefits from the energy unbalance between the in- and out-of-plane bonding present in the bulk structure. In general, exfoliation can be categorized into dry (mechanical) or wet (mechanical, chemical, or electrochemical).

I.4.2.1. Dry exfoliation

Mechanical exfoliation, pioneered by R. F. Frindt,[79] relies on putting in contact a multi-layered 2H-MoS_2 crystal with a viscoelastic surface (typically provided by a piece of Scotch tape[43,79] or a stamp of polymer nature)[80] in such a way that the adhesive forces between both materials are much stronger than the interlayer vdW ones (40–70 meV). In the conventional Scotch tape method (see **Figure I-9**), a strip of adhesive tape supporting a crystal is first folded over itself, carefully matching the two sticky extremes. Then, gentle pressure is imparted to the plasticized material. Finally, the unfolding step provokes the cleavage of MoS_2 into crystallites, which remain stuck to the tape just through the previously contacted planes. This process can be repeated several times until reaching the monolayer limit. In contrast to the Scotch tape method, the stamp-based one avoids the contamination of flakes by adhesive residues.

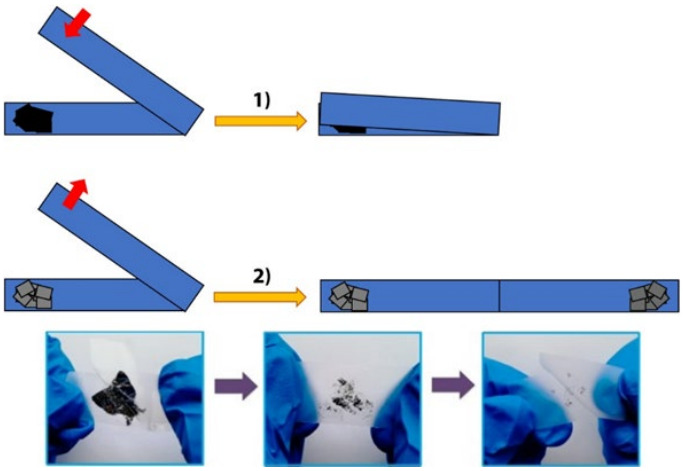

Figure I-9. Schematic representation and pictures showing the conventional Scotch tape method. Adapted from ref 81.

I.4.2.2. Wet exfoliation

Albeit dry mechanical exfoliation has been renowned as the best strategy to obtain the highest quality 2D MoS_2 for building up electronic and optoelectronic devices, it suffers from high dispersion of flakes with different thickness and low throughput of single layers.[47] Therefore, for large-scale production of ultrathin flakes, another strategy is required. In this respect, wet exfoliation techniques sacrifice the qualitative criterion for the benefit of the quantitative one.

Liquid-phase exfoliation

In liquid-phase exfoliation (LPE),[10,82] several mechanical forces (succinctly, shear and compression forces *via* wet ball milling and shearing mixing, or vibration and cavitation forces *via* ultrasonication) act upon bulk 2H-MoS_2 immersed in a suitable solvent or mixture of solvents, in presence or not of surfactants (see **Figure I-10**).[83–86] Proper solvents are those that not only improve the exfoliation yield as a result of a good matching of their surface tension with that of the layered crystals but also stabilize and prevent the resultant suspended flakes from immediate reaggregation and/or stacking.[83]

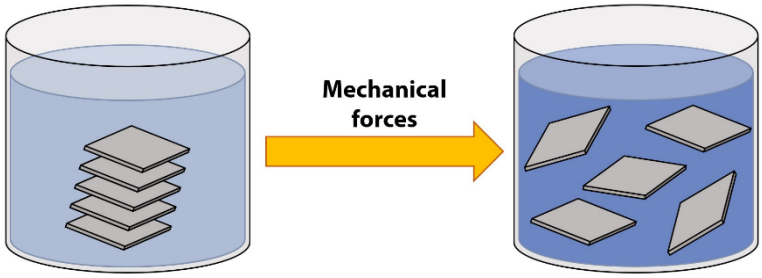

Figure I-10. Schematic representation of LPE.

Chemical exfoliation

In contrast to LPE, chemical exfoliation (see **Figure I-11a**) includes an intercalation step before the exfoliation *per se*, which involves some degree of chemical modification of MoS_2. The original method, pioneered by P. Joensen, R. F. Frindt, and S. R. Morrison, entails the *i*) synthesis of Li_xMoS_2 by heating polycrystalline 2H-MoS_2 soaked in a solution of *n*-butyllithium (*n*-BuLi, where *n* refers to the unbranched structure) for at least 48 h, under inert atmosphere, and *ii*) its

subsequent sonication in water, methanol, ethanol, or isopropanol.[57] Until now, several variations[70,87,88] of the primigenial recipe[57] as well as alternative protocols[58,89,90] have been developed. In all of them, the insertion of alkali metal ions (Li^+, Na^+, or K^+) into bulk structure leads to an expansion of the vdW gap, accompanied by an electron injection (*i.e.*, a chemical reduction) to the *d* band of the host 2H-MoS_2 layers and a partial 2H→1T polytype transition.[91,92] The enlargement of the interlayer distance is proportional to the volume of the intercalated species. The expansion lattice effect weakens the interlayer adhesion, reducing the energy barrier to exfoliation. Additionally, the further exfoliation of the alkali-intercalated MoS_2 in water results in the formation of hydrogen within the vdW gap, which pushes layers apart and facilitates even more the disassembling of the 3D structure.[57,93] In 2014, K. P. Loh's group proposed a two-step expansion and intercalation method to prepare MoS_2 sheets with a flake size up to 400 μm^2.[58] In this salient work, lithium, potassium and sodium naphthalenides were employed as intercalants. Recently, A. Criado, M. Prato *et al.* have reported an efficient chemical exfoliation based on the simultaneous intercalation of Na^+ and K^+ (under the form of NaK alloy) to produce highly enriched 1T-phase MoS_2 (94.5%).[90] In order to reduce the risk of explosion, safer alkali sources and milder reaction conditions have to be sought. In this vein, the highly pyrophoric *n*-BuLi diluted in hexane has been satisfactorily replaced by solid lithium borohydride ($LiBH_4$).[89] In this particular case, the absence of solvents and the gaseous nature of by-products leave alkali-intercalated MoS_2 free of impurities.

Electrochemical exfoliation

In electrochemical exfoliation (see **Figure I-11b**), the additional electric driving force enables far greater control over the intercalation extent, so that larger amounts of species can be accommodated in between MoS_2 layers in shorter lapses. Furthermore, the electrochemical approach maximizes the nanosheet size and yield in the exfoliation step.[94] For a typical electrochemical intercalation, 2H-MoS_2 is utilized as cathode, an alkali metal as anode and a solution containing metal ions as electrolyte.[95] A galvanostatic mode is applied to conduct the reaction at room temperature. The main limitation of this strategy is that only a little amount of the MoS_2 shaped into the electrode can undergo intercalation.[96]

In 2018, Y. Huang, X. Duan *et al*. achieved to prepare highly uniform phase-pure 2H-MoS_2 nanosheets by electrochemical insertion of tetraheptylammonium ions (THA^+) into a thin cleaved 2H-MoS_2 crystal and further sonication in a polyvinylpyrrolidone/dimethylformamide (PVP/DMF) solution.[97] For the fabrication of the electrochemical cell, a 2H-MoS_2 crystal was used as cathode, a graphite rod as anode and a solution of tetraheptylammonium bromide (THABr) in acetonitrile as electrolyte. Due to its large volume, the insertion of THA^+ causes an enormous expansion of the interlayer space, which substantially weakens vdW interactions in pursuit of the long-desired exfoliation efficiency.

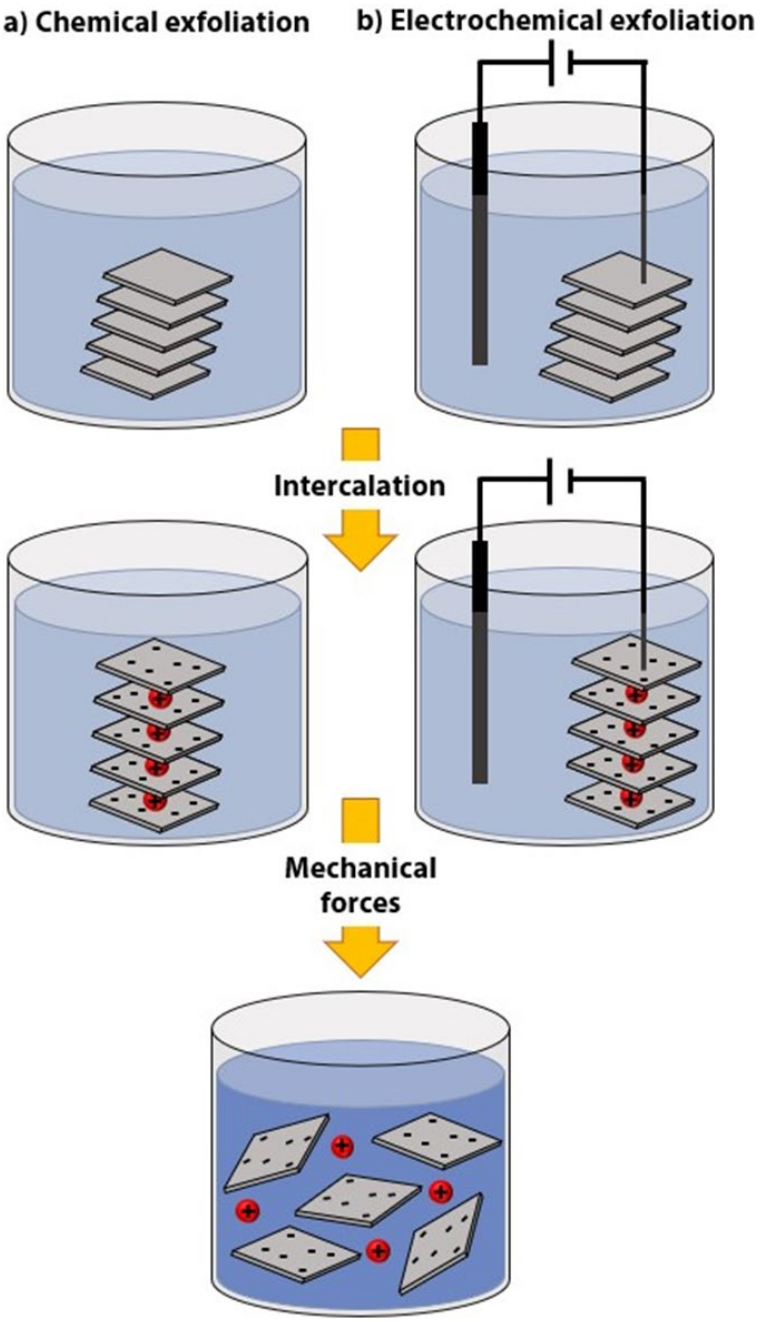

Figure I-11. Schematic representation of chemical and electrochemical exfoliation.

Insights on chemical exfoliation based on the insertion of alkali cations

As all the results collected in this Thesis are based on the chemical exfoliation of MoS_2 flakes, it is convenient to explain certain aspects in much more detail, such as the negative-charged nature of ce-MoS_2 flakes thus produced, the final purification step, and the pros and cons of this approach.

While some reports state that alkali-doped MoS_2 layers become neutral immediately after hydration, most of them consider that the suppression of the surface charge does not occur so quickly, providing negative zeta potential values as supporting evidence.[98] According to the latter trend of thought, interlayer electrostatic repulsions stabilize chemically exfoliated (ce) flakes in suspension.[99] Curiously, after reaggregation, the aged material is not well-dispersed, not even sonicating for 1 h.[59] So far, the neutralization of negative-charged MoS_2 flakes and the chemical species responsible for the reduction of water to hydrogen are still under study.

The hydrolysis reaction of the alkali-intercalated MoS_2 gives rise to the formation of alkali hydroxide. At this point, it is important to have in mind that corrosive media may damage the morphology of ce-MoS_2 flakes.[59] For this reason, freshly prepared suspensions demand a purification treatment, not only for removing alkali excess in form of hydroxide but also the unexfoliated material. In this regard, dialysis and centrifugation techniques play a paramount role. Henceforth, the so-called liquid cascade centrifugation (LCC) protocol, introduced by J. Coleman and co-workers for wet mechanical exfoliation, could be also applied to sequentially isolate ce flakes in dispersion according to their number of constituent layers.[100]

Remarkedly, MoS_2 flakes resultant from the intercalation of alkali cations always reveal coexistence of 1T and 2H polytypes, with a general metallic behaviour. Notwithstanding, they can recover their pristine semiconducting properties by controlled annealing.[76,101]

Usually, ce-MoS_2 flakes are plagued with defects and significantly smaller than those obtained by dry mechanical exfoliation. These two factors, along with the incomplete removal of solvents (specially, those having high boiling points) and/or chemical residues once deposited onto a substrate, can compromise their physical properties.

Nevertheless, the chemical exfoliation technique combined with a centrifugation-assisted flake-size selection process enables the large-scale production of ultrathin negative-charged flakes rich in 1T polytype, which are more reactive than their 2H analogues.

I.4.3. Composites based on MoS_2 flakes

The fabrication of composite materials (usually abbreviated as composites) represents an excellent strategy for overcoming the inherent limitations of MoS_2 or optimizing its properties in pursuit of a specific application, enabling the creation of advanced engineering (or at least more functional) materials. MoS_2-based composites are those resulting from the combination of MoS_2 (in any of its forms) with one or more different materials, so that the final material shows clearly distinguishable interfaces as well as improved properties in comparison to their constituents separately. The synthesis of composites can involve a simple physical mixture or a more complex chemical mixing (functionalization). The better performance of MoS_2-based composites arises from a synergistic effect between all components.

Once purified, ce-MoS_2 flakes can serve as building blocks in the preparation of composites in solution.[102,103] The properties and functions of MoS_2 nanosheet-based composites are not only reliant on their composition, crystal phase and structure but also on the spatial organization/assembly, surface exposure, distribution and interaction of/between each component.[104] They have been extensively used in fields as varied as energy conversion and storage, catalysis, sensing, or electronics, just to cite a few.[104]

So far, a plethora of materials (*e.g.*, noble metals, oxides, polymers or carbonaceous materials) have been coupled with MoS_2 nanosheets.[104] Noble metals, such as Au,[62,105–110] Pd,[109,111,112] Pt,[109,111] and Ag,[109,111] have been grown on MoS_2 flakes by solution-based chemical reduction. Moreover, MoS_2 nanosheets can either be decorated with Fe_3O_4 NPs by hydrothermal approach[113] or partially oxidized by thermal treatment to generate MoS_2/MoO_3 composites.[114] They can also be harnessed as templates for directing the assembly of organic molecules[115] or even functionalized with polymers *via* physical adsorption or weak non-covalent chemical bonding.[116,117] MoS_2 sheets have also been combined with amorphous carbon,[118,119] TiO_2 nanobelts/tubes,[120,121] SnO_2 nanotubes,[122] and other TMDCs.[102] Moreover, the construction of

hierarchical structures by compositing MoS_2 flakes with 1D, 2D, or 3D carbonaceous nanomaterials is an effective strategy to retain the large specific surface area of MoS_2 to a certain extent.[123–137]

When forming a composite, the most common synthetic strategies are the following ones:

- *i*) direct mixing of the components without[102,133] or with a specific chemical reaction between them, which is commonly known as *functionalization* of the 2D layer (see **MoS_2 functionalization** section).
- *ii*) CVD growth of one component onto the other.[131]
- *iii*) blending of MoS_2 precursor with the other/s components at room temperature or through hydro/solvothermal approach.[121–123,137]

I.4.4. MoS_2 functionalization

The molecular functionalization represents a step forward to the exfoliation, study and application of pure 2D materials. When preparing novel materials, the molecular functionalization unlocks a broad spectrum of possibilities as it permits to add functional groups to the lattice,[138–140] alter the properties of the exfoliated material,[141,142] combine the properties of the 2D platform with those of the attached molecular systems,[143] or create synergistic effects between the interconnected components.[144,145]

MoS_2 functionalization methods can be classified into non-covalent (*via* vdW or electrostatic interactions), coordinative (by means of coordination reactions) and covalent (through the formation of S–Mo or C–S bonds at S vacancies or on the basal plane, respectively).[80,92-95]

Non-covalent functionalization

2H-MoS_2 has been non-covalently functionalized by weak vdW interactions with dopants as varied as tetracyanoquinodimethane (TCNQ),[150,151] tetracyanoethylene (TCNE),[151] tetrathiafulvalene (TTF),[151] fullerenes (C_{60}),[152] thionine,[153] perylene diimides,[154] porphyrins,[154] phthalocyanines,[155–157] and photochromic molecules (see Chapter IV),[158] just to cite a few. The assembly of negative-charged

ce-MoS_2 flakes with cationic species due to electrostatic interactions is deemed to be another modality of non-covalent functionalization.[144,159]

Coordinative functionalization

The so-called coordinative functionalization (**Figure I-12a**) relies on coordinating surface S atoms of 2H-MoS_2 to metal centres. In a similar way to the reaction between inert 3D MoS_2 NPs and multidentate ligands,[160] S atoms have been linked to $M(OAc)_2$ salts (M = Ni, Cu, Zn, and OAc = acetate), yielding the maximum functionalization percentage with that based on copper.[161] Interestingly, on account of its surface modification, the resultant material was well dispersed in unconventional solvents (like isopropanol and acetone).

Covalent functionalization

An alternative to the previous approaches stems from the possibility of performing chemistry at S vacancies with thiol molecules.[141,162] Although S vacancies are naturally present in any MoS_2 lattice, they can be generated on purpose by means of defect engineering with the aim of increasing the functionalization percentage.[163] Therefore, these defects are acknowledged to be reactive sites, in which mercaptan molecules or derivatives can bind to unsaturated Mo atoms (**Figure I-12b**), giving rise to surface healing (if the C–S bond is cleaved after the chemisorption of thiol groups) or MoS_2 functionalization (if there is no bond breaking after the thiol attachment).[147] However, spectroscopic studies have called into question this covalent functionalization route, stressing that mercaptans can be first transformed into disulphides and then physisorbed onto MoS_2 basal planes.[164]

In contrast to the aforementioned option, the direct covalent attachment of organic moieties to the basal plane of MoS_2 does not take benefit from defects but from the nucleophilicity of surface S atoms conferred by the lone pairs and the good capacity of halide and diazo moieties as leaving groups (**Figure I-12c**). The nucleophilic attack targets the electrophilic C atom attached to the leaving group. The first reported example was based on the functionalization of negative-charged 1T-MoS_2 flakes by exploiting organohalide species.[138] Once functionalized, the electronic properties of MoS_2 were drastically affected from metallic to semiconducting nature. Thus, the

modification of band structure *via* covalent functionalization led to the reappearance of PL.

Following a strategy similar to that described above, 1T-MoS_2 nanosheets have been satisfactorily functionalized on the basal plane with commercial *para*-substituted diazonium compounds.[139] This achievement was also supported by density functional theory (DFT) calculations. The good dispersibility of the resultant material in anisole was regarded as a solid proof of surface modification.

Although the first results were obtained from 1T-MoS_2 (due to its higher reactivity), there are also interesting works that put the focus on 2H-MoS_2. For instance, 2H-MoS_2 flakes have been functionalized under mild conditions by using iodobenzene,[165] aryl diazonium salts,[166] or maleimides.[140,167] In the latter case, MoS_2 reacts with maleimides (prototypical electrophiles for sulphur-based nucleophiles) through Michael addition. In this reaction, the nucleophilic attack does not demand the presence of a leaving group.

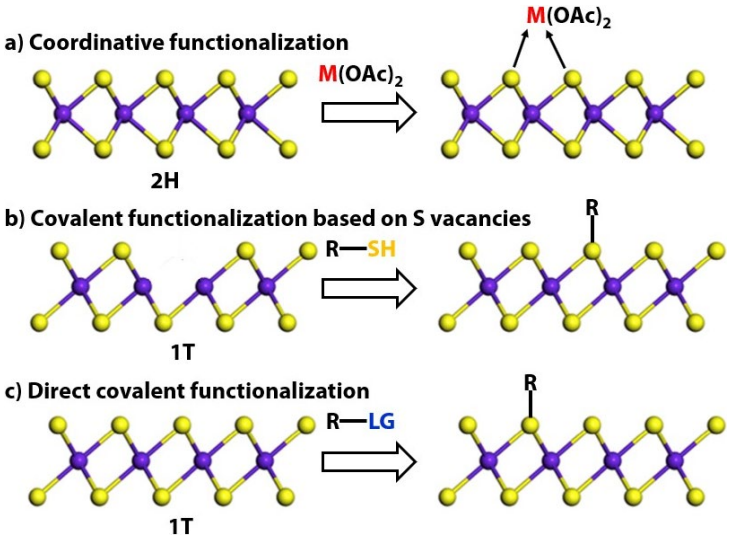

Figure I-12. Schematic representation of coordinative and covalent functionalization strategies. Structures extracted from ref 75. M = Ni, Cu, Zn; OAc = acetate; R = carbon backbone, SH = thiol group, LG = leaving group.

I.5. References

1. Roduner, E. Size matters: Why nanomaterials are different. *Chem. Soc. Rev.* **35**, 583–592 (2006).

2. Pokropivny, V. V. & Skorokhod, V. V. Classification of nanostructures by dimensionality and concept of surface forms engineering in nanomaterial science. *Mater. Sci. Eng. C* **27**, 990–993 (2007).

3. Mas-Ballesté, R., Gómez-Navarro, C., Gómez-Herrero, J. & Zamora, F. 2D materials: To graphene and beyond. *Nanoscale* **3**, 20–30 (2011).

4. Mannix, A. J., Kiraly, B., Hersam, M. C. & Guisinger, N. P. Synthesis and chemistry of elemental 2D materials. *Nat. Rev. Chem.* **1**, 0014 (2017).

5. Deng, D. *et al.* Catalysis with two-dimensional materials and their heterostructures. *Nature Nanotech.* **11**, 218–230 (2016).

6. Anichini, C. *et al.* Chemical sensing with 2D materials. *Chem. Soc. Rev.* **47**, 4860–4908 (2018).

7. Zhang, X., Hou, L., Ciesielski, A. & Samorì, P. 2D Materials Beyond Graphene for High-Performance Energy Storage Applications. *Adv. Energy Mat.* **6**, 1600671 (2016).

8. Xue, Y. *et al.* Opening Two-Dimensional Materials for Energy Conversion and Storage: A Concept. *Adv. Energy Mat.* **7**, 1602684 (2017).

9. Nguyen, E. P. *et al.* Electronic Tuning of 2D MoS_2 through Surface Functionalization. *Adv. Mater.* **27**, 6225–6229 (2015).

10. Ippolito, S., Ciesielski, A. & Samorì, P. Tailoring the physicochemical properties of solution-processed transition metal dichalcogenides via molecular approaches. *Chem. Commun.* **55**, 8900–8914 (2019).

11. Novoselov, K. S. *et al.* Electric field effect in atomically thin carbon films. *Science.* **306**, 666–669 (2004).

12. Butler, S. Z. *et al.* Progress, challenges, and opportunities in two-dimensional materials beyond graphene. *ACS Nano* **7**, 2898–2926 (2013).

13. Das, S., Robinson, J. A., Dubey, M., Terrones, H. & Terrones, M. Beyond Graphene: Progress in Novel Two-Dimensional Materials and van der Waals Solids. *Annu. Rev. Mater. Res.* **45**, 1–27 (2015).

14. Bhimanapati, G. R. *et al.* Recent Advances in Two-Dimensional Materials beyond Graphene. *ACS Nano* **9**, 11509–11539 (2015).

15. Yang, Z. *et al.* The prospective two-dimensional graphene nanosheets: Preparation, functionalization, and applications. *Nano-Micro Lett.* **4**, 1–9 (2012).

16. Balendhran, S., Walia, S., Nili, H., Sriram, S. & Bhaskaran, M. Elemental analogues of graphene: Silicene, germanene, stanene, and phosphorene. *Small* **11**, 640–652 (2015).

17. Pumera, M. & Sofer, Z. 2D Monoelemental Arsenene, Antimonene, and Bismuthene: Beyond Black Phosphorus. *Adv. Mat.* 29, 1605299 (2017).

18. Wang, Z. *et al.* Fabrication of Boron Nitride Nanosheets by Exfoliation. *Chem. Rec.* **16**, 1204–1215 (2016).

19. Emanet, M., Sen, Ö., Taşkin, I. Ç. & Çulha, M. Synthesis, Functionalization, and Bioapplications of Two-Dimensional Boron Nitride Nanomaterials. *Front. Bioeng. Biotechnol.* **7**, 363 (2019).

20. Rono, N., Kibet, J. K., Martincigh, B. S. & Nyamori, V. O. A review of the current status of graphitic carbon nitride. *Crit. Rev. Solid State* (2020).

21. Wang, Q. H., Kalantar-Zadeh, K., Kis, A., Coleman, J. N. & Strano, M. S. Electronics and optoelectronics of two-dimensional transition metal dichalcogenides. *Nature Nanotechnol.* **7**, 699–712 (2012).

22. Chhowalla, M., Shin, H., Eda, G. & Li, L. The chemistry of two-dimensional layered transition metal dichalcogenide nanosheets. *Nature Chem.* **5**, 263–275 (2013).

23. Chhowalla, M., Liu, Z. & Zhang, H. Two-dimensional transition metal dichalcogenide (TMD) nanosheets. *Chem. Soc. Rev.* **44**, 2584–2586 (2015).

24. Cui, Y. *et al.* Versatile Crystal Structures and (Opto)electronic Applications of the 2D Metal Mono-, Di-, and Tri-Chalcogenide Nanosheets. *Adv. Funct. Mat.* 1900040 (2019).

25. Sun, M., Liu, H., Qu, J. & Li, J. Earth-Rich Transition Metal Phosphide for Energy Conversion and Storage. *Adv. Energy Mat.* **6**, 1600087 (2016).

26. Zhou, X. *et al.* Booming development of group IV–VI semiconductors: Fresh blood of 2D family. *Adv. Sci.* **3**, 1600177 (2016).

27. Yang, Z. & Hao, J. Recent Progress in 2D Layered III–VI Semiconductors and their Heterostructures for Optoelectronic Device Applications. *Adv. Mat. Technol.* **4**, 1900108 (2019).

28. Anasori, B., Lukatskaya, M. R. & Gogotsi, Y. 2D metal carbides and nitrides (MXenes) for energy storage. *Nat. Rev. Mat.* **2**, 16098 (2017).

29. Susner, M. A., Chyasnavichyus, M., McGuire, M. A., Ganesh, P. & Maksymovych, P. Metal Thio- and Selenophosphates as Multifunctional van der Waals Layered Materials. *Adv. Mat.* **29**, 1602852 (2017).

30. Tan, H. T., Sun, W., Wang, L. & Yan, Q. 2D Transition Metal Oxides/Hydroxides for Energy-Storage Applications. *ChemNanoMat* **2**, 562–577 (2016).

31. Yin, H. & Tang, Z. Ultrathin two-dimensional layered metal hydroxides: An emerging platform for advanced catalysis, energy conversion and storage. *Chem. Soc. Rev.* **45**, 4873–4891 (2016).

32. Kalantar-zadeh, K. *et al.* Two dimensional and layered transition metal oxides. *Appl. Mat. Today* **5**, 73–89 (2016).

33. Chen, Y. *et al.* Two-dimensional nanomaterials for photocatalytic CO_2 reduction to solar fuels. *Sustain. Energy and Fuels* **1**, 1875–1898 (2017).

34. García de Arquer, F. P. *et al.* 2D Metal Oxyhalide-Derived Catalysts for Efficient CO_2 Electroreduction. *Adv. Mater.* **30**, 1802858 (2018).

35. Hu, Y. *et al.* A review on low dimensional metal halides: Vapor phase epitaxy and physical properties. *J. Mat. Res.* **32**, 3992–4024 (2017).

36. Zhang, L., Liu, Y., Yang, Z. & Liu, S. (Frank). Two dimensional metal halide perovskites: Promising candidates for light-emitting diodes. *J. Energy Chem.* **37**, 97–110 (2019).

37. Lan, C., Zhou, Z., Wei, R. & Ho, J. C. Two-dimensional perovskite materials: From synthesis to energy-related applications. *Mater. Today Energy* **11**, 61–82 (2019).

38. Jia, F. & Song, S. Exfoliation and characterization of layered silicate minerals: A review. *Surf. Rev. Lett.* **21**, 1430001 (2014).

39. Zhu, H. & Liu, D. The synthetic strategies of metal-organic framework membranes, films and 2D MOFs and their applications in devices. *J. Mater. Chem. A* **7**, 21004–21035 (2019).

40. Zheng, W., Tsang, C. S., Lee, L. Y. S. & Wong, K. Y. Two-dimensional metal-organic framework and covalent-organic framework: synthesis and their energy-related applications. *Mater. Today Chem.* **12**, 34–60 (2019).

41. Alaskar Y., Arafin S., Martinez-Velis I., Wang K. L., in Two-dimensional Materials – Synthesis, Characterization and Potential Applications, U.K.: IntechOpen Limited, 2016.

42. Wang, Q. H., Kalantar-Zadeh, K., Kis, A., Coleman, J. N. & Strano, M. S. Electronics and optoelectronics of two-dimensional transition metal dichalcogenides. *Nat. Nanotechnol.* **7**, 699–712 (2012).

43. Novoselov, K. S. *et al.* Two-dimensional atomic crystals. *Proc. Natl. Acad. Sci. U. S. A.* **102**, 10451–10453 (2005).

44. Voiry, D., Mohite, A. & Chhowalla, M. Phase engineering of transition metal dichalcogenides. *Chem. Soc. Rev.* **44**, 2702–2712 (2015).

45. Chhowalla, M. & Amaratunga, G. A. J. Thin films of fullerene-like MoS_2 nanoparticles with ultra-low friction and wear. *Nature* **407**, 164–167 (2000).

46. Huang, M. & Cho, K. Density functional theory study of CO hydrogenation on a MoS_2 surface. *J. Phys. Chem. C* **113**, 5238–5243 (2009).

47. Song, I., Park, C. & Choi, H. C. Synthesis and properties of molybdenum disulphide: From bulk to atomic layers. *RSC Adv.* **5**, 7495–7514 (2015).

48. Ding, Q., Song, B., Xu, P. & Jin, S. Efficient Electrocatalytic and Photoelectrochemical Hydrogen Generation Using MoS_2 and Related Compounds. *Chem* **1**, 699–726 (2016).

49. Wang, F. *et al.* Hydrothermal synthesis of flower-like molybdenum disulfide microspheres and their application in electrochemical supercapacitors. *RSC Adv.* **8**, 38945–38954 (2018).

50. Feng, X. *et al.* Novel mixed-solvothermal synthesis of MoS_2 nanosheets with controllable morphologies. *Cryst. Res. Technol.* **48**, 363-368 (2013).

51. Yu, Y. *et al.* Controlled scalable synthesis of uniform, high-quality monolayer and few-layer MoS2 films. *Sci. Rep.* **3**, 1866 (2013).

52. Huisman, R., de Jonge, R., Haas, C. & Jellinek, F. Trigonal-prismatic coordination in solid compounds of transition metals. *J. Solid State Chem.* **3**, 56–66 (1971).

53. Bullett, D. W. Electronic band structure and bonding in transition metal layered dichalcogenides by atomic orbital methods. *J. Phys. C Solid State Phys.* **11**, 4501–4514 (1978).

54. Jaegermann, W. & Tributsch, H. Interfacial properties of semiconducting transition metal chalcogenides. *Prog. Surf. Sci* **29**, 1–167 (1988).

55. Splendiani, A. *et al.* Emerging photoluminescence in monolayer MoS_2. *Nano Lett.* **10**, 1271–5 (2010).

56. Radisavljevic, B., Radenovic, A., Brivio, J., Giacometti, V. & Kis, A. Single-layer MoS_2 transistors. *Nat. Nanotechnol.* **6**, 147–150 (2011).

57. Joensen, P., Frindt, R. F. & Morrison, S. R. Single-layer MoS_2. *Mater. Res. Bull.* **21**, 457–461 (1986).

58. Zheng, J. *et al.* High yield exfoliation of two-dimensional chalcogenides using sodium naphthalenide. *Nat. Commun.* **5**, 2995 (2014).

59. Fan, X. *et al.* Fast and Efficient Preparation of Exfoliated 2H MoS_2 Nanosheets by Sonication-Assisted Lithium Intercalation and Infrared Laser-Induced 1T to 2H Phase Reversion. *Nano Lett.* **15**, 5956–5960 (2015).

60. Mieda, E. *et al.* Nanoprobe characterization of MoS_2 nanosheets fabricated by Li-intercalation. *Jpn. J. Appl. Phys.* **54**, 08LB07 (2015)

61. Lin, Y. C., Dumcenco, D. O., Huang, Y. S. & Suenaga, K. Atomic mechanism of the semiconducting-to-metallic phase transition in single-layered MoS_2. *Nat. Nanotechnol.* **9**, 391–396 (2014).

62. Kang, Y. *et al.* Plasmonic Hot Electron Induced Structural Phase Transition in a MoS_2 Monolayer. *Adv. Mater.* **26**, 6467–6471 (2014).

63. Zhu, J. *et al.* Argon Plasma Induced Phase Transition in Monolayer MoS_2. *J. Am. Chem. Soc.* **139**, 10216–10219 (2017).

64. Chi, Z. H. *et al.* Pressure-induced metallization of molybdenum disulfide. *Phys. Rev. Lett.* **113**, 036802 (2014).

65. Geng, X. *et al.* Two-Dimensional Water-Coupled Metallic MoS_2 with Nanochannels for Ultrafast Supercapacitors. *Nano Lett.* **17**, 1825–1832 (2017).

66. Wang, D. *et al.* Phase engineering of a multiphasic 1T/2H MoS_2 catalyst for highly efficient hydrogen evolution. *J. Mater. Chem. A* **5**, 2681–2688 (2017).

67. Wu, M. *et al.* Metallic 1T MoS_2 nanosheet arrays vertically grown on activated carbon fiber cloth for enhanced Li-ion storage performance. *J. Mater. Chem. A* **5**, 14061–14069 (2017).

68. Wu, C. *et al.* Engineering interfacial charge-transfer by phase transition realizing enhanced photocatalytic hydrogen evolution activity. *Inorg. Chem. Front.* **4**, 663–667 (2017).

69. Zhao, W. *et al.* Metastable MoS_2: Crystal Structure, Electronic Band Structure, Synthetic Approach and Intriguing Physical Properties. *Chem. Eur. J.* **24**, 15942–15954 (2018).

70. Acerce, M., Voiry, D. & Chhowalla, M. Metallic 1T phase MoS_2 nanosheets as supercapacitor electrode materials. *Nat. Nanotechnol.* **10**, 313–318 (2015).

71. Han, H. *et al.* Few-layered metallic 1T-MoS_2/TiO_2 with exposed (001) facets: Two-dimensional nanocomposites for enhanced photocatalytic activities. *Phys. Chem. Chem. Phys.* **19**, 28207–28215 (2017).

72. Lei, Z., Zhan, J., Tang, L., Zhang, Y. & Wang, Y. Recent Development of Metallic (1T) Phase of Molybdenum Disulfide for Energy Conversion and Storage. *Adv. Energy Mat.* **8**, 1703482 (2018).

73. Geng, X. *et al.* Pure and stable metallic phase molybdenum disulfide nanosheets for hydrogen evolution reaction. *Nat. Commun.* **7**, 10672 (2016).

74. Xiong, F. *et al.* Li Intercalation in MoS_2: In Situ Observation of Its Dynamics and Tuning Optical and Electrical Properties. *Nano Lett.* **15**, 6777–6784 (2015).

75. Jayabal, S., Wu, J., Chen, J., Geng, D. & Meng, X. Metallic 1T-MoS_2 nanosheets and their composite materials: Preparation, properties and emerging applications. *Mat. Today Energy* **10**, 264–279 (2018).

76. Eda, G. *et al.* Photoluminescence from chemically exfoliated MoS_2. *Nano Lett.* **11**, 5111–5116 (2011).

77. Reshmi, S., Akshaya, M. V., Satpati, B., Basu, P. K. & Bhattacharjee, K. Structural stability of coplanar 1T-2H superlattice MoS_2 under high energy electron beam. *Nanotechnology* **29**, 205604 (2018).

78. Yang, D., Jimenez Sandoval, S., Divigalpitiya, W. M. R., Irwin, J. C. & Frindt, R. F. Structure of single-molecular-layer MoS_2. *Phys. Rev. B* **43**, 12053 (1991).

79. Frindt, R. F. Single crystals of MoS_2 several molecular layers thick. *J. Appl. Phys.* **37**, 1928–1929 (1966).

80. Castellanos-Gomez, A., Agraït, N. & Rubio-Bollinger, G. Optical identification of atomically thin dichalcogenide crystals. *Appl. Phys. Lett.* **96**, 213116 (2010).

81. Li, W. *et al.* Gas Sensors Based on Mechanically Exfoliated MoS_2 Nanosheets for Room-Temperature NO_2 Detection. *Sensors (Basel).* **19**, 2123 (2019).

82. Grayfer, E. D., Kozlova, M. N. & Fedorov, V. E. Colloidal 2D nanosheets of MoS_2 and other transition metal dichalcogenides through liquid-phase exfoliation. *Adv. in Colloid and Interface Sci.* **245**, 40–61 (2017).

83. Coleman, J. N. *et al.* Two-dimensional nanosheets produced by liquid exfoliation of layered materials. *Science* **331**, 568–571 (2011).

84. Zhou, K. G., Mao, N. N., Wang, H. X., Peng, Y. & Zhang, H. L. A mixed-solvent strategy for efficient exfoliation of inorganic graphene analogues. *Angew. Chem.* **50**, 10839–10842 (2011).

85. Afanasiev, P., Xia, G. F., Berhault, G., Jouguet, B. & Lacroix, M. Surfactant-assisted synthesis of highly dispersed molybdenum sulfide. *Chem. Mater.* **11**, 3216–3219 (1999).

86. Smith, R. J. *et al.* Large-scale exfoliation of inorganic layered compounds in aqueous surfactant solutions. *Adv. Mater.* **23**, 3944–3948 (2011).

87. Huang, H. *et al.* Metallic 1T phase MoS_2 nanosheets for high-performance thermoelectric energy harvesting. *Nano Energy* **26**, 172–179 (2016).

88. Cheng, P., Sun, K. & Hu, Y. H. Memristive Behavior and Ideal Memristor of 1T Phase MoS_2 Nanosheets. *Nano Lett.* **16**, 572–576 (2016).

89. Voiry, D. *et al.* Conducting MoS_2 nanosheets as catalysts for hydrogen evolution reaction. *Nano Lett.* **13**, 6222–7 (2013).

90. Er, E. *et al.* High-Yield Preparation of Exfoliated 1T-MoS_2 with SERS Activity. *Chem. Mater.* **31**, 5725–5734 (2019).

91. Benavente, E., Santa Ana, M. A., Mendizábal, F. & González, G. Intercalation chemistry of molybdenum disulfide. *Coord. Chem. Rev.* **224**, 87–109 (2002).

92. Wu, L. *et al.* Unraveling the Role of Lithium in Enhancing the Hydrogen Evolution Activity of MoS_2: Intercalation versus Adsorption. *ACS Energy Lett.* **4**, 1733−1740 (2019).

93. Dines, M. B. Lithium intercalation via n-Butyllithium of the layered transition metal dichalcogenides. *Mater. Res. Bull.* **10**, 287–291 (1975).

94. Brent, J. R., Savjani, N. & O'Brien, P. Synthetic approaches to two-dimensional transition metal dichalcogenide nanosheets. *Prog. Mat. Sci.* **89**, 411–478 (2017).

95. Zeng, Z. *et al.* Single-layer semiconducting nanosheets: High-yield preparation and device fabrication. *Angew. Chem.* **50**, 11093–11097 (2011).

96. Shi, S., Sun, Z. & Hu, Y. H. Synthesis, stabilization and applications of 2-dimensional 1T metallic MoS_2. *J. Mater. Chem. A* **6**, 23932–23977 (2018).

97. Lin, Z. *et al.* Solution-processable 2D semiconductors for high-performance large-area electronics. *Nature* **562**, 254–258 (2018).

98. Hirsch, A. & Hauke, F. Post-Graphene 2D Chemistry: The Emerging Field of Molybdenum Disulfide and Black Phosphorus Functionalization. *Angew. Chem.* **57**, 4338–4354 (2018).

99. Gupta, A., Arunachalam, V. & Vasudevan, S. Water dispersible, positively and negatively charged MoS_2 nanosheets: Surface chemistry and the role of surfactant binding. *J. Phys. Chem. Lett.* **6**, 739–744 (2015).

100. Backes, C. *et al.* Production of highly monolayer enriched dispersions of liquid-exfoliated nanosheets by liquid cascade centrifugation. *ACS Nano* **10**, 1589–1601 (2016).

101. Min Sim, D. *et al.* Long-Term Stable 2H-MoS_2 Dispersion: Critical Role of Solvent for Simultaneous Phase Restoration and Surface Functionalization of Liquid-Exfoliated MoS_2. *ACS Omega* **2**, 4678–4687 (2017).

102. Anto Jeffery, A., Nethravathi, C. & Rajamathi, M. Two-dimensional nanosheets and layered hybrids of MoS_2 and WS_2 through exfoliation of ammoniated MS_2 (M = Mo,W). *J. Phys. Chem. C* **118**, 1386–1396 (2014).

103. Yang, C., Chen, Z., Shakir, I., Xu, Y. & Lu, H. Rational synthesis of carbon shell coated polyaniline/MoS_2 monolayer composites for high-performance supercapacitors. *Nano Res.* **9**, 951–962 (2016).

104. Tan, C. & Zhang, H. Two-dimensional transition metal dichalcogenide nanosheet-based composites. *Chem. Soc. Rev.* **44**, 2713–2731 (2015).

105. Kim, J., Byun, S., Smith, A. J., Yu, J. & Huang, J. Enhanced electrocatalytic properties of transition-metal dichalcogenides sheets by spontaneous gold nanoparticle decoration. *J. Phys. Chem. Lett.* **4**, 1227–1232 (2013).

106. Shi, Y. *et al.* Selective decoration of Au nanoparticles on monolayer MoS_2 single crystals. *Sci. Rep.* **3**, 1839 (2013).

107. Sreeprasad, T. S., Nguyen, P., Kim, N. & Berry, V. Controlled, defect-guided, metal-nanoparticle incorporation onto MoS_2 via chemical and microwave routes: Electrical, thermal, and structural properties. *Nano Lett.* **13**, 4434–4441 (2013).

108. Yin, Z. *et al.* Au nanoparticle-modified MoS_2 nanosheet-based photoelectrochemical cells for water splitting. *Small* **10**, 3537–43 (2014).

109. Yuwen, L. *et al.* General synthesis of noble metal (Au, Ag, Pd, Pt) nanocrystal modified MoS_2 nanosheets and the enhanced catalytic activity of Pd-MoS_2 for methanol oxidation. *Nanoscale* **6**, 5762–5769 (2014).

110. Su, S., Sun, H., Xu, F., Yuwen, L. & Wang, L. Highly Sensitive and Selective Determination of Dopamine in the Presence of Ascorbic Acid Using Gold Nanoparticles-Decorated MoS_2 Nanosheets Modified Electrode. *Electroanalysis* **25**, 2523–2529 (2013).

111. Huang, X. *et al.* Solution-phase epitaxial growth of noble metal nanostructures on dispersible single-layer molybdenum disulfide nanosheets. *Nat. Commun.* **4**, 1444 (2013).

112. Kim, J. S. *et al.* Multifunctional Schottky-diode circuit comprising palladium/molybdenum disulfide nanosheet. *Small* **10**, 4845–50 (2014).

113. Kong, D. *et al.* Fe_3O_4 quantum dot decorated MoS_2 nanosheet arrays on graphite paper as free-standing sodium-ion battery anodes. *J. Mater. Chem. A* **5**, 9122–9131 (2017).

114. Wu, J. *et al.* Layer thinning and etching of mechanically exfoliated MoS_2 nanosheets by thermal annealing in air. *Small* **9**, 3314–3319 (2013).

115. Tan, C. *et al.* Single-layer transition metal dichalcogenide nanosheet-assisted assembly of aggregation-induced emission molecules to form organic nanosheets with enhanced fluorescence. *Adv. Mater.* **26**, 1735–1739 (2014).

116. Liu, J. *et al.* Preparation of MoS_2-polyvinylpyrrolidone nanocomposites for flexible nonvolatile rewritable memory devices with reduced graphene oxide electrodes. *Small* **8**, 3517–3522 (2012).

117. Liu, T. *et al.* Drug delivery with PEGylated MoS_2 nano-sheets for combined photothermal and chemotherapy of cancer. *Adv. Mater.* **26**, 3433–3440 (2014).

118. Chang, K. *et al.* Graphene-like MoS_2/amorphous carbon composites with high capacity and excellent stability as anode materials for lithium ion batteries. *J. Mater. Chem.* **21**, 6251–6257 (2011).

119. Zhao, X., Zhu, H. & Yang, X. Amorphous carbon supported MoS_2 nanosheets as effective catalysts for electrocatalytic hydrogen evolution. *Nanoscale* **6**, 10680–10685 (2014).

120. Zhou, W. *et al.* Synthesis of few-layer MoS_2 nanosheet-coated TiO_2 nanobelt heterostructures for enhanced photocatalytic activities. *Small* **9**, 140–147 (2013).

121. Xu, X., Fan, Z., Ding, S., Yu, D. & Du, Y. Fabrication of MoS_2 nanosheet@TiO_2 nanotube hybrid nanostructures for lithium storage. *Nanoscale* **6**, 5245–5250 (2014).

122. Huang, Y. *et al.* Synthesis of few-layered MoS_2 nanosheet-coated electrospun SnO_2 nanotube heterostructures for enhanced hydrogen evolution reaction. *Nanoscale* **6**, 10673–10679 (2014).

123. Chang, K. & Chen, W. L-cysteine-assisted synthesis of layered MoS_2/graphene composites with excellent electrochemical performances for lithium ion batteries. *ACS Nano* **5**, 4720–8 (2011).

124. Huang, G. *et al.* Graphene-like MoS_2/graphene composites: cationic surfactant-assisted hydrothermal synthesis and electrochemical reversible storage of lithium. *Small* **9**, 3693–703 (2013).

125. Chang, K. *et al.* MoS_2/Graphene Cocatalyst for Efficient Photocatalytic H_2 Evolution under Visible Light Irradiation. *ACS Nano* **8**, 7078–7087 (2014).

126. Wang, C. *et al.* Hierarchical MoS_2 nanosheet/active carbon fiber cloth as a binder-free and free-standing anode for lithium-ion batteries. *Nanoscale* **6**, 5351–5358 (2014).

127. Zhu, C., Mu, X., van Aken, P. A., Yu, Y. & Maier, J. Single-layered ultrasmall nanoplates of MoS_2 embedded in carbon nanofibers with excellent electrochemical performance for lithium and sodium storage. *Angew. Chem.* **53**, 2152–2156 (2014).

128. Kong, D. *et al.* Rational design of MoS_2@graphene nanocables: Towards high performance electrode materials for lithium ion batteries. *Energy Environ. Sci.* **7**, 3320–3325 (2014).

129. Zhao, C. *et al.* Thin MoS_2 nanoflakes encapsulated in carbon nanofibers as high-performance anodes for lithium-ion batteries. in *ACS Appl.Mater. Inter.* **6**, 6392–6398 (2014).

130. Chang, K. & Chen, W. In situ synthesis of MoS_2/graphene nanosheet composites with extraordinarily high electrochemical performance for lithium ion batteries. *Chem. Commun.* **47**, 4252–4254 (2011).

131. Cao, X. *et al.* Preparation of MoS_2-coated three-dimensional graphene networks for high-performance anode material in lithium-ion batteries. *Small* **9**, 3433–3438 (2013).

132. Zheng, X. *et al.* Space-confined growth of MoS_2 nanosheets within graphite: The layered hybrid of MoS_2 and graphene as an active catalyst for hydrogen evolution reaction. *Chem. Mater.* **26**, 2344–2353 (2014).

133. David, L., Bhandavat, R. & Singh, G. MoS_2/graphene composite paper for sodium-ion battery electrodes. *ACS Nano* **8**, 1759–1770 (2014).

134. Zhou, X., Wan, L. J. & Guo, Y. G. Synthesis of MoS_2 nanosheet-graphene nanosheet hybrid materials for stable lithium storage. *Chem. Commun.* **49**, 1838–1840 (2013).

135. Yin, Z. *et al.* Memory devices using a mixture of MoS_2 and graphene oxide as the active layer. *Small* **9**, 727–731 (2013).

136. Ding, S., Chen, J. S. & Lou, X. W. Glucose-assisted growth of MoS_2 nanosheets on CNT backbone for improved lithium storage properties. *Chem. Eur. J.* **17**, 13142–13145 (2011).

137. Tai, S. Y. *et al.* Few-layer MoS_2 nanosheets coated onto multi-walled carbon nanotubes as a low-cost and highly electrocatalytic counter electrode for dye-sensitized solar cells. *J. Mater. Chem.* **22**, 24753–24759 (2012).

138. Voiry, D. *et al.* Covalent functionalization of monolayered transition metal dichalcogenides by phase engineering. *Nat. Chem.* **7**, 45–49 (2014).

139. Knirsch, K. C. *et al.* Basal-Plane Functionalization of Chemically Exfoliated Molybdenum Disulfide by Diazonium Salts. *ACS Nano* **6**, 6018–6030 (2015).

140. Vera-Hidalgo, M., Giovanelli, E., Navío, C. & Pérez, E. M. Mild Covalent Functionalization of Transition Metal Dichalcogenides with Maleimides: A 'click' Reaction for 2H-MoS_2 and WS_2. *J. Am. Chem. Soc.* **141**, 3767–3771 (2019).

141. Nguyen, E. P. *et al.* Electronic Tuning of 2D MoS_2 through Surface Functionalization. *Adv. Mater.* **27**, 6225–6229 (2015).

142. Bertolazzi, S., Gobbi, M., Zhao, Y., Backes, C. & Samorì, P. Molecular chemistry approaches for tuning the properties of two-dimensional transition metal dichalcogenides. *Chem. Soc. Rev.* **47**, 6845–6888 (2018).

143. McAdams, S. G. *et al.* Dual Functionalization of Liquid-Exfoliated Semiconducting 2H-MoS_2 with Lanthanide Complexes Bearing Magnetic and Luminescence Properties. *Adv. Funct. Mater.* **27**, 1703646 (2017).

144. Kabachii, Y. A. *et al.* Multifunctional nanohybrids by self-assembly of monodisperse iron oxide nanoparticles and nanolamellar MoS2 plates. *Chem. Mater.* **12**, 2434–2440 (2013).

145. Zhou, K., Liu, J., Wen, P., Hu, Y. & Gui, Z. A noncovalent functionalization approach to improve the dispersibility and properties of polymer/MoS_2 composites. *Appl. Surf. Sci.* **316**, 237–244 (2014).

146. Chen, X. & McDonald, A. R. Functionalization of Two-Dimensional Transition-Metal Dichalcogenides. *Adv. Mater.* **24**, 18246-18257 (2016).

147. Bertolazzi, S., Gobbi, M., Zhao, Y., Backes, C. & Samorì, P. Molecular chemistry approaches for tuning the properties of two-dimensional transition metal dichalcogenides. *Chem. Soc. Rev.* **47**, 6845–6888 (2018).

148. Stergiou, A. & Tagmatarchis, N. Molecular Functionalization of Two-Dimensional MoS_2 Nanosheets. *Chem. Eur. J.* **24**, 18246–18257 (2018).

149. Daukiya, L., Seibel, J. & De Feyter, S. Chemical modification of 2D materials using molecules and assemblies of molecules. *Adv. Phys.-X* **4**, 1625723 (2019).

150. Mouri, S., Miyauchi, Y. & Matsuda, K. Tunable photoluminescence of monolayer MoS_2 via chemical doping. *Nano Lett.* **13**, 5944–5948 (2013).

151. Jing, Y., Tan, X., Zhou, Z. & Shen, P. Tuning electronic and optical properties of MoS_2 monolayer via molecular charge transfer. *J. Mater. Chem. A* **2**, 16892–16897 (2014).

152. Baek, J. *et al.* Formation and Photodynamic Behavior of Transition Metal Dichalcogenide Nanosheet–Fullerene Inorganic/Organic Nanohybrids on Semiconducting Electrodes. *Chem. Eur. J.* **24**, 1561–1572 (2018).

153. Wang, T. *et al.* Direct detection of DNA below ppb level based on thionin-functionalized layered MoS_2 electrochemical sensors. *Anal. Chem.* **24**, 12064–12069 (2014).

154. Molina-Mendoza, A. J. *et al.* Engineering the optoelectronic properties of MoS_2 photodetectors through reversible noncovalent functionalization. *Chem. Commun.* **52**, 14365–14368 (2016).

155. Choi, J., Zhang, H. & Choi, J. H. Modulating optoelectronic properties of two-dimensional transition metal dichalcogenide semiconductors by photoinduced charge transfer. *ACS Nano* **1**, 1671–1680 (2016).

156. Kafle, T. R. *et al.* Charge Transfer Exciton and Spin Flipping at Organic-Transition-Metal Dichalcogenide Interfaces. *ACS Nano* **11**, 10184–10192 (2017).

157. Benjamin, C. J., Zhang, S. & Chen, Z. Controlled doping of transition metal dichalcogenides by metal work function tuning in phthalocyanine compounds. *Nanoscale* **10**, 5148–5153 (2018).

158. Zhao, Y., Ippolito, S. & Samorì, P. Functionalization of 2D Materials with Photosensitive Molecules: From Light-Responsive Hybrid Systems to Multifunctional Devices. *Adv. Opt. Mater.* 1900286 (2019).

159. Zhou, K., Liu, J., Wen, P., Hu, Y. & Gui, Z. A noncovalent functionalization approach to improve the dispersibility and properties of polymer/MoS_2 composites. *Appl. Surf. Sci.* **316**, 237–244 (2014).

160. Tahir, M. N. *et al.* Overcoming the Insolubility of Molybdenum Disulfide Nanoparticles through a High Degree of Sidewall Functionalization Using Polymeric Chelating Ligands. *Angew. Chem.* **118**, 4927–4933 (2006)

161. Backes, C. *et al.* Functionalization of liquid-exfoliated two-dimensional 2H-MoS_2. *Angew. Chem.* **54**, 2638–2642 (2015).

162. Chou, S. S. *et al.* Ligand conjugation of chemically exfoliated MoS_2. *J. Am. Chem. Soc.* **12**, 4584–4587 (2013).

163. Sim, D. M. *et al.* Controlled Doping of Vacancy-Containing Few-Layer MoS_2 via Highly Stable Thiol-Based Molecular Chemisorption. *ACS Nano* **12**, 12115–12123 (2015).

164. Chen, X., Berner, N. C., Backes, C., Duesberg, G. S. & McDonald, A. R. Functionalization of Two-Dimensional MoS_2: On the Reaction between MoS_2 and Organic Thiols. *Angew. Chem.* **55**, 5803–5808 (2016).

165. Vishnoi, P., Sampath, A., Waghmare, U. V. & Rao, C. N. R. Covalent Functionalization of Nanosheets of MoS_2 and $MoSe_2$ by Substituted Benzenes and Other Organic Molecules. *Chem. Eur. J.* **23**, 886–895 (2017).

166. Chu, X. S. *et al.* Direct Covalent Chemical Functionalization of Unmodified Two-Dimensional Molybdenum Disulfide. *Chem. Mater.* **30**, 2112–2128 (2018).

167. Quirós-Ovies, R. *et al.* Controlled Covalent Functionalization of 2H-MoS_2 with Molecular or Polymeric Adlayers. *Chem. Eur. J.* **26**, 6629–6634 (2020).

II. Prussian blue@MoS_2 layer composites as highly efficient cathodes for sodium- and potassium-ion batteries

II.1. Introduction

The dark blue compound known as Prussian Blue (PB) has been synthesized and exploited for more than three hundred years due to its properties as dye in clothes and paints. The name PB dates from 18th century in the wake of its use as dye for uniform coats in the Prussian army.[1]

PB is a mixed-valence Fe^{III}/Fe^{II} coordination compound and its strong blue colour results from an intervalence transition between Fe^{II} and Fe^{III} centres caused by the absorption of orange-red light from the visible spectrum (680–730 nm).[2] It is usually prepared by mixing *i*) Fe^{3+} and $[Fe^{II}(CN)_6]^{4-}$ or *ii*) Fe^{2+} and $[Fe^{III}(CN)_6]^{3-}$. Recently, it has been demonstrated that it can also be synthesized by combining Fe^{3+} and $[Fe^{III}(CN)_6]^{3-}$ (same oxidation state) in the presence of a reducing agent.[3]

PB has a general formula of $A_xFe^{III}[Fe^{II}(CN)_6]_y\cdot\square_{1-y}\cdot nH_2O$, where A is an alkaline metal (K or Na) and $\square$ represents $[Fe^{II}(CN)_6]^{4-}$ vacancies occupied by coordinated water ($0 < x < 1$; $0.75 < y < 1$).[4] Whilst coordinated water molecules complete the coordination sphere of Fe^{III} (see **Figure II-1**)[5], zeolitic water molecules, along with the charge-balancing alkali cations, are found in the voids/cavities (interstitial sites) formed by the 3D Fe^{II}–CN–Fe^{III} framework, in which Fe^{II} and Fe^{III} are octahedrally surrounded by C and N, respectively.[6]

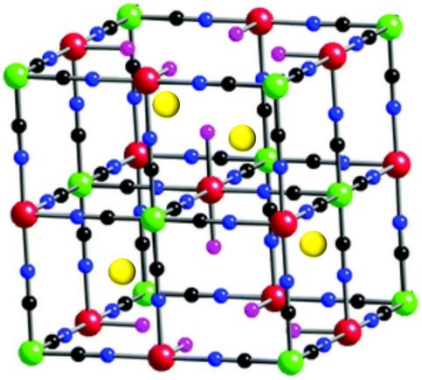

Figure II-1. Schematic representation of $A_xFe^{III}[Fe^{II}(CN)_6]_y\cdot\square_{1-y}\cdot nH_2O$ (zeolitic H_2O molecules have been omitted for clarity). Fe^{II} (green), Fe^{III} (red), C (black), N (blue), A^+ (yellow), and coordinated H_2O molecules (purple). Figure adapted from reference 7.

Concerning magnetic properties, PB is formed by paramagnetic high-spin (HS) Fe^{III} ions (S = 5/2) and diamagnetic low-spin (LS) Fe^{II} centres, giving rise to soft ferromagnetic order at low temperature (see **Figure II-2**).[8]

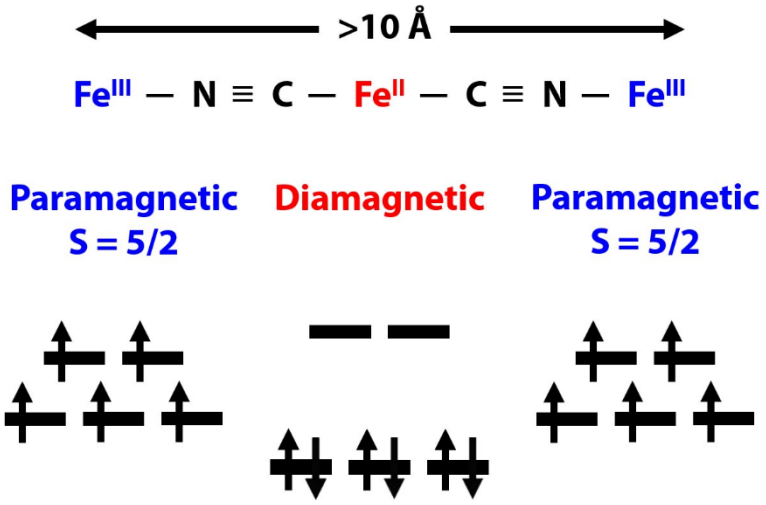

Figure II-2. Scheme of Fe^{III}–NC–Fe^{II}–CN–Fe^{III} entities in PB. The exchange interaction between the two paramagnetic Fe^{III} ions is very weak.

Prussian blue analogues (PBAs)[9,10] arises from substituting Fe^{II} or/and Fe^{III} by one or two transition metal ions with the same oxidation state, respectively, while maintaining the typical face-centred cubic (fcc) structure and electroneutrality of the compound.

PB, along with PBAs, can be easily large-scale synthesized through many cheap and eco-friendly approaches.[11]

PB energy applications

In the highly competitive field of energy storage systems, lithium-ion batteries (LIBs) have played a determinant role during last years.[12,13] However, motivated by the scarcity of Li on Earth, batteries based on other more available alkaline metals, like Na or K, have raised enormous interest.[14,15] The quest for alternative systems that can rival with LIBs performance has motivated the design and development of multifarious materials, including composites.[16]

Nowadays, PB is one of the most suitable cathode materials for fabricating sodium- and potassium-ion batteries (SIBs and KIBs, respectively) because of its wide diffusion tunnels, abundant redox-active sites, high structural stability, and low toxicity.[17] The interstitial voids present in these coordination polymers permit the insertion and de-insertion of alkaline cations without drastic structural modifications.

Albeit the calculated specific capacity of PB is close to 170 mA h g^{-1},[18,19] the hitherto reported capacities lag behind this theoretical value since the presence of structural defects, such as $[Fe(CN)_6]^{n-}$ vacancies, and water molecules occluded within interstitial voids may hinder the diffusion of alkaline cations, leading to low electronic conductivity, inferior rate capability, and poor cycling stability. In order to overcome this issue, crystalline-defect-free PB/PBAs are sought.[19]

PB has been also successfully integrated into different composites with the aim of bringing stability, homogeneous structuration at the nanoscale, ease of assembly, or enhanced conductivity to the final material. For example, previous research results have demonstrated that the formation of small particle size PB crystals uniformly distributed on a conducting carbon matrix can be very beneficial for the electrochemical performance of the system.[20] Such crystals, which shorter diffusion lengths, allow to boost the diffusion rates of alkali ions. Moreover, the strain produced by volume changes during ion charge and discharge processes is minimized, thereby enhancing rate capability and stability. Besides, as the surface area (SA) increases, the contact between the matrix and PB becomes more efficient, improving electron transport and structural resilience at the same time.[20]

In the same direction, materials with high surface-to-mass ratio, like graphene or graphene oxide (rGO), have been used in the design of 2D composites, in which the 2D material is decorated with PB nanoparticles (NPs) by reaction with iron-containing precursors in solution, most often under the assistance of a reducing agent.[21,22] Following this strategy, SIBs electrodes, with higher reversible capacities and better cyclability as opposed to PB alone,[23–25] have provided charge/discharge capacity and capacity retention values up to 160 mA h g^{-1} and 92.2% at 0.5 C-rate,[26] respectively. Notwithstanding,

the preparation of composites resulting from the combination of other 2D materials than graphene or its oxide with PB or PBAs remains almost unexplored.

In this scenario, it is interesting to pay attention to the potential of TMDCs, such as MoS_2. The electronic properties of MoS_2 have motivated the implementation of its layers in a plethora of electronic devices.[27] Additionally, MoS_2 can accommodate different metal ions in between its constituent layers and has been extensively used for electrochemical energy storage devices (LIBs, SIBs, and supercapacitors) with outstanding performances, either as bulk material or in the form of ce-MoS_2 nanosheets.[28]

Moreover, negative charges accumulated on ce-MoS_2, as a result of the exfoliation of lithium-intercalated MoS_2 (Li_xMoS_2) in water after *n*-BuLi treatment,[29] can be harnessed to promote the non-covalent functionalization of the 2D material with electrophile species[30,31] and metallic or PB NPs.[3,32] Nonetheless, the potential synergistic coupling between two high-performance energy storage materials, like PB and exfoliated MoS_2, within a new 2D composite may result in alkaline-ion batteries with improved properties.

In this Chapter, we report a strategy (see **Figure II-3**) in which ce-MoS_2 flakes are used as both reducing agent and platform for the ultrafast crystallization of continuous PB shells, which leads to the formation of a new composite (sample **1**). We have also exploited ce-MoS_2 networks deposited on SiO_2/Si substrates to evaluate the charge transfer degree between the components of the composite (samples **2** and **3**) and studied the transport properties by using Au prepatterned electrodes (sample **4**). Furthermore, mechanically exfoliated MoS_2 (me-MoS_2) has been subjected (sample **5**) or not (sample **6**) to a reducing process before its treatment with PB precursors, in order to find out whether the role of the negative charges on ce-MoS_2 surface was crucial in the successful PB growth and therefore composite formation.

Looking forward the functionality of sample **1** as cathode for KIBs and SIBs, a detailed electrochemical study has been carried out.

Finally, in order to explore the redox process between both counterparts of the composite, a new one (sample **7**) has been prepared

by increasing the {ce-MoS_2:Fe-containing reagents} molar ratio and shortening the reaction time.

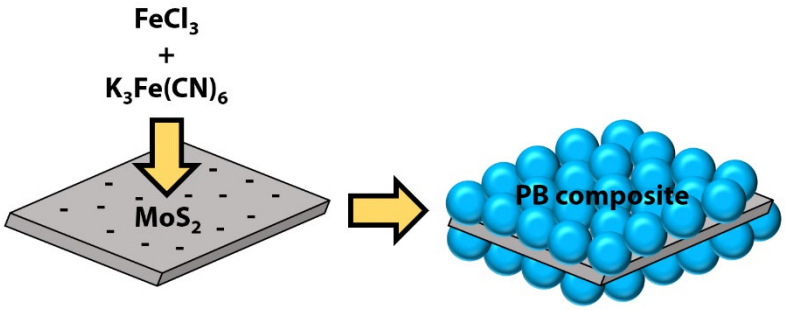

Figure II-3. Schematic representation of PB growth onto ce-MoS_2 flakes.

II.2. Results and discussion

II.2.1. Exfoliation and characterization of MoS_2

II.2.1.1. Evaluation of the intercalation extent

Ultrathin ce-MoS_2 flakes were prepared by the well-known *n*-BuLi method,[33] followed by the dispersion of Li_xMoS_2 in water under mild sonication conditions and a purification step (dialysis and centrifugation). Our procedure, inspired by the fast autoclave approach, is explained in much more detail in **Experimental section**. According to literature, when an excess of *n*-BuLi is used, ce-MoS_2 layers with a high percentage of 1T polytype are obtained.[31]

Prior to the dispersion of Li_xMoS_2, borosilicate glass capillaries containing this material were sealed in a N_2-rich glovebox ($[O_2] < 0.1$ ppm, $[H_2O] < 0.1$ ppm) and analysed by powder X-ray diffraction (PXRD) with the aim of obtaining useful information about the intercalation extent. Lithium intercalation in multi-layered MoS_2 results in a loss of symmetry along the *c*-axis. As observed in the PXRD diffractogram (**Figure II-4**), the disappearance of the (002) peak of 2H-MoS_2 at ≈14.46º and the apparition of the (001) peak of Li_xMoS_2 at ≈14.08º are the unequivocal signature of a quantitative intercalation reaction.

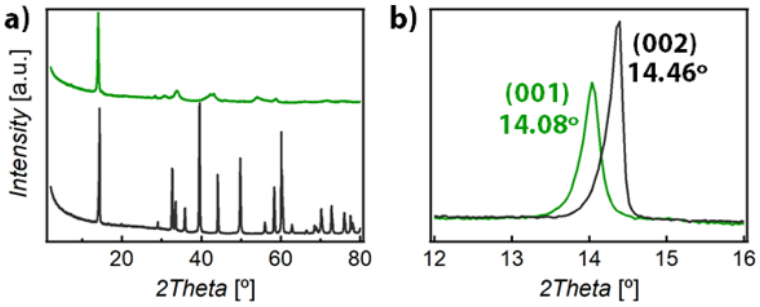

Figure II-4. a) PXRD patterns of commercial MoS_2 (grey) and Li_xMoS_2 (green); b) Zoom-in PXRD patterns in the 12–16° range.

At this point, it is noteworthy to indicate that, if exposed to air, Li_xMoS_2 can absorb moisture. The hydration of intercalated Li cations results in a shift of the (001) reflection of Li_xMoS_2 toward lower angles (see **Figure II-5**).[34,35]

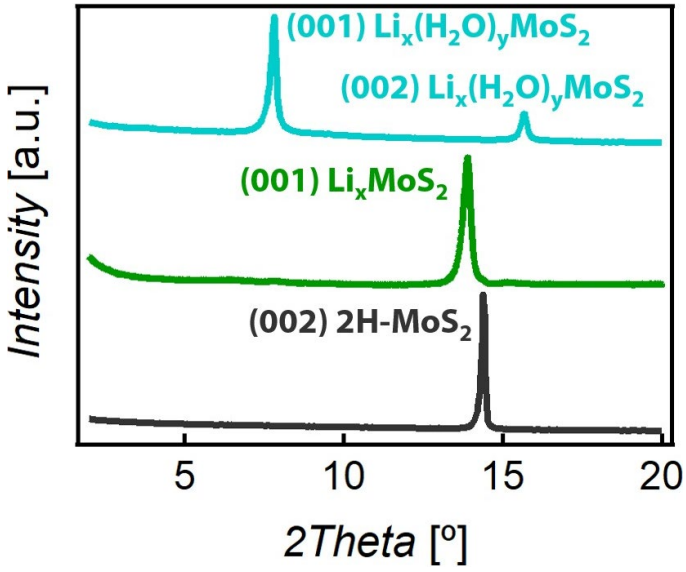

Figure II-5. PXRD patterns of commercial MoS_2 (grey), Li_xMoS_2 under N_2 atmosphere (green), and Li_xMoS_2 exposed to air (turquoise).

II.2.1.2. Characterization of ce-MoS_2

Dark suspensions of ce-MoS_2 flakes with an abundant percentage of 1T polytype result from sonicating Li_xMoS_2 in degassed water under mild conditions. After the purification step (dialysis and centrifugation), flakes were characterized by several techniques.

Ultraviolet/visible (UV/Vis) spectroscopy

The UV/Vis absorption spectrum of freshly prepared ce-MoS_2 flakes in water (**Figure II-6**) shows a monotonic change interrupted by two salient plasmon bands located at ≈257 and 308 nm, which are characteristic of 1T-MoS_2.[31,36] By contrast, the UV/Vis absorption spectrum of 2H-MoS_2 dispersed in water displays excitonic transitions related to two sets of excitons: D and C excitons in the 390–520 nm range and B and A in the 600–700 nm range.[31,37] Further information about how to calculate the concentration of freshly prepared suspensions is provided in **Appendix**.

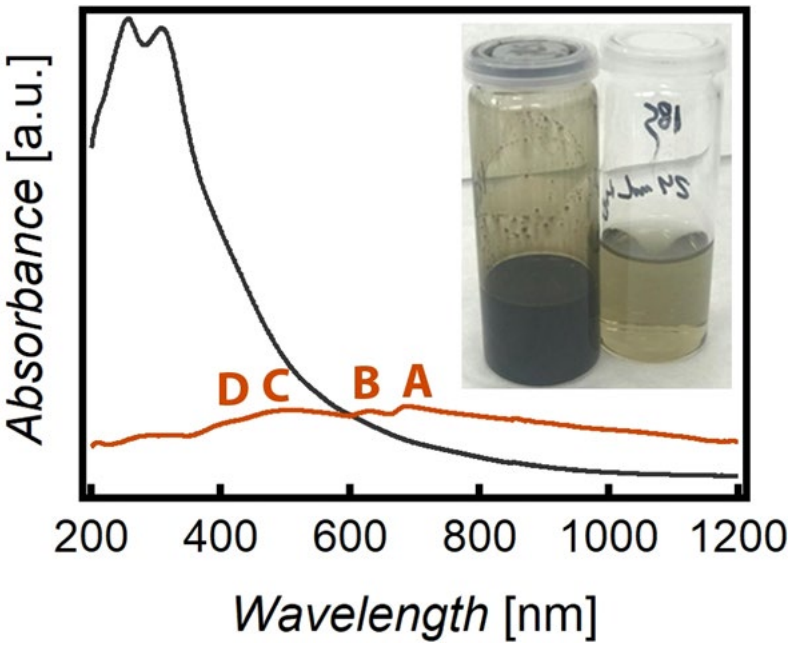

Figure II-6. UV/Vis spectra of commercial 2H-MoS_2 (brown) and ce-MoS_2 flakes (grey) in water. Inset: image of two purified suspensions of ce-MoS_2 flakes, the original suspension (left) and the (≈960 times) diluted one used for UV/Vis measurements (right).

Zeta potential (ZP)

According to ZP measurements (values of ≈-45 mV),[30] ce-MoS_2 flakes in Milli-Q water (pH ≈6–7) are negative-charged and form stable dispersions due to interlayer electrostatic repulsions.[38]

Raman spectroscopy

Raman spectroscopy provides excellent fingerprints of TMDCs. For MoS_2, it permits to extract useful information about the polytype and thickness of exfoliated layers.

The Raman spectrum of the starting commercial 2H-MoS_2 (**Figure II-7**) onto clean SiO_2 (285 nm)/Si substrates at 532 nm is dominated by two characteristic peaks at ≈381 and 406 cm^{-1}, which are assigned to the in-plane E^1_{2g} and out-of-plane A_{1g} modes, respectively. Whilst E^1_{2g} mode describes the opposite vibration of two S atoms respect to the Mo atom between them, A_{1g} is related to the transverse vibration of S atoms in opposite directions.[39] The Raman spectrum of ce-MoS_2 deposited by spin coating onto clean SiO_2 (285 nm)/Si substrates (**Figure II-7**) also at 532 nm shows, in addition to E^1_{2g} and A_{1g} modes, the so-called J peaks. The presence of J_1, J_2, and J_3 peaks (located at ≈152, 226 and 327 cm^{-1}, respectively) is typical of 1T-MoS_2. They arise from the longitudinal acoustic phonon modes of 1T-MoS_2.[40] In samples with a high content of 1T polytype, the intensity of E^1_{2g} and A_{1g} signals decreases respect to the J peaks. According to the frequency difference between the in-plane E^1_{2g} and out-of-plane A_{1g} peaks measured over several different ce-MoS_2 flakes, the estimated thickness was ≈1–5 nm.[41] In all cases, the Si peak at 521 cm^{-1} was used as reference.

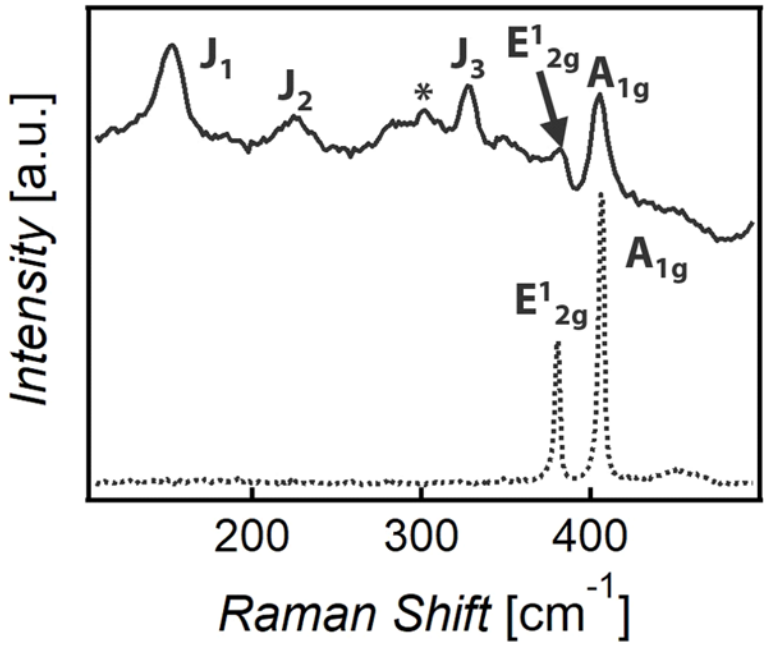

Figure II-7. Raman spectra of commercial 2H-MoS_2 (dashed line) and ce-MoS_2 (continuous line) onto a SiO_2/Si substrate at 532 nm.

Atomic force microscopy (AFM)

Once deposited, the topography of the flakes was scanned by atomic force microscopy (AFM) in tapping mode. According to AFM images and their corresponding height profile plots (**Figure II-8**), lateral and vertical dimensions of the obtained ce-MoS_2 flakes are comprised between 0.2–1.2 µm and 1–5 nm, respectively. These results are consistent with the deposition of ultrathin flakes.

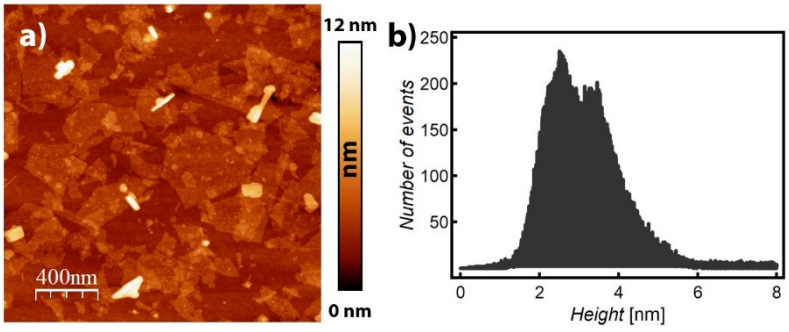

Figure II-8. a) AFM topographic image of a network of ce-MoS_2 flakes; b) Height histogram corresponding to the previous AFM topographic image.

High-resolution transmission electron microscopy (HRTEM)

The morphology and composition of ce-MoS_2 flakes were evaluated by HRTEM. As observed in **Figure II-9a**, the exfoliated ce-MoS_2 shows well-defined edges. Consistently, the selected-area electron diffraction (SAED) pattern (**Figure II-9b**) reveals the typical hexagonal pattern of MoS_2. The energy-dispersive X-ray spectroscopy (EDS) elemental mapping (**Figure II-9c** and **d**) evidences a homogeneous distribution of Mo and S along the flake.

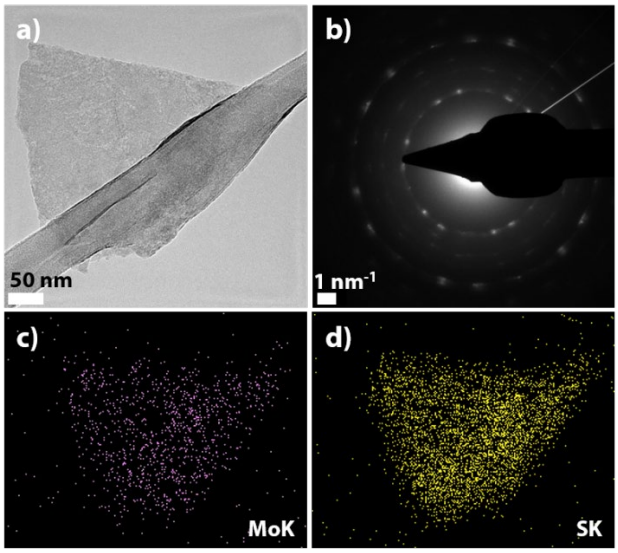

Figure II-9. a) HRTEM image of a ce-MoS_2 flake; b) SAED pattern of the flake shown in "a)"; c-d) EDS elemental mapping of the flake shown in "a)".

II.2.2. Synthesis and characterization of sample 1

In order to induce the growth of PB (and therefore the formation of the PB/MoS_2-based composite labelled as sample **1**), negatively charged ce-MoS_2 layers were employed for reducing the Fe^{III} present in the hexacyano complex to Fe^{II}.

Thus, a freshly prepared dispersion of ce-MoS_2 flakes in water was mixed with a 1:1 50×10^{-3} M $K_3Fe(CN)_6$:$FeCl_3$ aqueous solution. The mixture was allowed to react for 15 min under magnetic stirring. After this time, it was filtered and the resulting solid was copiously washed with water in order to remove the excess of unreacted iron salts.

Powder X-ray diffraction (PXRD)

The PXRD pattern of the isolated dark blue powder collected at room temperature (**Figure II-10**) displays characteristic PB peaks, proving the success of the followed synthetic strategy. Structure and phase purity of PB in **1** was confirmed with a Pawley refinement of the PXRD data by using the standard pattern for tetrairon(III) tris(hexacyanoferrate(II)) tetradecahydrate available from ICSD 1277. The most intense and well-resolved reflections are labelled with the corresponding plane. Full-profile fit yields acceptable cell parameters, agreement factors, and profile differences (a = 10.298 Å, R_p = 1.12, R_{wp} = 1.48%). An average particle size of approximately 11.1 nm was determined from the FWHM of (200) peak (0.60º) using Scherrer analysis. Noticeably, no MoS_2 peaks were observed,[3] which could be due to *i*) the fact that the most intense peaks in the diffractogram of MoS_2 correspond to (00*l*) planes and the functionalization with PB prevents the re-stacking of the layered structure of MoS_2 and *ii*) the lack or low amount of MoS_2 present in **1**.

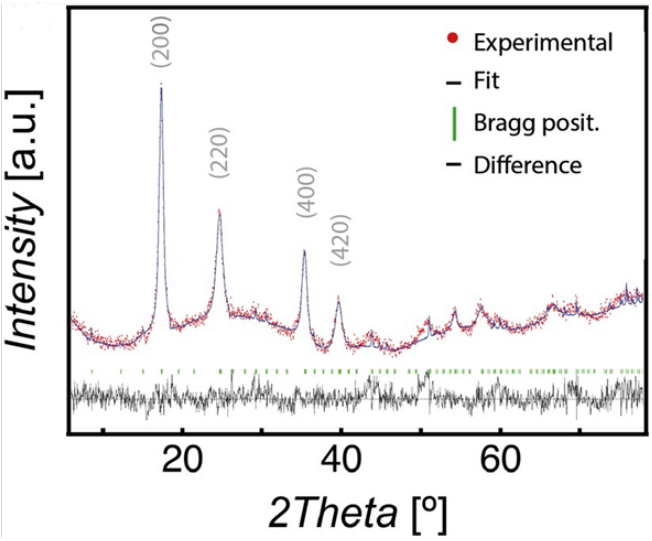

Figure II-10. Refined PXRD pattern of 1. It includes experimental (red dots), calculated (blue line), difference plots [(I_{obs}-I_{calc})] (black line), and Bragg positions (green ticks) for the Pawley refinement.

N_2 adsorption-desorption measurements

The experiments concerning porosimetry measurements were developed in collaboration with Dr. N. M. Padial and Dr. C. Martí-Gastaldo.

The porous nature of **1** was confirmed by N_2 adsorption-desorption measurements at 77 K (see **Figure II-11a**). As expected for PB particles, **1** displayed type-IV reversible N_2 uptake with no hysteresis. Therefore, the calculated value for multipoint Brunauer-Emmett-Teller (BET), 354 $m^2\ g^{-1}$, and the total pore volume, 0.26 $cm^3\ g^{-1}$, are remarkable. If compared to the use of other 2D templates like rGO,[26] nucleation onto MoS_2 yields PB particles with nearly 3 times higher specific SAs, which might result in superior electrochemical performance due to a more favourable ion diffusion. The analysis of the pore size distribution (PSD) by using non-linear solid density functional theory (NLDFT) indicates that porosity is dominated by micropores in accordance with the expected PB mean pore diameter of 5.7 Å at P/P0 = 0.0–0.3 and intergrain mesoporosity between 0.3 and 0.9 (see **Figure II-11b**).

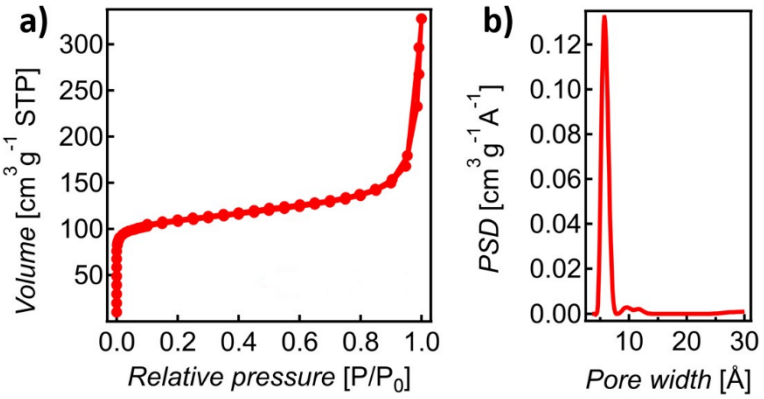

Figure II-11. a) N_2 adsorption-desorption isotherm of 1; b) Pore size distribution of 1.

Raman spectroscopy

In order to preserve **1** from burning, Raman spectroscopy was performed at 638 nm. The Raman spectrum of **1** (**Figure II-12**) is dominated by PB signals: a peak at ≈2155 cm^{-1} corresponding to the A_{1g} C≡N stretching vibrational band, a weak peak at ≈2097 cm^{-1} due to the E_g C≡N stretching vibrational mode and two smaller peaks at

≈540 and 270 cm^{-1} related to Fe–C stretching modes.[7,42,43] No additional peaks related to MoS_2 or MoO_3 can be distinguished.

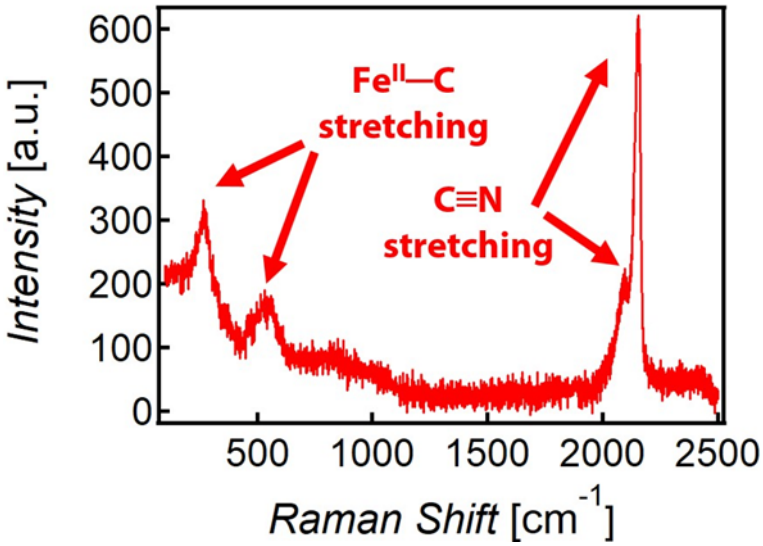

Figure II-12. Raman spectrum of 1 at 638 nm excitation wavelength.

Fourier transform infrared (FTIR) spectroscopy

The presence of Fe-coordinated C≡N groups was further confirmed by FTIR spectroscopy, which shows a vibrational band located at ≈2079 cm^{-1} ascribed to the Fe^{II}–C≡N stretching mode, and the bands located at ≈600 and 500 cm^{-1} referred to the Fe^{II}–C≡N–Fe^{III} bending modes. The presence of interstitial water molecules in sample **1** leads to the appearance of two additional bands near 3420 and 1616 cm^{-1}, which are attributed to the O−H stretching and H−O−H bending modes, respectively (see **Figure II-13**).[44,45]

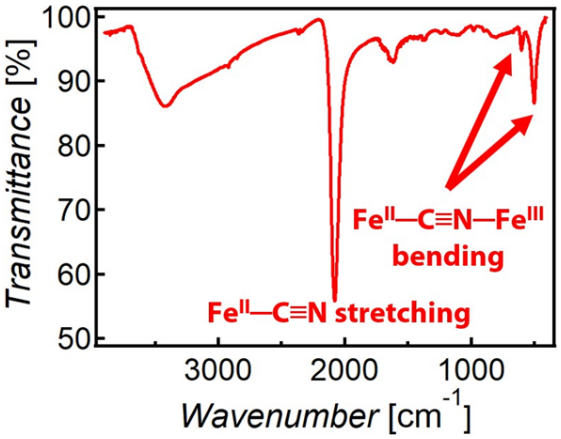

Figure II-13. FTIR spectrum of 1.

Regarding the most plausible forces between the 2D material and the mixed-valence compound, we propose non-covalent electrostatic interactions. This is supported by: *i*) the redox process between MoS_2 and Fe^{III} to induce the growth of PB, *ii*) the fact that the C≡N stretching vibrational bands in the Raman spectra of **1** do not show any significant shift respect to the Raman spectrum of bulk PB, *iii*) there are not additional peaks that could be assigned to the formation of new covalent bonds (*i.e.*, ν(S−CN)).

Mössbauer spectroscopy

The Mössbauer study was carried out in collaboration with Dr. J. C. Waerenborgh (from Universidade de Lisboa).

The mixed-valence nature of the PB in **1** was confirmed by means of Mössbauer spectroscopy. The Mössbauer spectrum of **1** (**Figure II-14**) is similar to those reported for PB compounds containing both LS Fe^{II}, S = 0, and HS Fe^{III}, S = 5/2. Using a similar analysis to that reported by Grandjean *et al.*,[7] a Fe^{II}:Fe^{III} ratio of ≈0.75 was calculated.

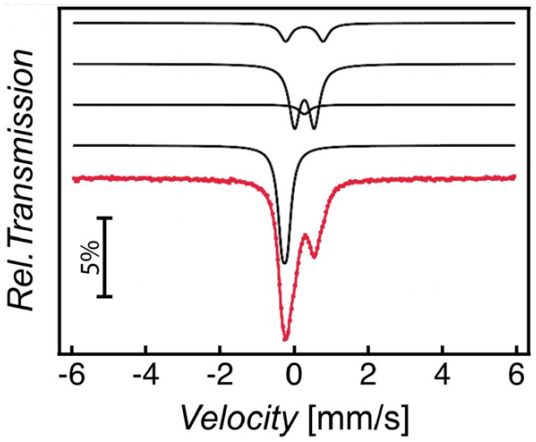

Figure II-14. Mössbauer spectrum of 1 taken at 295 K. The lines over the experimental points (slightly shifted for clarity) are the sum of three doublets and one singlet.

Inductively coupled plasma optical emission spectrometry (ICP-OES)

K:Fe and Fe:Mo molar ratios (≈0.07 and ≈16, respectively) were determined by using ICP-OES.

X-ray photoelectron spectroscopy (XPS)

XPS analysis of the sample **1** shows the presence of all expected peaks, except for those of sulphur (see **Figure II-15**). Probably, S signals are of the order of the experimental noise.

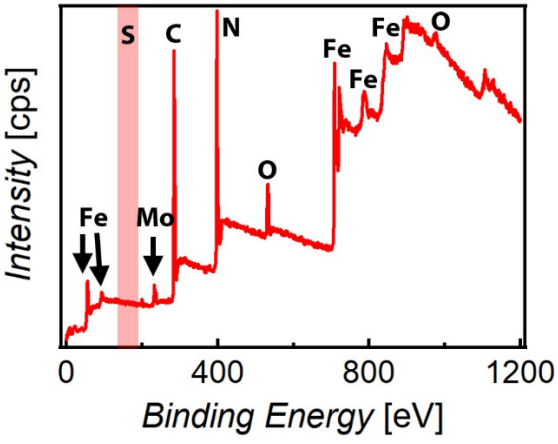

Figure II-15. XPS survey spectrum of 1. The typical S 2p XPS region is remarked in salmon color.

The Mo 3d XPS spectrum (**Figure II-16**) is dominated by a pair of doublets at 235.5/232.3 eV and 234.3/231.1 eV that contribute 40 and 60% to the overall Mo signal, respectively. According to the literature, they are identified as Mo^{VI} and Mo^{V} states.[46–48] Noticeably, no appreciable trace of $Mo^{IV}S_2$ states peaking at 229.2 and 232.3 eV are visible. Therefore, it would seem that during the reaction $K_3Fe(CN)_6$ overoxidizes ce-MoS_2 flakes, presumably to laminar H_xMoO_3[49,50] and/or MoS_yO_x species.[51] Mo 3d signal in **1** is highly attenuated in comparison to that in ce-MoS_2 due to the lower amount of Mo in **1** and the additional screening of Mo 3d photoelectron when going through the PB outer layer. This latter effect is expected to be stronger for S. **Table II-1** shows the Mo XPS values registered for commercial MoS_2, ce-MoS_2 flakes, and commercial MoO_3.

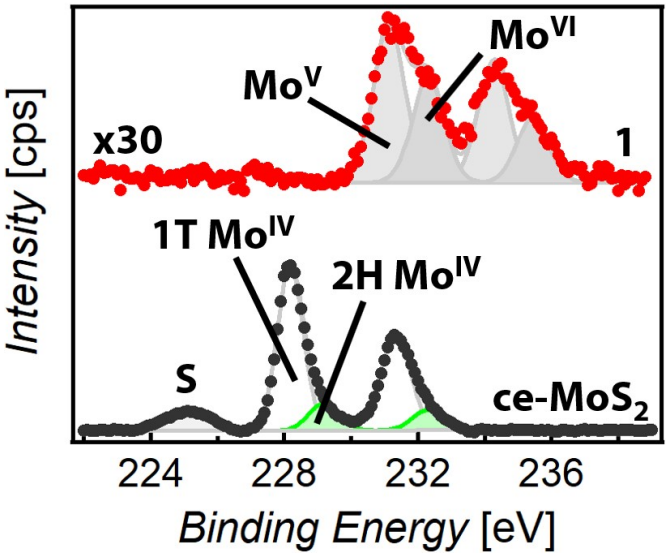

Figure II-16. Mo 3d spectra of 1 and ce-MoS_2.

Table II-1. Mo XPS values registered for commercial MoS_2, ce-MoS_2 flakes, and commercial MoO_3.

Material	Mo XPS signals
commercial 2H-MoS_2	≈229.2 eV Mo^{IV} $3d_{5/2}$ ≈232.3 eV Mo^{IV} $3d_{3/2}$
ce-MoS_2 flakes	≈228.2 eV Mo^{IV} $3d_{5/2}$ (1T) ≈231.3 eV Mo^{IV} $3d_{3/2}$ (1T) ≈229.2 eV Mo^{IV} $3d_{5/2}$ (2H) ≈232.3 eV Mo^{IV} $3d_{3/2}$ (2H)
commercial MoO_3	≈232.4 eV Mo^{VI} $3d_{5/2}$ ≈235.6 eV Mo^{VI} $3d_{3/2}$

Elemental analysis

In relation to the formation of less sulphur-rich species by overoxidation, the elemental analysis data (C = 17.8%, N = 19.0%, S = 1.1%) revealed only half of the expected sulphur.

Thermogravimetric analysis (TGA)

Finally, TGA was used to best estimate the water content. Whilst the two first mass drops correspond to the removal of both zeolitic and coordinated water molecules (≈32%), the third one above 278 °C is due to cyanide loss, as observed in **Figure II-17**.

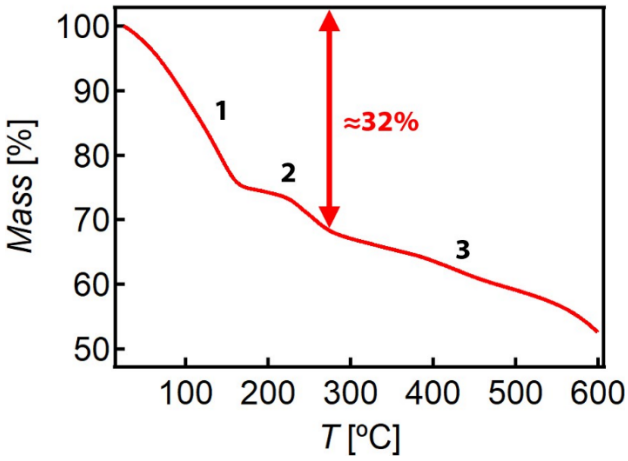

Figure II-17. TGA plot of 1. The mass drops labelled as 1, 2, and 3 represent the loss of zeolitic water, coordinated water, and cyanide from PB.

Considering the information provided by all the techniques, the composition of **1** can be approximated to $(K_{0.47}Fe_4^{III}[Fe^{II}(CN)_6]_{3.14})@(MoSO_{1.7})_{0.44}\cdot 26H_2O$.

Magnetic measurements

Due to the magnetic properties of PB, magnetic properties of **1** were studied using a superconducting quantum interference device (SQUID) magnetometer. In **Figure II-18a**, the bifurcation between ZFC and FC plots evidences magnetic order, as expected for a ferromagnetic order at low temperature. In **Figure II-18b**, the narrow hysteresis, along with a very low coercive field value, confirms a soft magnet behaviour. According to alternating current (*ac*) magnetic susceptibility measurements (**Figure II-18c)**, the Curie temperature (T_c) of the magnetic ordering is of ≈3.5 K, slightly lower than the expected for bulk PB crystals (5.5 K).[52] The observed T_C is in good agreement with the small particle size (≈11 nm) detected in sample **1**.[53]

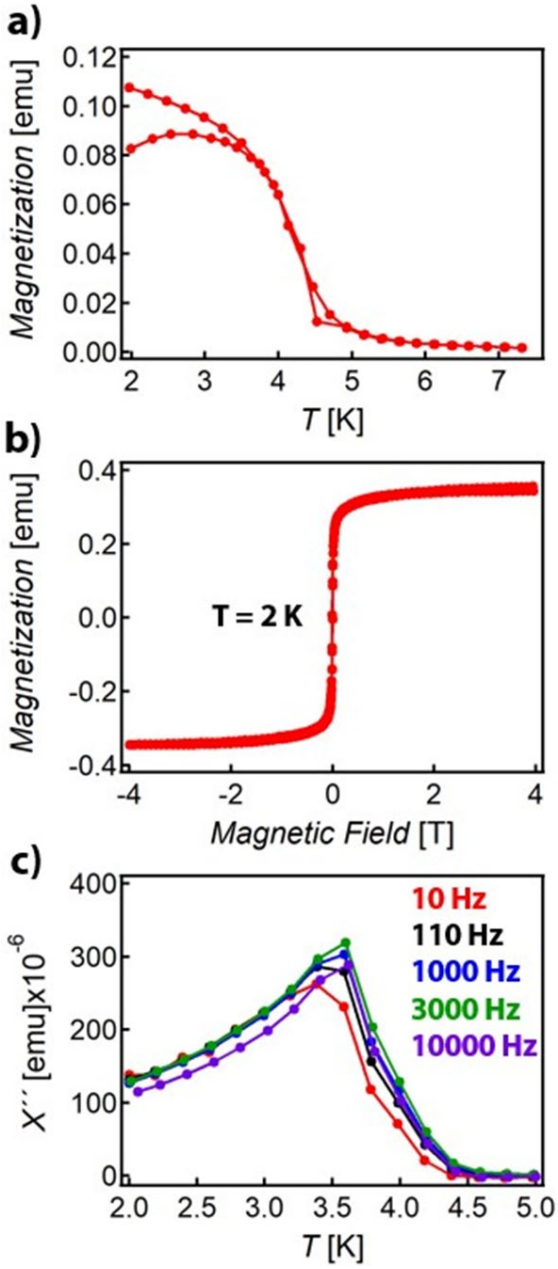

Figure II-18. a) Zero field cooled-field cooled (ZFC-FC) curves of 1. FC-ZFC plots are placed top and down, respectively; b) Magnetization hysteresis loop of 1 at 2 K; c) Thermal variation of the out of phase *ac* susceptibility measurements of 1 at different frequencies.

Transmission and scanning electron microscopies (TEM and SEM)
TEM and SEM were performed in order to evaluate the morphology of **1**. The composite keeps a lamellar structure with flakes fully covered by a continuous layer of PB nanocrystals. This is in contrast with other PB/2D composites reported in literature that show the presence of isolated cubic PB crystals more or less sparse over the MoS_2 surface.[3,21] Such difference arises from the double role played by ce-MoS_2, both as reducing agent and nucleation platform in the absence of any other surfactant or stabilizing surface agent. This gives rise to a quick nucleation and growth of PB small crystals all over the ce-MoS_2 surface (see **Figure II-19a**). Fast Fourier transform (FFT) analysis of HRTEM images of the PB NPs revealed a fcc pattern with a = 10.11 Å (see **Figure II-19b**), in close agreement with PXRD data. The homogeneous distribution of the hexacyanometallate network on the flakes is further confirmed by using EDS mapping (**Figure II-19d-h**), where Mo and S signals are perfectly correlated with Fe, C, and N signals.

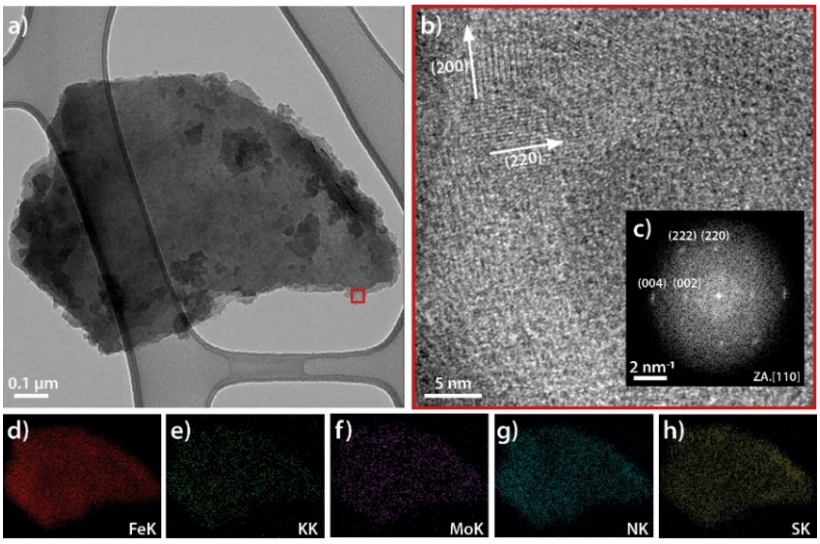

Figure II-19. a) TEM image of 1; b) HRTEM image corresponding to the red square area shown in "a)"; c) FFT resulting from "b)"; d-h) EDS elemental mapping of the sample shown in "a)".

The same homogeneous distribution was observed in SEM images (**Figure II-20**).

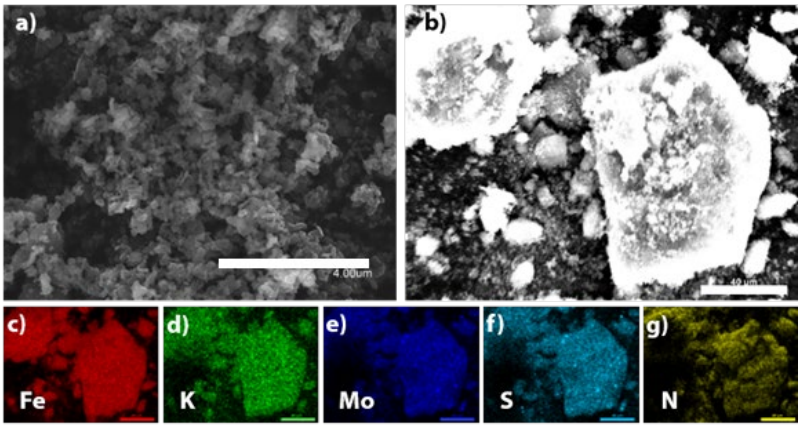

Figure II-20. a) SEM image of 1. Scale bar is 4 µm; b) SEM image chosen for EDS elemental mapping. Scale bar is 40 µm; c-g) EDS elemental mapping in the region shown in "b)". Scale bar is 40 µm.

II.2.3. Functionalization of MoS_2 on surface (samples 2-6)

II.2.3.1. Preparation and characterization of samples 2 and 3

In order to get a better control on the PB growth, we performed the functionalization of ce-MoS_2 flakes after their deposition onto SiO_2 (285 nm)/Si substrates. In this way, the reaction time between the $K_3Fe(CN)_6$:$FeCl_3$ aqueous solution and flakes can be more easily controlled since, when the reaction occurs in suspension, the reaction can progress even during the filtration process.

Firstly, networks of ce-MoS_2 flakes (samples **2** and **3**) were deposited by spin-coating a freshly dispersed suspension of ce-MoS_2 flakes on two SiO_2 (285 nm)/Si substrates; in a next step, a $K_3Fe(CN)_6$:$FeCl_3$ aqueous solution was spin-coated above the previous networks. Two Fe concentrations were used during these experiments: a 1:1 50×10^{-3} M $K_3Fe(CN)_6$:$FeCl_3$ solution for sample **2** and another one 2.5 times more diluted for sample **3**.

AFM

Only the topography of sample **3** was scanned by AFM since the sample **2** showed a tremendous amount of grown material. Thus, in sample **3**, AFM revealed a continuous thin film of material

preferentially grown on top of the flakes after few seconds of reaction with the iron solution (see **Figure II-21**).

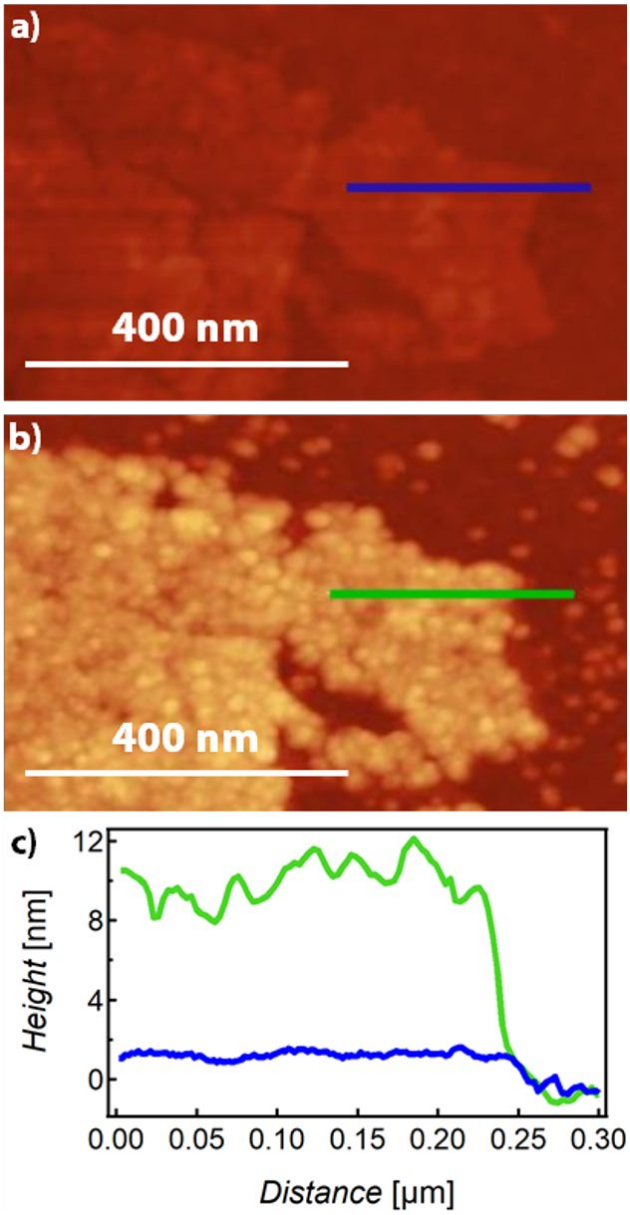

Figure II-21. a-b) AFM topographic images of sample 3 before and after $K_3Fe(CN)_6$:$FeCl_3$ treatment, respectively; c) Height profiles corresponding to "a)" and "b)" regions.

Raman spectroscopy

A clear difference between samples **2** and **3** was observed by confocal Raman spectroscopy (see **Figure II-22**). Thus, the spectrum recorded for **2** resembles the one of powder sample **1** and displays only PB peaks with no signals related to MoS_2 or its oxide. On the contrary, sample **3** shows the characteristic in-plane E^1_{2g} (≈382 cm^{-1}) and out-of-plane A_{1g} (≈406 cm^{-1}) MoS_2 signals, matching the frequency difference expected for thin MoS_2 flakes, 3–4 layers thick.[54] Moreover, in **3** the A_{1g} C≡N vibration is less intense and shifted to lower energies (≈2040 cm^{-1}). This shift is correlated to a decrease in the average valence state of Fe.[55–57]

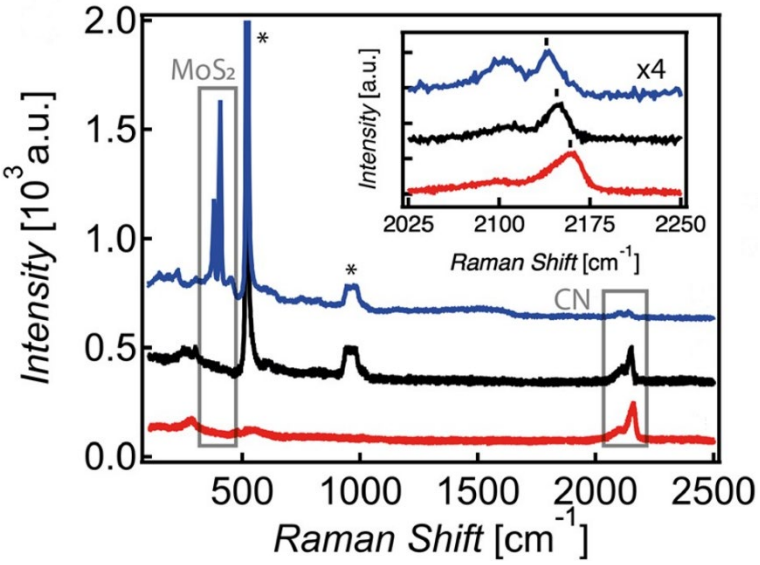

Figure II-22. Raman spectra of sample 1 (red), sample 2 (black), and sample 3 (blue). Peaks marked with * correspond to SiO_2.

Considering these results, we concluded that, when higher concentrations are employed (sample **2**), thicker shells are formed and Fe^{II}:Fe^{III} ratio decreases. In this case, negative-charged MoS_2 is oxidized to less crystalline species with higher oxidation states and its characteristic Raman signals are broadened and/or masked by the PB film and eventually lost. By contrast, when low concentration solutions of Fe^{III} are used, the amount of deposited material is lower (weak A_{1g} C≡N Raman signals), MoS_2 peaks can be detected (MoS_2 is preserved) and the deposited material is mostly reduced to Fe^{II}.

II.2.3.2. Preparation and transport properties of sample 4

In order to have some knowledge about the pathways that dominate the electronic transport through the new hybrid composite, the transport properties of the composite were studied on freshly ce-MoS_2 flakes deposited by spin-coating over commercial prepatterned interdigitated Au electrodes (sample **4**) and intensity-voltage (I-V) curves were recorded at room temperature (**Figure II-23**). These measurements were performed by Dr. Marta Galbiati. An almost linear response was observed, as expected for ce-MoS_2 (red line).[30,58] Right after this first measurement, a 1:1 50×10^{-3} M $K_3Fe(CN)_6$:$FeCl_3$ aqueous solution was spin-coated over Au electrodes and finally transport measurements were repeated. After functionalization, resistance was clearly increased and a semiconducting behaviour was observed (black line). Interestingly, the sample showed a completely insulating behaviour when it was measured under vacuum (grey line). The same semiconducting/insulating behaviour under vacuum was confirmed when sample **1** was dispersed by drop-casting over the prepatterned electrodes. These findings are in concordance with previous reports on solid-state PB electrical properties, where PB is described as a semiconductor when moisture is absorbed,[59,60] while it becomes an insulator when it is vacuum dried.[61] Moreover, this measurement points out that, after functionalization, a continuous PB shell covers the flakes and dominates the electrical transport in solid state.

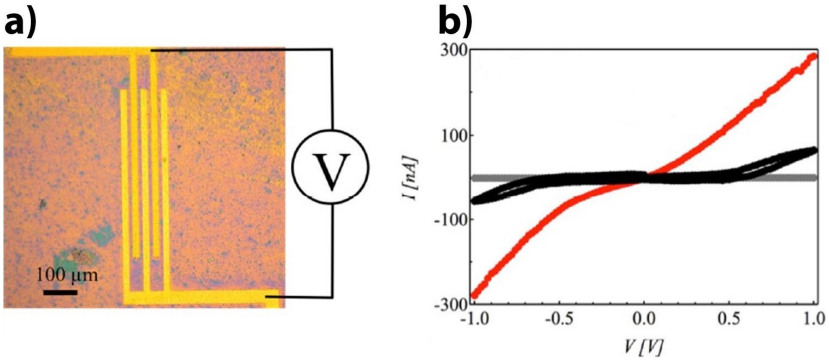

Figure II-23. a) Optical microscope image of sample 4; b) I-V plots under ambient atmosphere of a network of ce-MoS_2 before the Fe treatment (red curve) and the resultant sample 4 in air (black curve) and under vacuum (10^{-6} mbar, grey curve).

II.2.3.3. Preparation and characterization of samples 5 and 6

Next, looking for a better understanding about the process involved in the composite formation and highlight the crucial role played by the negative charges accumulated over ce-MoS_2 surface during the PB growth, surface experiments with MoS_2 flakes obtained by the well-known Scotch tape[62] were carried out. First, thin me-MoS_2 flakes were deposited on two SiO_2 (285 nm)/Si substrates and characterized by optical microscopy and AFM (samples **5** and **6**).

In order to reduce me-MoS_2 flakes, sample **5** was immersed in a solution of *n*-BuLi (1.6 M) in hexane for 24 h under inert atmosphere (in glovebox) and then copiously rinsed with solvent.[31] Finally, a 1:1 50×10^{-3} M $K_3Fe(CN)_6$:$FeCl_3$ solution (the same mixture used for the preparation of **1**) was spin-coated over both samples.

AFM

AFM topography images clearly show that sample **5** developed a very compact PB film (≈40 nm thick), contrary to what was observed in sample **6** (see **Figure II-24**), which was not previously reduced with *n*-BuLi (see **Figure II-25**). These results seem to confirm our hypothesis that negative-charged MoS_2 acts as a reducing agent and consequently its selective functionalization with hexacyanoferrates only takes a few seconds.

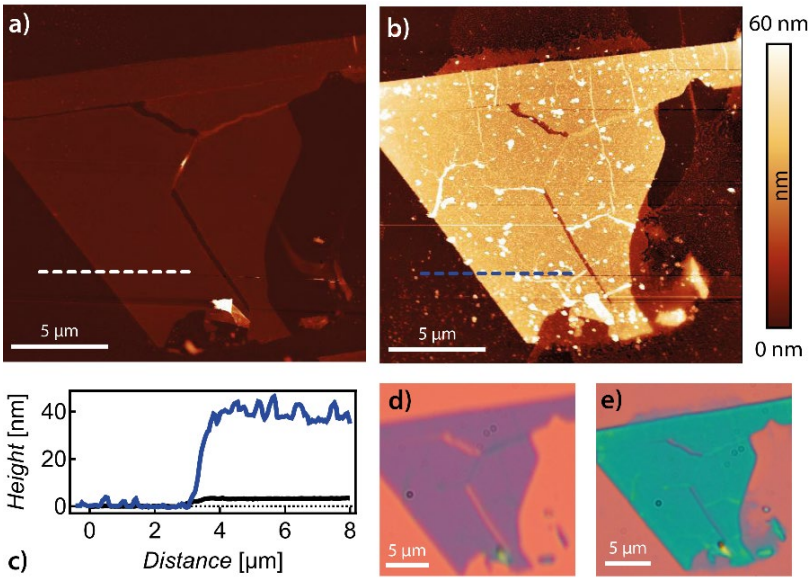

Figure II-24. a-b) AFM topographic images of 5 before and after treatment with *n*-BuLi and a $K_3Fe(CN)_6$:$FeCl_3$ aqueous solution, respectively; c) Height profiles corresponding to "a)" an "b)" regions; d-e) Optical images of 5 before and after PB functionalization, respectively.

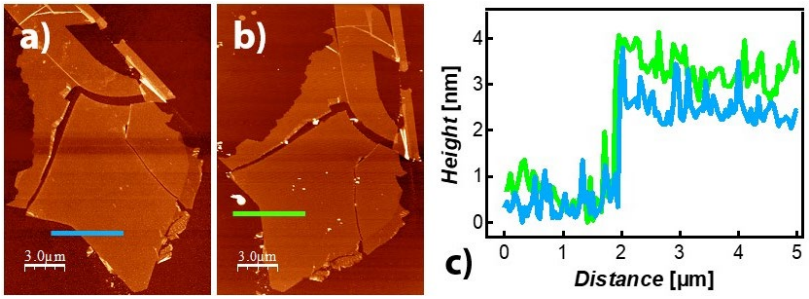

Figure II-25. a-b) AFM topographic images of 6 before and after treatment with a $K_3Fe(CN)_6$:$FeCl_3$ aqueous solution, respectively; c) Height profiles corresponding to "a)" and "b)" regions.

II.2.4. Electrochemical measurements and study of 1 as cathode material for SIBs and KIBs

The electrochemical study was performed in collaboration with R. Sanchis-Gual, J. Romero, Dr. Antonio Alberola, Dr. Leticia García-Cruz, and Prof. Vicente Montiel (these two latter from Universidad de Alicante).

The performance of sample **1** as potential cathode material for SIBs and KIBs was tested. The electrochemical performance of the material was evaluated in a typical three-electrode cell by cyclic voltammetry (CV) and galvanostatic charge/discharge cycles at different current densities in three different aqueous solutions of Na_2SO_4 (1 and 0.5 M) and K_2SO_4 (0.5 M) as electrolytes. In order to reach higher conductivity within the composite in the working electrode, **1** was deposited on a carbon felt previously calcined at 1000 °C.

Figure II-26a shows the CVs of **1** in 1 M Na_2SO_4 aqueous solution (electrolyte). CVs show two pairs of redox processes located between 0.2 and 0.5 V that, according to the literature,[63–65] are assigned to the oxidation and reduction of the Fe atoms coordinated to the C atom in the cyanide ligand (Fe^{II}–CN), and the Fe atoms coordinated to the N atom (Fe^{III}–NC), respectively. The presence of the second peak, although not clearly resolved probably due to a partial pseudocapacitive behaviour of the 2D composite shows that, contrary to what commonly observed, the electrochemical activity of Fe^{III} is not blocked due to the presence of neighbouring vacancies and contributes to total specific capacity.[20] Most importantly, these peaks match well with the main potential plateau at the discharge curves (see **Figure II-26b**).

Additionally, a plot of log(I) versus log(v) (I = peak current intensity, v = scan rate), that provides kinetic information about the electrochemical reaction, shows an almost perfect linear dependence (see **Figure VII-2** in **Appendix**). From the slope of the linear plot of log(I) a "b" value close to 0.5 for Na^+ insertion is obtained. This value strongly suggests that electroactive material reactions are mainly controlled by Na^+ diffusion steps associated with the Na^+ concentration in the lattice, as it occurs in battery-type processes.[66]

After pre-activation, discharge capacity values up to 177 mA h g^{-1} were obtained at a current density of 1 A g^{-1}, reaching a specific capacitance* of 354 F g^{-1} (see **Figure II-26c**), which evidences an excellent material performance.[20,23] As expected, the specific capacities† of **1** decrease rapidly under high current densities.

* total charge divided by the potential window and the mass of electroactive material (in F g^{-1}).
† total charge divided by the mass of electroactive material (in mA h g^{-1}).

It is worth noting that the charge and discharge capacities follow similar trends during the whole cycling experiment, with an outstanding capacity retention[‡] of ≈98% after 10.000 charge/discharge cycles at a current density of 10 A g^{-1} (see **Figure II-26d**). Thus, the calculated round-trip efficiency is 98.3% at the first cycle and 91.3% at cycle number 10.000. Moreover, rate capability was measured from 1 to 10 A g^{-1} (see **Figure II-26e**). The electrode shows an excellent capacity retention even if the current density increases. Furthermore, the capacity recovered when the current density was lowered again to 1 A g^{-1}, suggesting the presence of reversible reactions. The long-life cycling performance and excellent rate capability of **1** suggest a high structural and electrochemical stability for Na-storage reactions.

[‡] percentage of the capacity remaining after a given number of charge/discharge cycles respect to the initial capacity.

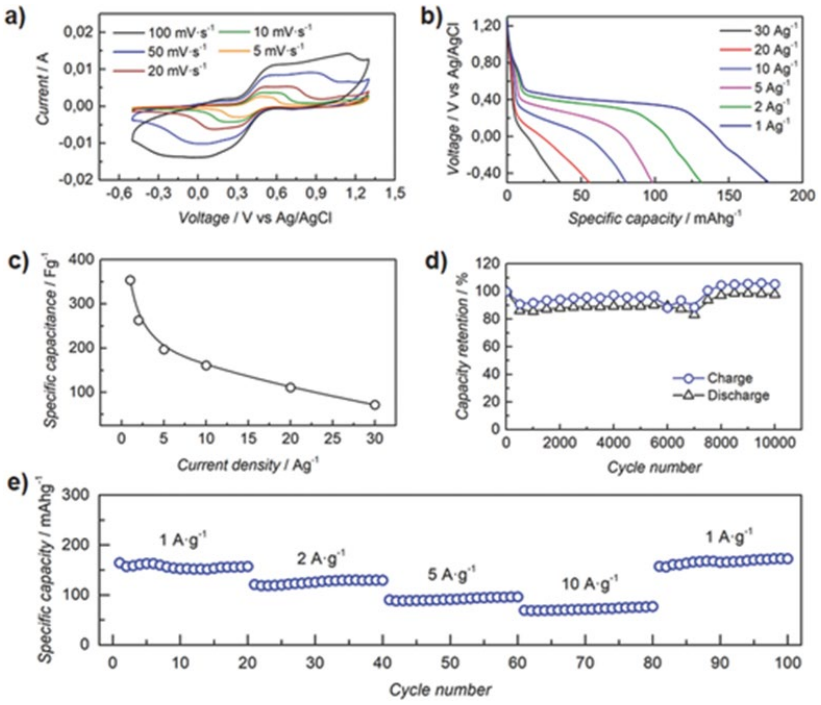

Figure II-26. Electrochemical measurements of 1 in a typical three-electrode cell using 1 M Na_2SO_4 aqueous solution. a) CVs at different scan rates; b) Galvanostatic discharge curves at different current densities; c) Specific capacitance at different discharge current densities; d) Capacity retention in 10.000 charge/discharge cycles; e) Rate capability at current rates ranging from 1 to 10 A g^{-1}.

Experiments performed when decreasing the Na^+ concentration in the electrolyte aqueous solution (0.5 M Na_2SO_4) present lower current values and differences in the width of the peaks (**Figure II-27a**), as previously described for thin films of PB analogues.[67] In fact, discharge capacity and specific capacitance values (see **Figure II-27b** and **c**, respectively) are much lower than those obtained in 1 M Na_2SO_4 aqueous solution (discharge capacity value of 105 mA h g^{-1} at 1 A g^{-1} and specific capacitance of 210 F g^{-1}). A combination of redox and intercalation pseudocapacitance renders this material a highly promising cathode material for SIBs.[68]

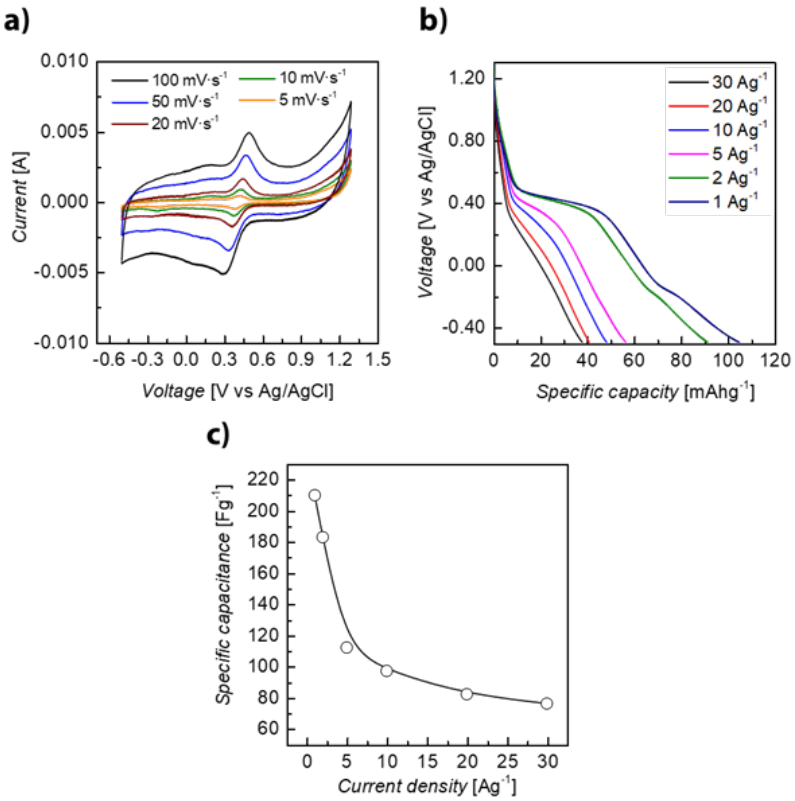

Figure II-27. a) CVs of 1 at different scan rates in a three-electrode cell using 0.5 M Na_2SO_4 aqueous solution; b) Galvanostatic discharge curves of 1 at different current densities using 0.5 M Na_2SO_4 aqueous solution; c) Specific capacitance of 1 at different discharge current densities using 0.5 M Na_2SO_4 aqueous solution.

Remarkably, when replacing Na^+ by K^+ (0.5 M K_2SO_4 electrolyte solution), although the CV curves (**Figure II-28a**) look very similar to those obtained in 1 M Na_2SO_4 aqueous solution, the values achieved by the discharge curves (215 mA h g^{-1} at 1 A g^{-1} with specific capacitance up to 489 F g^{-1}) are considerably higher than those achieved using Na^+ (177 mA h g^{-1} and 354 F g^{-1}). These values were extracted from **Figure II-28b** and **c**. In this case, capacity also remains stable, with a capacity retention of ≈97% after 10.000 charge/discharge cycles at a current density of 10 A g^{-1}, a value very close to that obtained with Na^+, as can be seen in **Figure II-28d**. Thus, the calculated round-trip efficiency is 95.9% at the first cycle and 90.0% at cycle number 10.000. As well as in the sodium behaviour, a similar

rate capability is obtained, with higher values of the specific capacitance (see **Figure II-28e**).

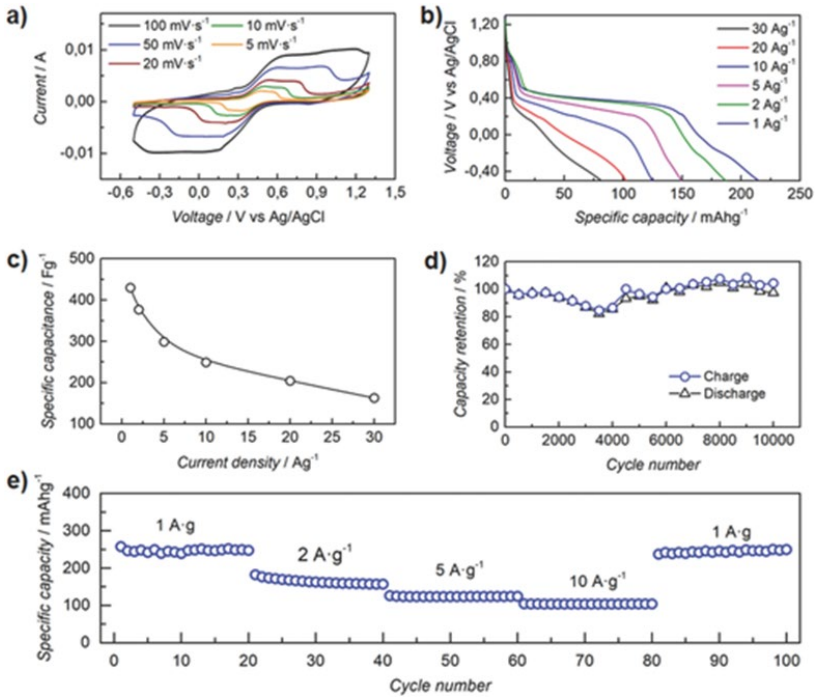

Figure II-28. Electrochemical measurements of 1 in a typical three-electrode cell using 0.5 M K_2SO_4 aqueous solution. a) CVs at different scan rates; b) Galvanostatic discharge curves at different current densities; c) Specific capacitance at different discharge current densities; d) Capacity retention in 10.000 charge/discharge cycles; e) Rate capability at current rates ranging from 1 to 10 A g^{-1}.

Here again, the electrode current changes with scan rate following an exponential order expected for a diffusion-controlled process (see **Figure VII-3** in **Appendix**). This indicates that electroactive material reactions are mainly controlled by K^+ diffusion.

Next, the electrochemical properties of the KIB electrode were tested using electrochemical impedance spectroscopy (EIS) experiments before and after the charge/discharge cycling treatment. The Nyquist diagram of the untreated electrode shows a classical behaviour exhibiting a semicircle at high frequencies and a diffusional region at medium and low frequencies (see **Figure VII-4** in **Appendix**).

The lower frequencies within the diffusion region show a slope of 50° near the theoretical value of 45° for a purely semi-infinite diffusion. An equivalent circuit depicted in **Figure VII-4d** in **Appendix** fits well with the experimental values in order to address the internal resistance regarding the migration of ions through the 3D carbon felt electrode. Moreover, a transition from semi-infinite to finite diffusion is observed at low frequencies, which is typical for porous electrodes. Owing to the intrinsic macroporosity and heterogeneity of the carbon felt electrode, which adds a remarkable difficulty when interpreting impedance results, EIS experiment of the pristine carbon felt in the absence of the composite was also performed under the same EIS experimental conditions (see **Figure VII-5** in **Appendix**). It is worth noting that the onset of the diffusion region for the pristine carbon felt does not respond to a purely diffusion process, showing a slope superior to 60°, when compared with the EIS behaviour of the untreated electrode.

After the activation of the electrode (by subjecting it to 50 charge/discharge cycles), a different EIS behaviour is observed for the Nyquist diagram at high and moderate frequencies, as depicted in **Figure II-29**, clearly showing a Nyquist diagram very representative for Na^+ kinetics in graphitized carbon electrodes.[69] We also used the representative equivalent circuit depicted in **Figure VII-4d** (in **Appendix**), which involves the appearance of two well-defined semicircles at high and moderate frequencies, respectively, in contrast to the EIS behaviour of the non-activated electrode. Accordingly, Q2 and R2 elements stand for the capacitance and resistance of the surface layer or passivating film (first semicircle), whereas the second semicircle is assumed to be related to charge transfer, though adsorption processes might also be taken into consideration.[70] Moreover, the onset of the diffusion region exhibits a slope 50° again near a purely semi-infinite process. Hence, charge/discharge cycling of the electrode led to the appearance of two well-defined physical phenomena in the region of high and moderate frequencies similar to those resulting from ion insertion into carbonaceous electrodes during battery charging.

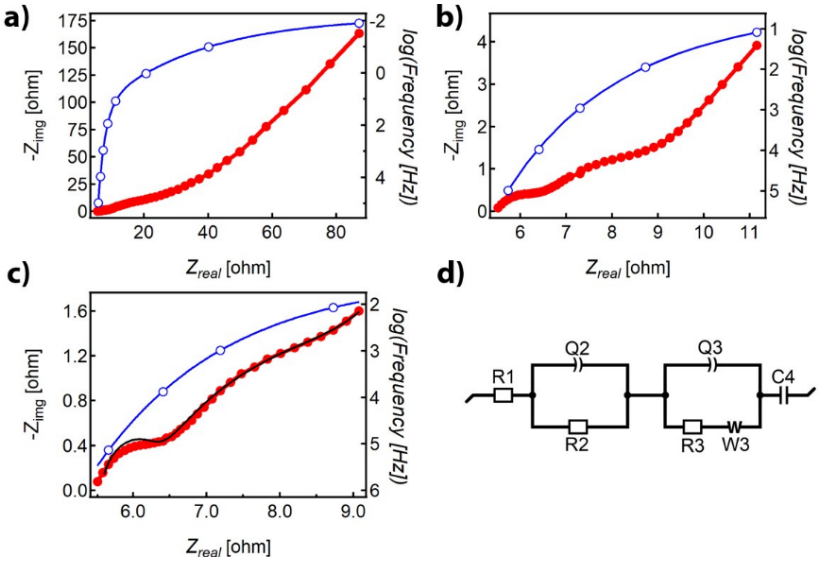

Figure II-29. Alternating current impedance (ACI) diagram of the KIB cathode after 50 charge/discharge cycles in 0.5 M K_2SO_4 aqueous solution. The frequency is given in a logarithmic scale in the graph; b) Zoom of the high frequencies in "a)"; c) Fit for the equivalent circuit described in the scheme "d)"; d) Circuit that represents the present electrochemical system. Frequency ranges for the experiment and fit are 0.2–10 and 0.2–100 mHz, respectively. X^2 is least for the model (0.1225).

In **Table II-2**, we compare the maximum specific capacity and cycling stability values of **1** to those observed in other similar composites based on a 2D carbonaceous platform and PB.

Table II-2. Comparative table between 1 and other similar composites in terms of maximum specific capacity and cycling stability.

Sample	Electrolyte	Maximum specific capacity		Cycling stability		References
		Current density [mA g^{-1}]	Specific capacity [mA h g^{-1}]	Cycle number	Capacity Retention [%]	
1	Na	1000	177	10000	98	**This work**
1	K	1000	215	10000	97	**This work**
PB@rGO	Na	500	159	1000	92	26
PB@rGO	Na	30	163	500	92	71
PB@rGO	Na	30	152	500	89	71
PB@rGO	Na	30	135	500	72	71
PB@GO	Na	25	150	50	93	23
PB@C	Na	100	123	2000	90	20

We attributed the outstanding performance of **1** as cathode material for SIBs or KIBs to its atypical morphology, where the original 2D layer is fully covered by a continuous shell of PB nanometric-size crystals, as a result of the rapid nucleation and growth of the PB on the surface of the ce-MoS_2 flakes. This yields a crystalline material with optimum grain size and increased surface area according to PXRD and gas sorption measurements, respectively. This particular morphology improves the accessibility of Na^+ and K^+ to the voids as well as the cation diffusion during the charge/discharge process, thus reducing maximum diffusion length, facilitating Fe^{III} and double-layer contributions to the overall capacitance, and promoting a closer contact between the carbon matrix and PB crystals. It is worth noting that we cannot discard a potential contribution of the underlying 2D material to the cathode performance, as the activity of (bulk and few-layer) MoS_2 and MoO_x for different energy storage processes has been largely demonstrated.[68,69] We attributed the good cyclability to the combination of the increased long-term resilience brought by the 2D matrix with the alleviated strain induced by volume changes during metalation/de-metalation in our smaller crystals. Finally, the improvement observed when using K^+ electrolyte solution can be justified by the fact that PB was synthetized starting from $K_3Fe(CN)_6$. This probably determines more optimum conditions for the diffusion and accommodation of K^+ ions versus Na^+ ions within the voids. Thus,

the preparation of the composite using sodium hexacyanoferrate as precursor could be a key strategy to upgrade the performance of the material in Na^+ electrolyte solution for its future application in SIBs.

II.2.5. Stability of 1 upon K^+ intercalation/de-intercalation

The stability of **1** upon K^+ intercalation/de-intercalation was evaluated by the chemical characterization of the working electrode material after 200 charge/discharge cycles in 0.5 M K_2SO_4 aqueous solution. PXRD and XPS results (see **Figure II-30** and **Figure II-31**, respectively) are comparable to those obtained before the activation and clearly confirm the stability of the PB component and the underlying 2D material.

PXRD patterns corresponding to the electrodes used before and after the electrochemical measurements (**Figure II-30**) show characteristic diffraction peaks of PB (marked with dashed lines) that appear next to those coming from the carbon matrix of the electrode. In the case of the electrode after the electrochemical test, XRD peaks coming from K_2SO_4 residues (electrolyte solution) are also detected.

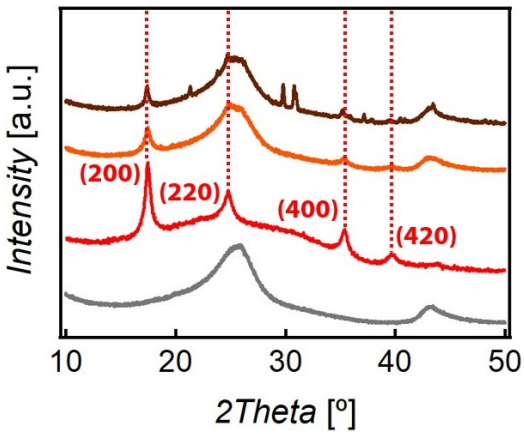

Figure II-30. PXRD patterns of the electrode carbon matrix (grey), sample 1 (red), and the electrode before (orange) and after (brown) 200 charge/discharge cycles in 0.5 M K_2SO_4 aqueous solution. Dashed lines remark the typical PB peaks.

XPS 3d Mo spectrum (**Figure II-31**) was performed to prove the stability of the layered component. After the charge/discharge process, XPS spectrum only decreases its intensity, which can be attributed to a copious rinsing of the used electrode in order to remove the electrolyte. This step can originate a partial loss of **1** in the electrode.

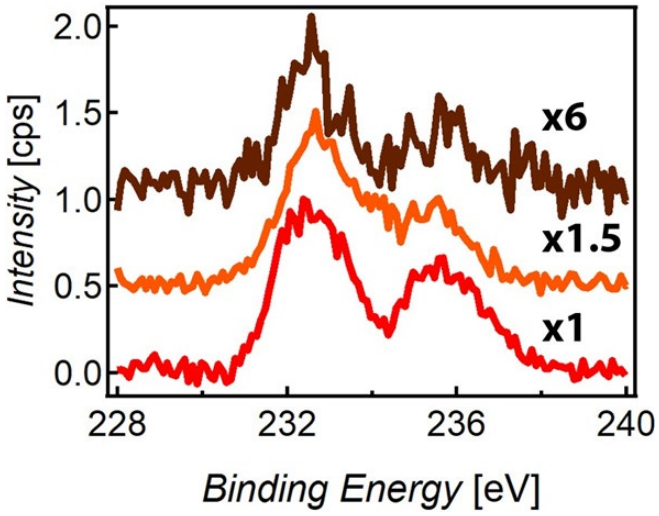

Figure II-31. Mo 3d XPS spectra of sample 1 (red), and the electrode before (orange) and after (brown) 200 charge/discharge cycles in 0.5 M K_2SO_4 aqueous solution.

II.2.6. Control over the oxidation of MoS_2 flakes when preparing PB composites in solution

In light of the results obtained from experiments on surface, we decided to minimize the oxidation degree of flakes by increasing the amount of ce-MoS_2 respect to PB precursors and reducing the reaction time at once. Therefore, we used a {ce-MoS_2:Fe-containing reagents} molar ratio 5 times higher than the required for preparing sample **1** and fixed the stirring time to 1 minute.

Thus, in order to check the validity of this strategy when preparing composites with non-oxidized MoS_2 flakes, the resulting composite (sample **7**) was characterized by XPS, PXRD, FTIR, Raman and Mössbauer spectroscopies, TEM, ICP-OES, and TGA. Ultimately, considering all the results provided by the previous techniques, we proposed a chemical formula for **7**.

XPS

In order to ascertain that our hypothesis was correct, the sample **7** was firstly subjected to XPS analysis. If compared to **1 (**see **Figure II-32** and **Table II-3**), the XPS survey of **7** clearly highlights the presence of S.

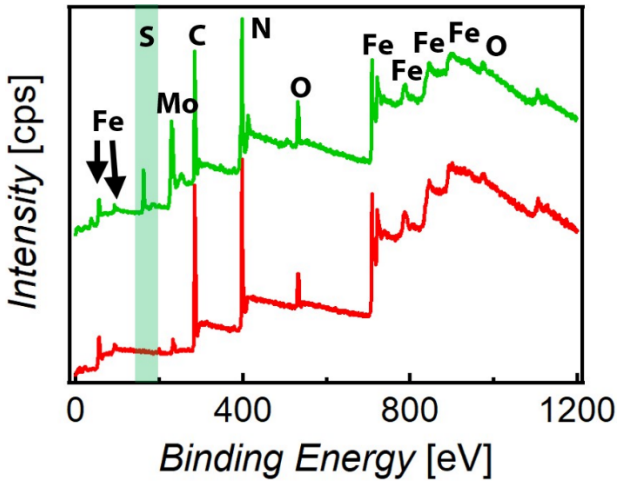

Figure II-32. XPS survey spectra of 1 (red) and 7 (green). The typical S 2p XPS region is remarked in green.

Table II-3. Mo and S XPS values observed in samples 1 and 7.

Sample	Mo XPS signals	S XPS signals
1	≈231.1 eV Mo^{V} $3d_{5/2}$ ≈234.3 eV Mo^{V} $3d_{3/2}$ ≈232.3 eV Mo^{VI} $3d_{5/2}$ ≈235.5 eV Mo^{VI} $3d_{3/2}$	Ø
7	≈229.2 eV Mo^{IV} $3d_{5/2}$ ≈232.3 eV Mo^{IV} $3d_{3/2}$	≈161.2 eV S^{-I} $2p_{3/2}$ ≈162.1 eV S^{-I} $2p_{1/2}$ ≈162.1 eV S^{-II} $2p_{3/2}$ ≈163.3 eV S^{-II} $2p_{1/2}$ ≈226.2 eV S^{-II} 2s

XPS S 2p spectrum of **7** (**Figure II-33**) consists of peaks located at ≈162.1 and 163.3 eV, which are assigned to S^{-II} $2p_{3/2}$ and $2p_{1/2}$ components in MoS_2, respectively.[72] Minor contributions appear at ≈161.2 and 162.1 eV, which are ascribed to S^{-I} $2p_{3/2}$ and $2p_{1/2}$ components, respectively, as observed in previous works.[31] More interestingly, XPS Mo 3d spectrum is dominated by peaks at ≈229.2 and 232.3 eV, which correspond to Mo^{IV} $3d_{5/2}$ and $3d_{3/2}$ components in 2H-MoS_2, respectively.[72] Interestingly, it seems that ce-MoS_2 undergo a total 1T→2H transition as a result of the non-covalent

functionalization. In comparison to **1**, MoO_3 contributions are negligible in **7**.

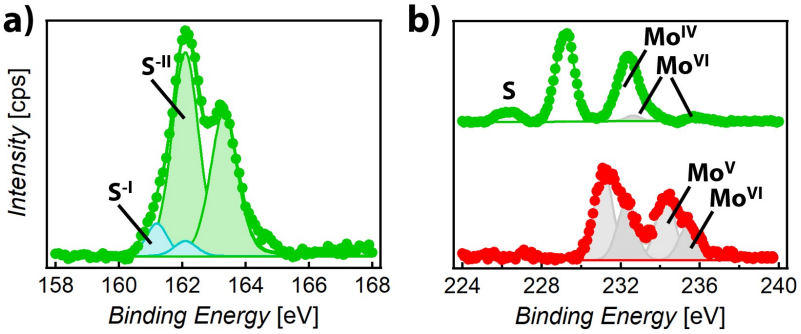

Figure II-33. a) S 2p XPS spectrum of 7; b) Mo 3d XPS spectra of 1 (red) and 7 (green).

PXRD

Remarkedly, in contrast to that of **1**, the PXRD diffractogram of **7** (**Figure II-34**) also reveals the (002) peak of MoS_2 at ≈14.3º. The position of PB peaks is comparable to that observed in the diffractogram of **1**. An average particle size of ≈10.0 nm, lower than the observed in **7** (≈11.1 nm), was determined from the FWHM of (200) peak (1.02º) using Scherrer analysis.

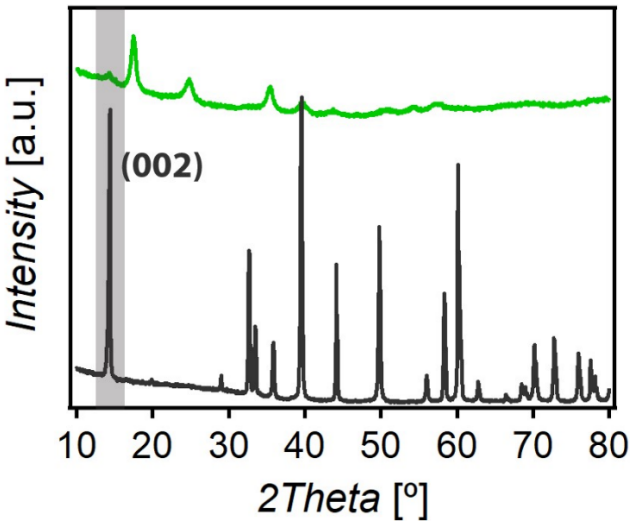

Figure II-34. PXRD spectra of commercial 2H-MoS_2 (grey) and 7 (green).

FTIR

The FTIR spectrum of **7** (**Figure II-35**) closely resembles that of **1**, displaying vibrational bands at ≈500, 600, and 2079 cm^{-1}. Whilst the latter band corresponds to the Fe^{II}–C≡N stretching mode, the other two are attributed to Fe^{II}–C≡N–Fe^{III} bending modes.

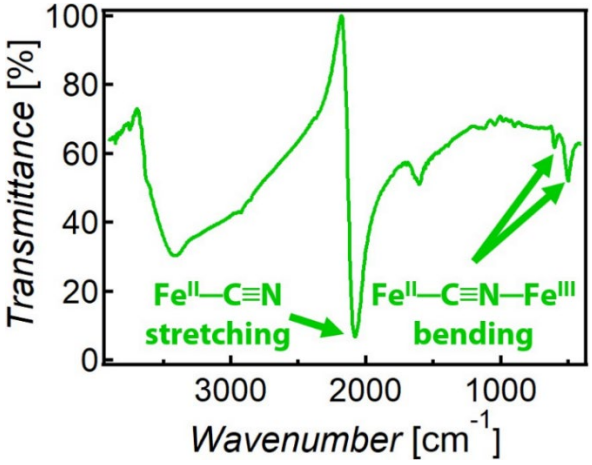

Figure II-35. FTIR spectrum of 7.

Raman spectroscopy

The Raman spectrum of **7** (**Figure II-36**), recorded as pellet in ambient conditions by using a wavelength of 638 nm, displays PB and MoS_2 peaks, as opposed to **1** (see **Table II-4**). MoS_2 peaks identified as the in-plane E^1_{2g}, out-of-plane A_{1g}, and 2LA(M) (second-order Raman mode involving two longitudinal acoustic phonons at the M point of the Brillouin zone)[73] are remarked in green. The rest of MoS_2 peaks are masked by PB signals. The joint detection of MoS_2 by XPS, PXRD, and Raman spectroscopy appears to point out that this compound is exempt from significant oxidation after functionalization.

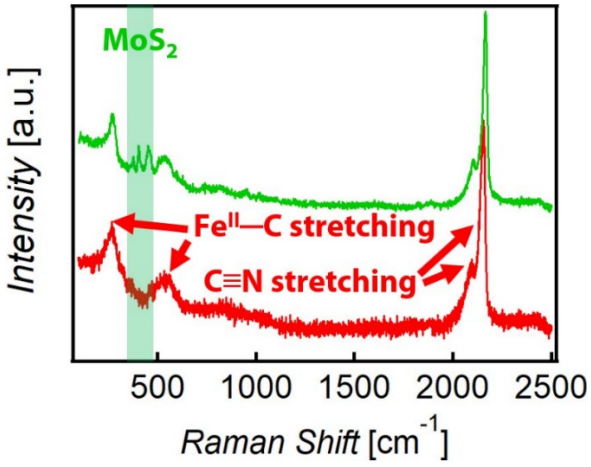

Figure II-36. Raman spectra of 1 (red) and 7 (green) at 638 nm excitation wavelength. The typical MoS_2 region is remarked in green.

Table II-4. Raman values observed in samples 1 and 7.

Sample	Raman signals
1	PB
	≈270 cm^{-1} (Fe–C stretching)
	≈540 cm^{-1} (Fe–C stretching)
	≈2097 cm^{-1} (E_g C≡N stretching)
	≈2155 cm^{-1} (A_{1g} C≡N stretching)
7	PB
	≈270 cm^{-1} (due to Fe–C stretching)
	≈538 cm^{-1} (due to Fe–C stretching)
	≈2102 cm^{-1} (due to E_g C≡N stretching)
	≈2165 cm^{-1} (due to A_{1g} C≡N stretching)
	MoS_2
	≈379 cm^{-1} (E^1_{2g})
	≈405 cm^{-1} (A_{1g})
	≈453 cm^{-1} (2LA(M))

Mössbauer spectroscopy

The Mössbauer spectrum of **7** (**Figure II-37**) was recorded at 295 K and fitted with the model described by Grandjean and co-workers. This spectrum, which is consistent with PB, shows one doublet attributed to LS Fe^{II} and three doublets assigned to HS Fe^{III}, all the peaks having the same line widths. In this case, Fe^{II}:Fe^{III} molar ratio was ≈0.82.

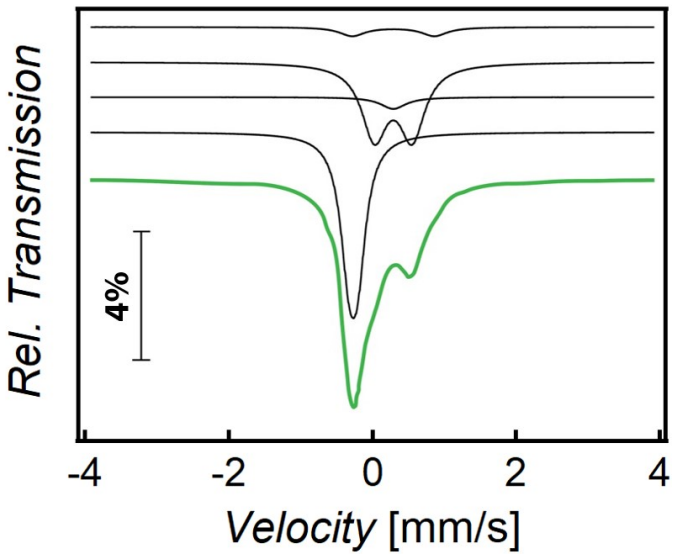

Figure II-37. Mössbauer spectrum of 7 taken at 295 K.

TEM

In order to evaluate the PB distribution over the 2D platform, the sample **7** was scanned by TEM. According to TEM analysis, PB is also found as a shell surrounding ce-MoS_2 flakes (see **Figure II-38a**) but to a lesser extent than in **1** since, in some cases, high Mo/Fe signal ratios confirm the existence of flakes with a poor (or not very compact) PB recovering. Interestingly, according to EDS elemental mapping, K, Fe, and N are homogeneously distributed over MoS_2 flakes (see **Figure II-38b-f**).

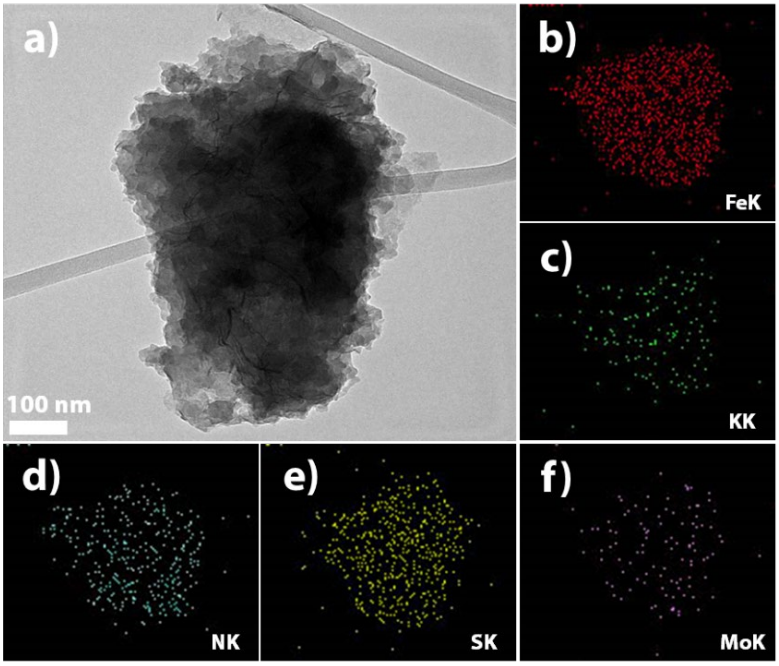

Figure II-38. a) TEM image of 7; b-f) EDS elemental mapping of the sample shown in "a)".

ICP-OES

According to ICP-OES analysis, K:Fe and Fe:Mo molar ratios are ≈0.13 and 4.88, respectively.

TGA

From the first mass drop (≈28%) observed in the TGA plot (**Figure II-39**), the number of physisorbed and structural water molecules related to the chemical formula of **7** was calculated.

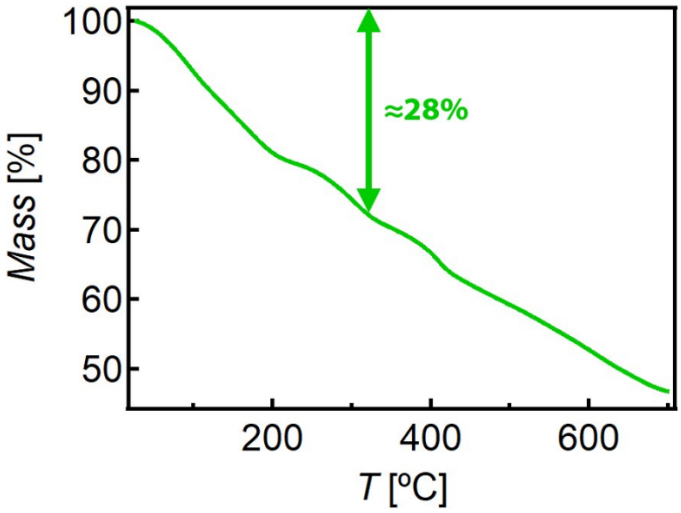

Figure II-39. TGA plot of 7.

Taking in consideration all this data, the chemical formula of **7** can be approached to $(KFe_4[Fe(CN)_6]_{3.27})@(MoS_2)_{0.61}\cdot 23H_2O$.

After determining the formula, the electrochemical performance of **7** was tested by galvanostatic discharge curves at different current densities, using the same set-up and measurement protocol as with **1**. However, owing to the bad quality of the preliminary results, the study was interrupted. We only could attribute the poor performance of **7** cathode material for SIBs and KIBs to the use of non-oxidized MoS_2 flakes. These results are difficult to interpret due to the laminar morphology of MoS_2 flakes and its oxidized analogues as well as the semiconducting nature of functionalized MoS_2 and molybdenum oxides.

II.3. Conclusions

In summary, in this Chapter, we have reported a straightforward approach for the preparation of PB/MoS_2-based composites with great potential for more efficient green energy batteries, both as powder samples and directly on surfaces.

Thus, ce-MoS_2 flakes provide a conductive matrix with a highly available SA, suitable for the formation of a homogeneous composite. The negative surface charge on the flakes plays a key role in the nucleation all over the MoS_2 surface of PB particles that combine high porosity and small crystal size, which renders better accessibility to the voids for alkaline cations.

According to our electrochemical studies, more favourable diffusion of alkali cations, along with the effective pseudocapacitive contribution arising from MoS_2, gives rise to the highest value of specific capacitance hitherto reported in literature for a composite based on the assembly of a 2D material with PB.

These results highlight the synergistic behaviour of these two electroactive components in the composite, prove the great potential of **1** as cathode material for SIBs and KIBs, and open the door to the combination of other TMDCs with PBAs for energy storage.

According to our preliminary electrochemical results obtained from **7**, it seems that the avoidance of the oxidation of ce-MoS_2 flakes (achieved by shortening the reaction time while increasing the amount of MoS_2 respect to that of the PB precursors) has a negative impact on the performance of the resultant composite. However, in this regard, a more thorough study should be carried out in order to understand why the absence of molybdenum oxide supresses the synergistic effect observed in **1**.

The results concerning the oxidized composite have been published in Prussian Blue@MoS_2 Layer Composites as Highly Efficient Cathodes for Sodium- and Potassium-Ion Batteries.

II.4. Experimental section

II.4.1. Materials

Molybdenum(IV) disulphide (MoS_2) was acquired from Alfa Aesar. The solution of *n*-butyllithium (*n*-BuLi) 1.6 M in hexane, iron(III) chloride ($FeCl_3$), and potassium hexacyanoferrate(III) ($K_3Fe(CN)_6$) were purchased from Sigma-Aldrich. Hydrochloric acid (37%) was purchased from Scharlau. Solvents were used without further purification. Milli-Q water was used in all the experiments. SiO_2 (285 nm)/Si substrates were bought from NOVA Electronic Materials LLC, Flower Mound, TX. Prepatterned interdigitated Au electrodes (type OFET/LOFET) were acquired from Fraunhofer IPMS. For dry mechanical exfoliation, a synthetic 2H-MoS_2 crystal with a lateral size of ≈0.8–1 cm was purchased from HQ Graphene. The Scotch tape (PVC film, SPV 240P) used for the micromechanical exfoliation of 2H-MoS_2 crystals was acquired from Nitto Denko Corporation.

II.4.2. Methods

II.4.2.1. Intercalation/chemical exfoliation of MoS_2

The synthetic method for performing the lithiation of MoS_2 was adapted from that reported by Zhou *et al.* (autoclave approach).[74] A Teflon autoclave reactor was charged with commercial polycrystalline MoS_2 powder (320.0 mg, 2.0 mmol) and *n*-BuLi (5 mL, 1.6 M in hexane, 8 mmol) inside a nitrogen-filled glovebox with low water vapour and oxygen levels (< 0.1 ppm). Afterward, the autoclave was tightly sealed and heated for 2 h at 100 °C in an oven. Then, the resulting mixture was filtered under nitrogen (in glovebox) and repeatedly washed with hexane. Immediately after exposing the solid to air, it was mixed with degassed Milli-Q water (10 mL) and bath-sonicated for 1 h. The suspension was dialyzed for 16 h to obtain a suspension with pH slightly below 7. Subsequently, the content of the dialysis membrane was transferred into a centrifuge tube. This mixture was first bath-sonicated for 30 min to redisperse the sediment and then centrifuged at 750 rpm for 30 min to remove the unexfoliated material. The obtained supernatant was used without further purification.

II.4.2.2. Synthesis of sample 1

$K_3Fe(CN)_6$ (164.6 mg, 0.5 mmol) in 10 mL of water was slowly added to 10 mL of $FeCl_3$ (81.1 mg, 0.5 mmol,) in HCl 0.01 M. Afterward, 6 mg of freshly dispersed ce-MoS_2 flakes in water were dropped into the previous solution and stirred for 15 min. Next, the final mixture was filtered and washed with abundant water to remove the unreacted PB precursors. The obtained solid was dried under vacuum at room temperature for 1 h and stored in the dark before further characterizations.

II.4.2.3. Non-covalent functionalization of ce-MoS_2 flakes on surface (samples 2 and 3)

A fresh suspension of MoS_2 flakes was spin-coated onto a clean SiO_2/Si substrate at 3000 rpm for 1 min. The resulting ce-MoS_2 network was functionalized by using 2 mL of the above $K_3Fe(CN)_6$:$FeCl_3$ solution. For sample **3**, a $K_3Fe(CN)_6$:$FeCl_3$ aqueous solution 2.5 times more diluted than the one used for **2** was drop-casted onto the modified substrate for 5 s and then spin-coated at 3000 rpm for 0.5 min.

II.4.2.4. Non-covalent functionalization of ce-MoS_2 flakes onto prepatterned interdigitated Au electrodes (sample 4)

A fresh suspension of MoS_2 flakes was spin-coated onto a clean SiO_2/Si substrate containing prepatterned interdigitated Au electrodes at 3000 rpm for 1 min. After that, a 1:1 50×10^{-3} M $K_3Fe(CN)_6$:$FeCl_3$ aqueous solution was drop-casted onto the modified substrate for 5 s and then spin-coated at 3000 rpm for 0.5 min.

II.4.2.5. Non-covalent functionalization of me-MoS_2 flakes on surface (samples 5 and 6)

Commercial 2H-MoS_2 crystal was mechanically exfoliated by the Scotch tape method[75] and the obtained flakes were deposited onto a clean SiO_2 (285)/Si substrate. Next, samples were introduced in a glovebox. Sample **5** was immersed in *n*-BuLi (1.6 M in hexane). After 24 h, it was immersed in hexane, ethanol, and isopropanol and dried with a N_2 stream. Afterward, in ambient conditions, 2 mL of the $K_3Fe(CN)_6$:$FeCl_3$ aqueous solution (the same mixture used for the synthesis of sample **1**) was drop-casted onto the modified substrate for

15 s and then spin-coated at 3000 rpm for 1 min. For sample **6**, the same procedure was followed except for the *n*-BuLi treatment.

II.4.2.6. Synthesis of the sample 7

$K_3Fe(CN)_6$ (98.8 mg, 0.3 mmol) in 6 mL of water was slowly added to 6 mL of $FeCl_3$ (48.7 mg, 0.3 mmol) in HCl 0.01 M. Afterward, 18 mg of freshly dispersed ce-MoS_2 flakes in 10.5 mL (10.7 M) of water were dropped into the previous solution and stirred for 1 min. Next, the final mixture was filtered and washed with abundant water to remove the unreacted PB precursors. The obtained solid was dried under vacuum at room temperature for 1 h and stored in the dark before further characterizations.

II.4.3. Characterization techniques

AFM

The substrates were imaged with a Digital Instruments Veeco Nanoscope IVa AFM microscope in tapping mode, using silicon tips with resonance frequency of 300 kHz and with an equivalent constant force of 40 N m^{-1}. AFM images were treated with Gwyddion[76] and WSxM softwares.[77]

Analysis of N_2 adsorption/desorption isotherms at 77 K

Gas adsorption measurements were carried out with Micromeritics 3Flex after activation of the solids at 425 K and 10^{-6} mbar for 16 h by using a Smart VacPrep unit. Surface area, pore size, and volume values were calculated from nitrogen adsorption–desorption isotherms at 77 K. Specific surface area was calculated by multipoint BET method. Total pore volume was calculated at $P/P_0 = 0.96$. Pore size distribution was analysed by using the NLDFT for the adsorption branch assuming a cylindrical pore model with SAIEUS.

Electrochemical measurements

For the electrochemical measurements, a mixture of **1**, acetylene black, and PVDF in ethanol in a mass ratio of 80:10:10 was prepared and deposited on a carbon felt electrode previously calcined at 1000 °C. The as-prepared carbon felt was dried for 2 h at 80 °C. The stability of the PB after the electrode preparation process was confirmed by PXRD. Each working electrode contained about 1 mg of electroactive material and had a geometric surface area of about 1 cm^2. A typical

three-electrode cell equipped with a steel sheet as the counter electrode and a Metrohm Ag/AgCl (3 M KCl) as the reference electrode was used for the electrochemical characterization of **1** trapped by the working electrodes. The electrochemical measurements were carried out in three different aqueous solutions (1 and 0.5 M Na_2SO_4 and 0.5 M K_2SO_4) as electrolytes. All the electrochemical experiments were performed at room temperature using a Gamry 1000E potentiostat-galvanostat controlled by Gamry software. The specific capacitance (C) was calculated from the cyclic chronopotentiometric curves according to $C = I\Delta t/m\Delta V$, where I is the charge/discharge current, Δt is the time for a full charge or discharge, m is the weight in grams of the active material in the electrode layer, and ΔV is the voltage change after a full charge or discharge.

Electrode characterization was also performed by electrochemical impedance spectroscopy. The measurements were performed (by Dr. Leticia García-Cruz, from Institute of Electrochemistry, Universidad de Alicante) using a VMP3 multichannel potentiostat–galvanostat BioLogic Science Instruments with a three-electrode electrochemical cell as described above. The impedance spectra were measured at a formal potential of 0.25 V versus Ag/AgCl (3.5 M KCl) over a frequency range between 10 mHz and 0.2 MHz, with an amplitude potential of 0.010 V. A solution of 0.5 M K_2SO_4 was used as electrolyte and all impedance spectra were monitored at room temperature. Before the impedance measurements, an equilibration time was required to reach an open-circuit potential until a constant value of 0.25 V, which is almost in agreement with the formal potential of the first redox couple shown by cyclic voltammetry in **Figure II-28a**. The impedance data were fitted by using the BioLogic software.

Elemental CNS analysis

CNS analysis was performed by elementary analyser AE CHNS1110 CE Instruments, using a thermal conductivity detector in SCSIE, Universitat de València. Helium and oxygen (99.995% of purity) were used as the carrier and combusting gases, respectively. Combustion tube was set up at 1027 °C and reduction tube at 600 °C. Sulfanilamide was used as CHNS standard.

Field emission scanning electron microscopy (FESEM)
FESEM studies were performed without metallization on a Hitachi S-4800 microscope operating at an accelerating voltage of 20 kV in SCSIE, Universitat de València.

FTIR spectroscopy
FTIR spectra were recorded by a FTIR Nicolet 5700 spectrometer (Thermo Scientific, Waltham, MA, EEUU) in the 400–4000 cm^{-1} range using KBr pellets.

HRTEM
HRTEM studies were carried out on a Tecnai G2 F20 microscope operating at 200 kV in SCSIE, Universitat de València. Samples were prepared by dropping suspensions on lacey formvar/carbon copper grids (300 mesh). The employed suspensions were prepared by two different methods: *i*) by diluting an aliquot of the mother MoS_2 suspension in water and *ii*) by dispersing a little amount of **1** or **7** in Milli-Q water.

ICP-OES
The ICP-OES analysis of **1** and **7** was conducted at the Universidad Complutense de Madrid (CAI de Técnicas Geológicas). Samples were digested in a mixture of hydrochloric and nitric acids using a high-pressure microwave oven.

Magnetic measuremens
Magnetic data were collected with a Quantum Design MPMS XL-5 susceptometer equipped with a SQUID sensor. Direct current (*dc*) FC and ZFC magnetization measurements were performed under 100 Oe applied magnetic field. Thus, *ac* magnetic susceptibility measurements were collected in the 2–8 K range at zero *dc* field and an applied oscillating field of 5 Oe at different frequencies.

Mössbauer spectroscopy
Mössbauer spectra (measured by Dr. João C Waerenborgh, from Centro de Ciências e Tecnologias nucleares, Instituto Superior Técnico, Universidade de Lisboa) were collected at room temperature in transmission mode using a conventional constant acceleration spectrometer and a 25 mCi ^{57}Co source in a Rh matrix in three different samples. The velocity scale was calibrated using α-Fe foil. Isomer shifts are given relative to this standard at room temperature. The

absorber was obtained by packing the powdered samples into a Perspex holder. The spectra were fitted to Lorentzian lines using a nonlinear least-squares method.[78] The areas and widths of both peaks in a quadrupole doublet were constrained to remain equal during the refinement procedure.

PXRD

Samples were filled into 1 mm diameter borosilicate glass capillaries prior to being mounted and aligned on an Empyrean PANalytical powder diffractometer, using Cu Kα radiation (λ = 1.54056 Å) with an PIXcel detector, operating at 40 mA and 45 kV. At least three repeated measurements were collected in the 2–80° range with a step size of 0.017°, at room temperature, and merged in a single diffractogram. Capillaries containing Li_xMoS_2 were sealed in inert atmosphere. Unit cell parameters values were calculated by Pawley refinement of experimental PXRD data as implemented in HighScore Plus.

Raman spectroscopy

Raman spectra were acquired with a Raman Emission Horiba-MTB Xplora Spectrometer in ambient conditions. Samples **1** and **7** were measured as a pellet (compressed powder) with a laser wavelength of 638 nm in order to preserve the stability of the sample during the measurement. The rest of samples was recorded with a laser wavelength of 532 nm.

TGA

TGA was conducted at the Universidad de Alicante (Unidad de Análisis Térmico y Sólidos Porosos) and was carried out with a Mettler Toledo TGA/SDTA851/1100/SF apparatus in the 25–600 °C temperature range under a 5 °C min^{-1} scan rate and N_2 flow of 100 mL min^{-1}.

Transport measurements

Intensity *vs* voltage (I-V) curves were measured using interdigitated prepatterned Au electrodes (Fraunhofer IPMS) with a channel length of 10 μm and measured in a probe station using a Yokogawa GS200 voltage source and a Keithley 6517B electrometer. When necessary, system was dynamically pumped down to 10^{-6} mbar.

UV/Vis spectroscopy

UV/Vis absorption spectrum was recorded on a Jasco V-670 spectrophotometer in baseline mode in the 190–1200 nm range, using 1.000 cm optical path quartz cuvettes.

XPS

Samples were analysed ex situ at the X-ray Spectroscopy Service at the Universidad de Alicante using a K-ALPHA Thermo Scientific spectrometer. All spectra were collected using Al Kα radiation (1486.6 eV), monochromatized by a twin crystal monochromator, yielding a focused X-ray spot (elliptical in shape with a major axis length of 400 μm) at 30 mA and 2 kV. The alpha hemispherical analyser was operated in the constant energy mode with survey scan pass energies of 200 eV to measure the whole energy band and 50 eV in a narrow scan to selectively measure the particular elements. XPS data were analysed with Avantage software. A smart background function was used to approximate the experimental backgrounds. Charge compensation was achieved with the system flood gun that provides low energy electrons and low energy argon ions from a single source. Commercial MoS_2 sample was used as reference (Mo $3d_{5/2}$ = 229.1 eV).

ZP measurements

ZP measurements were performed at room temperature with a Zetasizer Nano ZS instrument (Malvern Instruments Ltd.).

II.5. References

1. Guari, Y. & Larionova, J., Prussian Blue-Type Nanoparticles and Nanocomposites: Synthesis, Devices, and Applications, Singapore: Pan Stanford Publishing Pte. Ltd., 2019.

2. Robin, M. B. The Color and Electronic Configurations of Prussian Blue. *Inorg. Chem.* **1**, 337–342 (1962).

3. Su, S. *et al.* Facile Synthesis of a MoS_2-Prussian Blue Nanocube Nanohybrid-Based Electrochemical Sensing Platform for Hydrogen Peroxide and Carcinoembryonic Antigen Detection. *ACS Appl. Mater. Interfaces* **9**, 12773–12781 (2017).

4. Buser, H. J., Ludi, A., Schwarzenbach, D. & Petter, W. The Crystal Structure of Prussian Blue: $Fe_4[Fe(CN)_6]_3 \cdot xH_2O$. *Inorg. Chem.* **16**, 2704–2710 (1977).

5. Paolella, A. *et al.* A review on hexacyanoferrate-based materials for energy storage and smart windows: Challenges and perspectives. *Journal of Materials Chemistry A* **5**, 18919–18932 (2017).

6. Qian, J. *et al.* Prussian Blue Cathode Materials for Sodium-Ion Batteries and Other Ion Batteries. *Adv. Energy Mater.* **8**, 1702619 (2018).

7. Grandjean, F., Samain, L. & Long, G. J. Characterization and utilization of Prussian blue and its pigments. *Dalt. Trans.* **45**, 18018–18044 (2016).

8. Mayoh, B. & Day, P. Charge transfer in mixed-valence solids. Part VIII. Contribution of valence delocalisation to the ferromagnetism of Prussian Blue. *J. Chem. Soc. Dalt. Trans.* **15**, 1483–1486 (1976).

9. Wang, B. *et al.* Prussian Blue Analogs for Rechargeable Batteries. *iScience* **3**, 110–133 (2018).

10. Hurlbutt, K., Wheeler, S., Capone, I. & Pasta, M. Prussian Blue Analogs as Battery Materials. *Joule* **2**, 1950–1960 (2018).

11. Dunbar, K. R. & Heintz, R. A. Chemistry of transition metal cyanide compounds: Modern perspectives. *Prog. Inorg. Chem.*, **45**, 283–391 (2007).

12. Nishi, Y. Lithium ion secondary batteries; Past 10 years and the future. *J. Power Sources* **100**, 101–106 (2001).

13. Wu, L., Lee, W. H. & Zhang, J. First principles study on the electrochemical, thermal and mechanical properties of $LiCoO_2$ for thin film rechargeable battery. *Mater. Today: Proceedings* **1**, 82–93 (2014).

14. Yabuuchi, N., Kubota, K., Dahbi, M. & Komaba, S. Research development on sodium-ion batteries. *Chem. Rev.* **114**, 11636–11682 (2014).

15. Liu, Y., He, D., Han, R., Wei, G. & Qiao, Y. Nanostructured potassium and sodium ion incorporated Prussian blue frameworks as cathode materials for sodium-ion batteries. *Chem. Commun.* **53**, 5569–5572 (2017).

16. Hwang, J. Y., Myung, S. T. & Sun, Y. K. Sodium-ion batteries: Present and future. *Chem. Soc. Rev.* **46**, 3529–3614 (2017).

17. Itaya, K., Uchida, I. & Neff, V. D. Electrochemistry of Polynuclear Transition Metal Cyanides: Prussian Blue and Its Analogues. *Acc. Chem. Res.* **19**, 162–168 (1986).

18. Lee, H. W. *et al.* Manganese hexacyanomanganate open framework as a high-capacity positive electrode material for sodium-ion batteries. *Nat. Commun.* **5**, 5280 (2014).

19. You, Y., Wu, X. L., Yin, Y. X. & Guo, Y. G. High-quality Prussian blue crystals as superior cathode materials for room-temperature sodium-ion batteries. *Energy Environ. Sci.* **7**, 1643–1647 (2014).

20. Jiang, Y. *et al.* Prussian Blue@C Composite as an Ultrahigh-Rate and Long-Life Sodium-Ion Battery Cathode. *Adv. Funct. Mater.* **26**, 5315–5321 (2016).

21. Cao, L., Liu, Y., Zhang, B. & Lu, L. In situ controllable growth of Prussian blue nanocubes on reduced graphene oxide: Facile synthesis and their application as enhanced nanoelectrocatalyst for H_2O_2 reduction. *ACS Appl. Mater. Interfaces* **2**, 2339–2346 (2010).

22. Zhang, L., Zhang, A., Du, D. & Lin, Y. Biosensor based on Prussian blue nanocubes/reduced graphene oxide nanocomposite for detection of organophosphorus pesticides. *Nanoscale* **4**, 4674–4679 (2012).

23. Prabakar, S. J. R., Jeong, J. & Pyo, M. Highly crystalline Prussian blue/graphene composites for high-rate performance cathodes in Na-ion batteries. *RSC Adv.* **5**, 37545–37552 (2015).

24. Wang, J. G., Zhang, Z., Liu, X. & Wei, B. Facile synthesis of cobalt hexacyanoferrate/graphene nanocomposites for high-performance supercapacitor. *Electrochim. Acta* **235**, 114–121 (2017).

25. Zhang, M., Hou, C., Halder, A., Ulstrup, J. & Chi, Q. Interlocked graphene–Prussian blue hybrid composites enable multifunctional electrochemical applications. *Biosens. Bioelectron.* **89**, 570–577 (2017).

26. Wang, H. *et al.* Crystallographic-plane tuned Prussian-blue wrapped with RGO: a high-capacity, long-life cathode for sodium-ion batteries. *J. Mater. Chem. A* **5**, 3569–3577 (2017).

27. Wang, Q. H., Kalantar-Zadeh, K., Kis, A., Coleman, J. N. & Strano, M. S. Electronics and optoelectronics of two-dimensional transition metal dichalcogenides. *Nat. Nanotechnol.* **7**, 699–712 (2012).

28. Tan, C. *et al.* Recent Advances in Ultrathin Two-Dimensional Nanomaterials. *Chem. Rev*. **117**, 6225−6331 (2017).

29. Joensen, P., Frindt, R. F. & Morrison, S. R. Single-layer MoS_2. *Mater. Res. Bull.* **21**, 457–461 (1986).

30. Voiry, D. *et al.* Covalent functionalization of monolayered transition metal dichalcogenides by phase engineering. *Nat. Chem.* **7**, 45–49 (2014).

31. Knirsch, K. C. *et al.* Basal-Plane Functionalization of Chemically Exfoliated Molybdenum Disulfide by Diazonium Salts. *ACS Nano* **9**, 6018–30 (2015).

32. Kim, J., Byun, S., Smith, A. J., Yu, J. & Huang, J. Enhanced electrocatalytic properties of transition-metal dichalcogenides sheets by spontaneous gold nanoparticle decoration. *J. Phys. Chem. Lett.* **4**, 1227–1232 (2013).

33. Joensen, P., Frindt, R. F. & Morrison, S. R. Single-layer MoS_2. *Mater. Res. Bull.* **21**, 457–461 (1986).

34. Mieda, E. *et al.* Nanoprobe characterization of MoS_2 nanosheets fabricated by Li-intercalation. *Jpn. J. Appl. Phys*. **54**, 08LB07 (2015)

35. Fan, X. *et al.* Fast and Efficient Preparation of Exfoliated 2H MoS_2 Nanosheets by Sonication-Assisted Lithium Intercalation and Infrared Laser-Induced 1T to 2H Phase Reversion. *Nano Lett.* **15**, 5956–5960 (2015).

36. Paredes, J. I. *et al.* Impact of Covalent Functionalization on the Aqueous Processability, Catalytic Activity, and Biocompatibility of Chemically Exfoliated MoS_2 Nanosheets. *ACS Appl. Mater. Interfaces* **8**, 27974–27986 (2016).

37. Wilson, J. A. & Yoffe, A. D. The transition metal dichalcogenides discussion and interpretation of the observed optical, electrical and structural properties. *Adv. Phys.* **18**, 193–335 (1969).

38. Gupta, A., Arunachalam, V. & Vasudevan, S. Water dispersible, positively and negatively charged MoS_2 nanosheets: Surface chemistry and the role of surfactant binding. *J. Phys. Chem. Lett.* **6**, 739–744 (2015).

39. Li, H. *et al.* From Bulk to Monolayer MoS_2: Evolution of Raman Scattering. *Adv. Funct. Mater.* **22**, 1385–1390 (2012).

40. Nayak, A. P. *et al.* Pressure-dependent optical and vibrational properties of monolayer molybdenum disulfide. *Nano Lett.* **15**, 346–53 (2015).

41. Lee, C. *et al.* Anomalous lattice vibrations of single- and few-layer MoS_2. *ACS Nano* **4**, 2695–2700 (2010).

42. Barsan, M. M., Butler, I. S., Fitzpatrick, J. & Gilson, D. F. R. High-pressure studies of the micro-Raman spectra of iron cyanide complexes: Prussian blue ($Fe_4[Fe(CN)_6]_3$), potassium ferricyanide ($K_3[Fe(CN)_6]$), and sodium nitroprusside ($Na_2[Fe(CN)_5(NO)]\cdot 2H_2O$). *J. Raman Spectrosc.* **42**, 1820–1824 (2011).

43. Nossol, E., Souza, V. H. R. & Zarbin, A. J. G. Carbon nanotube/Prussian blue thin films as cathodes for flexible, transparent and ITO-free potassium secondary battery. *J. Colloid Interface Sci.* **478**, 107–116 (2016).

44. Wilde, R. E., Ghosh, S. N. & Marshall, B. J. The Prussian Blues. *Inorg. Chem.* **9**, 2512–2516 (1970).

45. Wang, G., Zhang, G., Huang, H. & Wang, L. Graphene-Prussian blue/gold nanoparticles based electrochemical immunoassay of carcinoembryonic antigen. *Anal. Methods* **3**, 2082–2087 (2011).

46. Kim, D. W. *et al.* Direct observation of molybdenum disulfide, MoS_2, domains by using a liquid crystalline texture method. *Nano Lett.* **15**, 229–234 (2015).

47. Frey, G. L., Reynolds, K. J., Friend, R. H., Cohen, H. & Feldman, Y. Solution-processed anodes from layer-structure materials for high-efficiency polymer light-emitting diodes. *J. Am. Chem. Soc.* **125**, 5998–6007 (2003).

48. Chou, S. S. *et al.* Controlling the metal to semiconductor transition of MoS_2 and WS_2 in solution. *J. Am. Chem. Soc.* **137**, 1742–1745 (2015).

49. Zhou, C. X., Wang, Y. X., Yang, L. Q. & Lin, J. H. Syntheses of hydrated molybdenum bronzes by reduction of MoO_3 with $NaBH_4$. *Inorg. Chem.* **40**, 1521–1526 (2001).

50. Hu, X. K. *et al.* Comparative study on MoO_3 and H_xMoO_3 nanobelts: Structure and electric transport. *Chem. Mater.* **20**, 1527–1533 (2008).

51. Hu, Y. & Chua, D. H. C. Synthesizing 2D MoS_2 Nanofins on carbon nanospheres as catalyst support for Proton Exchange Membrane Fuel Cells. *Sci. Rep.* **6**, 28088 (2016).

52. Ito, A., Suenaga, M. & Ôno, K. Mössbauer study of soluble prussian blue, insoluble prussian blue, and turnbull's blue. *J. Chem. Phys.* 48, 3597–3599 (1968).

53. Uemura, T. & Kitagawa, S. Prussian blue nanoparticles protected by poly(vinylpyrrolidone). *J. Am. Chem. Soc.* **125**, 7814–7815 (2003).

54. Li, H. *et al.* From bulk to monolayer MoS_2: Evolution of Raman scattering. *Adv. Funct. Mater.* **22**, 1385–1390 (2012).

55. You, Y., Yu, X., Yin, Y., Nam, K. W. & Guo, Y. G. Sodium iron hexacyanoferrate with high Na content as a Na-rich cathode material for Na-ion batteries. *Nano Res.* **8**, 117–128 (2014).

56. Zhao, J. *et al.* Electrochemical deposition of Prussian blue on hydrogen terminated silicon(111). *Thin Solid Films* **515**, 1847–1850 (2006).

57. Mažeikien, R., Niaura, G. & Malinauskas, A. Electrocatalytic reduction of hydrogen peroxide at Prussian blue modified electrode: An in situ Raman spectroelectrochemical study. *J. Electroanal. Chem.* **660**, 140–146 (2011).

58. Kim, J. S. *et al.* Electrical Transport Properties of Polymorphic MoS_2. *ACS Nano* **10**, 7500–7506 (2016).

59. Ganguli, S. & Bhattacharya, M. Studies of different hydrated forms of Prussian Blue. *J. Chem. Soc. Faraday Trans. 1* **79**, 1513–1522 (1983).

60. Tennakone, K. & Dharmaratne, W. G. D. Experimental and theoretical study of electronic conduction in H_2O-doped Prussian blue. *J. Phys. C Solid State Phys.* **16**, 5633–5639 (1983).

61. Pajerowski, D. M., Watanabe, T., Yamamoto, T. & Einaga, Y. Electronic conductivity in Berlin green and Prussian blue. *Phys. Rev. B - Condens. Matter Mater. Phys.* **83**, 153202 (2011).

62. Li, H., Wu, J., Yin, Z. & Zhang, H. Preparation and applications of mechanically exfoliated single-layer and multilayer MoS_2 and WSe_2 nanosheets. *Acc. Chem. Res.* **47**, 1067–1075 (2014).

63. Lu, Y., Wang, L., Cheng, J. & Goodenough, J. B. Prussian blue: A new framework of electrode materials for sodium batteries. *Chem. Commun.* **48**, 6544–6546 (2012).

64. Pajor-Świerzy, A., Kruk, T. & Warszyński, P. Enhancement of the Electrocatalytic Properties of Prussian Blue Containing Multilayer Films Formed by Reduced Graphene Oxide. *Colloids Interface Sci. Commun.* **1**, 6–9 (2014).

65. Hazen, R., Spaulding, R., Kasem, K. & Sigle, E. Electrochemistry in Thin Solid Films of Prussian Blue: A Model Demonstration of Reversible Behavior. *Am. J. Undergrad. Res.* **2**, 27–36 (2003).

66. Wu, W., Shabhag, S., Chang, J., Rutt, A. & Whitacre, J. F. Relating electrolyte concentration to performance and stability for $NaTi_2(PO_4)_3/Naf_{0.44}MnO_2$ aqueous sodium-ion batteries. *J. Electrochem. Soc.* **162**, 803–808 (2015).

67. Zamponi, S. *et al.* Influence of experimental conditions on electrochemical behavior of Prussian blue type nickel hexacyanoferrate film. *Electrochim. Acta* **48**, 4261–4269 (2003).

68. Wang, J. *et al.* Pseudocapacitive materials for electrochemical capacitors: From rational synthesis to capacitance optimization. *Natl. Sci. Rev.* **4**, 71–90 (2017).

69. Lvovich, V. F., Impedance spectroscopy: applications to electrochemical and dielectric phenomena. New Jersey: John Wiley & Sons, 2012.

70. Franger, S., Bach, S., Farcy, J., Pereira-Ramos, J. P. & Baffier, N. An electrochemical impedance spectroscopy study of new lithiated manganese oxides for 3 V application in rechargeable Li-batteries. *Electrochim. Acta* **48**, 891–900 (2003).

71. Yang, D. *et al.* Prussian blue without coordinated water as a superior cathode for sodium-ion batteries. *Chem. Commun.* **51**, 8181–8184 (2015).

72. Kibsgaard, J., Chen, Z., Reinecke, B. N. & Jaramillo, T. F. Engineering the surface structure of MoS_2 to preferentially expose active edge sites for electrocatalysis. *Nat. Mater.* **11**, 963–969 (2012).

73. Huang, S. *et al.* Low-Frequency Interlayer Raman Modes to Probe Interface of Twisted Bilayer MoS_2. *Nano Lett.* 1435–1444 (2016).

74. Zhou, L., He, B., Yang, Y. & He, Y. Facile approach to surface functionalized MoS_2 nanosheets. *RSC Adv.* **4**, 32570–32578 (2014).

75. Novoselov, K. S. *et al.* Electric field effect in atomically thin carbon films. *Science.* **306**, 666–669 (2004).

76. Nečas, D. & Klapetek, P. Gwyddion: An open-source software for SPM data analysis. *Cent. Eur. J. Phys.* **10**, 181–188 (2012).

77. Horcas, I. *et al.* WSXM: A software for scanning probe microscopy and a tool for nanotechnology. *Rev. Sci. Instrum.* **78**, 013705 (2007).

78. Waerenborgh, J. C. *et al.* Influence of thermal treatment and crystal growth on the final composition and magnetic properties of the YFe_xAl_{12-x} ($4 \leq x \leq 4.2$) intermetallics. *Chem. Mater.* **12**, 1743–1749 (2000).

III. **Prussian blue@MoS_2 layer composite with photomagnetic properties**

III.1. Introduction

Photomagnetism (or photomagnetic effect) can be defined as the change in magnetic properties of a material in response to light.[1] In molecular materials, photomagnetism can be achieved when light (as external stimulus) induces the spin change of a transition-metal complex from HS to LS (or from LS to HS)[1] what is known as spin crossover (SCO), or when light gives rise to an electron transfer coupled to a spin transition (ETCST).

In PBAs, photomagnetism was observed for the first time in the compound $K_{0.2}Co_{1.4}[Fe(CN)_6]\cdot 6.9H_2O$ (FeCo PBA).[2] In this case this property is linked to an ETCST from the LS Fe^{II} to the LS Co^{III} through the cyanide (CN) bridge, thus obtaining LS Fe^{III} and HS Co^{II} atoms interconnected by CN ligands. This electron communication is accompanied by a significant change in the magnetic behaviour (*i.e.*, from diamagnetic to paramagnetic) of the system (see **Figure III-1).**[3]

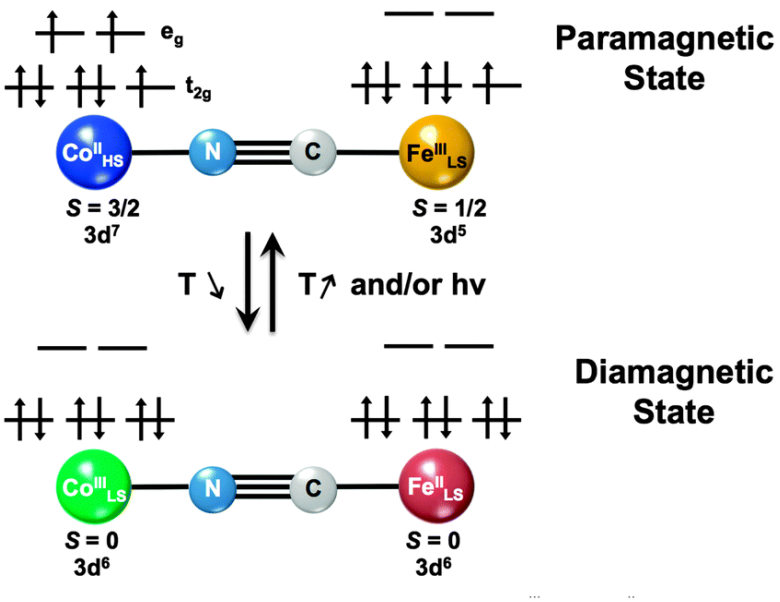

Figure III-1. Pictorial representation of the interconversion between two states (diamagnetic Co^{III}_{LS}–CN–Fe^{II}_{LS} and paramagnetic Co^{II}_{HS}–CN–Fe^{III}_{LS} electronic configurations) trough photo- or thermally-induced ETCST process. In diamagnetic state, Co^{III} and Fe^{II} are both in t_{2g}^6 configuration. In paramagnetic state, Co^{II} and Fe^{III} are in t_{2g}^5 e_g^2 and t_{2g}^5 configurations, respectively. Extracted from ref 3.

ETCST process is induced by light but also thermally, and in any case, it depends on the chemical composition of the PBA compounds and therefore on their microstructure.[4,5] In general, PBAs are non-stoichiometric and lack a well-defined coordination sphere.[6,7] Thus, in order to study photomagnetism in systems having a precise coordination sphere, molecular analogues have been prepared.[8–11] One system that exemplifies this approach has been provided by discrete FeCo cyanide complexes with a cubic shape. The synthetic strategy to obtain these cubes relies on mixing Fe^{III} building blocks with a reduced number of CN ligands and Co^{II} building blocks with a reduced number of labile sites.[3,12,13] Some of these molecular species are soluble in several organic solvents, displaying a more versatile chemistry in solution and facilitating the insertion of the functional units into the final advanced hybrid material.[11] As in extended PBAs, their central cage permits to encapsulate cations that can be exchanged. Interestingly, it has been reported that the replacement of encapsulated K^+ by Cs^+ can enhance the stability and redox flexibility of the discrete FeCo cubes, while tuning the photomagnetic effect.[11]

On the basis of the results obtained from sample **1** (Chapter II), we thought about the interest of preparing a composite where discrete FeCo cubes were attached to the surface of ce-MoS_2 sheets. In addition to bring resilience, ce-MoS_2 layers could assist to effectively disperse a pre-synthesized FeCo cube over a conductive 2D platform, thereby reducing aggregation effects and making structural cavities more accessible to cation exchange for potential energy storage applications. Furthermore, the nature of the MoS_2-based conductive matrix could provide an additional strategic advantage when designing composites with (opto)electronic applications. Moreover, another important aspect would be to study whether there is an electron transfer between both components of the new composite and how the (photo)magnetic properties of FeCo cubes are affected after the interaction with the new 2D surface.

The composite resulting from the electrostatic interactions between ce-MoS_2 flakes and the cationic FeCo cube counterpart will be designated as FeCo@MoS_2 hereafter. To our best knowledge, no 2D material with this kind of functionalization has been reported.

III.2. Results and discussion

III.2.1. Preparation of FeCo@MoS_2

The discrete FeCo cluster chosen for this purpose was $Cs\subset\{[Fe^{II}(Tp)CN)_3]_4[Co^{III}(Tp)]_4\}ClO_4$, where Tp stands for tris(pyrazolyl)borate ligand (synthesized by J. Glatz under Dr. R. Lescouëzec's supervision, from Sorbonne Université in Paris). The perchlorate anion compensates the cationic charge of the inserted Cs^+ cation (this is what indicates $\subset$ symbol), in such a way that the positive charge of the cubic cage becomes neutral (see **Figure III-2**). For simplicity, this compound is referred as dia-FeCo cube (where dia means diamagnetic). Having in mind the redox properties reported for other similar FeCo cubes,[14] this complex could also accommodate mono- and divalent cations in its porous cyanide-bridge framework, a property highly exploited when fabricating materials suitable for batteries. This system belongs to a family of FeCo cages,[11,15,16] where slightly different changes in synthesis conditions, coordination ligands or crystallization solvent molecules, modulate the resultant photomagnetic properties. Therefore, dia-FeCo cube was chosen as a starting model system in this study, especially due to its cationic nature and its good stability in partly aqueous media. However, dia-FeCo cube lacks photomagnetic properties, which means this would limit in principle the relevance of the new composite.

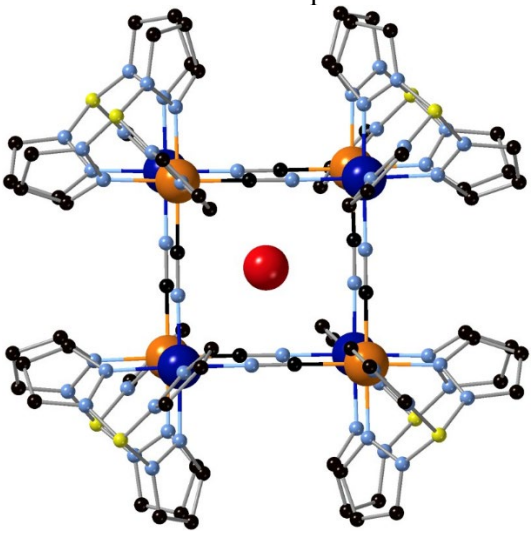

Figure III-2. Crystal structure representation of dia-FeCo cube. C (black), N (pale blue), B (yellow), Cs (red), Fe^{II} (orange), and Co^{III} (dark blue). ClO_4^- anion has been omitted.

Thus, to prepare the FeCo@MoS_2 composite, an aqueous suspension of ce-MoS_2 flakes was directly mixed with a solution of dia-FeCo cube in CH_3CN for 1 h at room temperature, under inert atmosphere and magnetic stirring, in such a manner that the monocationic dia-FeCo cube interacts with negative-charged MoS_2 layers. Then, the resulting solid was washed by repeated redispersion-centrifugation cycles and vacuum-dried for at least 12 h.

III.2.2. Characterization of FeCo@MoS_2

TEM

The morphology of the FeCo@MoS_2 was analysed by TEM. According to TEM images (**Figure III-3a**), FeCo@MoS_2 reflects the typical lamellar structure of MoS_2 flakes. The SAED image (**Figure III-3b**) shows the usual hexagonal pattern of MoS_2.[17] Moreover, EDS elemental mapping (**Figure III-3c-g**) confirms that Cs, Fe, and Co elements (and therefore FeCo cubes) are distributed along ce-MoS_2 flakes.

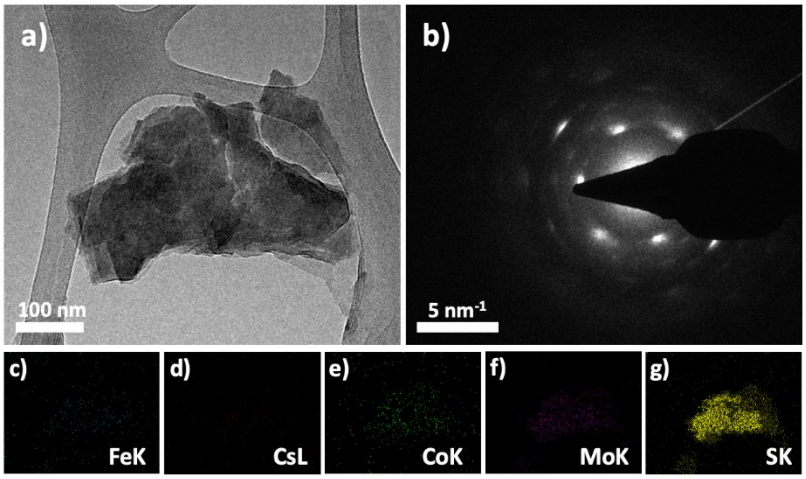

Figure III-3. a) TEM image of FeCo@MoS_2; b) SAED pattern of the sample shown in "a)"; c-g) EDS elemental mapping of the sample shown in "a)".

XPS

In order to extract information about the chemical composition, FeCo@MoS_2 was analysed by XPS. The XPS survey (**Figure III-4**) shows all the elements expected for both components except for Cl, which would indicate that ClO_4^- anions are lost when the cationic

counterpart of dia-FeCo cube is deposited on negative-charged ce-MoS_2 flakes.

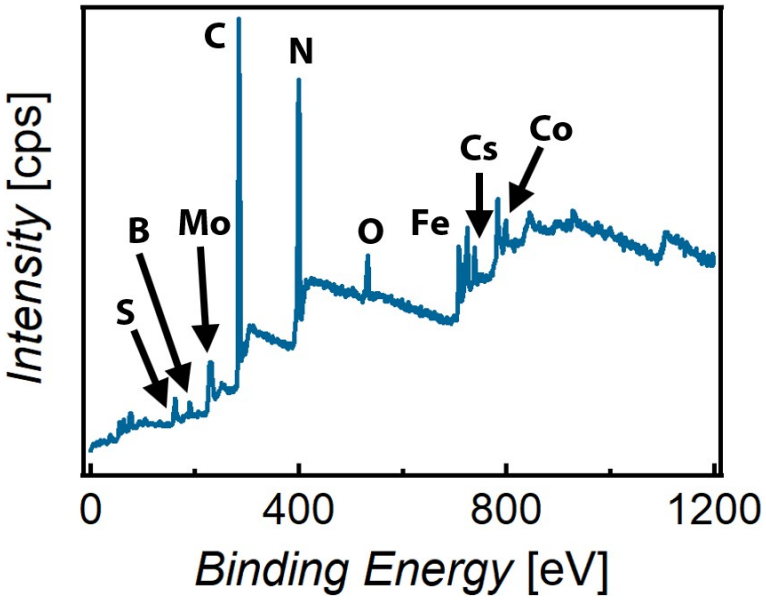

Figure III-4. XPS survey of FeCo@MoS_2

The Mo 3d spectrum (**Figure III-5**) is composed of six peaks at ≈228.1, 229.2, 229.8, 231.2, 232.3, and 232.9 eV, which would correspond to Mo^{IV} (1T-MoS_2) $3d_{5/2}$, Mo^{IV} (2H-MoS_2) $3d_{5/2}$, Mo^{IV} (MoO_2) $3d_{5/2}$, Mo^{IV} (1T-MoS_2) $3d_{3/2}$, Mo^{IV} (2H-MoS_2) $3d_{3/2}$, and Mo^{IV} (MoO_2) $3d_{3/2}$ components, respectively.[18–20]

From the total amount of Mo, ≈48.5% corresponds to 1T-MoS_2, ≈43.1% to 2H-MoS_2 and a very small amount (≈8.4%) to oxide. The 1T:2H ratio in FeCo@MoS_2 is much lower than the one observed in non-functionalized ce-MoS_2 flakes (≈1.1 and 3.8, respectively), which implies that during the functionalization process there is a partial phase conversion of the layers.

In order to get information about the degree of functionalization reached on MoS_2 layers, Fe:Mo ratio was calculated (≈2). This value indicates that there are 0.5 FeCo cubes per each MoS_2 unit.

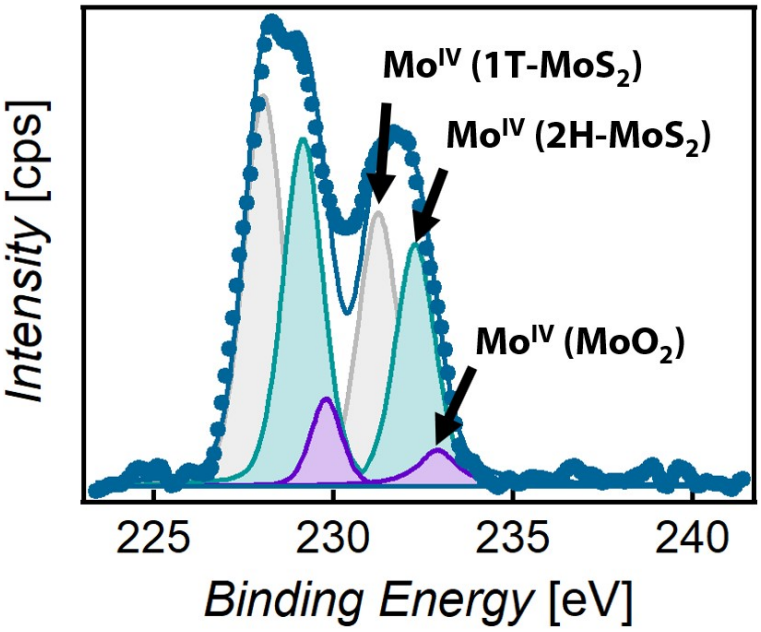

Figure III-5. Mo 3d XPS spectrum of FeCo@MoS_2.

The Co 2p spectrum (**Figure III-6**) is dominated by four peaks at ≈781.1, 782.6, 796.1, and 797.7eV, which would correspond to Co^{II} $2p_{3/2}$, Co^{III} $2p_{3/2}$, Co^{II} $2p_{1/2}$, and Co^{III} $2p_{1/2}$, respectively.[21,22] Minor contributions are due to satellite peaks. The fact of finding Co^{II} points out to the hypothesis that Co^{III} is partially reduced to Co^{II} in the presence of negative-charged ce-MoS_2 flakes. This fact would be consistent with the formation of the paramagnetic $Cs\subset\{[Fe^{II}(Tp)CN)_3]_4[Co^{III}(Tp)]_3[Co^{II}(Tp)]\}$ (para-FeCo cube, in short), where one of the Co atoms located on the vertexes of the cage (see **Figure III-2**) is present as HS Co^{II} (unpaired electrons). This difference is the responsible for the paramagnetic and photomagnetic behaviour.[15]

From the total amount of Co, ≈71.7% corresponds to Co^{III} and the rest (≈28.3%) to Co^{II}. The obtained percentages could fit quite well with those expected for a quantitative conversion from the diamagnetic system to the paramagnetic one (75% of Co^{III} and 25% of Co^{II}).

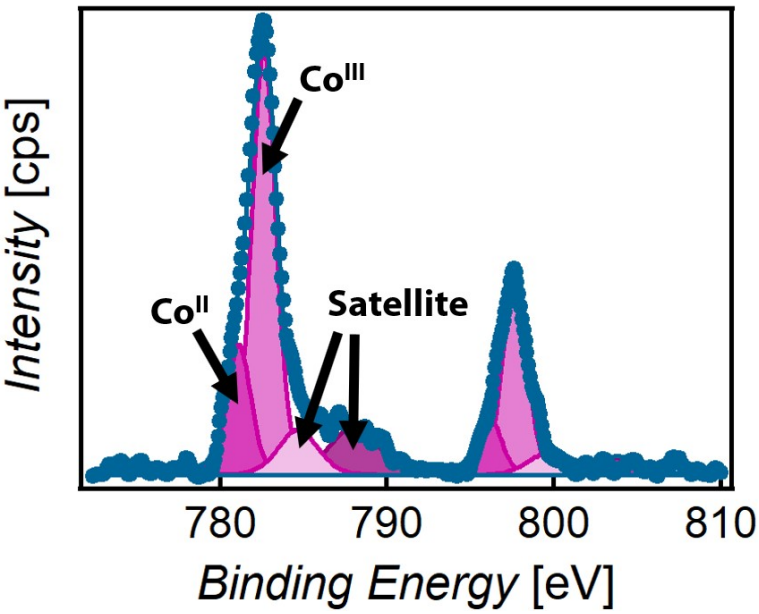

Figure III-6. Co 2p XPS spectrum of FeCo@MoS_2.

Although the Fe 2p XPS (**Figure III-7**) spectrum seems to be dominated by Fe^{II} peaks, a small contribution arising from Fe^{III} cannot be discarded. As the interpretation of Fe signals is not trivial, Fe peaks are shown without deconvolution. XPS peaks appearing at 708.4, 721.1, 724.4, and 738.2 eV correspond to Fe^{II} $2p_{3/2}$, Fe^{II} $2p_{1/2}$, Cs^{I} $3d_{5/2}$ and Cs^{I} $3d_{3/2}$ components, respectively. The Fe:Co molar ratio was estimated to be equal to 1.0, which is consistent with the stoichiometry of FeCo cubes.

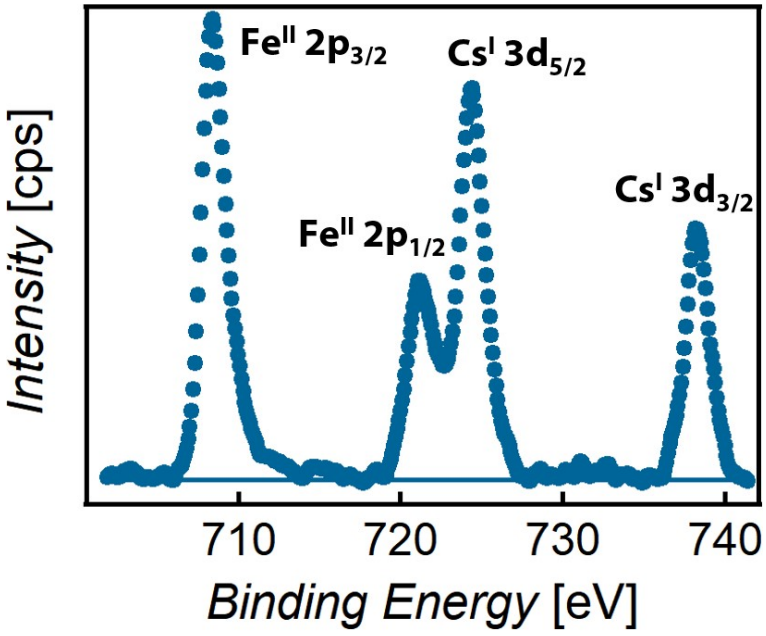

Figure III-7. Fe 2p and Cs 3d XPS region of FeCo@MoS_2.

For clarity, the most significant peaks registered for FeCo@MoS_2 are collected in the **Table III-1**.

Table III-1. XPS values of the most significant peaks registered for FeCo@MoS_2.

Element	XPS values
Mo	≈228.1 eV Mo^{IV} (1T-MoS_2) $3d_{5/2}$ ≈231.2 eV Mo^{IV} (1T-MoS_2) $3d_{3/2}$
	≈229.2 eV Mo^{IV} (2H-MoS_2) $3d_{5/2}$ ≈232.3 eV Mo^{IV} (2H-MoS_2) $3d_{3/2}$
	≈229.8 eV Mo^{IV} (MoO_2) $3d_{5/2}$ ≈232.9 eV Mo^{IV} (MoO_2) $3d_{3/2}$
Co	≈781.1 eV Co^{II} $2p_{3/2}$ ≈796.1 eV Co^{II} $2p_{1/2}$
	≈782.6 eV Co^{III} $2p_{3/2}$, ≈797.7 eV Co^{III} $2p_{1/2}$
Fe	≈708.4 eV Fe^{II} $2p_{3/2}$ ≈721.1 eV Fe^{II} $2p_{1/2}$
Cs	≈724.4 eV Cs^{I} $3d_{5/2}$ ≈738.2 eV Cs^{I} $3d_{3/2}$

Nuclear magnetic resonance (NMR)

Because of the presence of Cs^+ within the cubic cage, it was though that ^{133}Cs NMRs would be a powerful technique to obtain information about the FeCo cluster component.

The ^{133}Cs NMR spectrum of the starting dia-FeCo in CD_3CN at room temperature (**Figure III-8**), referenced respect to a 0.1 M solution of CsCl in D_2O (CsCl peak at 13.1 ppm), shows only one peak at ≈54.6 ppm, which would be associated to the diamagnetic signal of FeCo cubes.

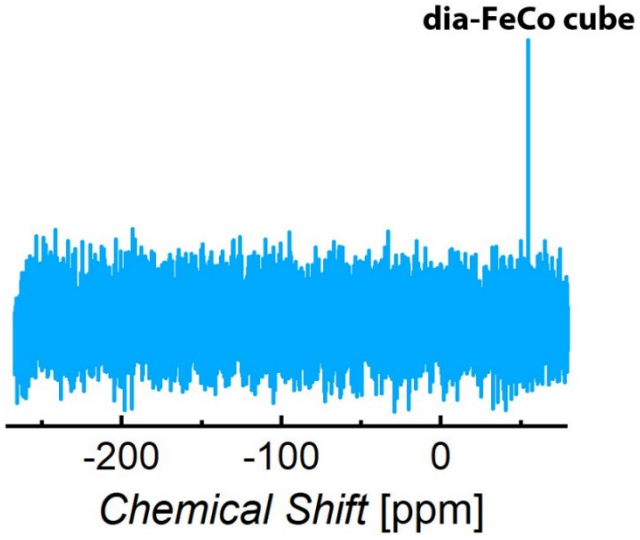

Figure III-8. ^{133}Cs spectrum of the starting dia-FeCo cube in CD_3CN referenced respect to a ≈0.1 M solution of CsCl in D_2O.

In contrast, the ^{133}Cs NMR spectrum of FeCo@MoS_2 in CD_3CN at room temperature (**Figure III-9**), referenced respect to a 0.1 M solution of CsCl in D_2O (CsCl peak at 13.1 ppm), shows two peaks located at ≈-229.9 and 54.6 ppm, which would correspond to para- and dia-FeCo cubes, respectively. These results would be consistent with those reported for a similar compound, $Cs⊂\{[Fe^{II}(Tp)(CN)_3]_4[Co^{III}(^{pz}Tp)]_3[Co^{II}(^{pz}Tp)]\}\cdot 12CH_3CN$, where T stands for tetrakis(pyrazolyl)borate. In this case, a significative paramagnetic signal was detected at ≈-236 ppm in the ^{133}Cs NMR spectrum.[11]

Although that ^{133}Cs RMN is also sensitive to the solvent, these results indicate that Cs is not free but remains trapped in the cubic structure. The presence of dia-FeCo cube can be explained considering different hypothesis: *i*) not all the starting dia-FeCo cube is transformed into para-FeCo cube, but only that attached to negative-charged 1T-MoS_2 or *ii*) FeCo cube units are partially detached from MoS_2 flakes after sonication during the NMR tubes preparation, thus establishing probably an equilibrium between diamagnetic and paramagnetic species in solution. In principle, according to our XPS data, the option *i*) should be discarded since the absence of Cl signal indicates that dia-FeCo cube is not a part of the composite.

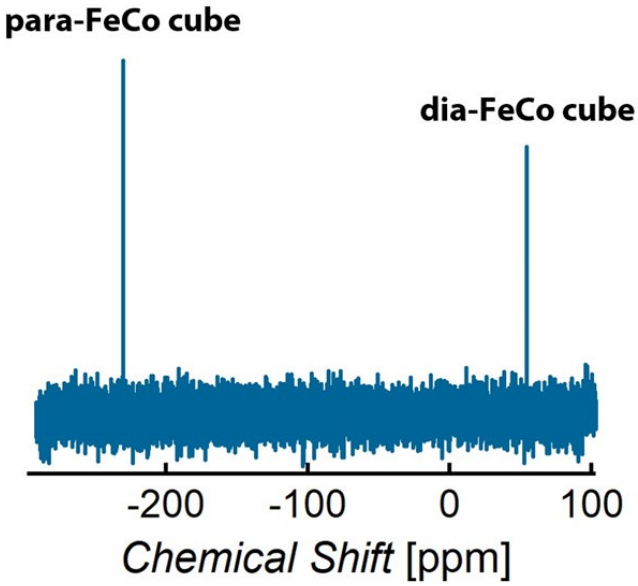

Figure III-9. ^{133}Cs RMN spectrum of FeCo@MoS_2 in CD_3CN referenced respect to a ≈0.1 M solution of CsCl in D_2O.

Attenuated total reflectance (ATR)

Both the starting dia-FeCo cube and FeCo@MoS_2 were analysed by ATR. The ATR spectrum of FeCo@MoS_2 (**Figure III-10**) is dominated by bands stemming from the FeCo cube. In the measuring range, the unique characteristic peak expected for MoS_2 (at ≈ 470 cm^{-1}) seems to be masked by more intense neighbouring FeCo cage signals. The ATR spectrum of FeCo@MoS_2 perfectly matches with that of pure dia-FeCo cube. Because of its low intensity, the small shoulder band (at ≈ 2080 cm^{-1}) expected for para-FeCo cube is not visible (as also

happens in para-FeCo cube spectra of this specific derivative). Whilst the vibration band designated as **a** (at ≈2488 cm^{-1}) corresponds to the B–H stretching of Tp ligands, those dubbed as **b** and **c** (at ≈2104 and 2123 cm^{-1}) are related to the C≡N stretching in the Fe^{II}–C≡N–Co^{III} unit.[23] Signals located in the 700–1504 cm^{-1} range arise from Tp units.

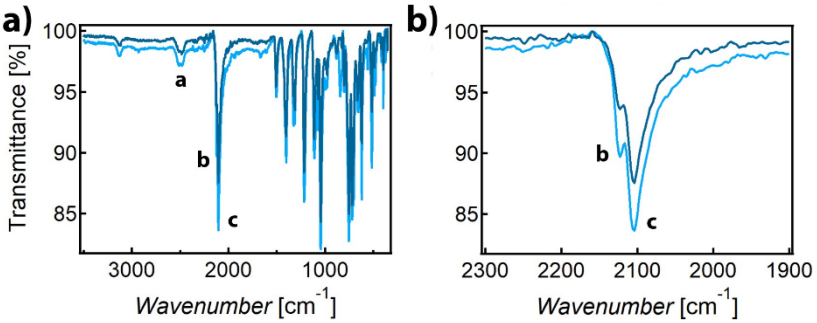

Figure III-10. ATR spectra of the starting dia-FeCo cube (light blue) and FeCo@MoS_2 (dark blue); b) Zoomed ATR spectra of dia-FeCo cube (light blue) and FeCo@MoS_2 (dark blue) in the 2300–1900 cm^{-1} range. Vibrations denoted as a, b, and c appear at 2488, 2104, and 2123 cm^{-1}, respectively.

Raman spectroscopy

Complementarily to ATR results, Raman spectrum of FeCo@MoS_2 (**Figure III-11**) is dominated by MoS_2 peaks. The observation of unclear J peaks (characteristic of 1T polytype) is probably related to a non-significant dominance of 1T-MoS_2 over 2H-MoS_2.

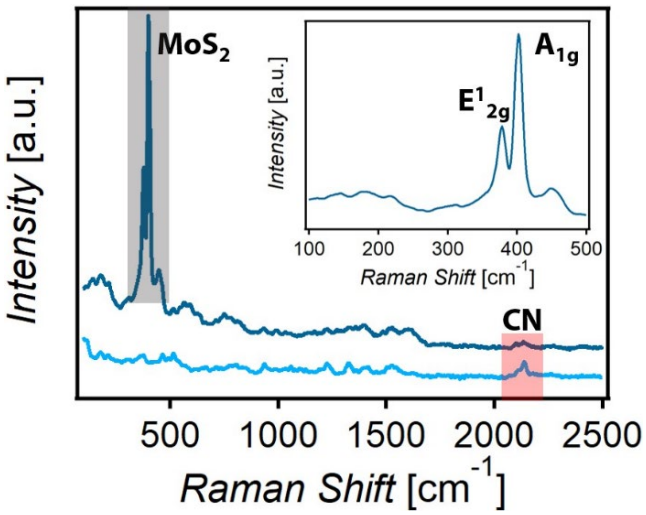

Figure III-11. Raman spectra of dia-FeCo cube (light blue) and FeCo@MoS_2 (dark blue). Inset: Raman spectrum of FeCo@MoS_2 in the 100–500 cm^{-1} range showing the typical peaks of MoS_2.

Electron paramagnetic resonance (EPR) spectroscopy

The EPR study was developed in collaboration with J. M. Carbonell-Vilar (from Universitat de València).

The EPR technique is very sensitive to local environments of paramagnetic species. In light of the paramagnetic character of FeCo@MoS_2 (imparted by the FeCo cube) revealed by RMN results, it was thought that more detailed information about the paramagnetic HS Co^{II} centres (and therefore unpaired electrons) could be extracted from EPR measurements, even at the risk of having interferences coming from the metallic 1T-MoS_2.[24]

In an octahedral environment HS Co^{II} is described by a $^4T_{1g}$ electronic term, whose microstates are split in 12 Kramers doublets under the combined effect of the spin-orbit coupling and the distortion. In these circumstances, the ground Kramers doublet is well separated from the excited ones (by more than 100 cm^{-1}). Therefore, at low enough temperatures (below *ca.* 50 K), only this Kramers doublet is populated in such a way that, at these temperatures, HS Co^{II} can be described through an effective electron spin S=1/2).[15,25,26] Thus, the para-FeCo cube should exhibit an EPR similar to that of the analogous $Cs\subset\{[Fe^{II}(Tp)(CN)_3]_4[Co^{III}(^{pz}Tp)]_3[Co^{II}(^{pz}Tp)]\}$ cube already reported

in literature (**Figure III-12**), with two remarked signals centred at ≈1000 and 3700 G (corresponding to $g_{eff||}$ = 7.71 and $g_{eff\perp}$ = 1.85, respectively),[15] which agrees with an slight axial distortion of the octahedron.

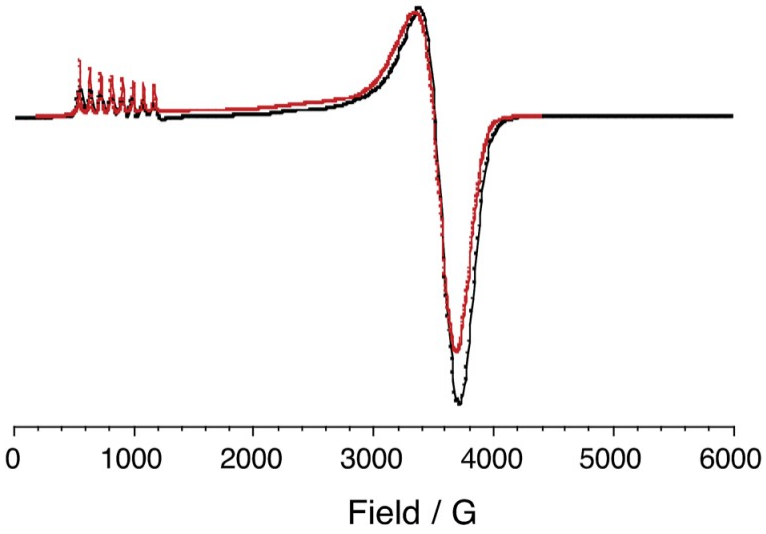

Figure III-12. X-band EPR spectrum of Cs⊂{[Fe^{II}(Tp)$(CN)_3$]$_4$[Co^{III}($^{pz'}$Tp)]$_3$[Co^{II}($^{pz'}$Tp)]} in powder at 4 K (experimental in black and simulated in red). The EPR spectrum in CH_2Cl_2 solution at 4 K perfectly resembles the measurements in solid. Extracted from ref 15.

The EPR spectra of FeCo@MoS_2 (in CH_3CN) and ce-MoS_2 flakes (in powder) were measured at 5 K (**Figure III-13**). In order to simulate the experimental spectrum, in addition to the expected presence of para-FeCo cube and MoS_2 layers, it is necessary to consider a third component (centred at ≈2000 G range). This additional species, with a significant contribution, could be a Co^{II} monomer. This fact would affect the Co^{III}:Co^{II} ratio estimated from the XPS of the FeCo@MoS_2 composite. Therefore, more experiments are required for completing the present work.

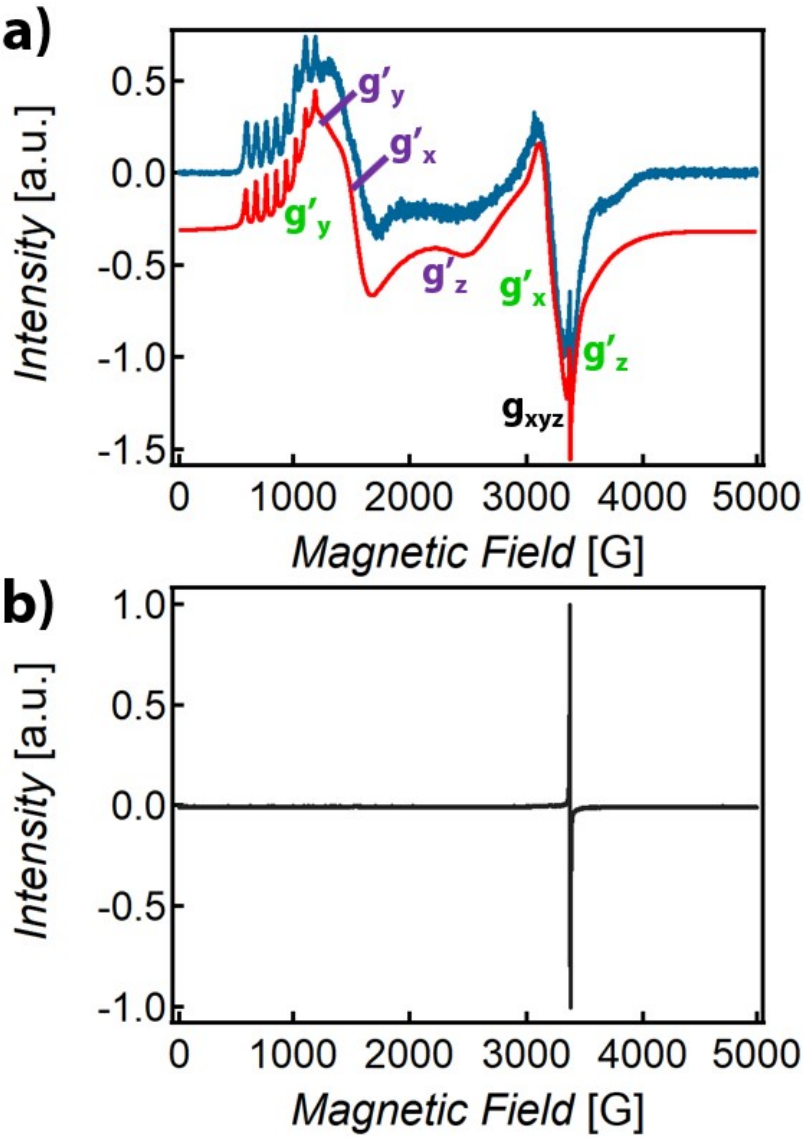

Figure III-13. X-band EPR of a) FeCo@MoS_2 in CH_3CN (experimental in blue and simulated in red) and b) ce-MoS_2 flakes in powder at 5 K. In "a)", both spectra have been shifted for clarity and the values of g in green, purple, and black correspond to para-FeCo cube, the unknown Co^{II} species, and 1T-MoS_2, respectively. Simulated spectrum by J. M. Carbonell-Vilar (from Universitat de València).

Thus, having in mind the third contribution required for the simulation of the EPR spectrum, the following g values are obtained: g = 2.01 for

MoS_2; $g'_y = 2.67$, $g'_x = 4.40$, and $g'_z = 5.74$ for the unknown Co^{II} species; $g'_y = 1.97$, $g'_x = 2.09$, and $g'_z = 7.55$ for para-FeCo cube. They indicate that the symmetry of Co^{II} is rhombic.

In essence, the preliminary EPR results seem to demonstrate that one of the four Co^{III} centres present in para-FeCo cube is reduced by one electron, giving rise to a paramagnetic behaviour.

With the aim of casting some light on this analysis, the EPR of the starting dia-FeCo cube was also performed in CH_3CN at 5 K. Surprisingly, although RMN results excluded the existence of para-FeCo cube in the starting material, the corresponding EPR spectrum reveals paramagnetic signals (para-FeCo cube and the unknown Co^{II} species). It is important to emphasize that EPR is only sensitive to paramagnetic species (in our case, those containing Co^{II}). In contrast to EPR, the ^{133}Cs RMN permits to detect both diamagnetic and paramagnetic species, provided that they contain Cs trapped inside their cage. Therefore, EPR technique is impractical when estimating the proportion of diamagnetic species with respect to the paramagnetic compounds. In order to obtain more conclusive information, it would be necessary to prepare new batches of FeCo@MoS_2 and repeat the EPR study.

Magnetic measurements

In order to check the magnetic behaviour of FeCo@MoS_2 and its potential photomagnetism (it has to be notice that dia-FeCo cube used as precursor does not have photomagnetic properties but para-FeCo does), several magnetic susceptibility measurements were performed in a SQUID apparatus.

First of all, the molar magnetic susceptibility multiplied by temperature ($\chi_m T$) *vs* temperature (T) plot of ce-MoS_2 flakes (**Figure III-14**) was measured in powder. The obtained results confirmed the paramagnetic character of 1T-MoS_2.

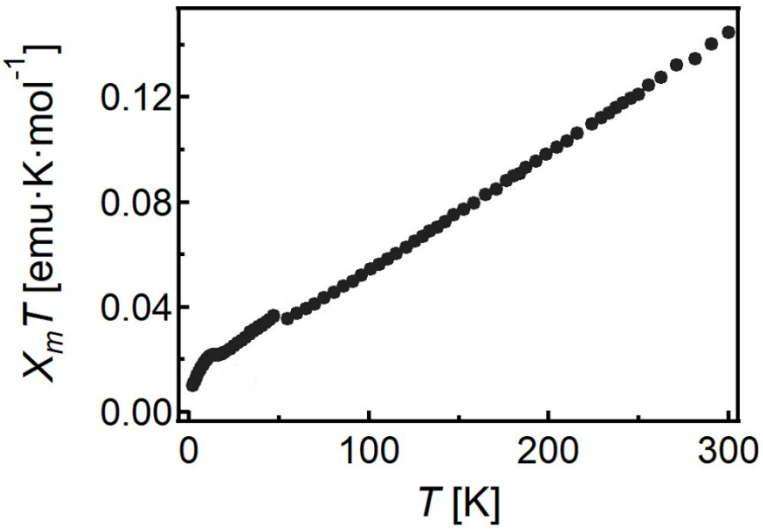

Figure III-14. $\chi_m T$ *vs* T plot of ce-MoS_2 flakes. The contribution of the diamagnetism of the capsule has been removed but no temperature independent paramagnetism (TIP) correction has been included.

Prior to start the photomagnetic measurements of FeCo@MoS_2 composite, we expected photomagnetic results similar to those observed for $Cs\subset\{[Fe^{II}(Tp)(CN)_3]_4[Co^{III}(^{pz}Tp)]_3[Co^{II}(^{pz}Tp)]\}$ (see **Figure III-15**).[15]

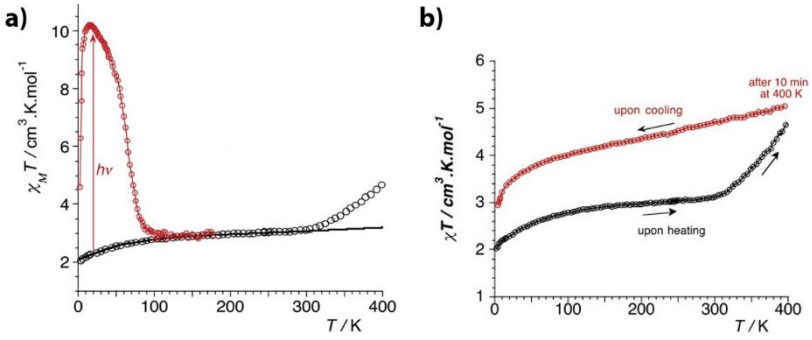

Figure III-15. $\chi_m T$ *vs* T plot of $Cs\subset\{[Fe^{II}(Tp)(CN)_3]_4[Co^{III}(^{pz}Tp)]_3[Co^{II}(^{pz}Tp)]\}$ a) on the bulk upon heating (in black) and after irradiation at 808 nm (in red) and b) upon heating (in black) and upon cooling (in red) after leaving the sample 10 minutes at 400 K in the SQUID magnetometer. Extracted from 15.

For the molar magnetic susceptibility calculations of FeCo@MoS_2, a chemical formula of $Cs\subset\{[Fe^{II}(Tp)CN)_3]_4[Co^{III}(Tp)]_3[Co^{II}(Tp)]\}\cdot[MoS_2]_2$ was roughly

estimated on the basis of XPS results (quantitative formation of the paramagnetic species and a molar ratio of Fe:Mo of ≈2). Therefore, the molecular weight (M_w) calculated for FeCo@MoS_2 was 2928.61 g mol^{-1}. However, we are aware of the imprecision of this approximation, due to the presence of the unknown paramagnetic Co(II) species detected by EPR in an unknown amount.

In the non-irradiated FeCo@MoS_2 sample (red curve in **Figure III-16**), the magnetic response is consistent with the presence of paramagnetic Co^{II}. The susceptibility signal is expected to be dominated by the Co^{II} since the paramagnetic susceptibility arising from 1T-MoS_2 is almost negligible.[24]

Then, the photomagnetic behaviour of FeCo@MoS_2 was evaluated. The measurements upon irradiation with a source of 808 nm at 20 K are plotted in blue (heating from 20 to 400 K) and black (cooling from 400 K to 2 K).

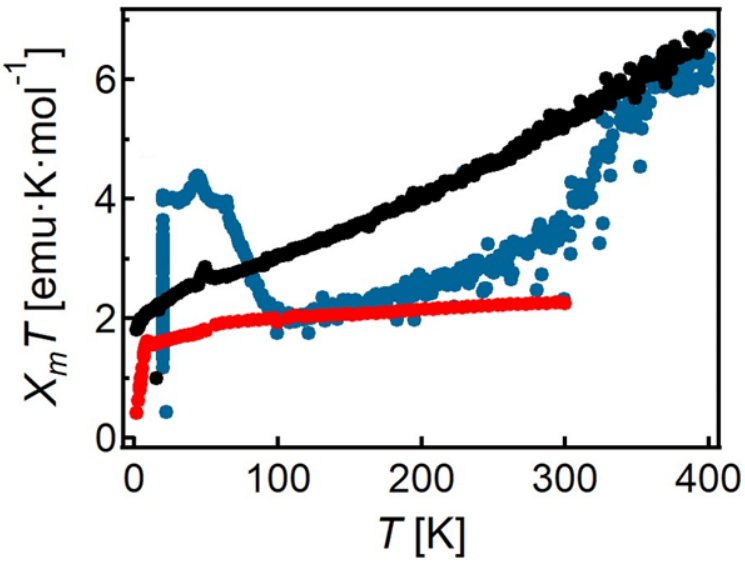

Figure III-16 χ_mT *vs* T plots of FeCo@MoS_2 without irradiation (red), upon heating after the irradiation of the sample at 20 K with a source of 808 nm for 6 h (blue), and upon cooling down next from 400 K (black). The small peak detected at ≈50 K indicates the presence of traces of O_2 in the cryostat, which solidifies during the measurement.

Interestingly, upon irradiation a clear photo-induced ETCST effect is observed at ≈20 K, with a sharp increase in χ_mT from 1 to

4 emu K mol^{-1}. This metastable state persists until ≈85 K, undergoing a fast thermal relaxation at higher temperatures, in agreement with the behaviour observed in other similar paramagnetic FeCo cubes.[15] Still, some differences can be noted with the behaviour of the analogous cubes. The main one concerns the photoconversion rate, which is lower for FeCo@MoS_2.[15] This could be originated by the interaction between the cube and the MoS_2 surface, which may hinder a full electronic transfer process. In this sense, the presence of a high number of ce-MoS_2 layers in the sample may also contribute to decrease the conversion rate since it could partially obstruct the light path from the exciting source. Moreover, the presence of the unknown paramagnetic species with no photomagnetic properties, would clearly support a smaller photoconversion rate of the whole material.

By further heating the sample, we observe a gradual but marked increase in $\chi_m T$ above 300 K, which agrees with the existence of a thermally-induced ETCST effect. This process has already been reported for compounds similar to para-FeCo cube. As in that case, the electron transfer inside the cube is only partial since a clear plateau in $\chi_m T$ is not reached.[15] Moreover, in agreement also with the behaviour of the isolated cubes, the thermally-induced ETCST is not reversible after cooling the sample from 400 K to low temperatures (**Figure III-16**, black curve). This could be due to a thermal degradation of the material.

Remarkably, the partial electron transfer observed in both photo- and thermally-induced processes is similar in terms of magnitude. This observation may support that the main reason for a partial photo-ETCST cannot be exclusively due to the blocking of the light caused by the presence of the MoS_2 layers.

In order to check that the photoexcitation was preserved after a mild heating, FeCo@MoS_2 was measured again with thermal cycling in a lower temperature range, 20-250 K, after roughly three months of its preparation (**Figure III-17**). The results obtained confirm that the photodegradation of the sample is supressed if high temperatures are not reached.

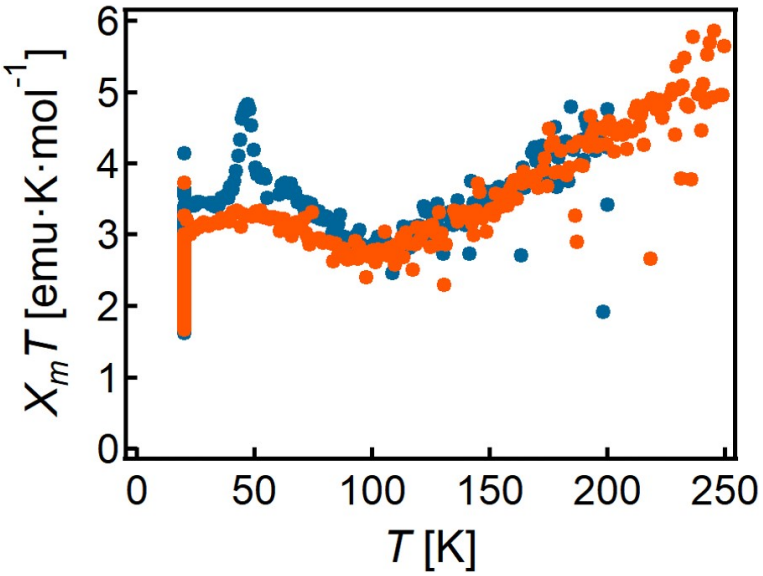

Figure III-17. χ_mT *vs* T plots of FeCo@MoS_2 upon heating after the irradiation of the sample at 20 K with a source of 808 nm for 6 h (first and second heating processes in blue and orange, respectively).

All these results corroborate the detection of Co^{II} in FeCo@MoS_2 performed by XPS, NMR, and EPR. Moreover, they seem to support the idea that ce-MoS_2 flakes can partially reduce Co^{III} to Co^{II}, thus generating the paramagnetic FeCo cube. This redox process was already encountered in the PB synthesis over the ce-MoS_2 flakes (see Chapter II), where the electrons required for the Fe^{III}→Fe^{II} reduction were taken from the negative charge accumulated on ce-MoS_2 flakes. However, at this point, it is important to remark the fact that we need to repeat this study with new batches of impurity-free FeCo@MoS_2 to get more reliable and conclusive information.

III.3. Conclusions

In this Chapter, we have prepared a novel molecular/2D composite by combining ce-MoS_2 flakes with preformed discrete FeCo cubes.

According to XPS, whilst the integrity of ce-MoS_2 flakes is preserved, in this FeCo@MoS_2 composite the dia-FeCo cube (initially formed by 4 Fe^{II} and 4 Co^{III} ions) is partially reduced to para-FeCo cube, in which 1 Co^{III} is reduced to Co^{II}, as a result of an electron transfer from the negatively-charged ce-MoS_2 flakes. This gives rise to a paramagnetic behaviour in the new composite, a feature that is confirmed by EPR. Moreover, the absence of Cl signals in the XPS survey supports the idea that the initial perchlorate counter anion is not a part of the composite.

SQUID magnetic measurements confirm again the paramagnetic nature of the cubes attached to the ce-MoS_2 layers. Apart from that, we note that the photomagnetism typical of a paramagnetic FeCo cube is preserved when these FeCo species are in contact with ce-MoS_2 flakes. Thus, a clear photo-induced ETCST effect has been observed at ≈20 K, also accompanied by a thermally-induced ETCST effect at ≈300 K.

An important issue when dealing with hybrid materials obtained by combining two components is to examine the novel properties that may emerge from such a combination. We have seen the profound effect that the MoS_2 flakes have on the properties of the starting compound. Thus, thanks to the redox process that occurs when these two components are mixed, the starting dia-FeCo cube accepts one electron and becomes photomagnetic. It should be also of interest to check the complementary question: Which is the influence of the resulting para-FeCo cube on the properties of the MoS_2 layers? To answer this question, the transport properties of the composite will be examined in the near future.

In essence, the methodology proposed here permits to decorate the surface of MoS_2 flakes with the photomagnetic para-FeCo cube by taking advantage of the electron transfer occurring from negative-charged MoS_2 flakes to the starting dia-FeCo cube, which is easier to synthesize and isolate. The resultant composite, where cubes are dispersed over a conductive MoS_2 matrix, could find fascinating

applications in photoelectronics, sensing or energy storage, and conversion fields.

As a future work, it would be interesting to test the electrochemical performance of FeCo@MoS_2 as cathode material for batteries playing with different cations. Moreover, another exciting line would be to prepare a new composite by mixing ce-MoS_2 flakes with para-FeCo cube and compare the emerging magnetic properties of this one with those of FeCo@MoS_2 and the starting paramagnetic species.

Although the preliminary results look promising, there is still a lot to do. First of all, it is imperative to characterize better the properties of the starting dia-FeCo cube and study its stability over time in order to discard the presence of impurities. The use of pure reagents would considerably assure a more reliable interpretation of the results obtained from the composite. Despite the fact that XPS, NMR, and EPR data confirm the existence of the para-FeCo cube in the FeCo@MoS_2 composite, the Co^{III}:Co^{II} ratio provided by XPS does not perfectly match what is observed in NMR (detection of diamagnetic and paramagnetic signals) and EPR spectra (need of assuming another paramagnetic Co^{II} species when simulating the spectrum). Even if the detection of a diamagnetic signal in the ^{133}Cs NMR spectrum of FeCo@MoS_2 can be justified through a partial detachment of FeCo cube units that gives rise to an equilibrium between diamagnetic and paramagnetic species in solution, EPR results indicate the presence of paramagnetic contamination in both dia-FeCo cube and FeCo@MoS_2. Therefore, as soon as possible, a new batch of FeCo@MoS_2 composite will be first prepared by using pure dia-FeCo cube and then thoroughly characterized.

III.4. Experimental section

III.4.1. Materials

For the chemical exfoliation of MoS_2, see **Materials** in Chapter II. Acetonitrile was used without further purification. Milli-Q water was used in all the experiments.

III.4.2. Methods

III.4.2.1. Intercalation/chemical exfoliation of MoS_2

See **Methods** in Chapter II.

III.4.2.2. Synthesis of $[Cs(Fe^{II}Tp)_4(Co^{III}Tp)_4]ClO_4$

$[Cs(Fe^{II}Tp)_4(Co^{III}Tp)_4]ClO_4$ cluster was synthesized by J. Glatz under the supervision of Dr. R. Lescouëzec, from Institut Parisien de Chimie Moléculaire (IPCM), Faculté des Sciences & Ingénierie, Sorbonne Université.

III.4.2.3. Synthesis of FeCo@MoS_2

Prior to the reaction, a freshly prepared suspension of ce-MoS_2 flakes and 2 mL of $[Cs(Fe^{II}Tp)_4(Co^{III}Tp)_4]ClO_4$ (100.0 mg, 36.9 µmol, 1 eq) in acetonitrile were separately degassed under flowing argon in order to remove oxygen. Next, still under inert atmosphere, 2 mL of ce-MoS_2 suspension (18.5 µmol, 0.5 eq) were poured into the reaction system and magnetically stirred for 1 h at room temperature. Subsequently, the final mixture was centrifuged at 13.4 krpm for 30 min. After decanting the supernatant, the sediment was dispersed in acetonitrile and centrifuged at 13.4 krpm for 0.5 h. The previous dispersion-centrifugation-collection step was repeated twice more. Finally, the sediment was dried by vacuum for at least 7 h.

III.4.3. Characterization techniques

ATR spectroscopy

ATR spectra of dia-FeCo PBA and FeCo@MoS_2 were collected in an Agilent Cary 630 FTIR spectrometer in the 6500−4000 cm^{-1} range in absence of KBr pellets.

EPR

EPR measurements were performed with a X-band Bruker E-580 ELEXSYS spectrometer on FeCo@MoS_2 in CH_3CN and ce-MoS_2 flakes in solid at 5 K.

^{133}Cs NMR

^{133}Cs RMN spectra of dia-FeCo cube and FeCo@MoS_2 were referenced respect to a solution pattern of CsCl in D_2O (≈0.1 M). In both cases, spectra were recorded on a Bruker DRX 500 (500 MHz) spectrometer at 298 K.

Photomagnetic measurements

The same SQUID magnetometer described in Chapter II was used. Once introduced in the magnetometer, the sample (a thin film of FeCo@MoS_2 deposited onto a double-sided tape or powder packed inside a polyethylene bag) was first frozen at 100 K and, before cooling to 20 K, purged under vacuum at 100 K. Photomagnetic measurements were performed on the thin film of FeCo@MoS_2 by using a laser of 808 nm coupled to the cavity of the magnetometer through an optical fibre. The power on the surface sample was adjusted to 5 mW cm^{-2}. The sample was irradiated at 20 K and 1000 G for 6 h. After withdrawing the light source, the sample was heated to 400 K. Then, the sample was cooled down to 2 K. During the entire process, 1000 G were applied. The sample of ce-MoS_2 flakes was measured as powder inside a polyethylene bag. In order to avoid the introduction of artefacts, the temperature-independent paramagnetism (TIP) contribution was not subtracted from the measurements.

Raman

Raman spectra of dia-FeCo PBA and FeCo@MoS_2 were recorded with a Raman Emission Horiba-MTB Xplora spectrometer in ambient conditions onto a clean SiO_2 (285 nm)/Si substrate by using a laser of 532 nm. A 100x objective was used to focus the laser beam. All samples were placed onto clean SiO_2 (285 nm)/Si substrates in order to use the Si peak as reference.

TEM

See **HRTEM** in Chapter II.

XPS

See **XPS** in Chapter II. XPS spectra were deconvoluted by using Origin program.

III.5. References

1. Bleuzen, A., Marvaud, V., Mathoniere, C., Sieklucka, B. & Verdaguer, M. Photomagnetism in clusters and extended molecule-based magnets. *Inorg. Chem.* **48**, 3453–3466 (2009).

2. Sato, O., Iyoda, T., Fujishima, A. & Hashimoto, K. Photoinduced magnetization of a cobalt-iron cyanide. *Science.* **272**, 704–705 (1996).

3. Aguilà, D., Prado, Y., Koumousi, E. S., Mathonière, C. & Clérac, R. Switchable Fe/Co Prussian blue networks and molecular analogues. *Chem. Soc. Rev.* **45**, 203–224 (2016).

4. Cartier Dit Moulin, C., Champion, G., Cafun, J. D., Arrio, M. A. & Bleuzen, A. Structural rearrangements induced by photoexcitation in a RbCoFe Prussian blue derivative. *Angew. Chemie - Int. Ed.* **46**, 1287–1289 (2007).

5. Escax, V. *et al.* Photoinduced ferrimagnetic systems in Prussian blue analogues $C^{I}_{x}Co_4[Fe(CN)_6]_y$ (C^{I} = Alkali Cation). 3. Control of the photo- and thermally induced electron transfer by the $[Fe(CN)_6]$ vacancies in cesium derivatives. *J. Am. Chem. Soc.* **123**, 12536–12543 (2001).

6. Flambard, A., Köhler, F. H. & Lescouëzec, R. Revisiting Prussian blue analogues with solid-state MAS NMR spectroscopy: Spin density and local structure in $[Cd_3\{Fe(CN)_6\}_2]\cdot 15H_2O$. *Angew. Chem.* **48**, 1673 –1676 (2009).

7. Flambard, A., Köhler, F. H., Lescouëzec, R. & Revel, B. Probing spin density and local structure in the prussian blue analogues $CsCd[Fe/Co(CN)_6]\cdot 0.5H_2O$ and $Cd_3[Fe/Co(CN)_6]_2\cdot 15H_2O$ with solid-state MAS NMR spectroscopy. *Chem. Eur. J.* **17**, 11567–11575 (2011).

8. Zhang, Y. *et al.* Reversible thermally and photoinduced electron transfer in a cyano-bridged $\{Fe_2Co_2\}$ square complex. *Angew. Chemie - Int. Ed.* **49**, 3752–3756 (2010).

9. Mercurol, J. *et al.* $[Fe^{II}_{LS}Co^{III}_{LS}]_2 \leftrightarrow [Fe^{III}_{LS}Co^{II}_{HS}]_2$ photoinduced conversion in a cyanide-bridged heterobimetallic molecular square. *Chem. Commun.* **46**, 8995–8997 (2010).

10. Koumousi, E. S. *et al.* Metal-to-metal electron transfer in Co/Fe prussian blue molecular analogues: The ultimate miniaturization. *J. Am. Chem. Soc.* **136**, 15461–15464 (2014).

11. Jiménez, J. R. *et al.* A new $\{Fe_4Co_4\}$ soluble switchable nanomagnet encapsulating Cs^+: Enhancing the stability and redox flexibility and tuning the photomagnetic effect. *Dalt. Trans.* **46**, 15549–15557 (2017).

12. Lescouëzec, R. *et al.* Design of single chain magnets through cyanide-bearing six-coordinate complexes. *Coordination Chemistry Reviews* **249**, 2691–2729 (2005).

13. Berlinguette, C. P. *et al.* A charge-transfer-induced spin transition in a discrete complex: The role of extrinsic factors in stabilising three electronic isomeric forms of a cyanide-bridged Co/Fe cluster. *J. Am. Chem. Soc.* **127**, 6766–6779 (2005).

14. Wessells, C. D., Huggins, R. A. & Cui, Y. Copper hexacyanoferrate battery electrodes with long cycle life and high power. *Nat. Commun.* **2**, 550 (2011).

15. G arnier, D. *et al.* $K\subset\{[Fe^{II}(Tp)(CN)_3]_4[Co^{III}(^{pz}Tp)]_3[Co^{II}(^{pz}Tp)]\}$: A neutral soluble model complex of photomagnetic Prussian blue analogues. *Chem. Sci.* **7**, 4825–4831 (2016).

16. Kim, D. W. *et al.* Direct observation of molybdenum disulfide, MoS_2, domains by using a liquid crystalline texture method. *Nano Lett.* **15**, 229–234 (2015).

17. Eda, G. *et al.* Coherent atomic and electronic heterostructures of single-layer MoS_2. *ACS Nano* **6**, 7311–7 (2012).

18. Geng, X. *et al.* Pure and stable metallic phase molybdenum disulfide nanosheets for hydrogen evolution reaction. *Nat. Commun.* **7**, 10672 (2016).

19. Choi, J. G. & Thompson, L. T. XPS study of as-prepared and reduced molybdenum oxides. *Appl. Surf. Sci.* **93**, 143–149 (1996).

20. Sun, Y., Hu, X., Luo, W. & Huang, Y. Ultrafine MoO_2 nanoparticles embedded in a carbon matrix as a high-capacity and long-life anode for lithium-ion batteries. *J. Mater. Chem.* **22**, 425–431 (2012).

21. Okamoto, Y., Nakano, H., Imanaka, T. & Teranishi, S. X-Ray Photoelectron Spectroscopic Studies of Catalysts — Supported Cobalt Catalysts —. *Bull. Chem. Soc. Jpn.* **48**, 1163–1168 (1975).

22. Velasco-Velez, J. J. *et al.* Photoelectron Spectroscopy at the Graphene-Liquid Interface Reveals the Electronic Structure of an Electrodeposited Cobalt/Graphene Electrocatalyst. *Angew. Chem.* **54**, 14554–14558 (2015)

23. Berlinguette, C. P. *et al.* A charge-transfer-induced spin transition in a discrete complex: The role of extrinsic factors in stabilising three electronic isomeric forms of a cyanide-bridged Co/Fe cluster. *J. Am. Chem. Soc.* **127**, 6766–6779 (2005).

24. Yan, S. *et al.* Enhancement of magnetism by structural phase transition in MoS_2. *Appl. Phys. Lett.* **106**, 012408 (2015).

25. Jesson, J. P. Isotropic nuclear resonance shifts in some trigonal Co(II) and Ni(II) chelate systems. *J. Chem. Phys. **47**, 582* (1967).

26. Pietrzyk, P., Srebro, M., Radoń, M., Sojka, Z. & Michalak, A. Spin ground state and magnetic properties of cobalt(II): Relativistic DFT calculations guided by EPR measurements of bis(2,4-acetylacetonate)cobalt(II)-based complexes. *J. Phys. Chem. A.* **155**, 2316–2324 (2011).

IV. Covalent functionalization of MoS_2 layers with photochromic molecules

IV.1. Introduction

IV.1.1. Photochromic molecules

Photochromic molecules are those that undergo efficient and reversible photochemical isomerization between at least two (meta)stable states displaying markedly different physical properties like solubility, colour, geometrical structure, dipole moment, dielectric constant, conductivity, magnetism, refractive index, hydrophobicity, viscosity, and stability, and different chemical properties like chelating capacity and redox potentials.[1] This kind of molecules may be useful in the development of different technological devices like the rewritable compact discs and DVDs,[2] 3D data storage devices,[3] systems of vision in the human eye,[4] or light-triggered molecular motors.[5,6]

Among photochromic molecules, the diarylethene family deserves special attention because some of its members show good thermal stability and high fatigue resistance.[7] As deduced from the name, this class of compounds are characterized by possessing two aromatic groups (*i.e.*, aryl substituents) linked by an ethene bridge. Stilbene, systematically known as 1,2-diphenylethene, is the simplest example and exists as two possible stereoisomers (*cis* or *Z* and *trans* or *E* forms), as shown in **Figure IV-1**. These isomers can be interconverted through a rotation of 180º around the central ethene bond.

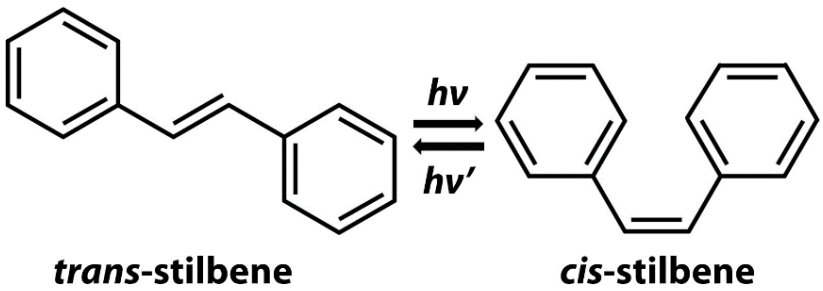

Figure IV-1. Schematic representation of the photoisomerization of stilbene.

Unfortunately, the *cis*-stilbene molecule can be degraded into 9,10-dihydrophenanthrene by electrocyclic ring closure and this, in turn, into phenanthrene by irreversible oxidative aromatization (dehydrogenation).[8] Although oxidation represents the main encumbrance in applications based on reversible photoswitching,[7] it can be supressed by an appropriate molecular design. Thus, the

substitution of hydrogens *ortho* to the ethene bridge by alkyl or alkoxy groups renders stilbene derivatives stable against oxidation.[9] Furthermore, the thermal life of such carbocyclic disubstituted dihydrophenanthrenes can be notably elongated when replacing phenyl rings by thiophenes,[10] thereby emerging the so-called **dithienylethene** subgroup.

These latter systems, discovered by M. Irie and co-workers,[7,11] show maximum stabilization when the following conditions are fulfilled: *i*) thiophenes are methylated in 2 position, and *ii*) the ethylene bridge is incorporated into a small ring (*e.g.*, cyclopentene or cyclohexene).[12] Whilst the first requirement ensures a good photodegradation resistance, the second one blocks the dithienylethene molecule into *cis* form, giving rise to another kind of photoswitching mechanism consisting in pericyclic ring opening and closure reaction, differing from the typical *cis*-*trans* conversion of stilbenes (see **Figure IV-2**).[13] Hence, dithienylethene molecules in solution can adopt parallel and anti-parallel conformations, of which only the anti-parallel can be cyclized.[14]

In dithienylethene molecules, the open-to-close switching is usually driven by UV light, whereas the back process is induced by visible light.[15]

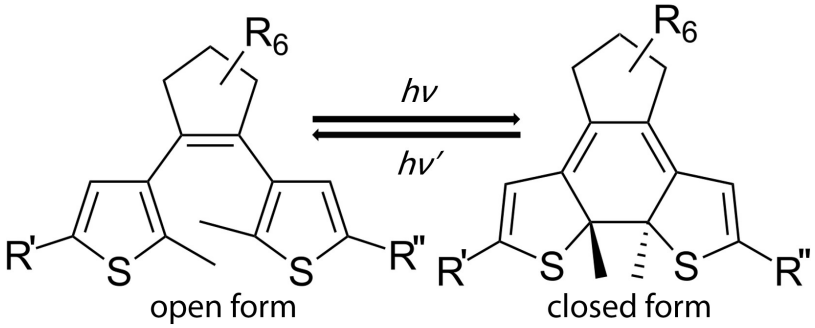

Figure IV-2. Schematic representation of the photoswitching process of dithienylethene molecules. Generally, R_6 refers to six equal substituents (H or F atoms).

Because of the subtle differences in molecular geometry between both isomers, the interconversion can quickly take place even in a solid matrix, in contrast to what occurs in most of photochromic molecules.[10]

Open and closed isomers significantly differ in terms of conjugation. This is the reason why closed and open forms are generally coloured and colourless, respectively. In the open-ring structure, conjugation is localized on thiophenes. Conversely, the closed-form π conjugation delocalizes electrons over the entire molecule backbone, leading to a lower gap between the highest occupied molecular orbital (HOMO) and the lowest unoccupied molecular orbital (LUMO), if compared to its open counterpart.[16] Therefore, the closed form exhibits higher conductivity.[17–19]

IV.1.2. Photochromic molecules and MoS_2

Due to their large surface-to-area ratio, 2D materials have been successfully interfaced with photochromic molecules in order to fabricate high-performance light-responsive hybrid systems.[15] In this case, the molecule-flake interaction represents an interesting way to tailor the doping of the 2D material while allowing a fine control over its physical properties. Besides, in some cases, the interaction of both components may give rise to the appearance of novel properties and therefore exciting applications.[20–24]

The combination of 2D materials with molecular switches is still a nascent field, in which TMDCs are gaining importance.[15] Concerning non-covalent functionalization, vdW interactions have been exploited in order to hold together carbonaceous or non-carbonaceous 2D materials with different photochromic molecules (azobenzenes,[21] diarylethenes,[22,23] spiropyrans,[24] and dihydroazulenes)[20] into advanced hybrid systems. Usually, the followed approach only involves the direct placing of one material on top of the other. In relation to non-covalent MoS_2 functionalization, for example, it has been demonstrated that the pristine PL of a 2H-MoS_2 monolayer can be quenched if the 2D material is placed on top of self-assembled monolayers (SAMs) based on light-responsive electropositive azobenzenes in their *trans* form (*n*-type doping). By contrast, when the *cis* form is recovered (*p*-type doping), the resultant PL is enhanced by a factor of 3.[21] Essentially, the PL of 2H-MoS_2 monolayer is modulated depending on the form of the azobenzenes (and therefore type of doping). Apart from that, high-performance electronic devices showing precise control over the local charge carrier density have been fabricated by interfacing MoS_2 monolayer (or graphene) with SAMs of spiropyrans.[24]

In contrast to weak non-covalent interactions between molecular switches and 2D materials, the formation of covalent bonds between both counterparts permits a stronger connexion, thus easing the charge and/or energy transfer between the light-responsive moiety and the 2D material. Until now, only few species have been grafted to MoS_2 flakes in order to fabricate photosensitive materials. For instance, a photosensitizer has been prepared through a complexation reaction between $[Ru^{II}(bpy)_2Cl_2]$, where bpy stands for 2,2'-bipyridine ligands, and ce-MoS_2 nanosheets covalently functionalized with bpy.[25] Also, liquid-exfoliated 2H-MoS_2 flakes have been combined with preformed Eu^{III} and Gd^{III} complexes, proving that magnetic and luminescent properties were kept post functionalization.[26] However, in none of these cases, organic photochromic molecules have been used. Therefore, this gap represents a serious call to action to couple MoS_2 with photochromic molecules by forming covalent bonds between them.

The aim of this Chapter is to prove that the transport properties of MoS_2 can be modified after its functionalization with a photochromic system, a dithienylethene derivative (hereafter DD-NH_2), that transits between open and closed forms (ODD-NH_2 and CDD-NH_2, respectively), as illustrated in **Figure IV-3**. For this end, we established the following action plan: *i*) preparation of the dithienylethene molecule, *ii*) covalent functionalization of ce-MoS_2 flakes by means of the *in-situ* diazotization of the photochromic molecule, and *iii*) study of the photoswitching capacity of the organic system once attached to the 2D material.

As explained in Chapter I, the diazonium salt strategy approach relies on the nucleophilic attack of S atoms from ce-MoS_2 flakes to the C atoms adjacent to the diazo moiety ($-N_2^+$), which is removed from the organic backbone as leaving group.

The use of a dithienylethene derivative bearing two terminal amino groups (potential reactive sites) leads us to consider the possibility of performing MoS_2 cross-linking[27,28] (extended networks of flakes physically and electronically interconnected through molecular linkers).

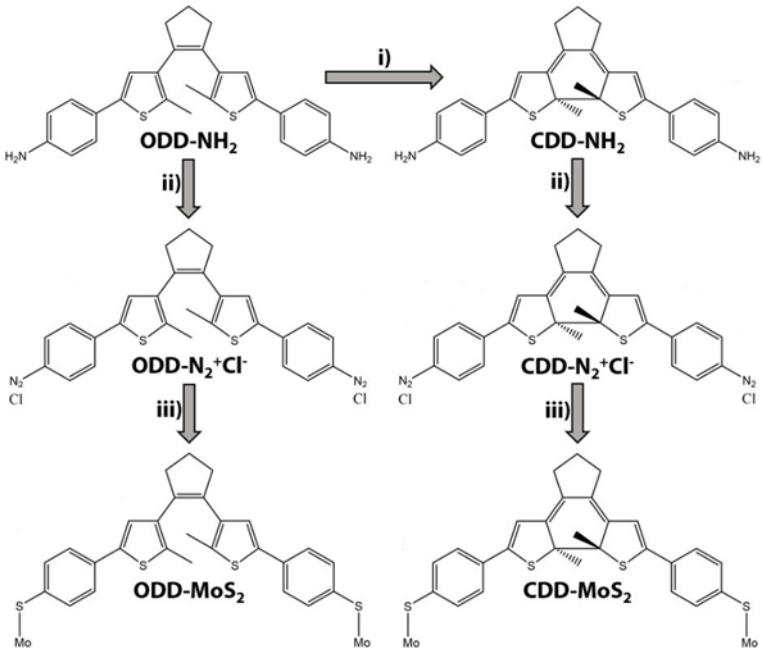

Figure IV-3. Pictorial representation of ODD-MoS_2 and CDD-MoS_2 synthesis (left and right, respectively). Steps labelled as i), ii), and iii) represent photoconversion, diazotization and covalent functionalization of MoS_2, respectively.

IV.2. Results and discussion

IV.2.1. ODD-NH_2→CDD-NH_2 photoconversion

The experimental work was developed in collaboration with J. M. Carbonell-Vilar and Dr. M. Viciano-Chumillas, who synthesized all the dithienylethene derivatives used in this Chapter.

For this research, the starting photochromic dithienylethene molecule was 1,2-bis[2-methyl-5-(4-aminophenyl)-thien-3-yl]cyclopentene (DD-NH_2, see **Figure IV-3**). Unlike ODD-NH_2 which was directly synthesized,[29] in order to generate the closed form, ODD-NH_2 was first dissolved in methanol (MeOH) and then subjected to UV irradiation. UV/Vis spectroscopy was used to follow the cyclization of the structure (different colour and absorption spectrum for each form), thereby allowing us to estimate the time necessary for yielding a considerable amount of CDD-NH_2 (without appreciable signs of degradation).

For the interconversion of dithienylethene molecules, the irradiation wavelengths depend on the substitution in thiophene units. The closing process requires more energy than the opening of the ring. Specifically, for generating the open and closed forms while avoiding the formation of photodegraded products (*i.e.*, annulated isomers formed as a result of a 1,2-dyotropic rearrangement), samples were irradiated at ≈350 and >540 nm, respectively.

Logically, the irradiation time is proportional to the concentration of DD-NH_2 in solution. Therefore, the more molecules absorbing energy, the longer time is required for carrying out the photoconversion. This statement was experimentally proven, as described below. Two solutions of ODD-NH_2 in methanol (MeOH) (≈0.07 and 0.7 mM) were irradiated at 350 nm. Whilst quantitative ODD-NH_2→CDD-NH_2 transformation was observed after ≈120 s of irradiation for the diluted one, the concentrated one took ≈900 s. The absorbance spectrum of ODD-NH_2 is dominated by a band at ≈315 nm (**Figure IV-4**, at the inception of the experiment). During the ODD-NH_2→CDD-NH_2 photoconversion, the optimum irradiation time was achieved when observing no significant increase in the absorbance of the band located at ≈528 nm, corresponding to the CDD-NH_2 system (**Figure IV-4**, at the end of the experiment). For larger time frames, photodegraded species were generated. Overall, these experiments served to determine the optimum irradiation conditions (15 min at 350 nm for the solution of ≈0.7 mM) for the ODD-NH_2→CDD-NH_2 transformation, prior to the diazotization reaction.

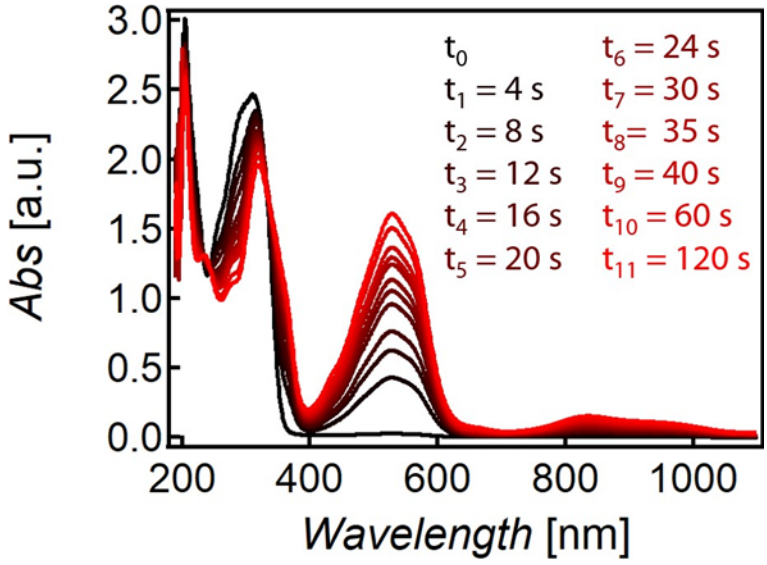

Figure IV-4. UV/Vis absorption spectra of ODD-NH_2 in MeOH (≈0.07 mM) at different irradiation times.

IV.2.2. Covalent functionalization of ce-MoS_2 by using DD-NH_2

Diazonium salts were formed by mixing DD-NH_2 with sodium nitrite in hydrochloric medium at 0 ºC (ice bath), under magnetic stirring and inert atmosphere. Whereas the solution containing ODD-NH_2 turned yellowish/orangish as the diazotization evolved, no visible changes were appreciated for that containing CDD-NH_2 due to the original strong purple colour of the closed-structure form. One hour later, a freshly prepared suspension of MoS_2 flakes was poured into the reaction system and allowed to react for 24 h at room temperature.

For both cases, reaction products were filtered by using a nylon membrane and sequentially washed with *i*) ultrapure (Milli-Q) water, *ii*) dimethyl sulfoxide (DMSO), and *iii*) MeOH, in order to sequentially remove *i*) diazonium salts and nitrite residues (with water), *ii*) the remaining (non-diazotized) DD-NH_2 (with DMSO), and *iii*) the high-boiling point DMSO, respectively (with MeOH). UV/Vis spectroscopy turned to be crucial when monitoring the removal of diazonium and nitrite salts from functionalized MoS_2 flakes. Both dark solids were rinsed with water until obtaining two featureless UV/Vis spectra for each aqueous filtrate. The first filtrate coming from the

treatment with DMSO was yellow and strong purple for ODD and CDD, respectively. The washing process with DMSO was interrupted when the absorbance of the filtrate was approximately zero. Subsequently, MeOH was employed to purify both solids from DMSO molecules, thus facilitating the final drying step. At this point, it is noteworthy to remark the importance of using DMSO between the washings with water and MeOH as the remaining non-diazotized DD-NH_2 is more soluble in DMSO than in MeOH.

For simplicity, the products resultant from mixing ce-MoS_2 flakes with the diazonium salts (*i.e.*, ODD-$N_2^+Cl^-$ and CDD-$N_2^+Cl^-$) are designated as ODD-MoS_2 and CDD-MoS_2, respectively. The DD-MoS_2 abbreviation encompasses ODD-MoS_2 and CDD-MoS_2.

IV.2.3. Characterization of DD-MoS_2

UV/Vis spectroscopy

Before analysing DD-MoS_2 samples by UV/Vis spectroscopy, the absorbance of a dispersion of ce-MoS_2 flakes in DMSO was measured (**Figure IV-5**). In this case, the UV/Vis absorption spectrum solely reveals a plasmon band at ≈311 nm since the other one was expected to appear below the cut-off wavelength value of the solvent (*i.e.*, 265 nm). At this point, it is convenient to underscore that plasmon bands are a signature of 1T-MoS_2 (see Chapter II).[30–32] By contrast, UV/Vis absorption spectra of DD-MoS_2 in DMSO were essentially featureless (as reported in some previous works).[31,32] However, the no detection of absorption bands coming from DD-NH_2 (expected at values close to those previously registered in MeOH) and diazonium salts (located in the 250–400 nm range)[33–35] corroborates the efficiency of the washing protocol. Unfortunately, the absence of clear plasmon bands[30–32] and excitonic transitions[36] (characteristic of 1T- and 2H-MoS_2, respectively) in the measuring range makes difficult to assign a polytype to functionalized MoS_2.

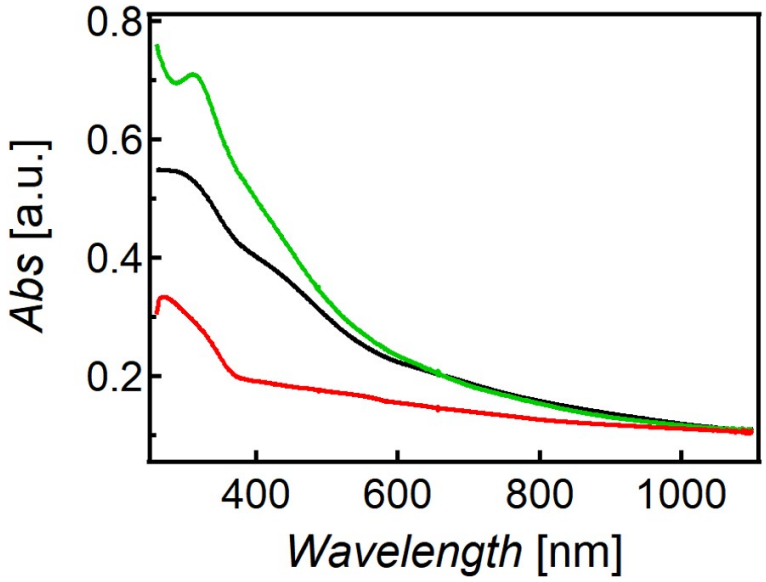

Figure IV-5. UV/Vis absorption spectra of CDD-MoS_2 (red), ODD-MoS_2 (black), and ce-MoS_2 (green) in DMSO.

FTIR

In order to get some insights about covalent functionalization of ce-MoS_2 with the organic system, the FTIR spectrum of 1,2-bis(2-methyl-5-phenylthien-3-yl)cyclopentene[37] in its open form (ODD-H) was compared with those of DD-MoS_2 (see **Figure IV-6**).

ODD-H (without any functional group attached to benzene rings) was prepared with the aim of analyzing the most similar molecule to that resulting from the covalent functionalization (denoted as DD hereafter). It is well-established that the tethering process implies the removal of diazonium groups from the benzene rings, which makes ODD-H closer to the final product than ODD-NH_2. However, it is also expected that the formation of a new C–S bond in *para* position respect to both benzene rings affects the pristine properties of the organic molecule.

In the FTIR spectrum of ODD-H, the broad band at ≈3440 cm^{-1} corresponds to the O–H stretching mode (absorbed water in KBr salt). The most intense vibration bands appear in: 3200–2700 cm^{-1} (C–H stretching), 1650–1450 (C–C stretching), and 800–650 (out-of-plane C–H bending of aromatic rings). Overtone bands of benzene rings are

also visible (1990–1650 cm^{-1}). The vibrations coming from the cyclopentene unit can be spotted in the 1620–1450 cm^{-1} region.[38]

In the FTIR spectra of DD-MoS_2, O–H and C–H stretching modes also appear. Probably, the O–H vibration is due to absorbed water in KBr powder and/or the presence of MeOH residues, the last solvent employed in the purification sequence of DD-MoS_2. Because of the prominent intensity of DD bands in functionalized MoS_2, it is difficult to unambiguously identify the Mo–S stretching at ≈470 cm^{-1}. The weak C–S stretching expected for both thiophene and the new bond derived from covalent functionalization was not clearly visible in the 715–630 cm^{-1} region.[39] However, the lack of bands associated to aryl diazo groups in the 2309–2136 cm^{-1} range[40] could be consistent with the attachment of DD to MoS_2 sheets. Moreover, the detection of a tenuous vibration band at ≈816–813 cm^{-1}, ascribable to the out-of-plane C-H bending in 1,4-disubstituted benzenes,[41,42] provides additional evidence of covalent functionalization as the grafting process adds a new functionality to both benzene rings in *para* position. Regretfully, the low spectral resolution impedes to distinguish between the exclusive vibrational modes of ODD-MoS_2 and those of CDD-MoS_2.

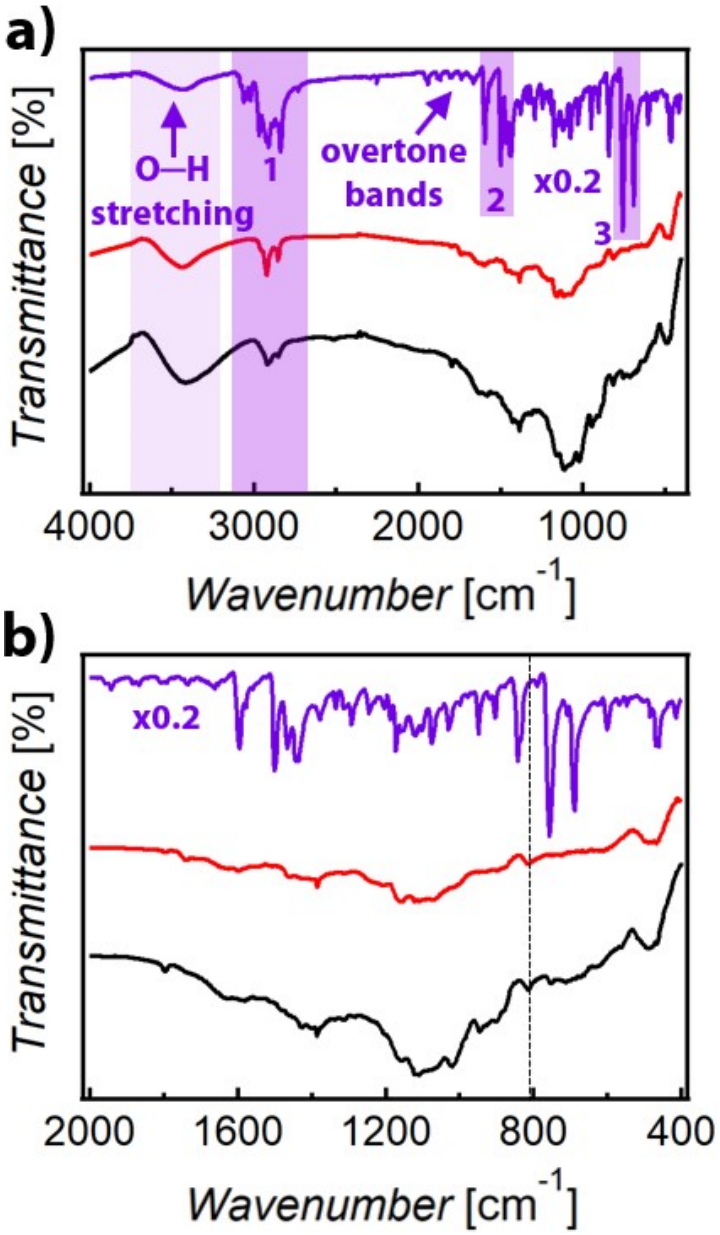

Figure IV-6. a) FTIR spectra of ODD-MoS_2 (black), and CDD-MoS_2 (red), and ODD-H (purple). Spectral regions labelled as 1, 2, and 3 correspond to C–H stretching, C–C stretching, and out-of-plane C–H bending of aromatic rings; b) Zoomed FTIR spectra shown in "a)". The dashed line represents the out-of-plane C-H bending in 1,4-disubstituted benzenes. All the samples were measured by means of the KBr pellet approach.

PXRD

The PXRD patterns of DD-MoS_2 materials perfectly resemble that of restacked MoS_2 sheets, where broadened (00*l*) and (10*l*) peaks indicate a decrease in the number of layers along the *c*-axis (see **Figure IV-7**).[43] The most intense (002) peak appears at ≈14.3º in both restacked MoS_2 and DD-MoS_2. The no detection of shifted (00l) peaks to lower 2θ values indicates that the separation between adjacent MoS_2 layers seems to remain unaffected after functionalization.

This result could mean that the length (or volume) of the intermolecular (or intramolecular) bridging linkage is not enough to expand the distance between adjacent MoS_2 layers in presence (or absence) of cross-linking. In the work about MoS_2 cross-linking by C. N. S. Rao, the assembly of flakes was done by using more rigid linkages.[27] In that case, the disappearance of XRD peaks of MoS_2 and the appearance of broad reflections at low 2θ values were taken as a proof of cross-linking, signatures that are not patent in our diffractograms.

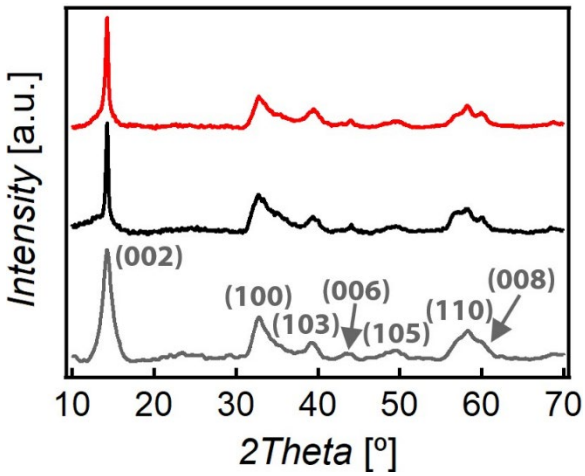

Figure IV-7. Normalized PXRD patterns of restacked ce-MoS_2 flakes (grey), ODD-MoS_2 (black), and CDD-MoS_2 (red).

XPS

To get useful information about the formation of the covalent C–S bond as well as the 1T/2H ratio in functionalized MoS_2, DD-MoS_2 samples were analysed by XPS (see **Figure IV-8**). The Mo 3d spectrum of ODD-MoS_2 (**Figure IV-8a**) is composed of seven peaks located at 226.2, 228.8, 229.9, 231.0, 232.0 233.0, and 234.3 eV, which

correspond to S^{-II} 2s, Mo^{IV} (2H-MoS_2) $3d_{5/2}$, Mo^{IV} (MoO_2) $3d_{5/2}$, Mo^{V} $3d_{5/2}$, Mo^{IV} (2H-MoS_2) $3d_{3/2}$, Mo^{IV} (MoO_2) $3d_{3/2}$, and Mo^{V} $3d_{3/2}$, respectively.[44–47] Remarkedly, XPS peaks coming from 1T-MoS_2 are missing over the entire spectral region. This absence strongly suggests that the typical 1T-MoS_2 flakes generated by using *n*-BuLi are totally transformed into the most thermodynamically stable 2H polytype.

These results are in stark contrast to those obtained by C. Backes and co-workers, who demonstrated that ce-MoS_2 covalently functionalized *via* the diazonium salt strategy kept its 1T nature but with unusual emerging semiconducting properties.[31] The fact of preparing *in situ* the diazonium salt and using other experimental conditions (and/or perhaps the covalent functionalization itself) may induce some structural changes. The Mo 3d spectrum of CDD-MoS_2 strongly matches with that of ODD-MoS_2 (see **Figure IV-8a**). Respect to the total Mo amount, ≈73.6 and 71.4% is present as 2H-MoS_2 in ODD-MoS_2 and CDD-MoS_2, respectively. In both cases, the remaining percentage corresponds to oxidized Mo.

The S 2p spectrum of ODD-NH_2 (**Figure IV-8b**) is dominated by two peaks located at 163.7 and 164.9 eV, which correspond to S^{-II} $2p_{3/2}$ and S^{-II} $2p_{1/2}$, respectively.[48] Both contributions arise from the sulphur belonging to thiophene rings. The S 2p spectra of ODD-MoS_2 and CDD-MoS_2 (**Figure IV-8b**) display six peaks at ≈161.2, 161.8, 162.1, 162.9, 163.7, and 164.9 eV, which correspond to S^{-I} $2p_{3/2}$, S^{-II} (MoS_2) $2p_{3/2}$, S^{-I} $2p_{1/2}$, S^{-II} (MoS_2) $2p_{1/2}$, S^{-II} (S-C) $2p_{3/2}$, and S^{-II} (S-C) $2p_{1/2}$ components, respectively. In DD-MoS_2, S-C contributions encompass S–C bonds coming from MoS_2 functionalization as well as thiophene rings. Consistently, the peaks dubbed as S-C are wider (FWHM of ≈1.5 eV) than those assigned to thiophene in ODD-NH_2 (FWHM ≈1.1 eV).

The N 1s spectrum of ODD-NH_2 (**Figure IV-8c**) uniquely shows a peak at ≈399.4 eV, whose origin is ascribed to terminal amino groups. Unlike DD-NH_2, DD-MoS_2 does not reveal clear N signals in the N 1s region but Mo $3p_{3/2}$ peaks, which would discard the presence of *i*) starting amino compounds, *ii*) nitrite residues, *iii*) diazonium salts, and *iv*) nitrogen-containing by-products, like azo compounds.

Therefore, for DD-MoS_2, the absence of significant N peaks and the detection of wider S-C signals prove the efficacy of diazo moieties as leaving groups and the attachment of DD backbone to ce-MoS_2 flakes.

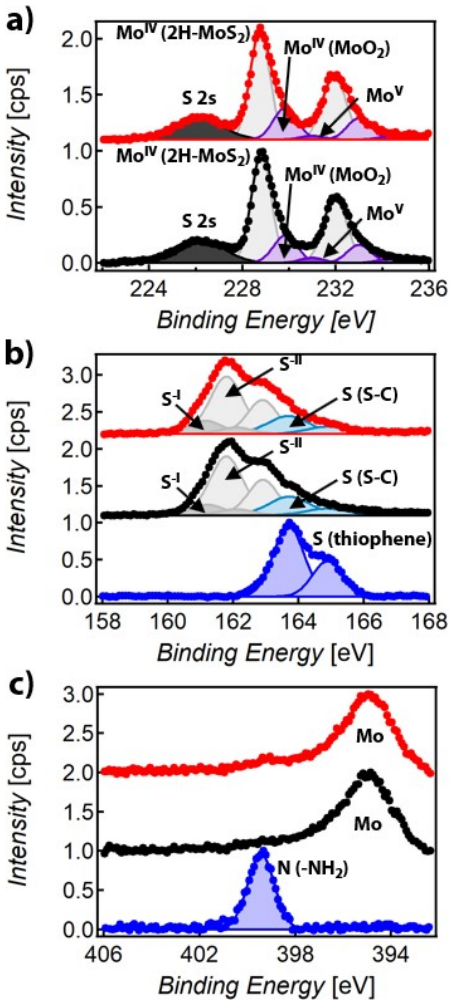

Figure IV-8. a) Normalized Mo 3d spectra of ODD-MoS_2 (black) and CDD-MoS_2 (red); b) Normalized S 2p spectra of ODD-NH_2 (blue), ODD-MoS_2 (black), and CDD-MoS_2 (red); c) Normalized N 1s spectra of ODD-NH_2 (blue), ODD-MoS_2 (black), CDD-MoS_2 (red). Each XPS spectrum is normalized respect to the highest value registered in its envelope.

For better clarity, XPS values observed in ODD-MoS_2, CDD-MoS_2, and ODD-NH_2 have been collected in **Table IV-1**.

Table IV-1 XPS values observed in ODD-MoS_2, CDD-MoS_2, and ODD-NH_2.

Material	Mo XPS signals	S XPS signals	N XPS signals
ODD-MoS_2	≈228.8 eV Mo^{IV} $3d_{5/2}$ (2H-MoS_2)	≈161.2 eV S^{-I} $2p_{3/2}$	
	≈232.0 eV Mo^{IV} $3d_{3/2}$ (2H-MoS_2)	≈162.1 eV S^{-I} $2p_{1/2}$	
	≈229.9 eV Mo^{IV} $3d_{5/2}$ (MoO_2)	≈161.8 eV S^{-II} $2p_{3/2}$ (MoS_2)	
	≈233.0 eV Mo^{IV} $3d_{3/2}$ (MoO_2)	≈162.9 eV S^{-II} $2p_{1/2}$ (MoS_2)	Ø
	≈231.0 eV Mo^{V} $3d_{5/2}$	≈163.7 eV S^{-II} $2p_{3/2}$ (S-C)	
	≈234.3 eV Mo^{V} $3d_{3/2}$	≈164.9 eV S^{-II} $2p_{1/2}$ (S-C)	
		≈226.2 eV S 2s	
CDD-MoS_2	≈228.8 eV Mo^{IV} $3d_{5/2}$ (2H-MoS_2)	≈161.2 eV S^{-I} $2p_{3/2}$	
	≈232.0 eV Mo^{IV} $3d_{3/2}$ (2H-MoS_2)	≈162.1 eV S^{-I} $2p_{1/2}$	
	≈229.9 eV Mo^{IV} $3d_{5/2}$ (MoO_2)	≈161.8 eV S^{-II} $2p_{3/2}$ (MoS_2)	
	≈233.0 eV Mo^{IV} $3d_{3/2}$ (MoO_2)	≈162.9 eV S^{-II} $2p_{1/2}$ (MoS_2)	Ø
	≈231.0 eV Mo^{V} $3d_{5/2}$	≈163.7 eV S^{-II} $2p_{3/2}$ (S-C)	
	≈234.3 eV Mo^{V} $3d_{3/2}$	≈164.9 eV S^{-II} $2p_{1/2}$ (S-C)	
		≈226.2 eV S 2s	
ODD-NH_2	Ø	≈163.7 eV S^{-II} $2p_{3/2}$	≈399.4 eV(N 1s)
		≈164.9 eV S^{-II} $2p_{1/2}$	

Raman spectroscopy

Raman spectroscopy was performed in order to double-check the 2H nature of MoS_2 in DD-MoS_2 (previously demonstrated by XPS results) and track the structure-sensitive bands characteristic of open and closed forms in DD-MoS_2, in the absence of conclusive UV/Vis data (featureless spectra).

First, bare DD-H was subjected to Raman spectroscopy (see **Figure IV-9)**. ODD-H, previously introduced in the FTIR section, was used for obtaining the corresponding closed system (CDD-H). Clear differences in Raman modes were spotted when using the 785-nm near-infrared (NIR) laser. The obtained values are comparable to those reported in literature.[38] Due to its closed structure (lower number of degrees of freedom), CDD-H displays less vibration bands than ODD-H. For other excitation wavelengths (638 and 532 nm), the emergence of PL, particularly accentuated for CDD-H, reduces the possibility of detecting other signatures in Raman spectra.

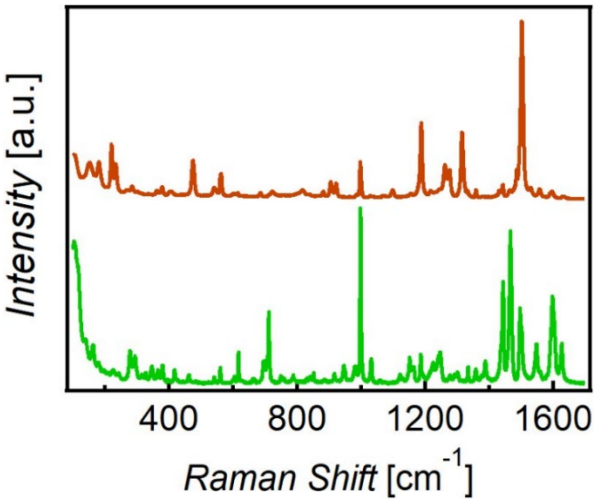

Figure IV-9. Normalized Raman spectra of ODD-H (green) and CDD-H (brown) at 785 nm wavelength.

Then, DD-MoS_2 powders were analysed at 785, 638, and 532 nm. Strikingly, the most evident differences between both Raman spectra were registered when using the laser of 532 nm. For the excitation wavelength of 785 nm, the signals of the organic moiety were not well resolved. For the excitation wavelength of 638 nm, a poor contrast between the Raman fingerprints of each form was appreciated.

Consistently, the Raman spectra of both systems (**Figure IV-10**) show coexistence of MoS_2 and DD signals. Whilst features appearing at ≈379 and 405 cm^{-1} correspond to MoS_2 (E^1_{2g} and A_{1g} modes, respectively), those located in the 1100–1700 cm^{-1} range are assigned to DD. No J peaks (characteristic of 1T-MoS_2) were detected. The signals observed in the 1100–1700 cm^{-1} region are different from those spotted for pure DD-H molecules since *i*) the aromatic ring breathing bands are sensitive to substitution,[38] and *ii*) the attachment of the photochromic system to MoS_2 most likely reduces the degrees of freedom of the organic backbone.

Interestingly, some of the bands related to DD are sensitive to the molecular structure. The spectrum of ODD-MoS_2 reveals bands at ≈1151, 1206, 1419, 1461, 1539, and 1613 cm^{-1}. The spectrum of CDD-MoS_2 shows bands at ≈1154, 1206, 1425, 1547, and 1614 cm^{-1}. Apart from certain differences in terms of relative intensity, it appears

that the band at ≈1425 cm^{-1} registered for CDD-MoS_2 is split up into two new bands at ≈1419 and 1461 cm^{-1} in the case of ODD-MoS_2.

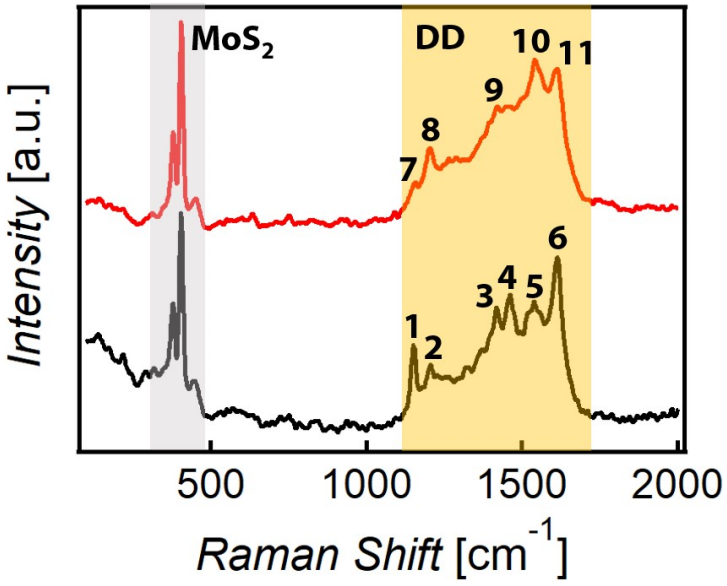

Figure IV-10. Normalized Raman spectra of ODD-MoS_2 (black) and CDD-MoS_2 (red) at 532 nm wavelength. For ODD-MoS_2, vibration bands appear at ≈1151 (1), 1206 (2), 1419 (3), 1461 (4), 1539 (5), and 1613 cm^{-1} (6). For CDD-MoS_2, vibration bands are located at ≈1154 (7), 1206 (8), 1425 (9), 1547 (10), and 1614 cm^{-1} (11).

The PL of DD-MoS_2 exhibits two characteristic bands of the 2H phase, at ≈1.79 and 1.95 eV (see **Figure IV-11**), whose origin is ascribed to A1 and B1 excitonic transitions, respectively.

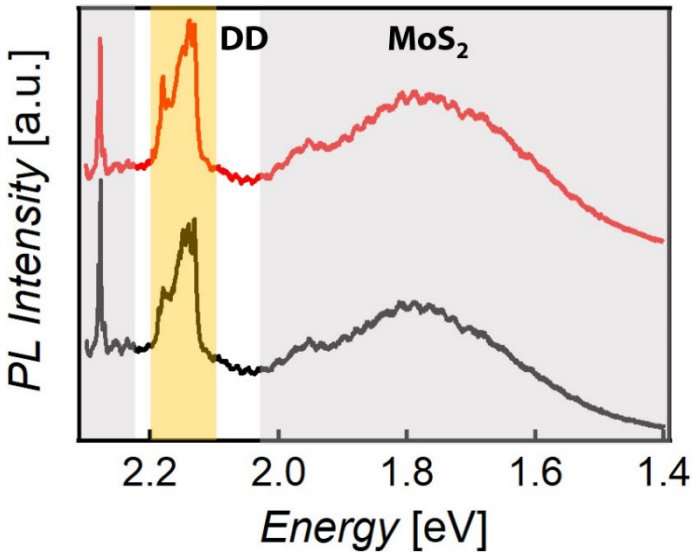

Figure IV-11. PL spectra of ODD-MoS_2 (black) and CDD-MoS_2 (red) at 532 nm wavelength.

Overall, the presence of PL, along with the no detection of the so-called J peaks, corroborates the 2H nature of the MoS_2 present in DD-MoS_2.

TGA

Finally, ce-MoS_2, DD-H, and DD-MoS_2 were characterized by TGA. According to TGA plots corresponding to DD-H (**Figure IV-12**), all the mass is lost at a temperature close to 350 ºC. Curiously, the TGA of ODD-H shows two mass drops. In this case, the first mass drop at ≈81 ºC corresponds to the removal of acetonitrile molecules from the crystalline structure since this solvent was precisely the one used for the recrystallization of ODD-H.

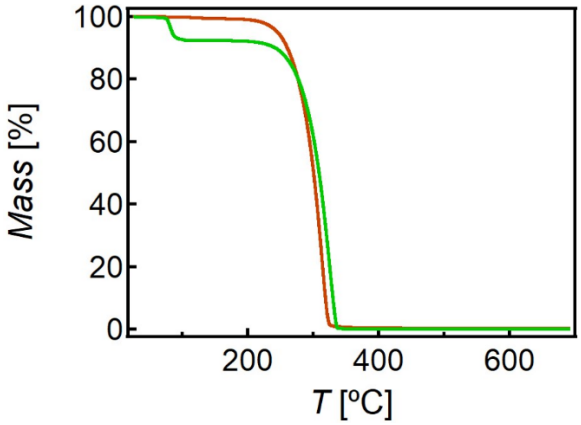

Figure IV-12. TGA plots of ODD-H (green) and CDD-H (brown).

For ODD-MoS_2 (see **Figure IV-13a** and **Figure IV-14**), a mass drop of ≈2.8% was detected in the 25–140 ºC range, which would correspond to the loss of physisorbed solvent molecules. Next, a mass drop of ≈6.1% and another one of ≈21.3% were registered in 140–325 and 325–700 ºC ranges, respectively. The functionalization percentage was calculated by assuming that all the mass lost in the 140–700 ºC interval arouse from the removal of ODD covalently grafted to the 2D material except for a little contribution (≈3.1%) corresponding to the degradation of S from MoS_2 (see Chapter V). Thus, considering that, a functionalization percentage of ≈24.3% was calculated.

For CDD-MoS_2 (see **Figure IV-13b** and **Figure IV-14**), a mass drop of ≈5.0% was detected in the 25–140 ºC range, which would be related to the loss of physisorbed solvent molecules. Next, a mass drop of ≈7.4% and another one of ≈14.5% were clearly detected in 140–325 and 325–700 ºC ranges, respectively. In this case, the obtained functionalization percentage was of ≈18.8%.

The functionalization yield for both samples is comparable.

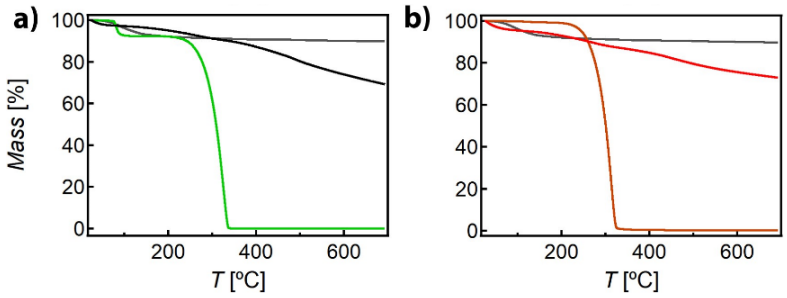

Figure IV-13. a) TGA plots of ODD-H (green), ODD-MoS_2 (black), and ce-MoS_2 flakes (grey). b) TGA plots of CDD-H (brown), CDD-MoS_2 (red) and ce-MoS_2 (grey).

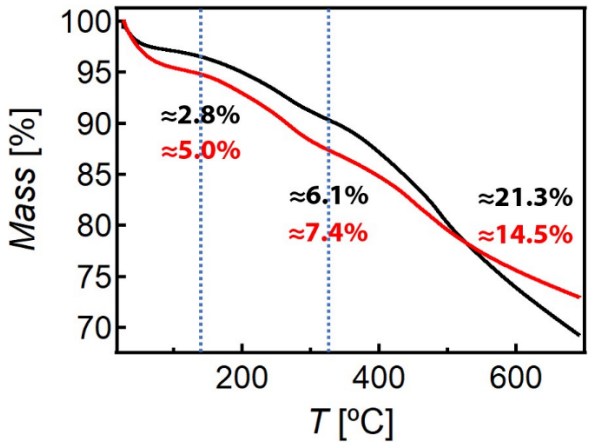

Figure IV-14. TGA plots of ODD-MoS_2 (black) and CDD-MoS_2 (red).

IV.2.4. Interconversion study

Once proved the covalent grafting and calculated the functionalization percentages, several samples of different nature were irradiated in solid and analysed by Raman spectroscopy, in order to know if the photoswitching capacity of DD was kept after its grafting to MoS_2.

This technique is more material-saving and material-friendly than, for example, UV/Vis spectroscopy in solid, where it is convenient to dilute the sample in KBr powder in order to avoid the signal saturation caused by the strong absorption of MoS_2.

First, DD-H molecules were studied to gain more insight into the most suitable irradiation conditions to be applied for the functionalized

MoS_2 since photoconversion of solid samples is not straightforward. DD-H molecules were dissolved in MeOH and deposited onto clean SiO_2 (285nm)/Si substrates by drop casting. Whilst two substrates containing ODD-H (one per experiment) were irradiated at 308 nm for 10 min and 1 h, a pair of substrates containing CDD-H (one per experiment) were irradiated at >540 nm for 1 h and 1 day. At this point, it is important to comment that longer irradiation times are required for triggering the CDD-H→ODD-H photoconversion because this process is slower than the reverse one. Next, the interconversion extent was evaluated by Raman spectroscopy at 785 nm (see **Figure IV-15**).

Raman results concerning ODD-H highlight that *i*) 10 min of irradiation are enough to induce a quantitative ODD-H→CDD-H transformation and *ii*) the CDD-H photogenerated in 10 min of light exposure shows no degradation features if the irradiation process is extended by 50 min (see **Figure IV-15a**). On the other hand, in relation to the samples prepared with CDD-H, the Raman bands characteristic of the closed structure underwent attenuation and changes in terms of relative intensity, followed by vanishment when enlarging the irradiation frame from 1 h to 1 day (see **Figure IV-15b**). Thus, in the latter case, the lack of signal strongly suggests photodegradation. Regretfully, no conclusive information about the minimum time required for inducing the CDD-H→ODD-H conversion without photodegradation could be extracted from the experiments realized with CDD-H. For the sake of clarity, in **Figure IV-15**, Raman spectra are zoomed in the 1200–1700 cm^{-1} region.

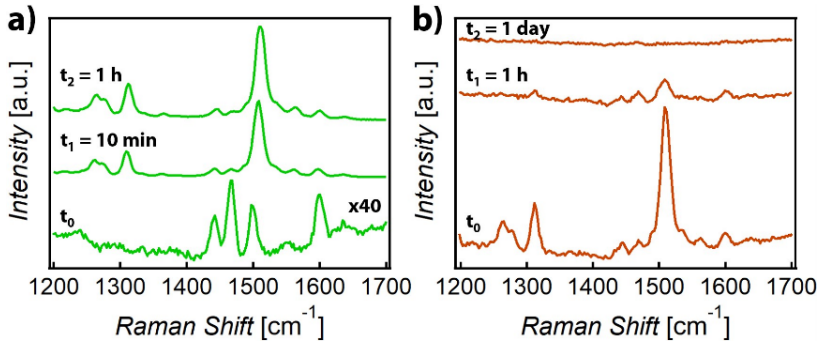

Figure IV-15. Raman spectra of a) ODD-H and b) CDD-H measured at 785 nm excitation wavelength before and after irradiation experiments.

Next, physical mixtures (denoted as DD-H+MoS_2) lacking chemical interactions between both components were studied by Raman as well. For this purpose, DD-H+MoS_2 mixtures, with a DD-H:MoS_2 molar ratio (of ≈0.1) similar to that used during the functionalization of ce-MoS_2 flakes, were dissolved/dispersed in MeOH and deposited onto clean SiO_2 (285nm)/Si substrates by drop casting.

Whilst one substrate containing ODD-H+MoS_2 was irradiated at 308 nm for 30 min, another one containing CDD-H+MoS_2 was irradiated at >540 nm for 12 h. Irradiation times were defined according to the previous Raman measurements of DD-H (see **Figure IV-15**). It was decided to use irradiation times between those fixed for first and second irradiation experiments concerning DD-H (t_1 and t_2, respectively) in order to *i*) reduce the duration of the experiments and *ii*) open a door to a new scenario in between the beginning of a possible change (at t_1) and the loss of signal (at t_2) for the ODD-H+MoS_2 sample.

The interconversion extent was analysed by Raman spectroscopy at 532 nm (see **Figure IV-16**). The PL of DD-H, particularly accentuated in the CDD-H+MoS_2 mixture, impeded to clearly recognize all the bands corresponding to the organic moiety. The possibility of having a significant PL contribution from ce-MoS_2 was completely discarded on the basis of its metallic nature (1T phase). Apart from that, in ODD-H+MoS_2, the PL bands were centred at ≈1.81 and 2.13 eV, in contrast to what observed in DD-MoS_2 (≈1.79 and 1.95 eV) and heated ce-MoS_2 flakes (see Chapter V), and the PL was even more intense than

the typically obtained from 2H-MoS_2 few-layers. Noteworthy, no changes were appreciated after irradiation.

Raman results of DD-H+MoS_2 at zero time (t_0) are in contrast with those previously obtained from DD-MoS_2 (see **Figure IV-11**), where PL did not overlap with other signals. Likely, the more uniform distribution of DD onto the chalcogenide surface expected for DD-MoS_2 and/or the covalent functionalization itself quenches the PL of the molecular unit, when using the laser of 532 nm, as opposed to what occurs with pure photochromic molecules.

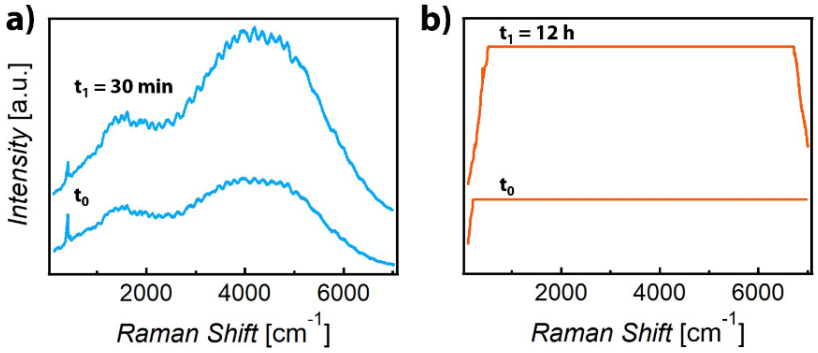

Figure IV-16. Raman spectra of a) ODD-H+MoS_2 and b) CDD-H+MoS_2 measured at 532 nm excitation before and after irradiation experiments. The plateaus registered for CDD+MoS_2 indicates saturation of PL signal.

Finally, irradiation experiments were applied to DD-MoS_2. DD-MoS_2 materials were first dispersed in DMSO and then centrifuged in order to remove DMSO. The idea was to break the aggregation of functionalized flakes and then replace DMSO by a solvent with a lower boiling point in order to accelerate the final drying process. Thus, the sediment of DD-MoS_2 was suspended in MeOH, deposited onto a couple of clean SiO_2 (285nm)/Si substrates by drop casting and finally irradiated at 308 and >540 nm for 1 day.

Raman measurements at 532 nm (see **Figure IV-17**) served to discard photo-induced changes because of both photoconversion and degradation. These results seem to prove that, once linked to the S atom of MoS_2, there is a charge transfer between the organic moiety and the TMDC, leading to a PL quenching coming from the DD backbone. For the sake of clarity, in **Figure IV-17**, Raman spectra are zoomed in the 1100–1700 cm^{-1} region.

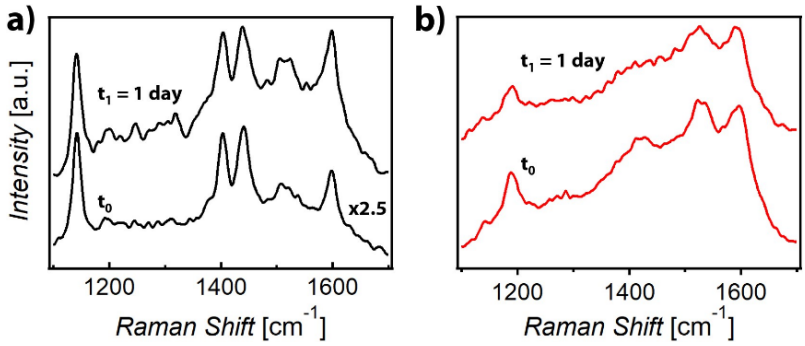

Figure IV-17. Raman spectra of a) ODD-MoS_2 and b) CDD-MoS_2 measured at 532 nm excitation before and after irradiation experiments.

From the photoconversion experiments, we extracted the following information:

- DD-H. The ODD-H→CDD-H transformation in solid takes (at most) 10 min. By contrast, the CDD-H→ODD-H transformation was not achieved/detected under the used experimental conditions. In the latter case, the registered changes (attenuation and loss of signal) cannot be related to a quantitative formation of ODD-H and an optimization of the irradiation time is required. To reach this goal, it would be interesting to work in the 1 h–1 day window.

- DD-H+MoS_2. The PL observed in physical mixtures arises from the organic molecules and hampers the identification of MoS_2 features. For the DD-H+MoS_2 system, there is a signal saturation. For none of the studied physical mixtures, photoconversion was appreciated.

- DD-MoS_2. For none of DD-MoS_2 samples, the photoswitching capacity was demonstrated (not even after 1 day of irradiation). In comparison to the results obtained from the physical mixture, it appears that there is a PL quenching in functionalized samples. Probably, the low {organic molecule/MoS_2} molar ratio makes this study more difficult.

IV.3. Conclusions

In this Chapter, we have prepared a photochromic dithienylethene derivative (DD-NH_2) under its open and closed forms (ODD-NH_2 and ODD-NH_2, respectively). Then, we have achieved the covalent functionalization of ce-MoS_2 flakes by means of the diazotization of the photochromic molecule.

The covalent functionalization has been proved by different characterization techniques. On one hand, the detection of a vibration band at ≈816–813 cm^{-1} (characteristic of 1,4-disubstituted benzenes) in the FTIR spectrum of DD-MoS_2, along with the absence of N XPS signals, gives indirect evidence of the formation of new C-S bonds. On the other hand, XPS and Raman spectra reveal coexistence of MoS_2 and DD signals. Remarkably, the XPS signals associated to C-S are wider than those typical of the starting amino compound (ODD-NH_2), suggesting that there is a new C-S contribution, in addition to that of thiophene rings.

Interestingly, XPS and Raman measurements highlight that the prominent 1T polytype expected for ce-MoS_2 flakes is quantitatively transformed into the 2H one, as a result of the functionalization. Concerning the Raman study, this was deduced from the absence of J peaks and the appearance of MoS_2 PL (A1 and B1 excitons).

Significant differences were appreciated in the Raman spectra of ODD-MoS_2 and CDD-MoS_2 on the basis of the structure of the organic backbone.

The functionalization percentage of DD-MoS_2 was calculated from the TGA plots by assuming that all the mass lost in the 140–700 ºC interval arouse from the removal of DD covalently grafted to the 2D material except for a little contribution (≈3.1%) corresponding to the degradation of S from ce-MoS_2.

The PL quenching observed when moving from physical mixtures to functionalized samples could be related to the functionalization itself and/or the fact of achieving a more homogeneous distribution of DD onto MoS_2 surface by means of this chemical approach, which would lead to a charge transfer between both interacting components.

The origin of the PL associated to physical mixtures was ascribed to the organic molecule. The contribution of ce-MoS_2 flakes to PL was discarded according to the metallic nature of ce-MoS_2 flakes. Not even assuming that the grinding process in the mortar can result in a 1T→2H transformation, the obtained results do not support this transition since the PL detected in these mixtures is more intense than that registered for few-layers of 2H-MoS_2, partially or completely masking MoS_2 features.

Once proved the covalent functionalization, we performed several irradiation experiments in order to check the photoswitching capacity of the organic system once attached to the 2D material.

Regretfully, the photoswitching capacity of the organic molecule post functionalization could not be proved under the used experimental conditions, being this the reason why we decided not to start the transport measurements. The idea of this study was to check if CDD-MoS_2 was more conductive than ODD-MoS_2, as expected due to the electron delocalization over the entire molecule characteristic of the closed form.

As a short-term work, we would like to analyse DD-MoS_2 by electrochemistry because maybe this way is more effective when tracking the photoswitching process.

Albeit that the formation of a network of 2D MoS_2 flakes cross-linked by photoresponsive molecules was not reached, we are conscious of the complexity/difficulty of this project. Once controlled, the functionalization could also be carried out by employing other photochromic molecules (like azobenzenes) or molecular wires as linkers, leading to study how the length and nature of the bridge molecule affect the conductivity of the resultant material.

Thus, another appealing approach would arise from the possibility of doing the same chemistry on surface, using for such effect ce-MoS_2 flakes deposited onto clean substrates. In this case, it could be worthy to try the non-covalent functionalization with flakes lacking excess of negative charge (*i.e.*, me-MoS_2) and analyse the doping effect in PL and/or conductivity terms. The conductivity of the functionalized material resulting from these experiments could be measured onto substrates containing prepatterned Au electrodes.

IV.4. Experimental section

IV.4.1. Materials

Sodium nitrite ($NaNO_2$) and hydrochloric acid (37%) were purchased from Sigma-Aldrich and Scharlau, respectively. Solvents were used without further purification. Milli-Q water was used in all the experiments.

IV.4.2. Methods

IV.4.2.1. Intercalation/chemical exfoliation of MoS_2

See **Methods** in Chapter II.

IV.4.2.2. Synthesis of ODD-H, CDD-H, ODD-NH_2, CDD-NH_2

All these molecules were prepared by J. M. Carbonell-Vilar under the supervision of Dr. M. Viciano-Chumillas, from Instituto de Ciencia Molecular (ICMol), Universitat de València.

IV.4.2.3. Synthesis of ODD-H+MoS_2

To prepare ODD-H+MoS_2 with a ODD-H:MoS_2 molar ratio of ≈0.1, 7.2 mg of ce-MoS_2 flakes and 2.3 mg of ODD-H were mixed and grinded in a mortar.

IV.4.2.4. Synthesis of CDD-H+MoS_2

To prepare CDD-H+MoS_2 with a CDD-H:MoS_2 molar ratio of ≈0.1, 7.4 mg of ce-MoS_2 flakes and 2.2 mg of CDD-H were mixed and grinded in a mortar.

IV.4.2.5. Synthesis of ODD-MoS_2

ODD-NH_2 (12.30 mg, 0.028 mmol) was introduced into an argon-filled round-bottom flask. Subsequently, sodium nitrite (5.77 mg, 0.084 mmol) and HCl 6M (511 μL) were poured into the reaction system at 0 ºC (ice bath), under a constant flow of argon and magnetic stirring. The resultant mixture was kept under stirring for 1 h until the suspension of ce-MoS_2 flakes (the volume corresponding to 0.28 mmol) was added. It was allowed to react at room temperature for 24 h. After that, the obtained mixture was filtered by using a nylon

membrane. Next, the solid collected on the filter was washed with ultrapure (Milli-Q) water, DMSO, and MeOH. Finally, the purified solid was vacuum-dried for at least 14 h in the darkness.

IV.4.2.6. Synthesis of CDD-MoS_2

In order to form CDD-NH_2, ODD-NH_2 (12.30 mg, 0.028 mmol) was first dissolved in 40 mL of MeOH and then subjected to UV irradiation (by means of UVA lamps centred at 350 nm) in a photoreactor for 15 min, under magnetic stirring. Next, the solution was rota-evaporated to yield solid CDD-NH_2. Finally, the protocol described for the synthesis of ODD-MoS_2 was followed.

IV.4.3. Characterization techniques

FTIR spectroscopy
See the FTIR section in Chapter II.

Photoirradiation experiments
All the photoirradiation experiments were performed inside a commercial photoreactor (LuzChem LZC-4V). To irradiate ODD-H, ODD-H+MoS_2, and ODD-MoS_2, 14 UVB (308 nm) lamps were used. To irradiate ODD-NH_2, 14 UVA FL8BL-B (350 nm) lamps were used. To irradiate CDD-H, CDD-H+MoS_2, and CDD-MoS_2, 12 Sylvania Cool White F8T5 (visible) lamps with LuzChem orange filters (>540 nm) were used.

PXRD

See the PXRD section in Chapter II. Samples were filled into 0.5 mm diameter borosilicate glass Three repeated measurements were collected in the 2–90° range with a step size of 0.017° (at room temperature) and merged in a single diffractogram.

Raman spectroscopy

Raman spectra were recorded with a Raman Emission Horiba-MTB Xplora Spectrometer in ambient conditions onto a clean SiO_2 (285 nm)/Si substrate by using lasers of different excitation wavelength (785 and 532 nm). A 100x objective was used to focus the laser beam. Whilst DD-H molecules were measured at 785 nm, DD-H+MoS_2 and DD-MoS_2 materials at 532 nm. All samples were placed onto clean SiO_2 (285 nm)/Si substrates in order to use the Si peak as reference. For irradiation experiments in solid, samples were deposited by drop casting.

TGA

TGA was conducted by using TA TGA550 and Mettler Toledo TGA/SDTA851/1100/SF apparatus in the 25–700 °C range under a 10 °C min^{-1} scan rate and N_2 flow of 100 mL min^{-1}.

UV/Vis spectroscopy

See the UV/Vis spectroscopy section in Chapter II.

XPS

See the XPS section in Chapter II. XPS spectra were deconvoluted by using Origin program.

IV.5. References

1. Orgiu, E. & Samorì, P. 25th Anniversary Article: Organic Electronics Marries Photochromism: Generation of Multifunctional Interfaces, Materials, and Devices. *Adv. Mater.* **26**, 1827–1845 (2014).

2. Nakatani K., Piard J., Yu P. & Métivier R. Introduction: Organic Photochromic Molecules in *Photochromic Materials: Preparation, Properties and Applications* (Eds: H. Tian, J. Zhang), Germany: Wiley-VCH Verlag GmbH & Co. KGaA, 2016, 1–45.

3. Hirshberg, Y. Reversible Formation and Eradication of Colors by Irradiation at Low Temperatures. A Photochemical Memory Model. *J. Am. Chem. Soc.* **78**, 2304–2312 (1956).

4. Wald, G. The molecular basis of visual excitation. *Nature* **219**, 800–807 (1968).

5. Koumura, N., Zijistra, R. W. J., Van Delden, R. A., Harada, N. & Feringa, B. L. Light-driven monodirectional molecular rotor. *Nature* **401**, 152–155 (1999).

6. Wilcken, R. *et al.* Complete Mechanism of Hemithioindigo Motor Rotation. *J. Am. Chem. Soc.* **140**, 5311–5318 (2018).

7. Irie, M. Diarylethenes for Memories and Switches. *Chem. Rev.* **100**, 1685–1716 (2000).

8. Mallory, F. B. & Mallory, C. W. Photocyclization of Stilbenes and Related Molecules. *Org. React.* **30**, 1–456 (1984).

9. Irie, M. & Mohri, M. Thermally Irreversible Photochromic Systems. Reversible Photocyclization of Diarylethene Derivatives. *J. Org. Chem.* **53**, 803–808 (1988).

10. Pianowski, Z. L. Recent Implementations of Molecular Photoswitches into Smart Materials and Biological Systems. *Chem. Eur. J.* **25**, 5128–5144 (2019).

11. Irie, M., Fukaminato, T., Matsuda, K. & Kobatake, S. Photochromism of diarylethene molecules and crystals: Memories, switches, and actuators. *Chem. Rev.* **114**, 12174−12277 (2014).

12. Robertus, J., Photochromic molecular switches : based on azobenzenes, dithienylethenes and hemithioindigos. Thesis (PhD). University of Groningen, 2015.

13. Zhang, X., Hou, L. & Samorì, P. Coupling carbon nanomaterials with photochromic molecules for the generation of optically responsive materials. *Nat. Commun.* **7**, 11118 (2016).

14. Kobatake, S., Uchida, K., Tsuchida, E. & Irie, M. Single-crystalline photochromism of diarylethenes: reactivity-structure relationship. *Chem. Commun.* 2804-2805 (2002).

15. Zhao, Y., Ippolito, S. & Samorì, P. Functionalization of 2D Materials with Photosensitive Molecules: From Light-Responsive Hybrid Systems to Multifunctional Devices. *Adv. Opt. Mater.* **7**, 1900286 (2019).

16. Reecht, G., Lotze, C., Sysoiev, D., Huhn, T. & Franke, K. J. Visualizing the Role of Molecular Orbitals in Charge Transport through Individual Diarylethene Isomers. *ACS Nano* **10**, 10555–10562 (2016).

17. Van Der Molen, S. J. *et al.* Light-controlled conductance switching of ordered metal-molecule-metal devices. *Nano Lett.* **9**, 76 80 (2009).

18. Logtenberg, H. *et al.* Electrochemical switching of conductance with diarylethene-based redox-active polymers. *J. Phys. Chem. C* **116**, 24136–24142 (2012).

19. Jia, C. *et al.* Covalently bonded single-molecule junctions with stable and reversible photoswitched conductivity. *Science* **352**, 1443−1445 (2016).

20. Li, Y. *et al.* Self-assembly of graphene oxide with a silyl-appended spiropyran dye for rapid and sensitive colorimetric detection of fluoride ions. *Anal. Chem.* **85**, 11456−11463 (2013).

21. Li, J. *et al.* Tuning the optical emission of MoS_2 nanosheets using proximal photoswitchable azobenzene molecules. *Appl. Phys. Lett.* **205**, 241116 (2014).

22. Kim, D. *et al.* Reversible switching phenomenon in diarylethene molecular devices with reduced graphene oxide electrodes on flexible substrates. *Adv. Funct. Mater.* **25**, 5918–5923 (2015).

23. Liu, Z. *et al.* Photoswitchable Micro-Supercapacitor Based on a Diarylethene-Graphene Composite Film. *J. Am. Chem. Soc.* **139**, 9443−9446 (2017).

24. Gobbi, M. *et al.* Collective molecular switching in hybrid superlattices for light-modulated two-dimensional electronics. *Nat. Commun.* **9**, 2661 (2018).

25. Chen, X. *et al.* Ru^{II} Photosensitizer-Functionalized Two-Dimensional MoS_2 for Light-Driven Hydrogen Evolution. *Chem. Eur. J.* **24**, 351–355 (2018).

26. McAdams, S. G. *et al.* Dual Functionalization of Liquid-Exfoliated Semiconducting 2H-MoS_2 with Lanthanide Complexes Bearing Magnetic and Luminescence Properties. *Adv. Funct. Mater.* **27**, 1703646 (2017).

27. Pramoda, K., Gupta, U., Ahmad, I., Kumar, R. & Rao, C. N. R. Assemblies of covalently cross-linked nanosheets of MoS_2 and of MoS_2-RGO: Synthesis and novel properties. *J. Mater. Chem. A* **4**, 8989–8994 (2016).

28. Rao, C. N. R., Pramoda, K. & Kumar, R. Covalent cross-linking as a strategy to generate novel materials based on layered (2D) and other low D structures. *Chem. Commun.* **53**, 10093–10107 (2017).

29. Browne, W. R. *et al.* Oxidative electrochemical switching in dithienylcyclopentenes, part 1: Effect of electronic perturbation on the efficiency and direction of molecular switching. *Chem. Eur. J.* **11**, 6414–6429 (2005).

30. Eda, G. *et al.* Photoluminescence from chemically exfoliated MoS_2. *Nano Lett.* **11**, 5111–5116 (2011).

31. Knirsch, K. C. *et al.* Basal-Plane Functionalization of Chemically Exfoliated Molybdenum Disulfide by Diazonium Salts. *ACS Nano* **9**, 6018–30 (2015).

32. Paredes, J. I. *et al.* Impact of Covalent Functionalization on the Aqueous Processability, Catalytic Activity, and Biocompatibility of Chemically Exfoliated MoS_2 Nanosheets. *ACS Appl. Mater. Interfaces* **8**, 27974–27986 (2016).

33. Zhang, X. & Bell, J. P. Studies of arenediazonium salts as a new class of electropolymerization initiator. *J. Appl. Polym. Sci.* **73**, 2265–2272 (1999).

34. Blanch, A. J., Lenehan, C. E. & Quinton, J. S. Dispersant effects in the selective reaction of aryl diazonium salts with single-walled carbon nanotubes in aqueous solution. *J. Phys. Chem. C* **116**, 1709–1723 (2012).

35. Yu, S. *et al.* An azo-coupling reaction-based surface enhanced resonance Raman scattering approach for ultrasensitive detection of salbutamol. *RSC Adv.* **8**, 5536–5541 (2018).

36. Wilson, J. A. & Yoffe, A. D. The transition metal dichalcogenides discussion and interpretation of the observed optical, electrical and structural properties. *Adv. Phys.* **18**, 193–335 (1969).

37. Lucas, L. N., De Jong, J. J. D., Van Esch, J. H., Kellogg, R. M. & Feringa, B. L. Syntheses of dithienylcyclopentene optical molecular switches. *European J. Org. Chem.* 155–166 (2003).

38. De Jong, J. J. D. *et al.* Raman scattering and FT-IR spectroscopic studies on dithienylethene switches - Towards non-destructive optical readout. *Org. Biomol. Chem.* **4**, 2387–2392 (2006).

39. Coates, J. Interpretation of Infrared Spectra, A Practical Approach in *Encyclopedia of Analytical Chemistry*; Meyers, R. A., Ed.; U.K.: J. Wiley, 2000; 10821−10822.

40. Nakamoto, K., Infrared and Raman spectra of inorganic and coordination compounds, 4th ed., New York: John Wiley & Sons, 1986.

41. Roeges N.P.G., A Guide to the Complete Interpretation of Infrared Spectra of Organic Structures, U.K.: Wiley, 1994.

42. Xu, L. *et al.* Electrosynthesis and characterization of an electrochromic material from poly(1,4-bis(2-thienyl)-benzene) and its application in electrochromic devices. *Electrochim. Acta* **56**, 2815–2822 (2011).

43. Du, G. *et al.* Superior stability and high capacity of restacked molybdenum disulfide as anode material for lithium ion batteries. *Chem. Commun.* **46**, 1106–1108 (2010).

44. Han, X. *et al.* Hydrogen Evolution Reaction on Hybrid Catalysts of Vertical MoS_2 Nanosheets and Hydrogenated Graphene. *ACS Catal.* **8**, 1828–1836 (2018).

45. Choi, J. G. & Thompson, L. T. XPS study of as-prepared and reduced molybdenum oxides. *Appl. Surf. Sci.* **93**, 143–149 (1996).

46. Sun, Y., Hu, X., Luo, W. & Huang, Y. Ultrafine MoO_2 nanoparticles embedded in a carbon matrix as a high-capacity and long-life anode for lithium-ion batteries. *J. Mater. Chem.* **22**, 425–431 (2012).

47. Li, X. *et al.* Ternary hybrids as efficient bifunctional electrocatalysts derived from bimetallic metal-organic-frameworks for overall water splitting. *J. Mater. Chem. A* **6**, 5789–5796 (2018).

48. Li, O. L., Shi, Z., Lee, H. & Ishizaki, T. Enhanced Electrocatalytic Stability of Platinum Nanoparticles Supported on Sulfur-Doped Carbon using in-situ Solution Plasma. *Sci. Rep.* **9**, 12704 (2019).

V. WS_2/MoS_2 heterostructures through thermal treatment of MoS_2 layers electrostatically functionalized with W_3S_4 molecular clusters

V.1. Introduction

Nowadays, in addition to downsizing layered materials to the 2D limit and functionalizing the layers with molecular systems (as shown in Chapters II, III and IV), the scientific community endeavours to study and harness the novel properties and synergistic effects arising from the combination of different 2D components into advanced functional heterostructures.[1,2] These vdW heterostructures have found applications in different fields like (bio)sensing,[3] electronics,[4] optoelectronics,[4] and (photo)catalysis.[5]

In this context, isostructural WS_2 and MoS_2 in their thermodynamically stable 2H phase are robust under wet conditions, including acidic media,[6] and exhibit exceptional light-matter interactions, like photovoltaic properties.[7,8] Apart from possessing a hydrogen binding energy close to that of Pt-group,[9] computational studies appear to indicate that the valence band edges of WS_2 and MoS_2 monolayers straddle the water oxidation potential.[10,11] Interestingly, in WS_2/MoS_2 heterostructures, the energy band alignment existing at the interface of both materials not only promotes the electron hole dissociation but also extends the charge carrier lifetime, enhancing the diffusion length, which renders this kind of heterojunction appealing for optoelectronic and light harvesting applications.[12,13]

As an example of the relevance of these heterostructures, high-quality large-area WS_2/MoS_2 heterojunctions synthesized by CVD have evidenced a noteworthy photocatalytic performance for salt-water oxidation.[14] However, also WS_2/MoS_2 heterostructures prepared by a straightforward and low-cost liquid-phase method can oxidize water in acidic environment (without the need of using co-catalysts and protective layers), while increasing the incident-photon-to-current-efficiency by a factor of 10, in comparison to individual constituents.[15] Also in photoanodes based on WS_2/MoS_2 heterostructures prepared by wet methods, photocurrent density of the WS_2/MoS_2 sample turned out to be 8 and 4 times higher than those reported for pure WS_2 and MoS_2, respectively. This enhancement suggests an efficient charge separation inside the photoanode as well as a low interface resistance of the electrode-electrolyte.[16]

The different strategies addressed to prepare WS_2/MoS_2 and other 2D/2D heterostructures can be classified in two main groups: *i*) solid-state approaches (**Figure V-1**) and *ii*) wet methods. The former refers to the stacking of flakes obtained through dry mechanical exfoliation methods (deterministic transfer, show in **Figure V-1a**). Albeit this approach ensures the high quality of the stacked layers, it suffers from several issues: active implication by the operator, difficulty to scale-up the process, possibility of enclosing contamination between layers, lack of control when stacking the 2D components, and relatively weak interlayer coupling. Nevertheless, solid-state methods also refer to the sequential or simultaneous growth of both 2D components *via* CVD or PVD (**Figure V-1b**), overcoming the scalability problem to some extent and often creating high-quality heterojunctions (epitaxial growth) in virtue of the isostructural nature of the components (*e.g.*, WS_2 and MoS_2). However, high temperature and vacuum conditions contribute to increase the complexity of this process.

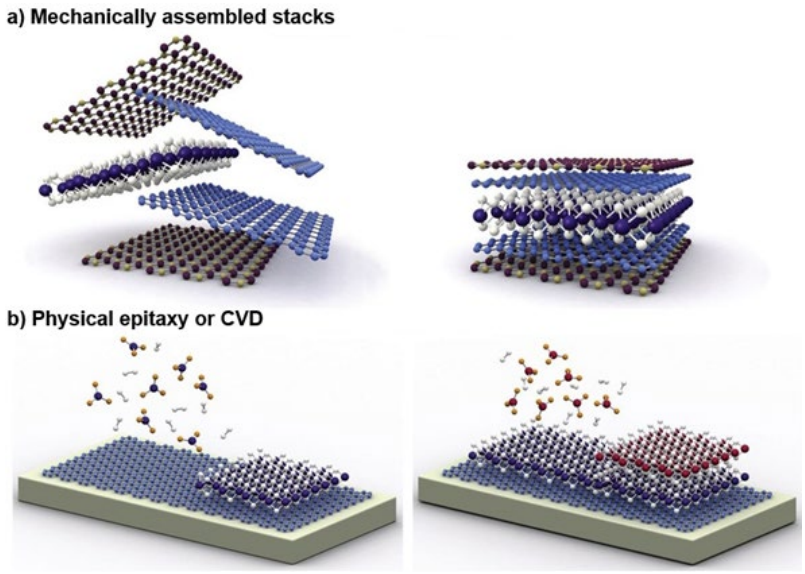

Figure V-1. Some examples of solid-state approaches for preparing vdW heterostructures. Extracted from ref. 2.

Alternatively, a simple and scalable option is the use of wet methods, like the electrostatic wet-chemical assembling of charged ultrathin layers[17] by means of layer by layer,[18] flocculation,[19,20] or

Langmuir-Blodgett techniques.[21] Nevertheless, these approaches have to face the uncontrolled organization of the flakes inside each slab of the final multilayer system and the fact that different species in solution can be occluded between the 2D components, hindering a good interaction between them.

Within the wet strategies, those involving chemical reactions are growing in popularity. Thus, 2D/2D heterostructures can also be prepared *via* hydrothermal growth of one 2D material on top of the other, or by decoration of one 2D component with a molecular system prone to undergo thermal decomposition into another 2D material. Some examples of this strategy are the hydrothermal growth of MoS_2 layers on WS_2 flakes[22] and the synthesis of WS_2 flakes on graphene by dry calcination.[23,24] The latter represents a unique way to guarantee the removal of residual organic molecules from the heterostructure, a clear advantage with respect to the hydrothermal approach.

Inspired by these methods, in this Chapter we present a new two-step strategy to form WS_2/MoS_2 heterojunctions (**Figure V-2**), which involves first the electrostatic functionalization of ce-MoS_2 layers with a tungsten cluster in methanol:water solution (herein referred as cluster@MoS_2) and second, a dry thermal treatment of this composite to form WS_2 flakes on the MoS_2 layers.

Figure V-2. Pictorial representation of WS_2/MoS_2 synthesis: i) Synthesis of cluster@MoS_2; ii) Calcination of cluster@MoS_2 to give rise to the final heterostructure formed by MoS_2 layers in between WS_2 flakes (WS_2/MoS_2).

The proposed method relies on the homogeneous distribution of the cluster over ce-MoS_2 layers thanks to the electrostatic interactions established between the cationic cluster and the anionic layers, which hinders cluster aggregation.

V.2. Results and discussion

To prepare the WS_2/MoS_2 heterostructures, we used $[W_3S_4(tu)_8(H_2O)]Cl_4 \cdot 2H_2O$ cluster (in short, W_3S_4 cluster), where tu stands for thiourea, as molecular source of WS_2 and ultrathin MoS_2 flakes (1–5 nm thick and 0.2–1.2 μm wide) produced by chemical exfoliation with *n*-BuLi[25] as underlying substrate.

W_3S_4 is considered the first triangular tungsten cluster with coordinated tu ligands.[26] This complex is stable at air and soluble in organic solvents. It has a structure analogous to that of $[Mo_3S_4(tu)_8(H_2O)]Cl_4 \cdot 4H_2O$ and can be used as precursor for the preparation of other trimetallic W_3S_4-core derivatives *via* ligand exchange reactions. The synthesis of W_3S_4 (**Figure V-3**) is based on mixing a solution of $[W_3S_4(H_2O)_9]^{4+}$ in 2 M HCl with a large excess of tu for 3 days, at room temperature. The colour of the solution changes gradually from violet to green as the coordination of tu ligands to W proceeds.

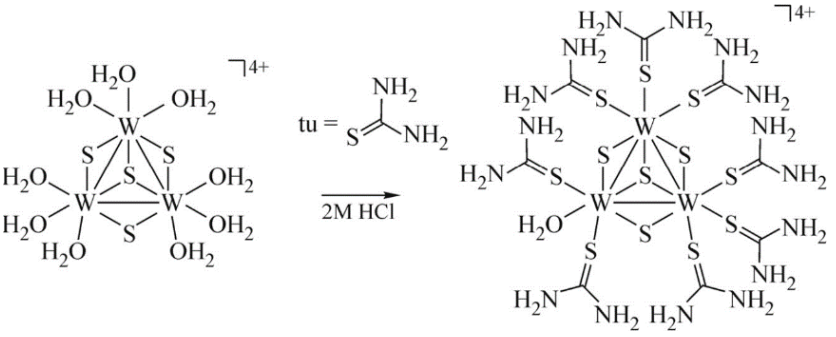

Figure V-3. Pictorial representation of W_3S_4 synthesis.

V.2.1. Preparation and characterization of WS_2 *via* calcination

Even though the synthesis and thermal decomposition of W_3S_4 cluster into WS_2 layers was reported in 2016,[26] the study on the morphology of the decomposition product has remained elusive until now. Thus, with the aim of completing the characterization process initiated by Dr. A. L. Gushchin and co-workers four years ago, HRTEM, along with XPS and Raman spectra, are provided hereafter.

W_3S_4 cluster was synthesized by N. Y. Shmelev under Dr. A. L. Gushchin's supervision (from University of Novosibirsk). Once received, it was purified according to the protocol described in **Experimental section**.

The calcination of the aforementioned W_3S_4 cluster in the 25–700 ºC range afforded ultrathin layers of WS_2. To minimize the oxidation of the ultrathin layers, the calcined material was preserved from the air exposure inside the TGA apparatus until it was completely cooled down to room temperature. If the W_3S_4 cluster is not well isolated from air, tungsten oxides can be formed.[24] Interestingly, equivalent Mo_3S_4 clusters can be synthetized and used as thermal precursors of MoS_2 layers.[27,28]

HRTEM

The morphology of the calcined material was analysed by HRTEM. According to TEM images (**Figure V-4a** and **b**), this material has a lamellar structure. In the HRTEM image (**Figure V-4c**), fringes with interplanar spacing values of ≈0.27 and 0.61 nm are observed. These values are assignable to (100)/(101) and (002) planes of WS_2, respectively.[29] The energy-dispersive X-ray spectroscopy (EDS) elemental mapping (**Figure V-4d** and **e**) highlights a good matching between W and S signals, as expected for WS_2 flakes. From inside to outside, the SAED rings correspond to (002), (100)/(101), (103), and (110) planes of WS_2, respectively (**Figure V-4f**). Moreover, the appearance of rings corroborates the polycrystalline nature of WS_2.

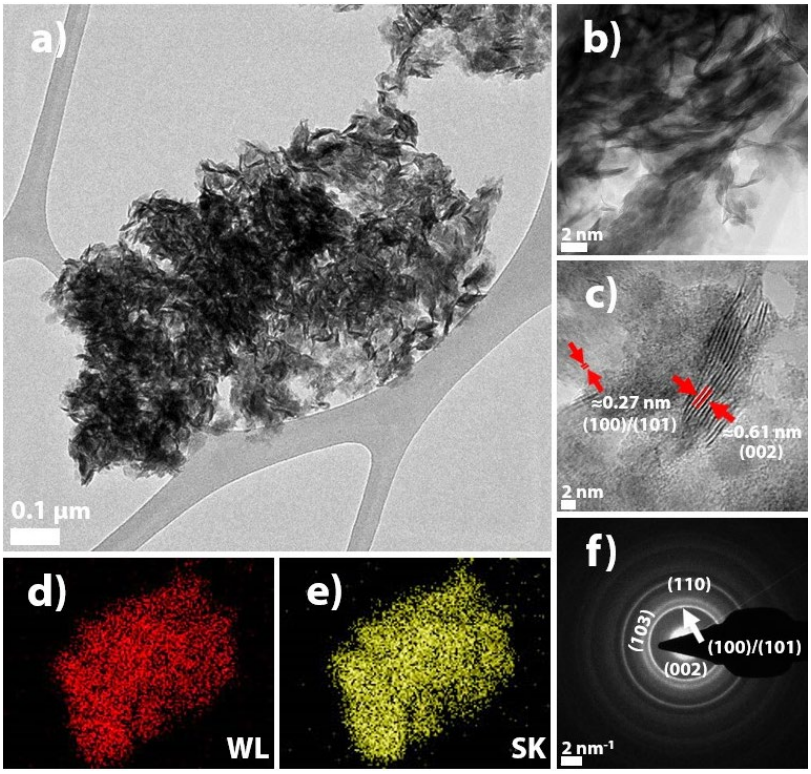

Figure V-4. a) TEM image of the material obtained by calcination of the W_3S_4 clusters; b) Zoomed TEM image showing the lamellar nature of the material; c) HRTEM image showing different interplanar *d*-spacing values; d-e) EDS elemental mapping of the sample shown in (a); f) SAED pattern of the sample shown in "a)".

XPS

The study of the composition of calcined material was conducted by XPS. W 4f spectrum (**Figure V-5a**) is dominated by two intense peaks centred at ≈33.1 and 35.2 eV, which are related to 2H W^{IV} $4f_{7/2}$ and 2H W^{IV} $4f_{5/2}$ components, respectively.[30] As expected, WS_2 layers obtained by thermal decomposition only contains the thermodynamically stable 2H phase. Minor contributions observed at ≈36.2 and 38.7 eV arise from W^{VI} $4f_{7/2}$, and W^{VI} $4f_{5/2}$ components, respectively, indicating certain degree of oxidation (≈12.0% of WO_3 from total W).[30] Curiously, the commercial 2H-WS_2 used as reference contains approximately the same oxide percentage. The explanation to this fact could be that WS_2 edges are spontaneously oxidized to certain extent if manipulated in ambient conditions.[31] S 2p spectrum (**Figure V-5b**)

displays two well-defined peaks at ≈162.3 and 163.5 eV, which correspond to S^{-II} $2p_{3/2}$ and $2p_{1/2}$ components, respectively. Thus, all these values are in good agreement with those measured for commercial WS_2. The S:W molar ratios of the calcined material and commercial WS_2 were estimated to be ≈2.15 and 2.33, respectively.

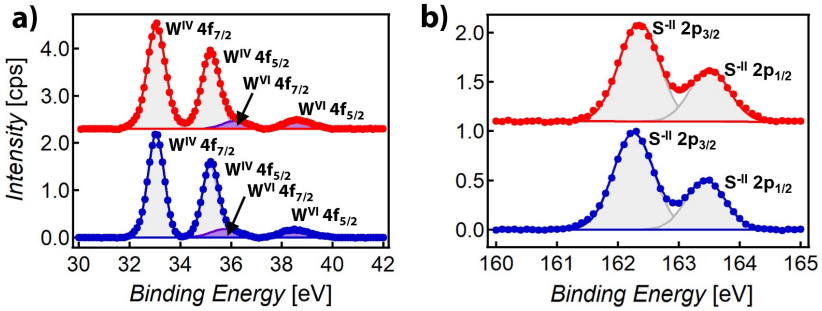

Figure V-5. W 4f XPS spectra of commercial WS_2 (blue) and calcined material (red) normalized using the S $2p_{3/2}$ signal; b) Normalized S 2p XPS spectra of commercial WS_2 (blue) and calcined material (red).

Raman spectroscopy

The definitive proof that the calcined material corresponds to WS_2 layers was obtained from Raman spectroscopy. The most intense 2LA(M)/E^1_{2g} and A_{1g} peaks appear at ≈352 and 416 cm^{-1}, respectively (see **Figure V-6**). Whilst 2LA(M) represents the longitudinal acoustic phonon at the M-point of the Brillouin zone (periodic compressions and expansions of the lattice that occur along the propagation direction),[32] the in-plane E^1_{2g} mode is related to the opposite vibration of two S atoms respect to the W atom between them and the out-of-plane A_{1g} mode describes the transverse vibration of S atoms in opposite directions.[33] The peak separation between 2LA(M)/E^1_{2g} and A_{1g} modes (≈64 cm^{-1}) is consistent with at most 2H-WS_2 bi- or tri-layer entities integrated into a turbostratic stacking.[40] Overall, these results confirm the WS_2 nature of the calcined material.

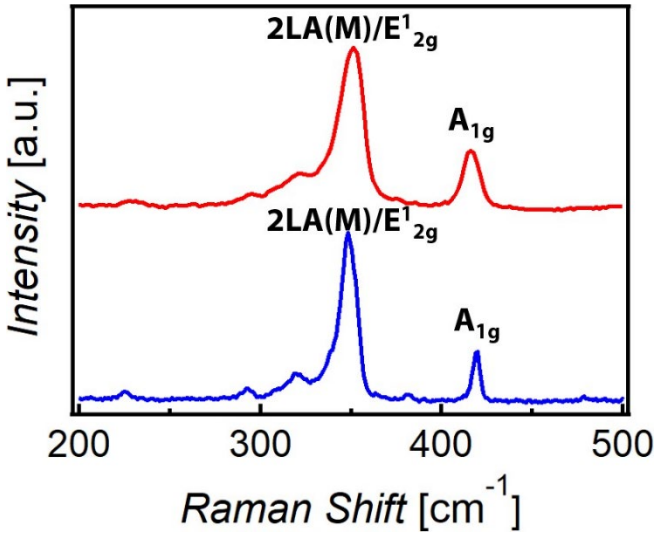

Figure V-6. Normalized Raman spectra of commercial WS_2 (blue) and calcined material (red) at 532 nm excitation wavelength.

V.2.2. Thermal stability of ce-MoS_2

Prior to the synthesis of WS_2/MoS_2 heterostructure, the thermal stability of ce-MoS_2 flakes under the conditions used to decompose the W_3S_4 clusters was evaluated. Thus, ce-MoS_2 flakes were calcined under inert atmosphere in the 25–700 °C range. In the TGA plot of ce-MoS_2 flakes (**Figure V-7**), a significant mass drop of ≈7.0% in the 25–150 ºC accompanied by a steady and scant mass loss of ≈3.4% in the 150–700 ºC range were observed. Whilst the first drop corresponds to the removal of physisorbed water, the second one is due to the loss of S pertaining to MoS_2 since as demonstrated in previous works, harsh intercalation conditions can affect the structural integrity of this compound.[34]

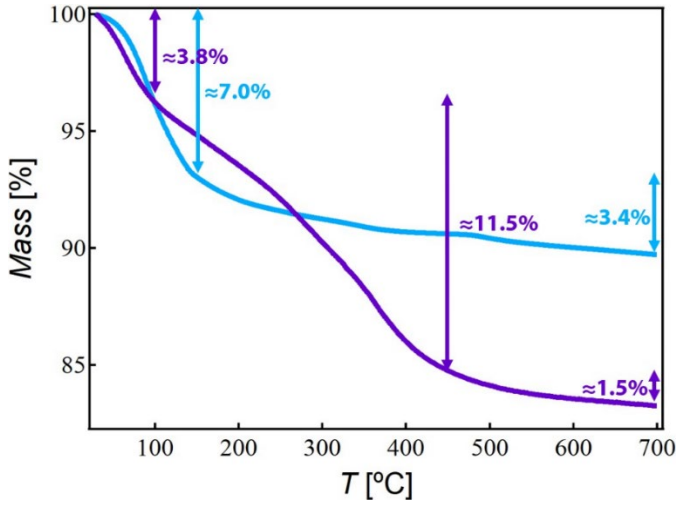

Figure V-7. TGA plots of ce-MoS_2 flakes (bright blue) and composite cluster@MoS_2 (purple).

V.2.3. Preparation and characterization of cluster@MoS_2

To synthesize cluster@MoS_2 (see **Figure V-2**), a freshly prepared suspension of ce-MoS_2 flakes in water was mixed with a methanolic $[W_3S_4(tu)_8(H_2O)]Cl_4 \cdot 2H_2O$ solution, in a molar proportion of 1:5, respectively, under argon atmosphere. The mixture was allowed to react for 1 h under magnetic stirring and, after that, centrifuged. Whilst the supernatant was discarded, the remaining sediment was washed by a couple of redispersion/centrifugation cycles (with the goal of removing the unattached W_3S_4 cluster) and then vacuum-dried. At this point, it is important to remark that, owing to its high lability toward ligand substitution, some coordinated tu ligands can be replaced by water and/or methanol molecules during the reaction and washing process, changing the original composition of the W_3S_4 cluster.

HRTEM

The morphology of cluster@MoS_2 was scanned by HRTEM. According to TEM images (**Figure V-8a**), ce-MoS_2 flakes show no morphological changes. TEM and HRTEM images (**Figure V-8b** and **c**) reveal black features over unmodified MoS_2 surface. The images showing black spots onto ce-MoS_2 flakes were acquired in collaboration with L. T. Norman and Prof. A. N. Khlobystov. In bright-field TEM, contrast is proportional to the square root of the

atomic number of the element at issue. This is the reason why W_3S_4 clusters are imaged as black spots on thin MoS_2 flakes. Moreover, the EDS elemental mapping (**Figure V-8d-f**) evinces a homogeneous coverage of ce-MoS_2 flakes with trimetallic clusters.

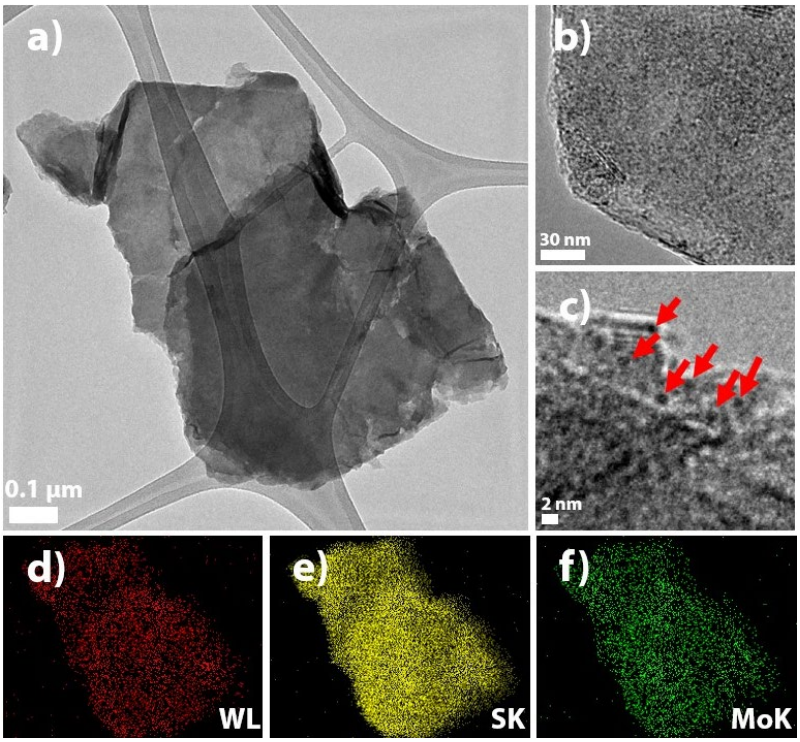

Figure V-8. a) TEM image of cluster@MoS_2; b) Zoomed TEM image of cluster@MoS_2; c) HRTEM image of cluster@MoS_2. Red arrows point to clusters over MoS_2 surface; d-f) EDS elemental mapping of cluster@MoS_2 shown in "a)".

XPS

To get useful information about the chemical composition, cluster@MoS_2 was analysed by XPS. W 4f spectrum (**Figure V-9a**) is dominated by two intense peaks centred at ≈33.0 and 35.1 eV, which are assigned to W^{IV} $4f_{7/2}$ and W^{IV} $4f_{5/2}$ components, respectively.[30] Minor contributions observed at ≈35.6 and 38.1 eV stem from W^{VI} $4f_{7/2}$, and W^{VI} $4f_{5/2}$ components, respectively, indicating certain degree of oxidation (≈9.1% of WO_3 from total W).[30] In this case, W^{IV} peaks are slightly shifted to high values respect to those of bare W_3S_4 cluster (32.6 and 34.7 eV, **Figure V-9a**). Most probably, this change indicates

that some tu molecules have been replaced by water and/or methanol, without affecting the pristine oxidation state of W. Mo 3d spectrum (**Figure V-9b**) shows five peaks located at ≈225.7, 228.5, 229.2, 231.6, and 232.3 eV, which correspond to S^{-II} 2s, 1T Mo^{IV} $3d_{5/2}$, 2H Mo^{IV} $3d_{5/2}$, 1T Mo^{IV} $3d_{3/2}$, and 2H Mo^{IV} $3d_{3/2}$ components, respectively.[35] 1T-MoS_2 (78.1%) dominates over 2H-MoS_2 (21.9%), as expected for ce-MoS_2 flakes prepared by using an excess of *n*-BuLi.[34] Thus, no phase transition is induced due to the attachment of the W_3S_4 cluster to the flakes. S 2p spectrum, located in the 159–166 eV range, (**Figure V-9c**) includes signals arising from several chemical environments (1T-MoS_2, 2H-MoS_2, W_3S_4 core, and tu ligands), encumbering the deconvolution of S spectral region. According to the atomic percentage (At%) data, there is a S loss of ≈4.75%, which would confirm the lability of tu ligands. W:Mo molar ratio was determined as 1.61. Moreover, the XPS survey reveals the presence of Cl, suggesting that the positive charge of W_3S_4 cluster is not completely compensated by the excess of negative charge accumulated onto MoS_2 surface.

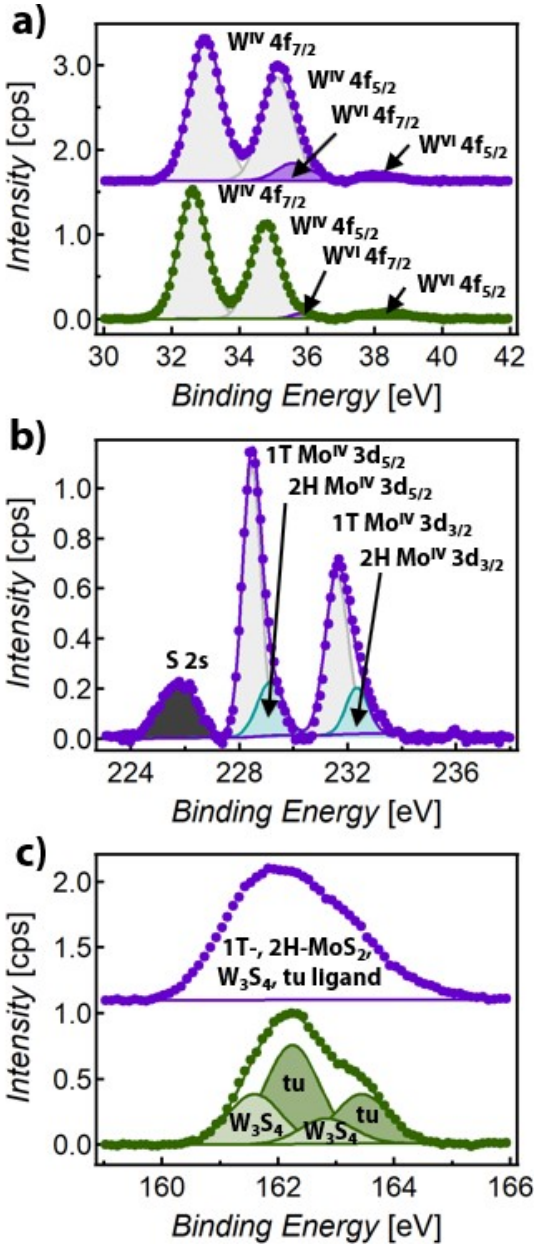

Figure V-9. a) W 4f XPS spectra of $[W_3S_4(tu)_8(H_2O)]Cl_4 \cdot 2H_2O$ (dark green) and cluster@MoS_2 (purple) normalized using the S $2p_{3/2}$ signal; b) Mo 3d spectrum of cluster@MoS_2 normalized using the S $2p_{3/2}$ signal; c) Normalized S 2p spectra of $[W_3S_4(tu)_8(H_2O)]Cl_4 \cdot 2H_2O$ (dark green) and cluster@MoS_2 (purple).

Raman spectroscopy

Cluster@MoS_2 was analysed by Raman spectroscopy at 532 nm. The resultant Raman spectrum (**Figure V-10**) uniquely shows MoS_2 peaks. The presence of the so-called J peaks at ≈152 (J_1), 220 (J_2), and 328 (J_3) cm^{-1}, characteristic of the superlattice structure of 1T-MoS_2,[36,37] reflects the abundance of this polytype in ce-MoS_2 flakes. J peaks arise from longitudinal acoustic phonon modes of 1T phase.[38] Because of the lower signal expected for the W_3S_4 cluster at the working excitation wavelength and the uniform distribution of this compound over MoS_2, no clear signatures of the W_3S_4 cluster were observed.

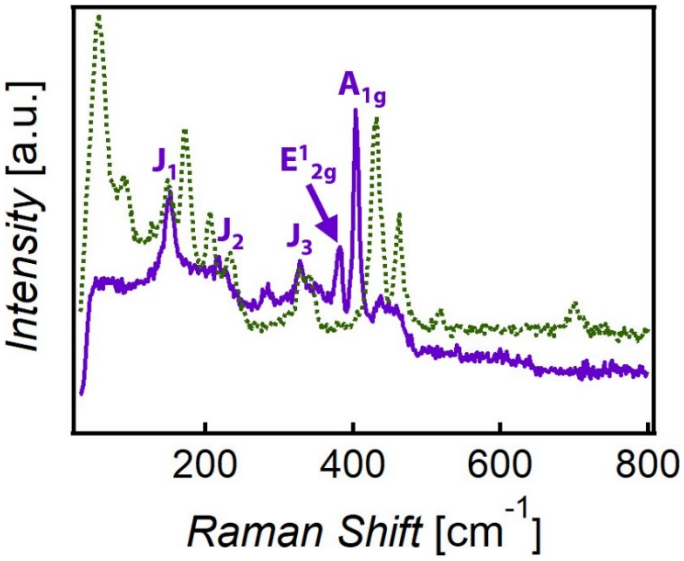

Figure V-10. Normalized Raman spectra at 532 nm excitation wavelength of $[W_3S_4(tu)_8(H_2O)]Cl_4 \cdot 2H_2O$ (dark green) and cluster@MoS_2 (purple).

V.2.4. Preparation and characterization of WS_2/MoS_2

Finally, cluster@MoS_2 was calcined in the 25–700 °C range, under inert atmosphere, to obtain the heterostructure formed by MoS_2 layers in between WS_2 flakes (WS_2/MoS_2 for simplicity). To minimize the oxidation of the ultrathin layers, the resultant calcined material was preserved from the air exposure inside the TGA apparatus until it was completely cooled down to room temperature. If these precautions are not taken, MoO_2 nanowires can be formed during the calcination process (see **Figure V-11**).[39]

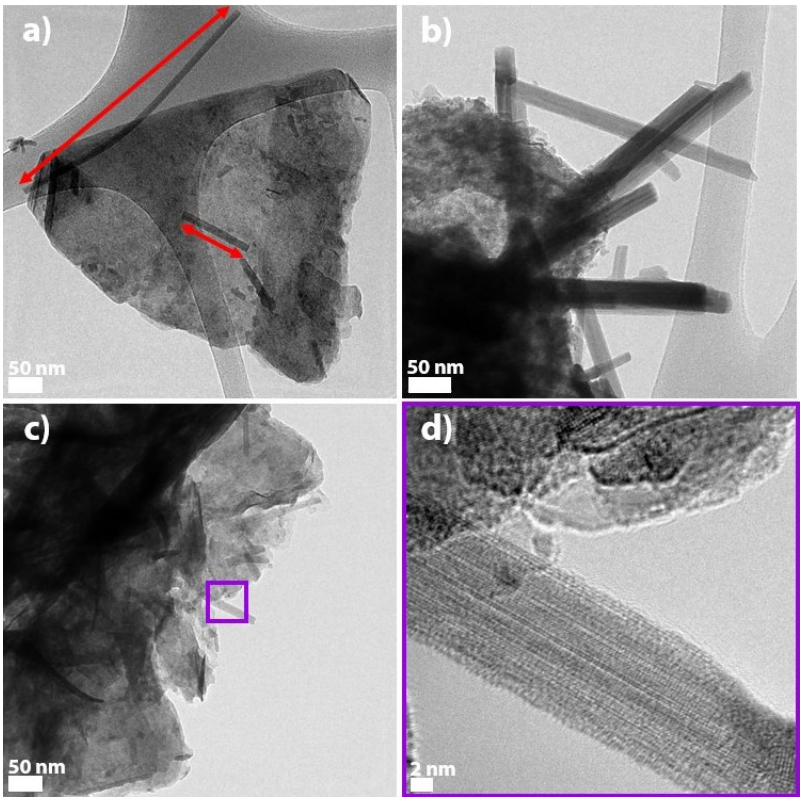

Figure V-11. a-d) TEM images of WS_2/MoS_2 showing MoO_2 nanowires. The HRTEM image shown in "d)" correspond to the purple square shown in "c)".

TGA

In contrast to what happens for ce-MoS_2 flakes, the TGA resulting from composite calcination (**Figure V-7**) shows two remarkable mass drops (≈3.8% in the 25–100 ºC range and ≈11.5% in the 100–450 ºC) followed by a steady mass loss (≈1.5% in the 450–700 ºC range). Whilst the first one would be associated with the removal of both methanol and water molecules, either physorbed or forming part of the W_3S_4 cluster, the second one would correspond to the dissociation of the remaining tu ligands. Additionally, it also cannot be ruled out the formation of volatile tungsten species, such as $WO_2(OH)_2$[40] and WCl_6. The final steady mass probably arises from a little loss of the S belonging to MoS_2 flakes.

HRTEM

The morphology of WS_2/MoS_2 was scanned by HRTEM. According to the TEM images (**Figure V-12a**), WS_2/MoS_2 maintains a characteristic lamellar structure. From inside to outside, the SAED elongated spots could correspond to (100)/(101), (103), and (110) planes of WS_2 as well as MoS_2, respectively, due to their isostructural nature (similar crystal system and lattice constants) (see **Figure V-12b**). Therefore, this SAED image could derive from superimposing the aforementioned patterns.[41] Furthermore, the detection of these elongated spots confirms the existence of polycrystalline material. The EDS elemental mapping of the sample shown in **Figure IV-12a** evinces no segregation (**Figure V-12c-e**).

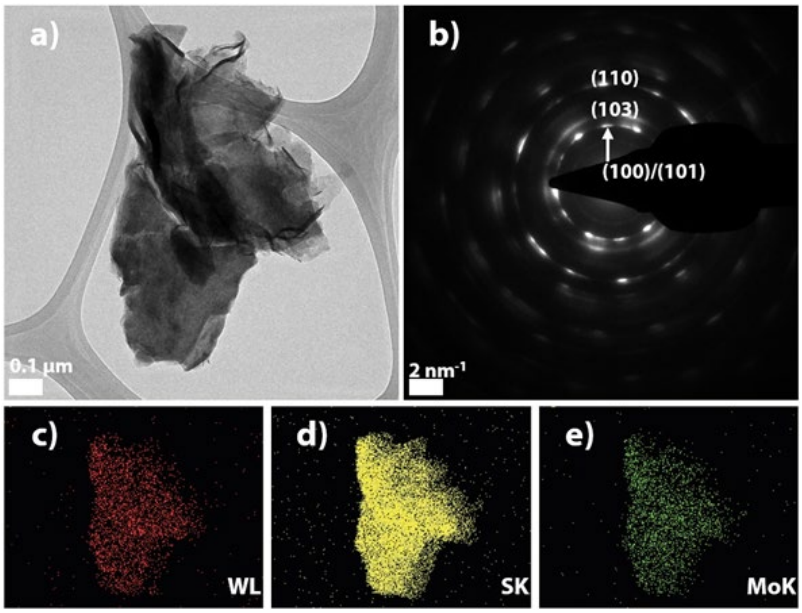

Figure V-12. a) TEM image of WS_2/MoS_2, b) SAED pattern of the sample shown in "a)"; c-e) EDS elemental mapping of the sample shown in "a)".

In the selected HRTEM image (**Figure V-13a**), W-containing nanodomains with high crystallinity are visualized. The observed interplanar d-spacings of ≈0.27, 0.32, and 0.60 nm are attributable to (100)/(101), (004), and (002) planes of WS_2, respectively.[29,42] In light of the good matching between W and Mo signals shown in the EDS elemental mapping (**Figure V-13b-d**), it can be concluded that W-containing nanopatches are homogeneously distributed over MoS_2

flakes. This analysis was developed in collaboration with L. T. Norman and Prof. A. N. Khlobystov.

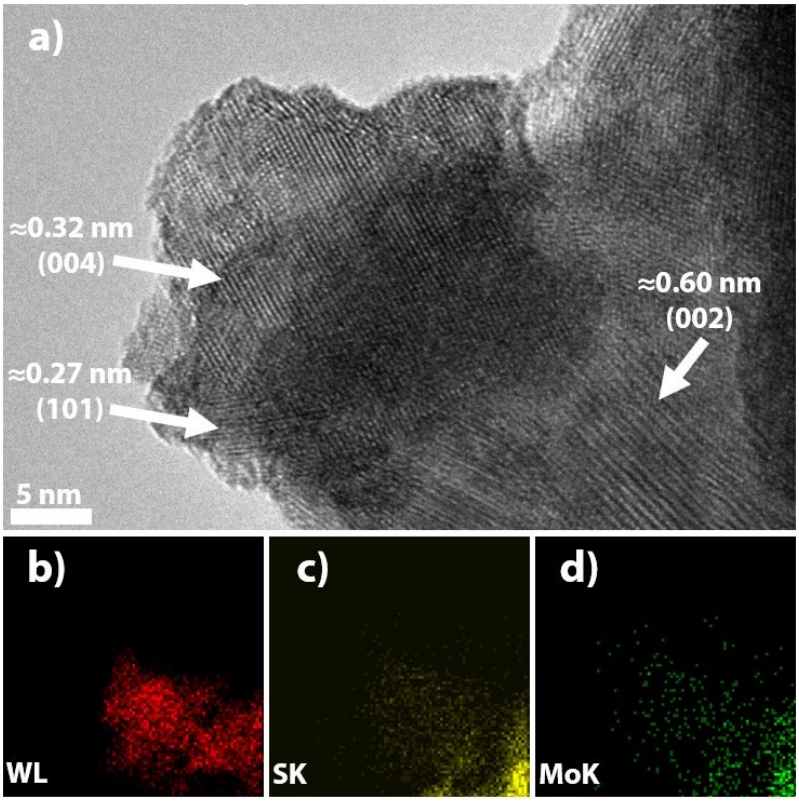

Figure V-13. a) HRTEM image of WS_2/MoS_2 showing high crystalline WS_2 nanodomains; d-f) EDS elemental mapping of the sample shown in "c)".

XPS

The chemical composition of WS_2/MoS_2 was investigated by XPS. W 4f spectrum (**Figure V-14a**) perfectly resembles that of the material obtained after calcination of the W_3S_4 cluster as well as that of the commercial 2H-WS_2. Mo 3d spectrum (**Figure V-14b**) shows three peaks located at ≈226.2, 229.2 and 232.3 eV, which correspond to S^{-II} 2s, Mo^{IV} $3d_{5/2}$ and $3d_{3/2}$ components in the thermodynamically stable 2H-MoS_2 phase, respectively.[35] As expected, Mo 3d spectrum perfectly resembles that of commercial 2H-MoS_2. S 2p spectrum (**Figure V-14c**) displays two well-defined peaks at ≈162.1 and 163.3 eV, which are assigned to S^{-II} $2p_{3/2}$ and $2p_{1/2}$ components from both 2H-MoS_2 and 2H-WS_2, respectively. Whilst Mo:W molar ratio was estimated at 1.42,

S:(Mo+W) molar ratio from MS_2 species was determined to be 2.28. Apparently, the latter value deviates from the stoichiometry expected for WS_2 as well as MoS_2. However, for bulk WS_2 and MoS_2, S:W and S:Mo molar ratios (≈2.33 and 2.32, respectively) are comparable to the previous one. Even though that ce-MoS_2 flakes were mixed with $[W_3S_4(tu)_8(H_2O)]Cl_4 \cdot 2H_2O$ in a molar proportion of 1:5, respectively, the loss of W could be explained according to *i*) the removal of unattached W_3S_4 cluster *via* sequential washing redispersion/centrifugation cycles, and *ii*) the generation of volatile tungsten oxide hydrates (e.g., $WO_2(OH)_2$)[40] and halides (e.g., WCl_6) during the thermal treatment.

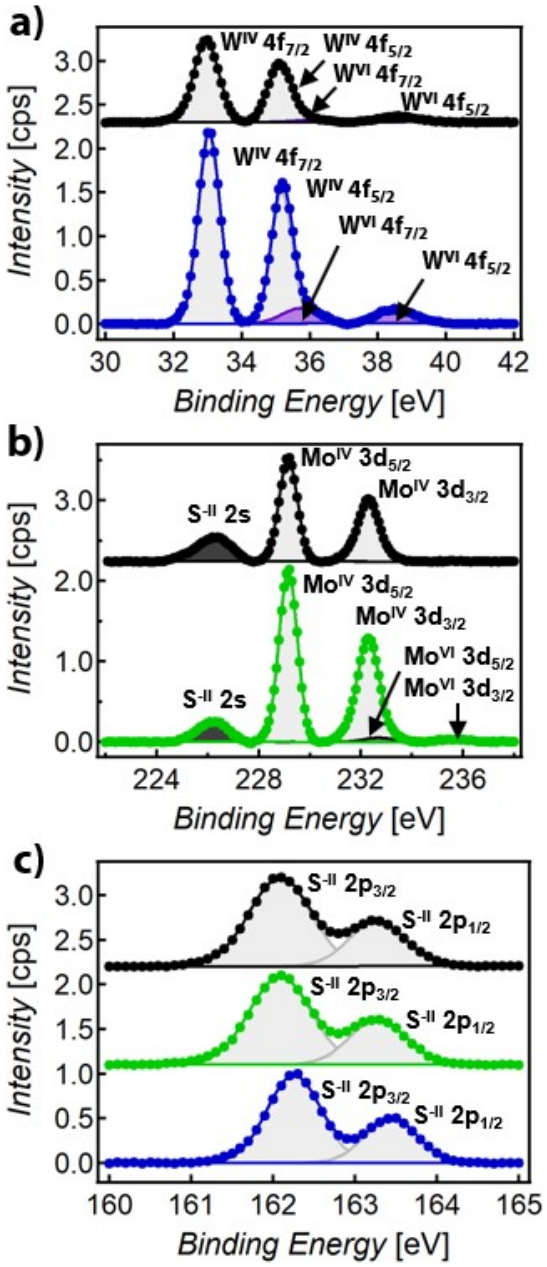

Figure V-14. a) W 4f XPS spectra of commercial WS_2 (blue) and WS_2/MoS_2 (black) normalized using the S $2p_{3/2}$ signal; b) Mo 3d XPS spectra of commercial MoS_2 (bright green) and WS_2/MoS_2 (black) normalized using the S $2p_{3/2}$ signal; c) Normalized S 2p XPS spectra of commercial WS_2 (blue), commercial MoS_2 (bright green) and WS_2/MoS_2 (black).

For better clarity, XPS values observed in commercial WS_2, commercial MoS_2, WS_2 obtained *via* calcination, cluster, cluster@MoS_2 composite, and WS_2/MoS_2 have been collected in **Table V-1**.

Table V-1. XPS values observed in commercial WS_2, commercial MoS_2, WS_2 obtained *via* calcination, cluster, cluster@MoS_2 composite, and WS_2/MoS_2. Minor contributions are marked with *.

Material	W XPS signals	Mo XPS signals	S XPS signals
WS_2	≈33.0 eV (W^{IV} $4f_{7/2}$) ≈35.2 eV (W^{IV} $4f_{5/2}$) ≈35.7 eV* (W^{VI} $4f_{7/2}$) ≈38.5 eV* (W^{VI} $4f_{5/2}$)	Ø	≈162.3 eV (S^{-II} $2p_{3/2}$) ≈163.4 eV (S^{-II} $2p_{1/2}$)
MoS_2	Ø	≈229.2 eV (Mo^{IV} $3d_{5/2}$) ≈232.3 eV (Mo^{IV} $3d_{3/2}$) ≈232.7 eV* (Mo^{VI} $3d_{5/2}$) ≈235.7 eV* (Mo^{VI} $3d_{3/2}$)	≈162.1 eV (S^{-II} $2p_{3/2}$) ≈163.3 eV (S^{-II} $2p_{1/2}$) ≈226.2 eV (S^{-II} 2s)
WS_2 obtained via calcination	≈33.1 eV (W^{IV} $4f_{7/2}$) ≈35.2 eV (W^{IV} $4f_{5/2}$) ≈36.2 eV* (W^{VI} $4f_{7/2}$) ≈38.7 eV* (W^{VI} $4f_{5/2}$)	Ø	≈162.3 eV (S^{-II} $2p_{3/2}$) ≈163.5 eV (S^{-II} $2p_{1/2}$)
cluster	≈32.6 eV (W^{IV} $4f_{7/2}$) ≈34.7 eV (W^{IV} $4f_{5/2}$) ≈35.9 eV* (W^{VI} $4f_{7/2}$) ≈38.1 eV* (W^{VI} $4f_{5/2}$)	Ø	≈161.6 eV (core S^{-II} $2p_{3/2}$) ≈162.8 eV (core S^{-II} $2p_{1/2}$) ≈162.3 eV (tu S^{-II} $2p_{3/2}$) ≈163.5 eV (tu S^{-II} $2p_{1/2}$)
cluster@MoS_2	≈33.0 eV (W^{IV} $4f_{7/2}$) ≈35.1 eV (W^{IV} $4f_{5/2}$) ≈35.6 eV* (W^{VI} $4f_{7/2}$) ≈38.1 eV* (W^{VI} $4f_{5/2}$)	≈228.5 eV (1T Mo^{IV} $3d_{5/2}$) ≈231.6 eV (1T Mo^{IV} $3d_{3/2}$) ≈229.2 eV (2H Mo^{VI} $3d_{5/2}$) ≈232.3 eV (2H Mo^{VI} $3d_{3/2}$)	≈225.7 eV (S^{-II} 2s) The rest is unclear
WS_2/MoS_2	≈33.0 eV (W^{IV} $4f_{7/2}$) ≈35.1 eV (W^{IV} $4f_{5/2}$) ≈36.1 eV* (W^{VI} $4f_{7/2}$) ≈38.5 eV* (W^{VI} $4f_{5/2}$)	≈229.2 eV (Mo^{IV} $3d_{5/2}$) ≈232.3 eV (Mo^{IV} $3d_{3/2}$)	≈162.1 eV (S^{-II} $2p_{3/2}$) ≈163.3 eV (S^{-II} $2p_{1/2}$) ≈226.2 eV (S^{-II} 2s)

Raman spectroscopy

In order to gain a better insight into the nature and thickness of the material formed over MoS_2 flakes, WS_2/MoS_2 was also inspected by Raman spectroscopy at 532 nm excitation wavelength.

Consistently, the spectrum (**Figure V-15**) only reveals peaks related to both 2H-WS_2 and 2H-MoS_2.[43] Whilst peaks appearing at ≈353, and 416 cm^{-1} correspond to 2H-WS_2,[32] the rest of them (located at ≈382 and 406 cm^{-1}) are ascribable to 2H-MoS_2.[44] The absence of J peaks indicates a total 1T→2H polytype transformation. The coexistence of two clearly distinguishable pairs of E^1_{2g}/A_{1g} peaks, one per chalcogenide, discards the presence of alloyed $Mo_xW_{1-x}S_2$ materials.[41,45–47] In addition, the peak separation between $2LA(M)/E^1_{2g}$ and A_{1g} modes (≈63 cm^{-1}) for WS_2 is also consistent with few-layered sheets (presumably, mono- and bilayers).[48]

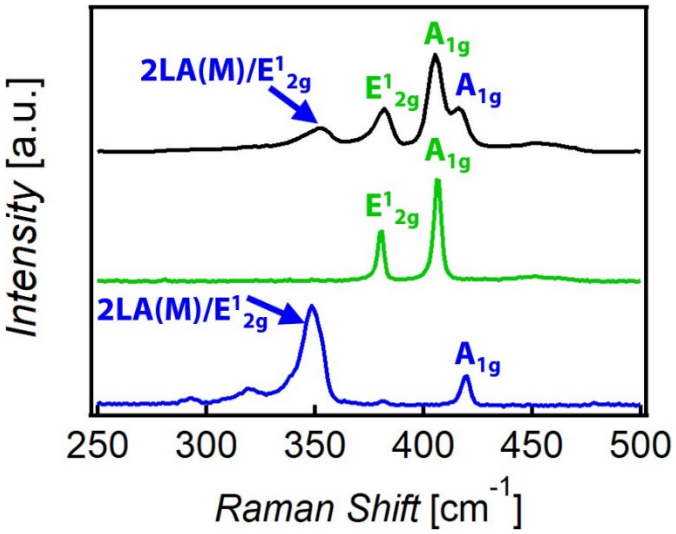

Figure V-15. Normalized Raman spectra at 532 nm excitation wavelength of commercial WS_2 (blue), commercial MoS_2 (bright green), and WS_2/MoS_2 (black).

For better clarity, Raman values observed in commercial WS_2, commercial MoS_2, WS_2 obtained *via* calcination, cluster, cluster@MoS_2 composite, and WS_2/MoS_2 have been collected in **Table V-2**.

Table V-2. Raman values observed in commercial WS_2, commercial MoS_2, WS_2 obtained *via* calcination, cluster, cluster@MoS_2 composite, and WS_2/MoS_2.

Material	Raman signals
Commercial WS_2	≈348 cm^{-1} (2LA(M)/E^1_{2g}) ≈420 cm^{-1} (A_{1g})
Commercial MoS_2	≈381 cm^{-1} (E^1_{2g}) ≈406 cm^{-1} (A_{1g})
WS_2 obtained *via* calcination	≈352 cm^{-1} (2LA(M)/E^1_{2g}) ≈416 cm^{-1} (A_{1g})
Cluster	≈55, 89, 126, 149, 171, 206, 233, 326, 341, 432, 463, and 702 cm^{-1}
Cluster@MoS_2	Cluster Ø MoS_2 ≈152 cm^{-1} (J_1) ≈220 cm^{-1} (J_2) ≈328 cm^{-1} (J_3) ≈382 cm^{-1} (E^1_{2g}) ≈404 cm^{-1} (A_{1g})
WS_2/MoS_2	WS_2 ≈353 cm^{-1} (2LA(M)/E^1_{2g}) 416 cm^{-1} (A_{1g}) MoS_2 ≈382 cm^{-1} (E^1_{2g}) ≈406 cm^{-1} (A_{1g})

V.2.5. Evaluation of the interaction strength between MoS_2 and WS_2 interfaces

Finally, preliminary PL measurements were carried out to get some information about the strength of the interaction between WS_2 and MoS_2 in the heterostructure (**Figure V-16**). As expected, the spectrum of thermally treated ce-MoS_2 flakes presents two peaks at 1.80 eV and 1.97 eV, characteristic of A1 and B1 excitonic transitions in ultrathin MoS_2 layers, respectively, while the spectrum of WS_2 layers shows the excitonic transition at 1.97 eV. In the case of WS_2/MoS_2

heterostructure, no clear peaks are detected in the corresponding spectrum. Interestingly, the intensity of this spectrum exhibits a dramatic decrease if compared to thermally threated ce-MoS_2 flakes. Indeed, it is well-known that the band alignment of WS_2 and MoS_2 layers in heterostructures prevents from the formation of correlated electron-hole pairs. Succinctly, the photogenerated holes are accumulated into WS_2 valence band while photogenerated electrons are promoted to MoS_2 conduction band.[12,49] As a result, the quenching of the PL signal observed for the present WS_2/MoS_2 heterostructure can be considered as an evidence of the interaction between both dichalcogenides, which can exchange charge and energy, proving potential optoelectronic applications in the fields of light harvesting or photocatalysis.

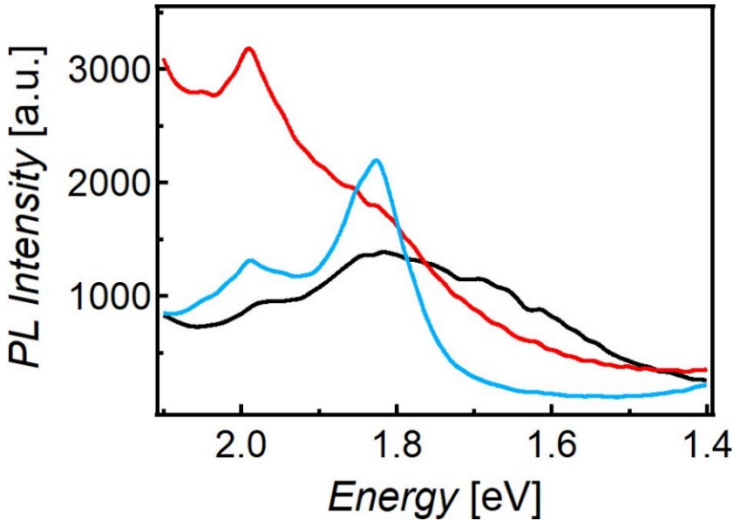

Figure V-16. PL spectra of WS_2 layers obtained through W_3S_4 cluster decomposition (red), ce-MoS_2 flakes treated under the same conditions used for preparing WS_2/MoS_2 heterostructure (blue), and WS_2/MoS_2 heterostructure (black).

V.3. Conclusions

In this Chapter, we have reported a straightforward two-step strategy for preparing high amounts of WS_2/MoS_2 heterostructures as powder materials. These results have been published in WS_2/MoS_2 Heterostructures via Thermal Treatment of MoS_2 Layers Electrostatically Functionalized with W_3S_4 Molecular Clusters.

In the first step, a homogeneous functionalization of MoS_2 surface is achieved thanks to the electrostatic interactions existing between negatively charged ce-MoS_2 flakes and $[W_3S_4(tu)_8(H_2O)]^{4+}$ cations dissolved in methanol. In the second step, the previous composite is calcined to give rise to heterostructures made from few-layer MoS_2 coated with mono- and/or bi-layer WS_2 coming from the thermal decomposition of the W_3S_4 cluster.

The presence of specific electrostatic forces between ce-MoS_2 and W_3S_4 cluster can avoid the agglomeration of the cluster and ensure a better coverage of the underlying ce-MoS_2 flakes. This results in a homogeneous distribution of thin WS_2 flakes all over MoS_2 surface. Besides, the dry thermal treatment involved in the synthetic strategy guarantees the removal of all residues that could hinder a strong interaction between both TMDCs, which seems to be actually supported by the experimental PL measurements.

Therefore, the combination of a simple, scalable and low-cost solution approach with a dry thermal decomposition, not only offers the advantages of most commonly used methods in solution, but also allows the good matching between 2D counterparts in the heterostructure, usually reached by more complex physical strategies like CVD, PVD, or deterministic transfer followed by annealing treatment. Interestingly, the proposed strategy could be applied to the synthesis of other 2D/2D heterostructures formed by thermally generated WS_2 or MoS_2 flakes on different anionic layers.

As a future work, we would like to perform photocurrent measurements and test the capacity of our WS_2/MoS_2 heterostructures for photoelectrochemical water oxidation. It also would be interesting to study the formation of these heterostructures on surface, starting from me-MoS_2 flakes deposited onto a clean SiO_2/Si substrate, with the aim of knowing which approach is the best one for preparing higher quality

heterojunctions. In this regard, me-MoS_2 flakes interfaced with W_3S_4 clusters would be calcined inside a conventional tubular furnace.

V.4. Experimental section

V.4.1. Materials

For the chemical exfoliation of MoS_2, see the **Materials section** in Chapter II. Methanol was used without further purification. Milli-Q water was used in all the experiments.

V.4.2. Methods

V.4.2.1. Intercalation/Chemical exfoliation of MoS_2

See **Methods** in Chapter II.

V.4.2.2. Synthesis of W_3S_4 cluster

W_3S_4 cluster was prepared by N. Y. Shmelev under the supervision of Dr. A. L. Gushchin (from Nikolaev Institute of Inorganic Chemistry, Siberian Branch of Russian Academy of Sciences), according to a well-stablished procedure.[26]

V.4.2.3. Purification of W_3S_4 cluster

W_3S_4 cluster was washed with a cold 1:1 water/ethanol mixture on a glass filter in order to purify it.

V.4.2.4. Synthesis of WS_2 layers

$[W_3S_4(tu)_8(H_2O)]Cl_4 \cdot 2H_2O$ (≈50 mg) was calcined in the 25–700 °C range under a 10 °C min^{-1} scan rate and N_2 flow of 100 mL min^{-1}. The resultant material was preserved from the air exposure inside the TGA apparatus until it was cooled down to room temperature.

V.4.2.5. Synthesis of cluster@MoS_2

The volume corresponding to ≈13.5 μmol of ce-MoS_2 flakes was poured into 4 mL of $[W_3S_4(tu)_8(H_2O)]Cl_4 \cdot 2H_2O$ (100.0 mg, ≈67.4 μmol) in MeOH. Subsequently, the mixture was magnetically stirred for 1 h under argon at room temperature. Then, it was centrifuged at 13.4 krpm for 1.5 h. After decanting the supernatant, the sediment was dispersed in methanol and centrifuged at 13.4 krpm for 0.5 h. The previous dispersion-centrifugation-collection step was repeated once more. Finally, the sediment was dried by vacuum for at least 7 h.

V.4.2.6. Synthesis of WS_2/MoS_2

Cluster@MoS_2 (≈10 mg) was calcined in the 25–700 °C range under a 10 °C min^{-1} scan rate and N_2 flow of 100 mL min^{-1}. The resultant material was preserved from the air exposure inside the TGA apparatus until it was cooled down to room temperature.

V.4.3. Characterization techniques

Raman and PL spectroscopy

Raman and PL spectra were recorded with a Raman Emission Horiba-MTB Xplora spectrometer in ambient conditions onto a substrate (532 nm). A 100x objective was used to focus the laser beam. For Raman measurements, powder samples were measured onto a clean SiO_2 (285 nm)/Si substrate. For PL measurements, with the aim of minimizing restacking effects, dispersions of calcined materials (through sonication in degassed methanol for 5 min) were spin-coated onto clean SiO_2 (285 nm)/Si substrates.

TGA

See the TGA section in Chapter II.

HRTEM and dark field scanning transmission electron microscopy (STEM)

Samples were prepared by dropping methanolic suspensions on lacey formvar/carbon copper grids (300 mesh). TEM studies were carried out on Tecnai G2 F20 and JEOL 2100 FEG-TEM microscopes, both of them operating at 200 kV. JEOL 2100 FEG-TEM was manipulated by L. T. Norman under the supervision of Prof. A. N. Khlobystov, from School of Chemistry, University of Nottingham.

XPS

See **XPS** in Chapter II. In this case, XPS spectra were deconvoluted by using Origin program. Commercial 2H-WS_2 and 2H-MoS_2 sample were used as reference (W $3d_{7/2}$ = 33.1 eV, Mo $3d_{5/2}$ = 229.1 eV). To determine molar ratios in WS_2 (from W_3S_4 cluster calcination), cluster@MoS_2 and WS_2/MoS_2, oxide contributions were ignored.

V.5. References

1. Geim, A. K. & Grigorieva, I. V. Van der Waals heterostructures. *Nature* **499**, 419–25 (2013).

2. Novoselov, K. S., Mishchenko, A., Carvalho, A. & Castro Neto, A. H. 2D materials and van der Waals heterostructures. *Science* **353**, 6298 (2016).

3. Loan, P. T. K. *et al.* Graphene/MoS_2 Heterostructures for Ultrasensitive Detection of DNA Hybridisation. *Adv. Mater.* **26**, 4838–4844 (2014).

4. Liu, Y. *et al.* Van der Waals heterostructures and devices. *Nat. Rev. Mater.* **1**, 16042 (2016).

5. Li, C. *et al.* Engineering graphene and TMDs based van der Waals heterostructures for photovoltaic and photoelectrochemical solar energy conversion. *Chem. Soc. Rev.* **47**, 4981–5037 (2018).

6. Chen, T. Y. *et al.* Comparative study on MoS_2 and WS_2 for electrocatalytic water splitting. *Int. J. Hydrogen Energy.* **38**, 12302–12309 (2013).

7. Pospischil, A., Furchi, M. M. & Mueller, T. Solar-energy conversion and light emission in an atomic monolayer p-n diode. *Nat. Nanotechnol.* **9**, 257–261 (2014).

8. Furchi, M. M., Pospischil, A., Libisch, F., Burgdörfer, J. & Mueller, T. Photovoltaic effect in an electrically tunable Van der Waals heterojunction. *Nano Lett.* **14**, 4785–4791 (2014).

9. Merki, D. & Hu, X. Recent developments of molybdenum and tungsten sulfides as hydrogen evolution catalysts. *Energy Environ. Sci.* **4**, 3878–3888 (2011).

10. Kang, J., Tongay, S., Zhou, J., Li, J. & Wu, J. Band offsets and heterostructures of two-dimensional semiconductors. *Appl. Phys. Lett.* **102**, (2013).

11. Singh, A. K., Mathew, K., Zhuang, H. L. & Hennig, R. G. Computational screening of 2D materials for photocatalysis. *J. Phys. Chem. Lett.* **6**, 1087–1098 (2015).

12. Hong, X. *et al.* Ultrafast charge transfer in atomically thin MoS_2/WS_2 heterostructures. *Nat. Nanotechnol.* **9**, 682–686 (2014).

13. Chen, K. *et al.* Lateral Built-In Potential of Monolayer MoS_2-WS_2 In-Plane Heterostructures by a Shortcut Growth Strategy. *Adv. Mater.* **27**, 6431–6437 (2015).

14. Sherrell, P. C. *et al.* Large-Area CVD MoS_2/WS_2 Heterojunctions as a Photoelectrocatalyst for Salt-Water Oxidation. *ACS Appl. Energy Mater.* **2**, 5877–5882 (2019).

15. Pesci, F. M. *et al.* MoS_2/WS_2 Heterojunction for Photoelectrochemical Water Oxidation. *ACS Catal.* **7**, 4990–4998 (2017).

16. Lu, C. *et al.* Band Alignment of WS_2/MoS_2 Photoanodes with Efficient Photoelectric Responses based on Mixed Van der Waals Heterostructures. *Phys. status solidi.* **216**, 1900544 (2019).

17. Lotsch, B. V. Vertical 2D Heterostructures. *Annu. Rev. Mater. Res.* **45**, 85–109 (2015).

18. Sasaki, T. *et al.* Layer-by-layer assembly of titania nanosheet/polycation composite films. *Chem. Mater.* **13**, 4661–4667 (2001).

19. Coronado, E. *et al.* Coexistence of superconductivity and magnetism by chemical design. *Nat. Chem.* **2**, 1031–1036 (2010).

20. Yang, M. Q. *et al.* Self-surface charge exfoliation and electrostatically coordinated 2D hetero-layered hybrids. *Nat. Commun.* **8**, 14224 (2017).

21. Li, B. W. *et al.* Engineered interfaces of artificial perovskite oxide superlattices via nanosheet deposition process. *ACS Nano* **4**, 6673–6680 (2010).

22. Luo, S. *et al.* Rational and green synthesis of novel two-dimensional WS_2/MoS_2 heterojunction via direct exfoliation in ethanol-water targeting advanced visible-light-responsive photocatalytic performance. *J. Colloid Interface Sci.* **513**, 389–399 (2018).

23. Zhou, H. *et al.* Highly active and durable self-standing WS_2/graphene hybrid catalysts for the hydrogen evolution reaction. *J. Mater. Chem. A* **4**, 9472–9476 (2016).

24. Luxa, J., Fawdon, J., Sofer, Z., Mazánek, V. & Pumera, M. MoS_2/WS_2-Graphene Composites through Thermal Decomposition of Tetrathiomolybdate/Tetrathiotungstate for Proton/Oxygen Electroreduction. *ChemPhysChem* **17**, 2890–2896 (2016).

25. Morant-Giner, M. *et al.* Prussian Blue@MoS_2 Layer Composites as Highly Efficient Cathodes for Sodium- and Potassium-Ion Batteries. *Adv. Funct. Mater.* **28**, 1706125 (2018).

26. Laricheva, Y. A., Gushchin, A. L., Abramov, P. A. & Sokolov, M. N. Structure and thermal properties of a tungsten sulfide cluster with thiourea ligands. *J. Struct. Chem.* **57**, 962–969 (2016).

27. Gushchin, A. L. *et al.* Homoleptic Molybdenum Cluster Sulfides Functionalized with Noninnocent Diimine Ligands: Synthesis, Structure, and Redox Behavior. *Eur. J. Inorg. Chem.* **2014**, 4093–4100 (2014).

28. Gushchin, A. L., Laricheva, Y. A., Sokolov, M. N. & Llusar, R. Tri- and tetranuclear molybdenum and tungsten chalcogenide clusters: on the way to new materials and catalysts. *Russ. Chem. Rev.* **87**, 670–706 (2018).

29. Schutte, W. J., De Boer, J. L. & Jellinek, F. Crystal structures of tungsten disulfide and diselenide. *J. Solid State Chem.* **70**, 207–209 (1987).

30. Mahler, B., Hoepfner, V., Liao, K. & Ozin, G. A. Colloidal synthesis of 1T-WS_2 and 2H-WS_2 nanosheets: Applications for photocatalytic hydrogen evolution. *J. Am. Chem. Soc.* **136**, 14121–14127 (2014).

31. Kotsakidis, J. C. *et al.* Oxidation of Monolayer WS_2 in Ambient Is a Photoinduced Process. *Nano Lett.* **19**, 5205–5215 (2019).

32. Berkdemir, A. *et al.* Identification of individual and few layers of WS_2 using Raman Spectroscopy. *Sci. Rep.* **3**, 1755 (2013).

33. Wang, F. *et al.* Strain-induced phonon shifts in tungsten disulfide nanoplatelets and nanotubes. *2D Mater.* **4**, (2017).

34. Knirsch, K. C. *et al.* Basal-Plane Functionalization of Chemically Exfoliated Molybdenum Disulfide by Diazonium Salts. *ACS Nano* **9**, 6018–30 (2015).

35. Geng, X. *et al.* Pure and stable metallic phase molybdenum disulfide nanosheets for hydrogen evolution reaction. *Nat. Commun.* **7**, (2016).

36. Lukowski, M. A. *et al.* Enhanced hydrogen evolution catalysis from chemically exfoliated metallic MoS_2 nanosheets. *J. Am. Chem. Soc.* **135**, 10274–10277 (2013).

37. Fan, X. *et al.* Fast and Efficient Preparation of Exfoliated 2H MoS_2 Nanosheets by Sonication-Assisted Lithium Intercalation and Infrared Laser-Induced 1T to 2H Phase Reversion. *Nano Lett.* **15**, 5956–5960 (2015).

38. Nayak, A. P. *et al.* Pressure-dependent optical and vibrational properties of monolayer molybdenum disulfide. *Nano Lett.* **15**, 346–53 (2015).

39. Vogl, L. M., Schweizer, P., Wu, M. & Spiecker, E. Transforming layered MoS_2 into functional MoO_2 nanowires. *Nanoscale* **11**, 11687–11695 (2019).

40. Ma, Y., Li, J., Liu, W. & Shi, Y. A large-scale fabrication of flower-like submicrometer-sized tungsten whiskers via metal catalysis. *Nanoscale Res. Lett.* **7**, 325 (2012).

41. Woods, J. M. *et al.* One-Step Synthesis of MoS_2/WS_2 Layered Heterostructures and Catalytic Activity of Defective Transition Metal Dichalcogenide Films. *ACS Nano* **10**, 2004–2009 (2016).

42. Dickinson, R. G. & Pauling, L. The crystal structure of molybdenite. *J. Am. Chem. Soc.* **45**, 1466–1471 (1923).

43. Li, L., Ma, R., Ebina, Y., Iyi, N. & Sasaki, T. Positively Charged Nanosheets Derived via Total Delamination of Layered Double Hydroxides. *Chem. Mater.* **17**, 4386–4391 (2005).

44. Li, H. *et al.* From bulk to monolayer MoS_2: Evolution of Raman scattering. *Adv. Funct. Mater.* **22**, 1385–1390 (2012).

45. Song, J. G. *et al.* Controllable synthesis of molybdenum tungsten disulfide alloy for vertically composition-controlled multilayer. *Nat. Commun.* **6**, 7817 (2015).

46. Wang, Z. *et al.* Chemical Vapor Deposition of Monolayer $Mo_{1-x}W_xS_2$ Crystals with Tunable Band Gaps. *Sci. Rep.* **6**, 21536 (2016).

47. Liu, X. *et al.* Monolayer $W_xMo_{1-x}S_2$ Grown by Atmospheric Pressure Chemical Vapor Deposition: Bandgap Engineering and Field Effect Transistors. *Adv. Funct. Mater.* **27**, 1606469 (2017).

48. Mitioglu, A. A. *et al.* Second-order resonant Raman scattering in single-layer tungsten disulfide WS_2. *Phys. Rev. B - Condens. Matter Mater. Phys.* **89**, 245442 (2014).

49. Mawlong, L. P. L., Bora, A. & Giri, P. K. Coupled Charge Transfer Dynamics and Photoluminescence Quenching in Monolayer MoS_2 Decorated with WS_2 Quantum Dots. *Sci. Rep.* **9**, 19414 (2019).

VI. General conclusions and outlook

In this Thesis, we have reported some examples of covalent and non-covalent functionalization of ce-MoS_2 flakes with different molecular systems with the aim of exploiting the emergent features of the resulting molecular/MoS_2 composites. We have pursued the modulation of pristine MoS_2 properties as much as a synergistic effect between the molecular and the 2D counterparts.

We have observed that the 2D platform really defines some properties of the systems with which it interacts, such as the particle size, oxidation and magnetic states, PL, or freedom degree. We have discovered exciting novel composites beyond the simple physical mixing of their components. Therefore, the compendium of results collected in this manuscript, potentially profitable in materials science and nanotechnology, represents a modest contribution to the rich chemistry of TMDCs.

At this point, it is important to remark that the manipulation of MoS_2 was not exempt from difficulties. On one hand, the metastable nature of ce-MoS_2 layers compels to use the freshly prepared suspensions as soon as possible, invalidating the possibility of storing them for long periods of time. On the other hand, ce-MoS_2 is susceptible to get oxidized under certain conditions (for example, in the presence of large amounts of PB precursors, as demonstrated in Chapter II). However, the *modus operandi* imposed by MoS_2 not only has allowed us to become familiar with the glovebox and autoclave approach but also to learn the basics of several characterization techniques, such as PXRD, HRTEM, and UV/Vis, FTIR and Raman spectroscopies.

In Chapter II, ce-MoS_2 flakes have been mixed with PB precursors (from $FeCl_3$ and $K_3Fe(CN)_6$) in order to prepare a cathode material suitable for SIBs and KIBs. In Chapter III, ce-MoS_2 flakes have been combined with dia-FeCo cube, giving rise to a photoswitchable composite with paramagnetic properties. In Chapter IV, ce-MoS_2 flakes have been covalently functionalized with a dithienylethene derivative, whose original photoswitching capacity could not be proved post functionalization. Finally, in Chapter V, WS_2/MoS_2 heterostructures were synthesized in a two-step process (non-covalent functionalization of ce-MoS_2 flakes with W_3S_4 cluster followed by thermal treatment under inert atmosphere).

As chemistry has not a lineal progression and every step redefines the next one, there are still open questions and pending tasks that we would like to tackle in the very near future. Concerning the preparation of cathode materials for SIBs and KIBs (explained in Chapter II), it is not yet known why the use of non-oxidized ce-MoS_2 flakes lead to a lower performance of the resultant composite, in contrast to what occurs when fully oxidized layers are employed. In relation to the composite based on photomagnetic FeCo cubes (described in Chapter III), it would be convenient to repeat EPR and photomagnetic measurements, study if the attachment of FeCo-cube to ce-MoS_2 flakes affects the properties of the underlying 2D material, and test the capacity of this material for cation exchange. Regarding the covalent functionalization of MoS_2 with dithienylethene molecules (expounded in Chapter IV), it would be interesting to understand which blocking mechanism hinders the photoswitching process after the attachment of the organic system. Respect to the formation of WS_2/MoS_2 heterostructures *via* thermal treatment (detailed in Chapter V), the next steps should be directed to study the photocatalytic activity for water oxidation of the material obtained according to our approach, assess the feasibility of constructing higher quality heterostructures (suitable for physical characterization) starting from me-MoS_2 (instead of ce-MoS_2), and create other interfaces by using the Mo_3S_4 cluster as MoS_2 precursor.

The importance of the present work is that, in principle, the expertise acquired with MoS_2 could be extended to the functionalization of other negative-charged TMDCs. However, one of the current challenges is to find a method that enables the production of massive amounts of high-quality flakes (*i.e.*, clean, ultrathin, large-area, without structural defects) in a fast, low-cost and eco-friendly way. Nowadays, no exfoliation method meets all these criteria. Another interesting aspect would be to selectively control the target region of the functionalization (basal plane or edges) and obtain materials functionalized in both sites with different molecular systems.

Wholeheartedly, we hope that the findings presented here serve to stimulate and spread the "virtues" of MoS_2 among the neophytes (specially, those students that have not chosen the topic of their PhD yet) and provide some guidelines for those doing similar experiments to ours.

VII. **Appendix**

VII.1. Estimation of the concentration from UV/Vis data

In order to calculate the concentrations of the obtained suspensions, we used the following equation:

$$\text{Absorbance}_{350nm} = 0.011935 + 12029[\text{Conc. (M)}]$$

This equation was determined from a calibration curve with a lineal fitting (see **Figure VII-1**). For this end, several aliquots of known volume from different aqueous suspensions of ce-MoS_2 flakes were filtered by using a nitrocellulose filter membrane. The amount of MoS_2 collected on the filter was calculated by weighting the membrane before and after the filtration/drying process and calculating the mass difference. Then, the absorbance registered at 350 nm was plotted against the concentration in M units. This latter is the result of dividing the mols of MoS_2 (from the mass collected on the membrane) by the volume of the filtered aliquot. We chose the absorbance at 350 nm since, at this value, there is a strong contribution from 1T-MoS_2, in addition to a local minimum in 2H-MoS_2.[1]

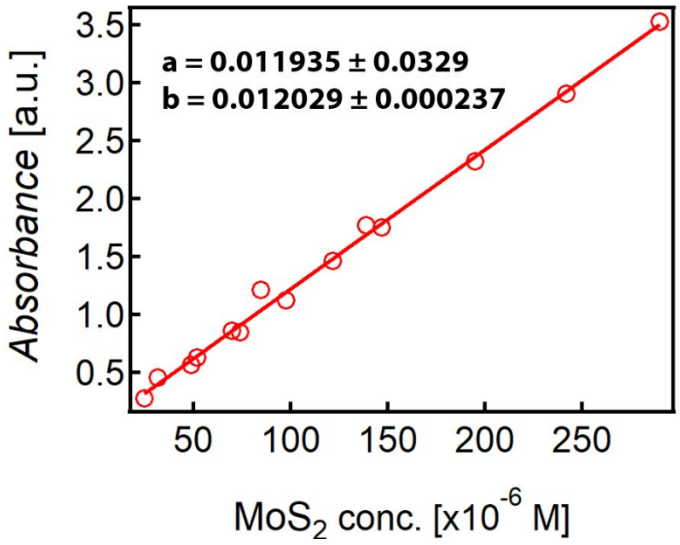

Figure VII-1. Absorbance vs MoS_2 concentration plot used for determining the calibration curve (a = y-intercept, b = slope).

VII.2. Details about Mössbauer spectra data treatment

Mössbauer data were fitted with the model described in detail in reference 2: one doublet attributed to LS Fe^{II} and one singlet and two doublets assigned to HS Fe^{III} (all the peaks having the same line widths, Γ). The areas and widths of both peaks in a quadrupole doublet were constrained to remain equal during the refinement procedure.[3] In the case of LS Fe^{II}, only a broad peak is observed because the quadrupole splitting (QS) of the corresponding doublet is lower than the line widths of the peaks. This model reflects the different Fe^{III} electronic environments and leads to refined Γ values closer to those observed for the inner lines of the α-Fe calibration spectra (0.26 mm s^{-1}). The estimated isomer shifts (ISs) relative to metallic α-Fe at 295K and QSs shown in **Figure II-14**) are in very good agreement with those found in the literature for Prussian blue compounds. The relative areas A^{II} and A^{III} reported in reference 2 for LS Fe^{II} and HS Fe^{III} within the 4–295 K range are equal within experimental error, which suggests that the recoilless factors for both species are not very different and the estimated A^{II} and A^{III} may be considered a good approximation of the fraction of Fe atoms present as LS Fe^{II} and HS Fe^{III}. The estimated parameters from the Mössbauer spectra of sample **1** collected at 295 K are presented in **Table VII-1**.

Table VII-1 Estimated parameters from the Mössbauer spectra of 1 taken at 295 K. Γ = full width at half height. Estimated errors are ≤ 0.02 mm s^{-1} for IS and QS and ≤ 2% for A.

Sample	IS (mm/s)	QS (mm/s)	Γ (mm/s)	A (%)	Fe species
1	-0.14	0.16	0.29	42	Fe^{II} S = 0
	0.41	0.00	0.29	4	Fe^{III} S = 5/2
	0.41	0.52	0.29	42	Fe^{III} S = 5/2
	0.41	1.02	0.29	12	Fe^{III} S = 5/2

VII.3. Formulae applied to electrochemical data

The specific capacity, Q (in mA h g^{-1}), was calculated from the cyclic chronopotentiometric measurements according to the following equation:

$$Q = I \cdot t/m$$

where "I" (in mA) is the charge/discharge current, "t" (in h) is the time and, "m" (in g) is the mass of the active material in the electrode.

The specific capacitance, C (in F g^{-1}), was calculated from the cyclic chronopotentiometric curves according to the following equation:

$$C = I \cdot \Delta t/(m \cdot \Delta V)$$

where I (in A) is the charge/discharge current, Δt (in s) is the time for a full charge or discharge, m (in g) the mass of the active material in the electrode, and ΔV (in V) is the voltage change after a full charge or discharge.

The electrode current changes with scan rate can be described using the power law equation:

$$I = a \cdot v^b$$

where I (in A) is the peak current and v (in mV s^{-1}) is the scan rate. As general rule, the electrochemical reaction would be a surface-limited (*i.e.*, capacitive) process if the value of a is close to 1, whereas it would be a diffusion-controlled mechanism for a value of b close to 0.5.[4]

The plot of log(I) versus log(v) provides an almost perfect linear dependence with a "b" value close to 0.5 for both Na^+ and K^+ insertion.

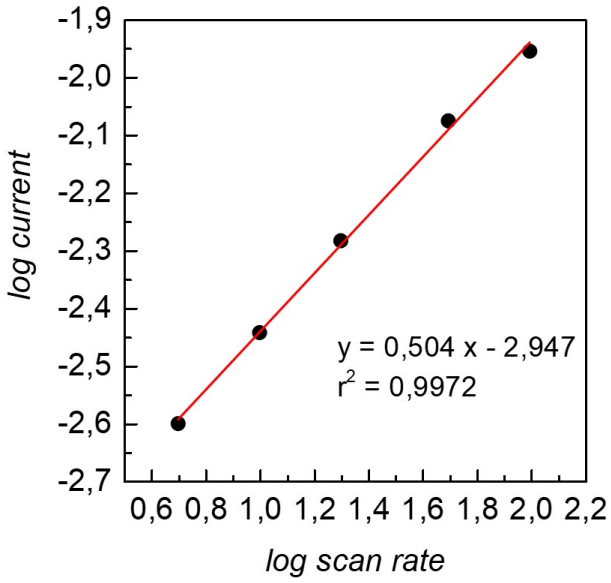

Figure VII-2. Log(peak current) versus log(scan rate) for 1 M Na_2SO_4 solution at different scan rates.

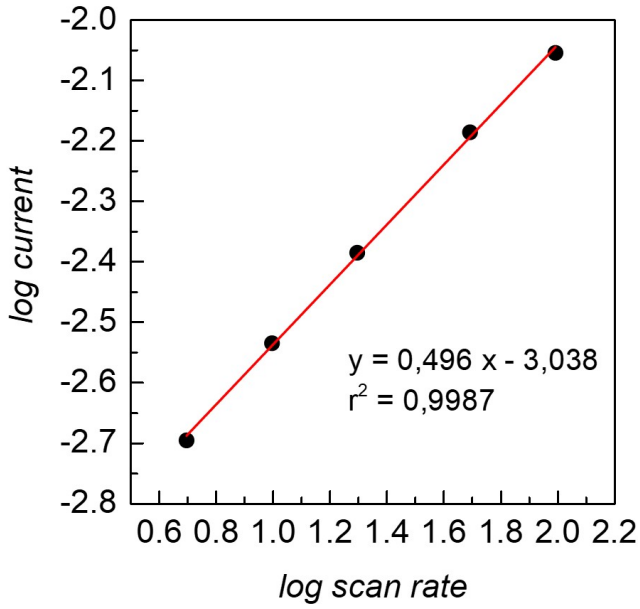

Figure VII-3. Log(peak current) versus log(scan rate) for 0.5 M K_2SO_4 solution at different scan rates.

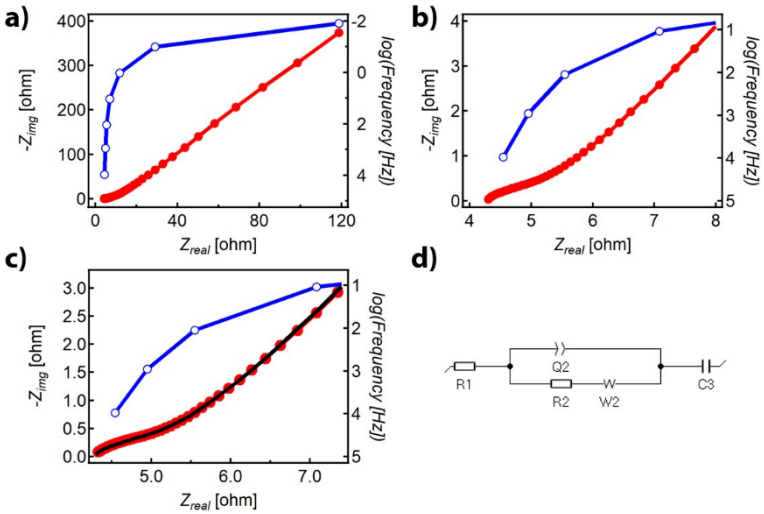

Figure VII-4. ACI diagram of the KIB cathode before charge/discharge cycles treatment in 0.5 M K_2SO_4 aqueous solution. The frequency is given in a logarithmic scale in the graph; b) Inset of "a)" in the 4–8 ohm range; c) Fit for the equivalent circuit described in the scheme "d)"; d) Circuit that represent the present electrochemical system. The frequency range for the experiment and fit is 0.1–10 mHz and 0.1–10 Hz. X^2 is least for the model (0.2237).

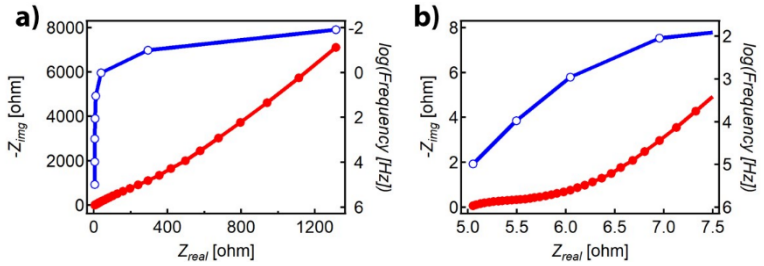

Figure VII-5. a) ACI diagram of the pristine carbon felt in 0.5 M K_2SO_4 aqueous solution. The frequency is given in a logarithmic scale in the graph. Frequency range for the experiment: 0.1–10 mHz; b) Zoom of "a)" in the 4–8 ohm range.

VII.4. References

1. Knirsch, K. C. *et al.* Basal-Plane Functionalization of Chemically Exfoliated Molybdenum Disulfide by Diazonium Salts. *ACS Nano* **9**, 6018–30 (2015).

2. Grandjean, F., Samain, L. & Long, G. J. Characterization and utilization of Prussian blue and its pigments. *Dalt. Trans.* **45**, 18018–18044 (2016).

3. Waerenborgh, J. C. *et al.* Influence of thermal treatment and crystal growth on the final composition and magnetic properties of the YFe_xAl_{12-x} ($4 \leq x \leq 4.2$) intermetallics. *Chem. Mater.* **12**, 1743–1749 (2000).

4. Lindström, H. *et al.* Li^+ ion insertion in TiO_2 (anatase). 2. Voltammetry on nanoporous films. *J. Phys. Chem. B* **101,** 7717–7722 (1997).

Resumen en castellano

El objetivo principal de esta Tesis es el estudio de la funcionalización de láminas bidimensionales de disulfuro de molibdeno (MoS_2) mediante el uso de diferentes sistemas de base molecular. En el transcurso del doctorado, hemos dirigido gran parte de nuestros esfuerzos a la preparación de nuevos materiales basados en láminas de MoS_2, con el fin de explotar los efectos sinérgicos existentes en materiales de tipo composite (también llamados composites) o modular las propiedades prístinas del MoS_2.

El presente manuscrito se divide en los siguientes apartados: seis Capítulos (uno de carácter introductorio, cuatro de contenido más específico y un compendio de conclusiones y perspectivas generales) y, por último, un apéndice con detalles técnicos referentes al Capítulo II. Para un mayor entendimiento, la sección experimental (organizada en materiales, métodos y técnicas de caracterización) se ha incluido al final de cada Capítulo.

Los **nanomateriales** (materiales diseñados a la carta en los que al menos una de sus dimensiones espaciales es menor o equivalente a 100 nm) han revolucionado prácticamente todas las áreas de la ciencia y tecnología ya que sus propiedades, distintas a las de sus correspondientes sólidos extendidos, vienen determinadas por el fuerte confinamiento quántico y efectos de superficie (mayor relación superficie/volumen). Por tanto, la posibilidad de establecer un control fino sobre la dimensionalidad del material sintetizado no solo permite la modulación de sus propiedades físicas y químicas sino también la posibilidad de miniaturizar dispositivos y máquinas.

En función del número de dimensiones espaciales que exceden la escala nanométrica (1 nm = 10^{-9} m), los nanomateriales pueden clasificarse en materiales de dimensión cero (**0D**), unidimensionales (**1D**) o bidimensionales (**2D**). Algunos ejemplos arquetípicos son los siguientes: nanopartículas (0D), nanocables (1D) y nanoláminas (2D).

Como esta Tesis está enmarcada en el contexto de los **materiales 2D**, el estudio de las otras categorías transciende nuestro objetivo. En

primer lugar, cabe aclarar que, desde una perspectiva lingüística, la expresión "materiales 2D" se ha extendido y se utiliza comúnmente no sólo para designar estrictamente monocapas bidimensionales (con espesor monoatómico), sino también materiales ultrafinos de pocas capas (bi-, tri-), es decir, materiales altamente anisotrópicos. Asimismo, incluso el material bulk, formado por láminas apiladas y susceptible de ser exfoliado en láminas ultrafinas, es habitualmente denominado también como "material 2D", siendo el contexto el que define finalmente el significado. En esta Tesis, dicho término hará referencia a los materiales ultrafinos (de una o pocas capas) con una marcada anisotropía en el plano 2D. Las características generales de estos materiales son que sus electrones solo se mueven libremente en el plano y que la mayor parte de los átomos que los constituyen se encuentra en la superficie (es decir, hay un mayor número de átomos expuestos al ambiente químico). Esta última característica hace que dichos materiales sean más reactivos que sus análogos tridimensionales (3D).

El grafeno, el primer material 2D en ser descubierto, fue aislado de un cristal de grafito mediante cinta adhesiva. Y, una vez probada su estabilidad, la comunidad científica se volcó en la búsqueda y estudio de otros ejemplos 2D, como los TMDCs de naturaleza laminar.

Los **TMDCs de naturaleza laminar** son compuestos formados por capas apiladas de tipo X-M-X. Su fórmula química general es MX_2, en donde M representa un metal de transición (generalmente, de los grupos IV-VII) y X, un calcogenuro (S, Se o Te). Dentro de cada capa X-M-X, una red de M está intercalada entre dos redes de X. Como las interacciones de van der Waals (vdW) entre láminas adyacentes son mucho más débiles que los enlaces covalentes dentro de cada lámina, se pueden obtener monocapas X-M-X por exfoliación con relativa facilidad. Esta familia de compuestos ofrece un amplio abanico de propiedades electrónicas que pueden variar drásticamente en función de la composición (naturaleza de M y X), estructura (politipo) y dimensionalidad (número de capas X-M-X). Esta versatilidad electrónica abarca propiedades tan diversas como carácter metálico, superconductor o semiconductor.

En su forma *bulk*, el **MoS_2** puede describirse como un apilamiento de capas S-Mo-S a través de interacciones débiles de vdW, en donde cada

átomo de Mo se encuentra coordinado a 6 átomos de S en una disposición trigonal prismática (politipos 1H, 2H y 3R) u octaédrica (politipo 1T). Cada politipo viene representado por un código alfanumérico. El dígito hace referencia al número de capas S-Mo-S por celda unidad, mientras que la letra designa la simetría estructural (T = tetragonal, H = hexagonal o R = romboédrica). De entre todos los **politipos del MoS_2**, los más conocidos son el 1T y el 2H (o 1H para el caso particular de la monocapa).

El **2H-MoS_2** en su forma *bulk* es químicamente inerte y termodinámicamente estable. Existe en la naturaleza como mineral de molibdenita. Las láminas finas de 1T/2H-MoS_2 suelen sintetizarse por aproximación hidrotermal o solvotermal, o deposición química de vapor (CVD). Su comportamiento diamagnético y semiconductor se debe al llenado completo del orbital d_{z^2} (2 electrones con espines apareados). Este semiconductor experimenta una transición de banda prohibida indirecta a banda prohibida directa (1.29 eV→1.90 eV), al pasar de *bulk* (2H) a monocapa (1H), respectivamente. Además, en su forma 1H, exhibe fotoluminiscencia (PL). Como el valor de la banda prohibida depende del número de capas que constituyen la estructura del MoS_2, este politipo se usa ampliamente en la fabricación de dispositivos electrónicos, como los transistores de efecto campo (FETs).

El **1T-MoS_2** tiene origen sintético y se puede preparar de múltiples maneras (intercalación de cationes seguida de exfoliación, síntesis hidrotermal o solvotermal, tratamiento con plasma de argón, etc.). Este politipo es metaestable y puede sufrir distorsiones estructurales, dando lugar a otros politipos inestables con dimerización o trimerización de átomos de Mo. Su comportamiento paramagnético y metálico viene determinado por el llenado parcial de los orbitales t_{2g} (2 electrones desapareados situados en diferentes orbitales). El comportamiento metálico, junto con la presencia de abundantes sitios activos tanto en el plano basal como en los bordes, le confiere excelentes propiedades electrocatalíticas. Además, este politipo presenta una mayor distancia entre láminas consecutivas, hidrofilia y transparencia óptica.

La **transición 1T→1H/2H** se puede dar tanto por tratamiento térmico como por irradiación con láser, exposición controlada a microondas o envejecimiento de la muestra.

A pesar de que láminas ultrafinas de MoS_2 pueden crecerse directamente a partir de sus componentes por complejos métodos *bottom-up* (por ejemplo; CVD), una de las técnicas más recurrentes a la hora de obtener láminas finas de MoS_2 es la **exfoliación** a partir del material en forma *bulk*. Esta se clasifica en dos grandes categorías: exfoliación seca (mecánica) y exfoliación húmeda (mecánica, química o electroquímica).

La **exfoliación seca** de MoS_2 se basa en el uso de cinta adhesiva o sellos de naturaleza polimérica, de tal manera que la interacción cristal-polímero es más fuerte que la existente entre láminas adyacentes. Al separar ambos sistemas, se rompen y extraen planos cristalinos procedentes de la muestra madre. La operación de contactar y despegar la cinta o sello del cristal de MoS_2 se puede repetir tantas veces como se desee, siendo posible incluso llegar al límite de la monocapa.

A pesar de que la exfoliación seca es compatible con la obtención de monocapas de alta calidad (idóneas para el estudio de las propiedades físicas y fabricación de nanodispositivos), el rendimiento es muy bajo.

Así pues, para producir monocapas de MoS_2 a gran escala, la opción más recomendable es la **exfoliación por vía húmeda**, dentro de la cual podemos diferenciar tres grandes aproximaciones: **exfoliación en fase líquida** (**LPE**), **exfoliación química** y **exfoliación electroquímica**. La LPE consiste en aplicar varias fuerzas mecánicas sobre un cristal sumergido en un disolvente o mezcla de disolventes, en ausencia o presencia de surfactantes. Por contra, en la exfoliación química, se antepone una etapa de intercalación a la exfoliación *per se*. Generalmente, se intercalan cationes alcalinos (Li^+, Na^+ o K^+), cuya inserción reduce la adhesión entre capas de S-Mo-S adyacentes. Además, la exfoliación en agua tiene como consecuencia la generación de hidrógeno dentro del espacio interlaminar, lo cual favorece aún más la separación entre láminas. Las láminas obtenidas a partir de intercalación de cationes alcalinos presentan un exceso de carga negativa sobre su superficie (reducción química), cuantificable mediante medidas de potencial zeta (ZP). Finalmente, la exfoliación electroquímica es una exfoliación química, en la que la intercalación se realiza electroquímicamente, favoreciendo un mayor control sobre el grado de intercalación del material.

Las láminas de MoS_2 obtenidas por exfoliación también pueden integrarse en un **material de tipo composite** (en donde el material 2D se combina generalmente con otro/s de base molecular), siendo ésta una estrategia perfecta para superar las limitaciones inherentes de dicho compuesto o bien potenciar/optimizar algunas de sus propiedades de cara a una aplicación específica. El composite se caracteriza por presentar interfases claramente distinguibles y mejores propiedades con respecto a sus componentes por separado. El mejor rendimiento de los composites se debe a la aparición de efectos sinérgicos entre sus componentes. Entre las estrategias sintéticas más usadas, destacan las siguientes: *i*) mezcla directa de los componentes en cuestión con reacción química específica entre ellos (funcionalización del MoS_2) o sin ella, *ii*) CVD de un componente sobre otro, *iii*) mezcla de los precursores del MoS_2 con otro/s componentes a temperatura ambiente o mediante síntesis hidro/solvotermal.

En este escenario, la **funcionalización molecular** del MoS_2 es de especial interés ya que con ella se va más allá de la exfoliación, estudio y aplicación de los materiales 2D puros. En la preparación de nuevos materiales, la funcionalización molecular abre muchas posibilidades ya que permite incorporar grupos funcionales sobre la superficie, modificar las propiedades originales del material exfoliado, combinar las propiedades del material 2D con las de otros sistemas o crear efectos sinérgicos entre los componentes interconectados.

Así pues, el MoS_2 exfoliado se puede funcionalizar de manera **no covalente** (**Capítulos II**, **III** y **V**), coordinativa o covalente (**Capítulo IV**). Dentro de la funcionalización covalente, se distinguen dos subcategorías: la que explota las vacantes de azufre (naturalmente presentes o creadas *ad hoc* en la estructura cristalina) y la covalente directa. Mientras que la primera se basa en el uso de tioles o derivados, la segunda explota el carácter electrofílico de especies tales como organohalogenados, sales de diazonio y maleimidas.

Antes de entrar en materia, es conveniente dar ciertos detalles sobre la metodología seguida para preparar las láminas finas de MoS_2. Las láminas se han obtenido por **exfoliación química** basada en el uso del ***n*-butil-litio** (***n*-BuLi**). En nuestro caso, el polvo cristalino comercial en fase 2H-MoS_2 se mezcla con una disolución 1.6 M de *n*-BuLi en hexano y se calienta durante 2 h a 100 ºC en atmósfera inerte (dentro

de un autoclave previamente cargado en caja seca). Después, el producto de la reacción se filtra y lava con hexano a fin de eliminar los posibles restos de *n*-BuLi (también en caja seca). A continuación, el material intercalado se mezcla con agua y se dispersa en baño de ultrasonidos. La dispersión resultante se dializa para eliminar el LiOH formado durante la reacción de hidratación, se sonica durante 30 min y, finalmente, se centrifuga a 750 rpm durante 30 min para descartar el material peor exfoliado. A partir de este método, obtenemos láminas finas de MoS_2, en fase mayoritariamente 1T y con carga superficial negativa, la cual les confiere estabilidad en suspensión acuosa y mayor reactividad.

En el **Capítulo II**, se ha investigado la posibilidad de formar un composite con aplicaciones potenciales en el campo de las baterías de ion sodio y potasio (SIBs y KIBs, respectivamente) combinando láminas finas de MoS_2 con $K_3Fe(CN)_6$ y $FeCl_3$ (que actúan como precursores del **azul de Prusia**, **PB**).

El PB es un compuesto de valencia mixta con una estructura altamente porosa, a través de la cual pueden difundir cationes alcalinos. Su fórmula química es $A_xFe^{III}[Fe^{II}(CN)_6]_y\cdot\square_{1-y}\cdot nH_2O$, donde A hace referencia a un metal alcalino (K o Na) y $\square$, a las vacantes de $[Fe^{II}(CN)_6]^{4-}$ ocupadas por moléculas de agua coordinadas al Fe^{III} ($0 < x < 1$; $0.75 < y < 1$).

La idea de partida era aprovechar la carga negativa acumulada en la superficie de las láminas a fin de inducir la reducción parcial de Fe^{III} a Fe^{II} en el compuesto $K_3Fe(CN)_6$ y favorecer la nucleación *in situ* del PB sobre las mismas. La formación de PB en el composite se comprobó principalmente por difracción de rayos X en polvo (PXRD), espectroscopía Raman y espectroscopía infrarroja de transformada de Fourier (FTIR). Sin embargo, en contra de lo esperado, no se detectaron señales características del MoS_2 en ningún difractograma o espectro a pesar de que, según las imágenes de microscopía electrónica de transmisión (TEM), el material resultante seguía presentando una morfología laminar. Además, el mapeo de los diferentes elementos mostraba una clara correlación entre las señales del MoS_2 (Mo y S) y aquellas provenientes del PB (K, Fe y N). Tras analizar la muestra por espectroscopía de fotoelectrones emitidos por rayos X (XPS), se

averiguó que las láminas estaban oxidadas (Mo^{V} y Mo^{VI} como resultado de la formación de láminas de H_xMoO_3 y/o MoS_xO_x.

Las medidas de absorción/desorción de N_2 evidenciaron que las partículas de PB crecidas sobre las láminas, tenían un área superficial específica tres veces mayor que la observada en otros composites similares basados en óxido de grafeno y PB. La relación Fe^{II}:Fe^{III} (≈0.75) se determinó por espectroscopía Mössbauer y las relaciones molares K:Fe (≈0.07) y Fe:Mo (≈16), por espectrometría de emisión atómica de plasma acoplado inductivamente (ICP-OES). Por otro lado, las curvas de análisis térmico gravimétrico y el análisis elemental sirvieron para estimar el contenido de agua y azufre presente en el composite, respectivamente. Así pues, teniendo en cuenta todos estos datos, se extrajo la siguiente fórmula química: $(K_{0.47}Fe_4^{III}[Fe^{II}(CN)_6]_{3.14})@(MoSO_{1.7})_{0.44}\cdot 26H_2O$.

Una vez determinada la fórmula, se llevó a cabo la funcionalización de redes extendidas de láminas obtenidas por exfoliación química previamente depositadas sobre sustratos de SiO_2 (285 nm)/Si con dos concentraciones diferentes. También se estudió la influencia de la carga negativa de las láminas de MoS_2 en la formación del PB. Para ello, se usaron dos sustratos de SiO_2 (285 nm)/Si con láminas de MoS_2 obtenidas por métodos físicos. Uno de ellos se sumergió en una disolución de *n*-BuLi (1.6 M) en hexano con la finalidad de reducir el MoS_2. A continuación, se dispersó una disolución acuosa de $K_3Fe(CN)_6$:$FeCl_3$ sobre ambos sustratos. Las medidas de microscopía atómica de fuerzas (AFM) revelaron que sólo las láminas previamente cargadas desarrollaban una cobertura de PB, evidenciándose así el papel clave de dicho exceso de carga negativa en la formación de PB.

Finalmente, los resultados de las medidas electroquímicas (excelentes valores de capacidad de descarga y capacitancia específica y elevados porcentajes de capacidad de retención) realizadas en tres disoluciones acuosas de Na_2SO_4 (1 y 0.5 M) y K_2SO_4 (0.5 M) atestiguaron el potencial de este composite como cátodo en el campo de las SIBs y KIBs. El alto rendimiento del composite totalmente oxidado como material de tipo cátodo para SIBs y KIBs se atribuyó al efecto sinérgico entre la matriz 2D (que aportaba resiliencia al sistema y determinaba la morfología con la que crecían las partículas de PB) y los cristales nanométricos de PB (que favorecían el acceso de Na^+ and K^+ a los

huecos, mejoraban la difusión catiónica y aliviaban la tensión inducida por los cambios de volumen durante los ciclos de carga y descarga). La mejora observada al usar K_2SO_4 como electrolito podría responder al hecho de que el PB se sintetizó a partir de $K_3Fe(CN)_6$, dando lugar a una estructura con poros de tamaño óptimo para la difusión de los cationes K^+. Al final del Capítulo, se explica cómo evitar la oxidación de las láminas de MoS_2 durante la formación del composite jugando con la estequiometría de los reactivos y el tiempo de reacción. No obstante, las medias electroquímicas preliminares del composite no oxidado arrojaron peores valores de capacitancia específica, en comparación con las del composite totalmente oxidado.

En el **Capítulo III**, dentro aún del campo de los composites basados en la familia del PB (**análogos del PB** con otros metales de transición: **PBA**), se describe el trabajo realizado con **sistemas moleculares discretos**, donde su estequiometría se controla en mucho mayor grado que en su forma extendida. Así, en este Capítulo, se ha reportado la síntesis de un nuevo composite ($FeCo@MoS_2$) preparado a partir de láminas de MoS_2 y un análogo de azul de Prusia discreto de carácter diamagnético, $Cs\subset\{[Fe^{II}(Tp)CN)_3]_4[Co^{III}(Tp)]_4\}ClO_4$ (abreviado como cubo dia-FeCo), donde el símbolo $\subset$ indica que el Cs está dentro de la cavidad cúbica y Tp se refiere al ligando tris(pirazolil)borato. Las medidas de XPS de $FeCo@MoS_2$ pusieron de manifiesto la coexistencia de Co^{III} y Co^{II}, y las medidas magnéticas de SQUID, el carácter fotomagnético del nuevo composite. Todos estos resultados inesperados se relacionaron con la formación de la especie $Cs\subset\{[Fe^{II}(Tp)CN)_3]_4[Co^{III}(Tp)]_3[Co^{II}(Tp)]\}$ (abreviada como cubo para-FeCo), siendo el Co^{II} en estado de alto espín, la causa del nuevo carácter paramagnético, confirmado también mediante las medidas de espectroscopía de resonancia paramagnética (EPR). Por medio de los datos de XPS (Fe:Mo ≈2.01, Fe:Co ≈1.03, ausencia de Cl), se determinó la fórmula química del composite: $Cs\subset\{[Fe^{II}(Tp)CN)_3]_4[Co^{III}(Tp)]_3[Co^{II}(Tp)]\}\cdot[MoS_2]_2$. Curiosamente, en el espectro de resonancia magnética nuclear (RMN) de ^{133}Cs, se detectaron dos señales (una correspondiente al cubo dia-FeCo y la otra al cubo para-FeCo). La explicación más plausible a este hecho es que probablemente, en disolución, se establece un equilibrio entre ambos sistemas. En esencia, el método descrito en este Capítulo permite decorar la superficie del MoS_2 exclusivamente con el cubo para-FeCo

aprovechando la transferencia electrónica que ocurre desde las láminas de MoS_2 al cubo dia-FeCo de partida, el cual es más fácil de sintetizar y aislar. La importancia de dicho composite es que podría tener aplicaciones interesantes en el campo de los sensores, la electroquímica o la fotoelectrónica.

En el **Capítulo IV**, se ha llevado a cabo la funcionalización de MoS_2 con **moléculas "photoswitchables"** de la familia de los ditieniletenos, a fin de modular las propiedades del material 2D mediante la modificación de la estructura del componente molecular a través de un estímulo externo (luz). Para ello, se ha recurrido a la funcionalización covalente de láminas de MoS_2, usando en este caso sales de diazonio generadas a partir de un derivado de ditieniléteno (DD-NH_2) fotocrómico, tanto en su forma abierta (ODD-NH_2, con apertura de ciclo) como cerrada (CDD-NH_2, fotociclada). El MoS_2 funcionalizado (ODD-MoS_2 y CDD-MoS_2) se caracterizó mediante diferentes técnicas. Por un lado, lo espectros de FTIR revelaron la presencia de vibraciones C–H características de bencenos sustituidos en posición *para*, así como la ausencia de señales asociadas a grupos diazonio. Esto último también se demostró por XPS (región espectral de N 1s dominada únicamente por señales de Mo). Además, los resultados de XPS pusieron de relieve una transformación 1T→2H de carácter cuantitativo. Por otro lado, los espectros Raman indicaron coexistencia de señales de MoS_2 y molécula orgánica. Todos estos resultados sirvieron para verificar de manera indirecta la funcionalización covalente. Las diferencias observadas entre los espectros Raman de ODED-MoS_2 y CDED-MoS_2 se relacionaron con la estructura (abierta o cerrada) de la molécula orgánica. Asimismo, los estudios de PL dejaron constancia de una posible transferencia de carga entre los dos sistemas interactuantes a través del enlace covalente. El porcentaje de funcionalización se calculó a partir de las curvas de TGA de ODED-MoS_2 y CDED-MoS_2 (24.3% y 18.8% para ODD-MoS_2 y CDD-MoS_2, respectivamente). Desafortunadamente, en ningún experimento de irradiación, se pudo probar la fotoconversión de los sistemas orgánicos, lo que parece indicar que el componente laminar bloquea la interconversión de la molécula entre sus dos estados.

En el **Capítulo V**, se ha desarrollado un nuevo método para preparar **heterostructuras de WS_2/MoS_2** a partir del tratamiento térmico de láminas de MoS_2 funcionalizadas electrostáticamente con

$[W_3S_4(tu)_8(H_2O)]Cl_4 \cdot 2H_2O$ (W_3S_4, en adelante), un **clúster trimetálico de tungsteno** previamente reportado en literatura. El método en cuestión consta de dos etapas. Mientras que la primera transcurre en disolución y favorece una distribución homogénea de W_3S_4 sobre el material 2D sin efectos significativos de agregación, la segunda tiene lugar en estado sólido y garantiza la eliminación de todos aquellos residuos orgánicos que pudieran debilitar la interacción entre las entidades laminares de MoS_2 y WS_2. Antes de abordar la preparación de la ya mencionada heterostructura, se profundizó un poco más en el estudio del clúster W_3S_4 una vez calcinado, completándose así el proceso de caracterización iniciado por algunos de nuestros colaboradores años atrás, con imágenes de TEM de alta resolución (HRTEM) y espectros de XPS y Raman. Mientras que las imágenes de HRTEM confirmaron la naturaleza laminar del material calcinado, el espectro de XPS de W confirmó la presencia de W^{IV}. Por otro lado, la naturaleza del material (WS_2) y su espesor (bicapas y/o tricapas, como máximo) se determinaron por espectroscopía Raman. Después de dicha caracterización, se abordó la funcionalización no covalente de las láminas de MoS_2 con el clúster W_3S_4 en disolución. La distribución de los clústeres sobre la superficie del MoS_2 se pudo visualizar por HRTEM. El estudio de XPS, además de indicar la coexistencia de 1T-MoS_2 y 2H-MoS_2, confirmó de nuevo que el material no se había oxidado (W^{IV}). No obstante, en el espectro Raman, no se observaron señales claras provenientes del clúster. Después de calcinar el composite anterior de la misma manera en que se procedió con el clúster W_3S_4 para obtener láminas de WS_2, las imágenes de HRTEM demostraron la existencia de nanodominios cristalinos asociados a la formación de WS_2, mientras que las posiciones de los picos XPS del S eran consistentes con las de los dicalcogenuros MoS_2 y WS_2. El espesor de los nanodominios de WS_2 (monocapas y/o bicapas como máximo) también se determinó por espectroscopía Raman. Por último, se observó atenuación en la PL de los componentes integrantes de la heterostructura, probándose así un acoplamiento interlaminar eficiente entre ambos. Por tanto, cabe destacar que la estrategia sintética aquí propuesta combina las ventajas típicas de un método en disolución (sencillez, escalabilidad y bajo coste) con la posibilidad de formar interfases de buena calidad, sin necesidad de recurrir a métodos físicos más complejos, como el CVD, la deposición física de vapor (PVD) o el ensamblado directo de ambos componentes.

En el **Capítulo VI**, se plasman las **conclusiones generales** de la Tesis:

En esta Tesis, se han descrito varios ejemplos de funcionalización covalente y no covalente de MoS_2 (exfoliado químicamente) con diferentes sistemas de base molecular, con objeto de explotar las características emergentes de los composites resultantes.

También hemos observado que la plataforma 2D modifica algunas de las propiedades de los sistemas con lo que interactúa, como el tamaño de partícula, los estados de oxidación, el comportamiento magnético, la PL o los grados de libertad. El compendio de resultados recogidos en estas páginas representa una modesta aportación al extenso campo de la química de los TMDCs.

Llegados a este punto, cabe destacar que la manipulación de las láminas obtenidas por exfoliación química entraña serias dificultades. Por un lado, la naturaleza metaestable del material obliga a darle un uso casi inmediato, invalidando la posibilidad de almacenarlo durante un tiempo prolongado. Por otro lado, hay que tener en cuenta que el MoS_2 exfoliado es susceptible de sufrir oxidación (por ejemplo, en presencia de una alta concentración de precursores de PB, tal y como se demostró en el Capítulo II). Sin embargo, el particular *modus operandi* impuesto por el MoS_2 no solo nos ha permitido familiarizarnos con autoclaves y cajas secas sino también conocer los fundamentos de algunas técnicas de caracterización.

Como la química no tiene una progresión lineal y cada paso redefine la dirección de avance del siguiente, no es de extrañar que hayan quedado algunas cuestiones abiertas y tareas pendientes. En relación con la preparación de materiales con potenciales aplicaciones en SIBS y KIBs (Capítulo II), se desconocen aún los motivos por los que el uso de láminas de MoS_2 no oxidado da lugar a un composite de menor rendimiento como material de tipo cátodo, a diferencia de lo que ocurre cuando se utilizan láminas totalmente oxidadas. Por lo que respecta al composite FeCo@MoS_2 (Capítulo III), sería interesante profundizar un poco más en las medidas fotomagnéticas y de resonancia paramagnética electrónica (EPR), estudiar la influencia del cubo FeCo sobre las propiedades del MoS_2 subyacente y testear la capacidad de intercambio catiónico del composite resultante. Respecto a la funcionalización covalente de MoS_2 con moléculas de ditienileteno (Capítulo IV), sería interesante averiguar qué mecanismo de bloqueo

impide la interconversión mediante luz de los sistemas orgánicos una vez anclados a la superficie del MoS_2. En cuanto a la formación de las heterostrucuras WS_2/MoS_2 por tratamiento térmico (Capítulo V), los próximos pasos deberían encaminarse al estudio de la actividad fotocatalítica de nuestro material en los procesos de oxidación de agua, la formación de heterostrucuras WS_2/MoS_2 de alta calidad (idóneas para la caracterización física) a partir de láminas de MoS_2 obtenidas por exfoliación mecánica y la creación de otras interfases usando el clúster Mo_3S_4 como precursor de MoS_2.

La importancia de esta Tesis es que los conocimientos extraídos de los experimentos realizados con MoS_2, en principio, podrían aplicarse a la funcionalización de otros TMDCS, siempre y cuando puedan prepararse como láminas cargadas negativamente. Sin embargo, hoy en día, el reto consiste en encontrar un método que permita la producción masiva de láminas de alta calidad (es decir, limpias, ultrafinas, de gran superficie y sin defectos estructurales) de manera más rápida, económica y sostenible. Actualmente, ningún método reúne todos estos requisitos. Otro aspecto interesante podría ser el control selectivo sobre la región en la que tiene lugar la funcionalización (plano basal o bordes) y obtener materiales funcionalizados en ambas áreas con diferentes sistemas moleculares.

Esperamos francamente que todos estos hallazgos sirvan para estimular y difundir las virtudes del MoS_2 entre los neófitos, y orientar a aquellos investigadores que estén llevando a cabo experimentos similares a los nuestros.